JOHANNES GUTENBERG UNIVERSITÄT MAINZ

JG|U

Investigations of Spin-excitations and Intramolecular-exchange Interaction of Mixed 3d-4f Molecular Moments Using Scanning Tunneling Microscopy and X-ray Magnetic Circular Dichroism

---

Dissertation submitted for the award of the title

"Doctor of Natural Sciences"

to the Faculty of Physics, Mathematics, and Computer Science

Johannes Gutenberg University Mainz

Submitted by

Ahmed H. E. Alhassanat

Born 15^{th} August 1989 in Doha, Qatar

Mainz, 13 January 2025

Thesis Advisors:

Prof. Dr. Hans-Joachim Elmers

[redacted]

Submitted: 13. Jan. 2025

Oral Examination: 02. Apr. 2025

Declaration

I declare that the thesis has been composed by myself and that the work has not been submitted for any other degree or professional qualification. I confirm that the work submitted is my own, except where work which has formed part of jointly-authored publications has been included.

Ingelheim am Rhein, Januaray 13, 2025

Ahmed H. E. Alhassanat

Ahmed Alhassanat
aalhassa@uni-mainz.de

Johannes Gutenberg-Universität
Institut für Physik
KOMET335
Staudingerweg 7, D-55099 Mainz

This work is dedicated to those who have shaped me

To my parents who gave me life, love, and perseverance

To all my teachers who taught me numbers, letters, and Physics

To my people who still struggle to build mosques, schools, and universities

Abstract

Molecular spintronics, a cutting-edge field at the intersection of molecular systems and spin physics, seeks to harness spin degrees of freedom for innovative technological applications. Within this context, diverse molecular systems have attracted considerable interest due to their multifunctionality. This thesis focuses on the magnetic properties of $3d-4f$ mixed-metallic-centered molecules, investigated through scanning tunneling spectroscopy, particularly inelastic electron tunneling spectroscopy (IETS), and x-ray magnetic circular dichroism (XMCD).

In the first part, IETS measurements were performed on the 3d-4f molecule $TbNi_2$. These experiments identified inelastic excitations on the in-plane Fe monolayer and additional excitations in out-of-plane magnetic regions. These variations in excitations suggest possible spin excitation phenomena, offering a foundation for future studies using advanced theoretical approaches to uncover the underlying mechanisms.

The second part explores polynuclear $3d-4f$ 15–MC–5 and 12–MC–4 metallacrowns through XMCD experiments, providing element-specific insights into spin and orbital magnetic moments.

The first XMCD measurement on $RENi_5$[15–MC–5] molecules revealed that antiferromagnetically coupled Ni(II) ions contributed minimally to the overall molecular moment. Rare-earth ions, such as Tb(III) and Dy(III), exhibited spin and orbital moments lower than the expected ionic Hund's rule values, attributed to finite magnetic anisotropy. To explain these discrepancies, a phenomenological model was proposed, enabling the determination of magnetic anisotropy energy barriers at the atomic level. This approach provides a nuanced alternative to conventional macroscopic magnetometry techniques.

Further XMCD studies on $RENi_8$[12–MC–4] double-decker metallacrowns examined the influence of solvents on magnetic properties. A significant spin-state crossover from low-spin to high-spin was observed in Ni(II) ions when dissolved in methanol, attributed to changes in coordination geometry, while dichloromethane preserved the initial spin state. Charge-transfer multiplet calculations supported these findings, underscoring the critical role of ligand fields in shaping spin behavior.

Finally, angular-dependent XMCD experiments on single crystals of $REMn_4$[12–MC–4], with RE=Dy(III) and Tb(III), revealed a fourth-order magnetic anisotropy. This behavior is linked to the anisotropic charge distribution of $4f$ orbitals within the tetragonal crystal field. Crystal-field multiplet simulations validated the experimental results after corrections, showing angular dependence in the magnetic moments of $DyMn_4$, with maxima and minima along the easy and hard axes, respectively.

Zusammenfassung

Molekulare Spintronik, ein innovatives Forschungsgebiet an der Schnittstelle von Molekülchemie und Spinphysik, zielt darauf ab, Spinfreiheitsgrade für technologische Anwendungen zu nutzen. In diesem Kontext haben vielfältige molekulare Systeme aufgrund ihrer vielseitigen Eigenschaften großes Interesse geweckt. Diese Dissertation untersucht die magnetischen Eigenschaften von 3d-4f metallzentrierten Molekülen mithilfe von Rastertunnelspektroskopie, insbesondere inelastischer Elektronentunnelspektroskopie (IETS), und Röntgen-magnetischem Zirkulardichroismus (XMCD).

Im ersten Teil wurden IETS-Messungen an dem 3d-4f Molekül $TbNi_2$ durchgeführt. Dabei wurden inelastische Anregungen auf der in-plane Fe-Monoschicht sowie zusätzliche Anregungen in den magnetischen Regionen außerhalb der Ebene festgestellt. Die Unterschiede in diesen Anregungen deuten auf mögliche Spinanregungen hin und bilden eine Basis für zukünftige Studien, die fortschrittliche theoretische Modelle verwenden, um die zugrunde liegenden Mechanismen zu klären.

Der zweite Teil befasst sich mit XMCD-Studien an polynuklearen 3d-4f 15-MC-5 und 12-MC-4 Metallacrowns, um element-spezifische Spin- und Orbitalmomente der beteiligten Atome zu bestimmen.

Erste XMCD-Messungen an $RENi_5$ [15–MC–5]-Molekülen zeigten, dass die Ni(II)-Ionen antiferromagnetisch gekoppelt sind und nur geringfügig zum Gesamtdrehmoment beitragen. Die Seltenen Erden Tb(III) und Dy(III) zeigten reduzierte Spin- und Orbitalmomente im Vergleich zu den Hund Regelwerten, was auf eine endliche magnetische Anisotropie zurückzuführen ist. Ein phänomenologisches Modell wurde entwickelt, um Energiebarrieren für magnetische Anisotropie auf atomarer Ebene zu bestimmen, wodurch eine genauere Alternative zu makroskopischen Magnetometrie-Methoden geboten wird.

Weitere XMCD-Untersuchungen an $RENi_8$[12–MC–4]-Doppeldeckermetallacrowns untersuchten den Einfluss von Lösungsmitteln auf die magnetischen Eigenschaften. Ein deutlicher Wechsel vom Low-Spin- zum High-Spin-Zustand der Ni(II)-Ionen wurde beobachtet, wenn die Moleküle in Methanol gelöst wurden. Diese Veränderung wird auf eine modifizierte Koordinationsgeometrie zurückgeführt. Im Gegensatz dazu bewahrte Dichlormethan den ursprünglichen Spin-Zustand.
Ladungstransfer-Multiplettberechnungen bestätigten diese Ergebnisse und unterstrichen die zentrale Rolle der Ligandenfelder im Spinverhalten.

Abschließend zeigten winkelabhängige XMCD-Experimente an Einkristallen von $REMn_4$[12–MC–4] mit RE = Dy(III) und Tb(III) eine magnetische Anisotropie vierter Ordnung, die auf die anisotrope Ladungsverteilung der 4f-Orbitale im tetragonalen Kristallfeld zurückzuführen ist. Simulierte Kristallfeld-Multipletts bestätigten die experimentellen Ergebnisse, wobei die magnetischen Momente von $DyMn_4$ eine Winkelabhängigkeit mit Maxima entlang der leichten und Minima entlang der schweren Achsen aufwiesen.

Contents

Chapter 1

Introduction: From Spin to Spintronics

The basic research in physics is curiosity-driven, seeking to uncover new laws of nature, while applied research is more solution-oriented, aimed at addressing specific problems using established fundamental knowledge to ultimately develop new products for the market. Thus, one can think of the basic research as a pacemaker for all technological progress. However, these two types of research are not always distinct; they often overlap and interact, especially when real-world challenges demand new scientific insights [1]. In recent years, the *spintronics* has emerged as a promising field, offering solutions to challenges faced by conventional electronics, such as Joule heating and the limitations of size reduction. This progress requires an in-depth understanding of the electron's spin as an additional degree of freedom in device functionality, beyond just its charge.

In 1921, Otto Stern and Walther Gerlach conducted a pivotal experiment to test Bohr's hypothesis regarding the space quantization of an atom's orbital magnetic moment [2, 3], which is that the electron's orbital angular momentum should be quantized along a particular direction, manifesting in two distinct orientations conventionally referred to as "up" and "down".

In their experiment, silver atoms were vaporized in a furnace within a vacuum system, maintained by a mercury-diffusion pump, which allowed the atoms to travel unimpeded through the apparatus. The silver atoms were then passed through two collimators to form a narrow beam, which was subsequently exposed to an inhomogeneous magnetic field, as illustrated in Fig. 1.1. The inhomogeneous magnetic field H exerts a magnetic force on the magnetic dipole m, given by $F_{mag} = \nabla(m.H)$, which induces a torque that influences the orientation of the silver atoms. These atoms, characterized by a single valence electron in the 5*s*-orbital, $[Kr]d^{10}5s^1$, were expected to produce a continuous distribution on the detector plate according to classical physics. However, the experiment revealed two distinct spots on the detector, rather than a continuous line, providing compelling evidence for the quantization of angular momentum.

Subsequently, G. Uhlenbeck and S. Goudsmit introduced the concept of intrinsic angular momentum, or "spin," based on the fine structure observed in atomic spectra due to spin-orbit coupling [4]. It was later understood that the silver atom's s-

orbital actually has zero orbital angular momentum ($l = 0$), meaning the experiment did not test the quantization of orbital angular momentum as initially intended. Instead, it became the first empirical confirmation of the quantization of spin angular momentum, with the two distinct points on the detector.

Before the discovery of spin angular momentum, it was classically believed that magnetism arose from electrons orbiting the nucleus, analogous to a current-carrying loop generating an orbital magnetic moment. In quantum mechanics, however, the orbital angular momentum is quantized along specific axes, typically referred to as the z-axis. The corresponding orbital magnetic moment is then expressed as

$$< \boldsymbol{m_o^z} >= -\frac{\mu_B}{\hbar} < \boldsymbol{l_z} > \tag{1.1}$$

where $\mu_B = \frac{e\hbar}{2m_e} = 0.927 \times 10^{-23}\,\mathrm{A.m^2}$ is the Bohr magneton, $\hbar$ is Planck constant and $< \boldsymbol{l_z} >= \hbar l_z$ [1].

The intrinsic spin angular momentum of an electron, similar to other $Fermions$, is characterized by a half-integer value, $s = \hbar/2$. This spin can have two possible projections along a given axis, typically denoted as $s_z = \pm\hbar/2$ which are conventionally referred to as "spin-up" ($|\uparrow>$) and "spin-down" ($|\downarrow>$). The corresponding spin magnetic moment is given by

$$< \boldsymbol{m_s^z} >= -2\frac{\mu_B}{\hbar} < \boldsymbol{s_z} > \tag{1.2}$$

An electron's spin state can be represented as a coherent superposition of the two spin projections, given by

$$\chi = a\,|\uparrow> + b\,|\downarrow> \tag{1.3}$$

where a and b are complex coefficients corresponding to the probability amplitudes of each spin state, with $|a|^2+|b|^2 = 1$. The spinor wave function, as introduced in eq. 1.3, describes the non-relativistic quantum behavior of a single spin, with the basis sates represented as

$$|\uparrow> = \begin{pmatrix} 1 \\ 0 \end{pmatrix} \tag{1.4}$$

$$|\downarrow> = \begin{pmatrix} 0 \\ 1 \end{pmatrix} \tag{1.5}$$

These basis states, together with the expectation values of the Pauli spin matrices σ_i (where $i = x, y, z$) [6, 7], provide the framework for calculating the spin-polarization vector of electrons along specific directions

$$\boldsymbol{P} = \begin{pmatrix} P_x \\ P_y \\ P_z \end{pmatrix} = \begin{pmatrix} <\sigma_x> \\ <\sigma_y> \\ <\sigma_z> \end{pmatrix} \tag{1.6}$$

[1] It is important to note that the superscript is often omitted since it is assumed that the observable is aligned along the z-axis, a convention followed throughout this thesis.

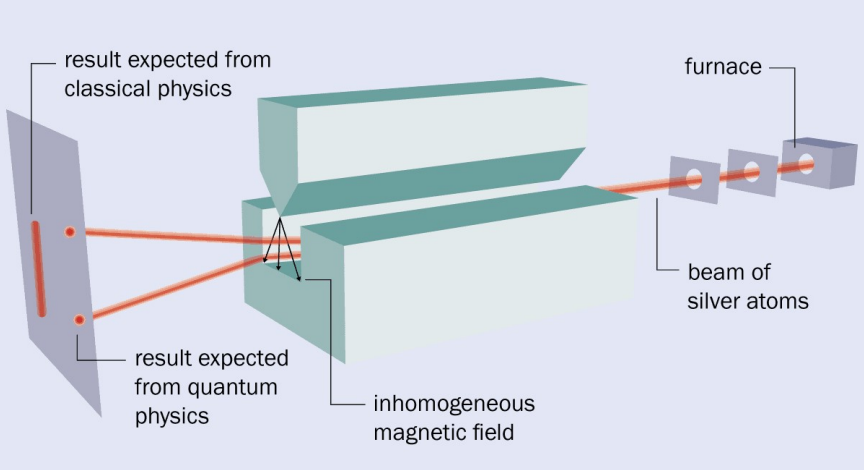

Figure 1.1: Schematic of the Stern-Gerlach Experiment: Vaporized silver atoms are emitted from a furnace and passed through two collimators towards an inhomogeneous magnetic field created by the pole pieces of an electromagnet—one shaped with a groove and the other with a knife-like edge. The detector plate illustrates the differing predictions of classical versus quantum physics. Adapted from [5]

For a beam of electrons, such as an electrical current, the spin polarization is determined by summing the spin-up and spin-down probabilities of individual electrons, yielding

$$P = \frac{n^{\uparrow} - n^{\downarrow}}{n^{\uparrow} + n^{\downarrow}} = \frac{I^{\uparrow\downarrow} - I^{\uparrow\uparrow}}{I^{\uparrow\downarrow} + I^{\uparrow\uparrow}} \tag{1.7}$$

where $n^{\uparrow}$ and $n^{\downarrow}$represents the number of electrons with spin-up and spin-down orientation, respectively. Here, $I^{\uparrow\uparrow} = I^{\downarrow\downarrow}$ refers to the intensity of spin-polarized electrons, in solid-state system, with parallel alignment relative to the sample magnetization (or an external magnetic field in a vacuum), while $I^{\uparrow\downarrow}$ denotes the antiparallel alignment.

This degree of freedom in electron spin opens up new possibilities for utilizing spin-dependent electron transport in various applications. One of the most significant advancements in this area is the discovery of Giant Magnetoresistance (GMR) [8, 9] and Tunneling Magnetoresistance (TMR) [10], which have become foundational technologies in modern data storage. The field dedicated to the study and application of electron spin manipulation is known as *Spintronics* or $spin - electronics$ [11].

The core research areas of Spintronics focus on spin transport, spin dynamics, and spin relaxation within solid-state systems [11]. Spin-polarized electrons, or pure spin currents, can be generated in solid-state systems through various methods,

including the application of electromagnetic waves [12], electrical spin injection from adjacent ferromagnetic materials [13–16], electric field application [17], or thermal gradient [18]. This ability to control spin currents has paved the way for innovative devices that hold promise as alternatives to traditional charge-based electronics, such as spin diodes [19], spin-torque oscillators [20], racetrack memory [21] and spin qubits [22].

The inevitable fate of the current conventional charge-transport electronics has been predicted by G. Moore in 1965 [23]. In his seminal paper, he introduced what is now known as "Moore's Law", stating that "the number of transistors integrated on a chip doubles every two years", as depicted in Fig. 1.2. This projection was based on the observation that the size of integrated transistors could be reduced by a factor of two every four years. However, this continuous miniaturization is bound to encounter physical limits, leading to significant challenges for integrated circuits, including issues like cross-talk and energy dissipation. The innovative spintronics devices mentioned earlier might offer promising solutions to these challenges. Yet, the continuous shrinking of the ICs (top-down approach) push the researchers towards conquering playgrounds other than the inorganic silicon wafers. This new promising land must provide building blocks as small as possible and can be assembled one by one upon request, which is known as 'bottom-up' approach. In 1974, the molecules raised as a promising building blocks for novel and futuristic electronic circuits with the discovery of some molecules, called hemiquinone, has the capability to pass the current only in one way from the cathode to anode similar to $p-n$ junction diodes, showing a molecular rectifier [24]. Later, other functions of electronic devices, e.g. switching, transmissions (molecular wires), amplification, and storage have been proven [25]. These findings are differ than the bulk-material-based molecular electronics found in some well-established technologies like dye lasers, OLEDs, and liquid-crystal displays, where this kind of novel molecular electronics contain only several single molecules embedded between the electrodes and performing the different electronics functions —rectification, amplification and storage— within the same molecule in a mono-molecular approach [25].

The integration of organic molecular properties and functionalities into the design of novel spintronic devices opens up exciting possibilities in the emerging field of *Molecular Spintronics* [27]. The molecular Spintronics, or spin-electronics, investigates the injection, manipulation and detection of the electronic spins in spin devices containing large area sets of molecules or in one unique molecule [26]. This field lies at the interface between organic spintronics, molecular magnetism, molecular electronics and quantum computing, as shown schematically in Fig. 1.3. This field offers significant advantages, primarily due to the versatility of molecules, which can be synthesized in various types and combinations at relatively low costs. Additionally, their electronic and magnetic properties can be tailored to specific needs through chemical synthesis.

When incorporating molecules into spintronic devices, two critical parameters — spin-relaxation time τ_s and spin-diffusion length l_s— must be thoroughly evaluated as they are key figures of merit for device performance. Early examples in this field, such as Alq_3 and Rubrene, exhibit long τ_s but short l_s [28]. In contrast, inorganic

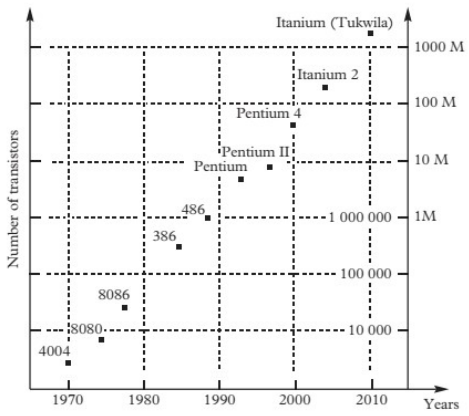

Figure 1.2: Moore's prediction of the exponential growth in the number of transistors integrated on a chip over time (logarithmic scale), with the names of well-known processors marked at their respective years of fabrication. Image adapted from Ref.[26]

semiconductors typically offer longer spin-diffusion lengths, facilitating more effective spin transport within devices. This difference arises from the distinct electronic structures of semiconductors and molecules. In semiconductors, electronic states merge to form bands, allowing electrons to move as quasi-free particles, resulting in higher mobility, as seen in p-doped Si with a mobility of $\mu = 450\,cm^2V^{-1}s^{-1}$. Conversely, in molecules, electrons occupy localized states and must hop between them, leading to lower mobility, such as the $\mu = 40\,cm^2V^{-1}s^{-1}$ observed in Rubrene [29].

The extended τ_s observed in organic materials can be attributed to weak spin-orbit coupling, especially since the elements commonly used in these materials are in the upper rows of the periodic table (low Z), resulting in reduced spin-dephasing. In addition to that, other spin-scattering mechanisms are minimized, e.g.: hyperfine interactions and scattering with paramagnetic impurities which can sustain long-lived spin states in organic molecules [27]. However, the combination of long τ_s and short l_s poses challenges for *Molecular Spintronics* applications, rendering the spins being manipulated and detected close to the injection point. This limitation confines potential applications to two primary strategies: (i) nano-scale devices with channel length smaller than 20 nm, or (ii) single-molecule devices [27]. The realization of single-molecule devices necessitates a microscopic understanding of spin transport and interfacial interactions between molecules and the supporting substrates or electrodes. High spatial resolution techniques, such as scanning tunneling microscopy (STM), are invaluable in these investigations. STM enables the examination of single molecules at the atomic level, providing insights into spin-dependent molecular orbitals, the hybridization between electronic states of the substrate and molecular orbitals, and the resulting spin-polarization at the interface. These phenomena are

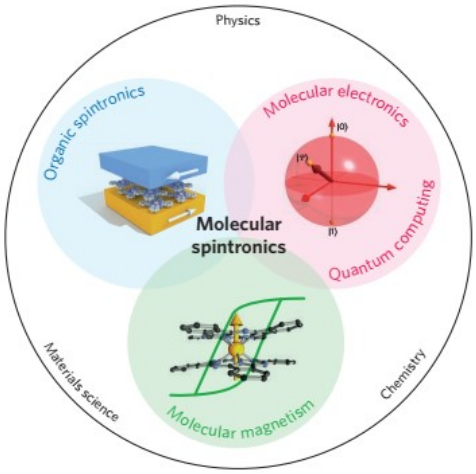

Figure 1.3: The interdisciplinary field molecular spintronics brings together physicists, chemists, and material scientists. It lies at the intersection of organic spintronics, molecular magnetism, molecular electronics and quantum computing. Image is adapted from Ref. [30]

central to the emerging sub-field known as $Spinterface$.

This thesis presents a comprehensive magnetic investigation of several single molecules containing mixed $3d-4f$ metallic centers, structured into five main chapters. Chapter 1 introduces the fundamental concepts related to the electronic structure and magnetic properties of both isolated and adsorbed molecules. It also includes a literature review of other relevant molecules, particularly single-molecule magnets. Chapter 2 provides an overview of the specific molecules studied in this work, detailing their structures and magnetic properties. Chapter 3 will cover the experimental techniques and instruments employed throughout the research. Chapter 4 focuses on the scanning tunneling microscopy and spectroscopy results obtained for $3d-4f$ molecules deposited on ferromagnetic substrates, specifically the Ni_2Tb molecule on 1.5 ML Fe (110) / W(110) substrate. Chapter 5 presents peer-reviewed results on 3d-4f metallacrown molecules, investigated using element-specific X-ray Magnetic Circular Dichroism (XMCD). This technique allowed for the separate measurement of the spin and orbital magnetic moments of each element within the molecule, providing insight into the magnetization-reversal energy barriers. Additionally, changes in the local coordination environment of metallic centers were linked to variations in the spin-ground states of the molecules in different solvents, and the anisotropy of the 4f states in certain $3d-4f$ metallacrowns was characterized through angular-dependent XMCD measurements. The thesis concludes with a summary of the key findings and an outlook on potential future research directions.

Chapter 2

Molecular Spintronics

2.1 Molecules: The Building Blocks of Molecular Spintronics

2.1.1 Isolated Molecules

Electronic structure

The electronic structure of free atoms have a discrete "quantized" nature, in a sense that only electrons can occupy some specific energy levels. The experimental evidence supporting this fact is extensive and well-documented. It is most directly derived from the selective absorption of radiation in which the absorbed radiation energy itself is discrete. This absorbed energy is the necessary energy to promote electrons between different atomic energy levels, $\Delta E = \hbar\omega$, where $\hbar$ is Planck constant divided by 2π yielding the unit of angular momentum and ω is the absorbed radiation angular frequency. This energy-levels discreteness is persistent when atoms combine to form molecules. The evaluation of the observations related to these molecular systems can be done by solving *Schrödinger Equations* [31] approximately in the framework of either valence band theory (VB) or molecular orbital theory (MO). The former has failed in determining the magnetism of some molecules and the light-absorption meanwhile the later presents a comprehensive understanding of the molecules and their energy levels [32].

In the MO theory, the molecular orbitals arise from the interaction between the atomic orbital of the constituting atoms and they spread over the entire region of space surrounding the molecule. This interaction is allowed once the symmetry of the interacting atomic orbitals are compatible with one another and relatively close in energy. Also, the resulted MOs must not outnumber the constituting atomic orbitals. It is possible to understand the MO theory in terms of the simple H_2 molecule where each H atom has one electron in 1s orbital with associated wavefunction $\psi_1$and ψ_2 for each. The linear combination of the atomic orbitals (LCAO) yield two MOs for that molecular system

$$\psi_{MO} = \psi_{bonding} = \frac{1}{\sqrt{2}}[\psi_1 + \psi_2] \tag{2.1}$$

and

$$\psi_{MO} = \psi_{antibonding} = \frac{1}{\sqrt{2}}[\psi_1 - \psi_2]. \tag{2.2}$$

Equations 2.1 and 2.2 refer to the two LCAO cases where once the wave function interfere constructively (bonding) and the other destructively (antibonding). The bonding MO is stabilized and have lower energy with respect to the H atomic 1s orbital, where the electrons in the bonding MO are attracted to both nuclei leading to a stable covalent bond. On the other hand, the antibonding MO is destabilized and have higher energy than the constituting atomic orbitals, as shown in Fig. 2.1. The bonding MO has high probability to find the electrons in the central region where the electronic density is concentrated between the two atoms. Meanwhile, the antibonding MO has a nodal plane in the middle where the electron density is zero and the electron density is concentrated in the opposite outer regions of the nuclei.

The MO has specific symmetry either σ- or π-symmetry, following the symmetry of the constituting atomic orbitals and their interference. The MO with σ-symmetry have center of inversion symmetry, i.e. the phase of the wave function does not change once rotated about the internuclear symmetry axis. Such MOs can be denoted by $\sigma_g(1s)^2$ for the bonding ground state indicating that the MO coming from 1s atomic orbitals and it is occupied by two electrons with even parity, i.e. no phase change around the center of inversion in the molecule. On the other hand, the antibonding state is denoted by $\sigma_g^*(1s)^2$ indicating to a phase change and the presence of a nodal plane in the central region. The σ-symmetry MOs are formed from head to head overlapping of s- and p_z-orbitals concentrating the electron density in the middle region between the nuclei amlong the internuclear axis. Meanwhile, the π-symmetry MO is formed from side-by-side overlapping of p_x- and p_y-orbitals concentrating the electron density above and below the internuclear axis. The overlapping integral in the π-symmetry MO is smaller than its counterpart in the σ- symmetry MO and the rotation about the internuclear axis changes the phase, as shown in Fig. 2.2. Such introductory concepts work well for simple diatomic homonuclear molecules but the more the nuclear charge of the atoms get increased the more orbital mixing occurs and things are more complicated. In the hetronuclear molecules, the symmetry condition of the interacting orbitals still a crucial mandate to form the MOs yet the orbitals energy determine the size of overlapping between the two atomic orbitals in each MO. Thus atomic orbitals with s-symmetry can overlap significantly with p_z-symmetry orbitals but not with p_x- and p_y- symmetry orbitals.

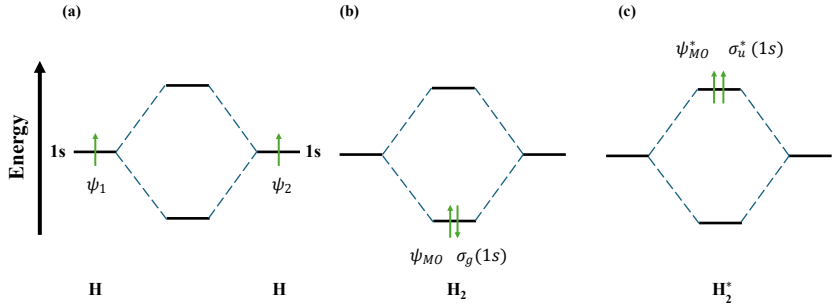

Figure 2.1: Schematic diagram of the H_2 molecular orbitals formed from the two 1s atomic orbital of two H atoms (a). The in-phase interference between the atomic orbital wave functions leads to bonding MO and forming stable H_2 molecule (b). Meanwhile, the out-phase interference forms anti-bonding MO and destabilized H^*_2 molecule (c).

The above mentioned discussion of the formation of the MOs can be handy and useful up to di- and triatomic molecules, where three set of orbitals can be depicted for the former (2 atomic orbitals + 1 MO) and four set of orbital for the later (3 atomic orbitals + 1 MO). Unfortunately, diagrams become more difficult to read and understand for polyatomic molecules. Thus, another approach is used to get a descriptive diagram with less orbitals which is the Ligand Group Orbital Approach (LGO). In this approach, the orbitals of the non-central atoms are grouped in LGO and following the symmetry of this LGO and the central atom orbital the bonding takes place to form the MO. The correspondence in the symmetry between the LGO and the central atom orbital is crucial to yield the MO, otherwise no bonding occurs and the orbital of the central atom will end up non-bonding. The derivation of MO in that case depends on the symmetry point group of the molecule and a quick example can be given to provide the reader with a general overview.

Fig. 2.3 shows for MOs of exemplary molecule XH_2 , where X is an arbitrary atom with 2s and 2p as valence orbitals. The $H-H$ fragment constitutes a ligand group wavefunction from the two 1s atomic orbitals with two possible phases: (i) in-phase: LGO1 $= \frac{1}{\sqrt{2}}[\psi_1(1s) + \psi_2(1s)]$, (ii) out-of-phase: LGO2 $= \frac{1}{\sqrt{2}}[\psi_1(1s) - \psi_2(1s)]$. The first LGO1 has σ_g- symmetry which enables it to bond with the central atom X $2s(\sigma_g)$ orbital forming bonding MO of the first ground state $\psi_1(\sigma_g)$ and anti-bonding MO $\psi^*_5(\sigma_g)$. On the other hand, the out-of-phase LGO2 has σ_u- symmetry which matches well with the $2p_z$orbital symmetry to form bonding and anti-bonding MOs, $\psi_2(\sigma_u)$ and $\psi^*_6(\sigma_u)$, respectively. The bonding MO $\psi_1(\sigma_g)$ and $\psi_2(\sigma_u)$ spread over all three atoms leading to a delocalized bonding. The remaining $2p_x$ and $2p_y$orbitals becomes non-bonding orbitals.

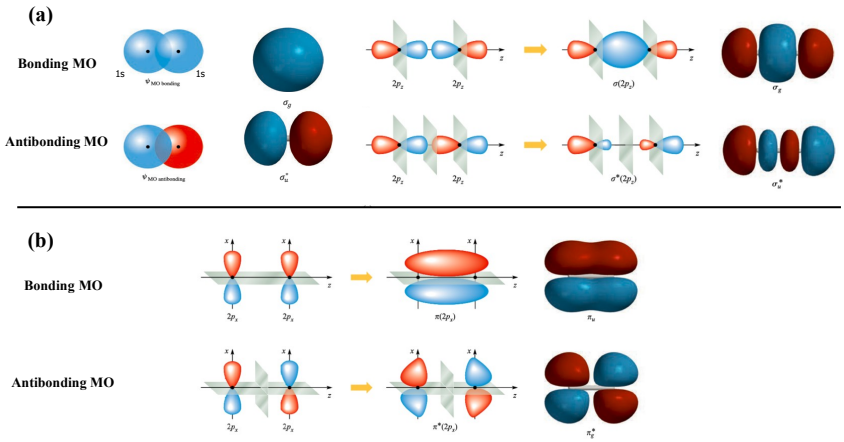

Figure 2.2: Graphical representation of σ-symmetry MO (a) and π-symmetry MO (b). The upper rows in both panels represent the bonding ground state where the wavefunction amplitude increases in the region between the nuclei. Meanwhile, the lower panel represents the antibonding MOs with nodal plane in the middle shows small probability to find the electrons in that region. colors: Blue and Red refers to the waves of different phases, Grey refers to the nodal plane , Black refers to the atoms nuclei. Image is taken from Ref. [32].

For more complex polyatomic molecules, the molecular orbitals (MOs) are treated as many-particle systems with atomic orbitals serving as the basis functions. If a molecule has n atoms, there are n orthonormal atomic orbitals: $\{\chi_1, \chi_2, \ldots\ldots\ldots \chi_n\}$. Consequently, MOs are formed from LCAOs as follows:

$$\psi_i = c_{1i}\chi_1 + c_{2i}\chi_2 + \ldots\ldots + c_{ni}\chi_n = \sum_{\mu} c_{\mu i}\chi_\mu \tag{2.3}$$

where $i = 1, 2, \ldots\ldots, n$, and $c_{\mu i}$ is the molecular orbital coefficient, whose magnitude indicates the contribution of atomic orbital μ in the corresponding MO. The MOs are orthonormal:

$$< \psi_i | \psi_j > = \delta_{ij} \tag{2.4}$$

where δ_{ij} is the Kronecker-Delta function, $\delta_{ij} = 1$ if $i = j$ and $\delta_{ij} = 0$ if $i \neq j$. The $c_{\mu i}$ values are obtained by solving the eigenvalue equation of the effective one-electron Hamiltonian, H^{eff}:

$$H^{eff}\psi_i = E_i\psi_i \tag{2.5}$$

where E_i is the energy of the MO ψ_i. The overlap between two atomic orbitals, χ_μ and χ_ν, centered on two different atoms will be expressed as the overlap integral:

$$S_{\mu\nu} = < \chi_\mu | \chi_\nu > . \tag{2.6}$$

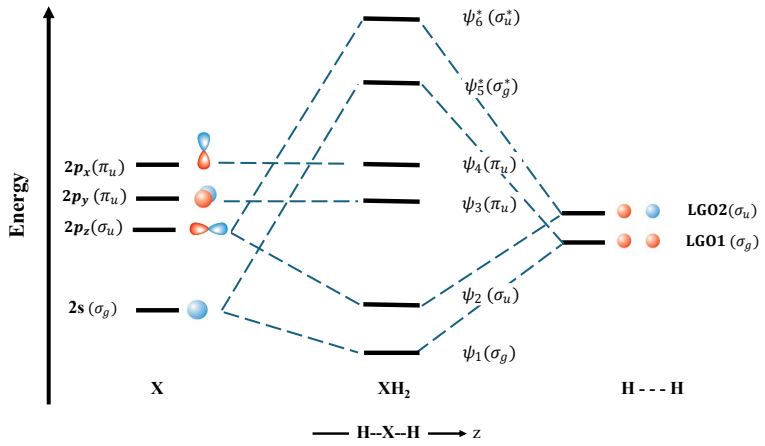

Figure 2.3: Schematic diagram of the electronic structure of the exemplary molecule XH_2. The molecule lying along the z-axis. 1s orbitals of H atoms form LGOs with two phases and two symmetries (far right). The bonding between these LGOs and the orbitals of X atom (far left) must fulfill the symmetry condition of the MO. The bonding MOs are $\psi_1(\sigma_g)$ and $\psi_2(\sigma_u)$, meanwhile their corresponding anti-bonding MOs are $\psi_5^*(\sigma_g)$ and $\psi_6^*(\sigma_u)$.

The symmetry of the orbitals influences this overlap integral $S_{\mu\nu}$ and dictates whether it vanishes or not and whether the resulting MO has σ- or π- symmetry. The more positive $S_{\mu\nu}$ is, the more stabilizing the MO, i.e.: bonding MO. The determination of the MOs energy can be obtained by solving a well-known mathematical result from that theory, called *secular determinant*:

$$\sum_{\mu} |H_{\mu\nu} - E_i S_{\mu\nu}| c_{\mu\nu} = 0 \tag{2.7}$$

where the coefficients $c_{\mu\nu}$ are chosen to minimize the energy according to the variational theorem. More rigorous and comprehensive explanation of deriving MOs of molecules and their corresponding energy can be found in chemistry resources like Ref. [32–34].

The most significant molecular orbitals (MOs) are the Highest Occupied Molecular Orbital (HOMO) and the Lowest Unoccupied Molecular Orbital (LUMO). The HOMO is the highest energy MO that contains electrons, while the LUMO is the lowest energy MO that is unoccupied. Similar to the density of states in solid-state physics, the HOMO can be likened to the top of the valence band, and the LUMO to the bottom of the conduction band. The energy difference between these two orbitals, known as the HOMO-LUMO gap, is essential in various molecular studies. It typically represents the lowest possible electronic excitation energy in a molecule. For instance, colorless substances have a large HOMO-LUMO gap, preventing them from absorbing any visible light wavelengths. The HOMO-LUMO gap of molecules can be determined experimentally through complementary techniques such as ultraviolet absorption spectroscopy [35] electron attachment spectroscopy, or cyclic voltammetry measurements [36]. Additionally, the high spatial resolution of Scanning Tunneling Spectroscopy allows for the measurement of the HOMO-LUMO gap

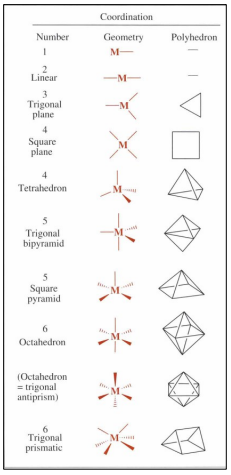

Figure 2.4: Schematic diagrams of coordination complexes geometries with coordination numbers 1 – 6. Original Image is taken from Ref.[41].

in single molecules [37–39]. Theoretically, the HOMO-LUMO gap can be calculated using Density Functional Theory (DFT) and Hartree-Fock methods [40].

In this thesis, we will explore an intriguing class of molecules known as coordination complexes, which are significant in the field of molecular magnetism due to their unique ability to exhibit magnetic properties through variations in their structural and electronic configurations [42–44]. Coordination complexes consist of a transition metal ($3d$) or lanthanide ($4f$) cation $\mathbf{M^{n+}}$ covalently bonded with several ligands (coordinated). These ligands can range from simple ions such as $\mathbf{C1^-}$, to small molecules such as $\mathbf{H_2O}$ or $\mathbf{NH_3}$, larger molecules such as $\mathbf{HNCH_2CH_2NH_2}$, or even macromolecules like proteins [41].

The ligands attach to the central metallic ion via donor atoms, which can vary in number: a single donor atom (unidentate), two donor atoms (didentate), or multiple donor atoms (polydentate) [32]. The coordinate covalent bond in coordination complexes differs from conventional covalent bonding in that the pair of electrons originates solely from the ligand, making the ligand a Lewis base and the metal ion a Lewis acid [45]. Hence, this bond is a specific type of covalent bond known as a coordinate covalent bond (or dative bond). The geometric structure of a complex is determined by the spatial orientation of these metal-bound groups and the number of donor atoms in the ligands, known as the coordination number. For instance, in a four-coordinate complex, the donor atoms can be arranged at the vertices of a tetrahedron, forming a tetrahedral geometry, or in a plane at the corners of a square, forming a square planar coordination geometry. It is important to note that the coordination number of a complex differs from the oxidation number of the central cation. For example, in the complex $\mathbf{[Co(NH_3)_6]^{3+}}$, the oxidation number of the cobalt ion is +3, whereas the coordination number is 6. The excess charge on the complex is referred to as the secondary valence, while the oxidation number is known as the primary valence. Some common idealized structure for coordination complexes with coordination numbers 1-6 are shown in Fig. 2.4.

The magnetic properties of coordination complexes can be understood through

the *Crystal Field theory* (CF) introduced by H. Bethe in 1929 [46]. According to this model, ligands are considered as point charges that generate an electrostatic field acting upon the *d*-orbitals of the central atom. If the *d*-orbitals experience a uniform electrostatic field intensity, the energies of all the d-orbitals would increase by the same amount. However, because the five *d*-orbitals have different anisotropic spatial distributions, as illustrated in Fig. 2.5a, they are affected differently, where some orbitals will be closer to the ligand point charges than others, leading to a lifting of their degeneracy. The resulting splitting of these orbitals is dependent on the strength of the crystal field and the spatial arrangement of the surrounding ligands. Here, we will explain two geometries: the octahedral ligand field splitting and the square planar ligand field splitting.

In an octahedral ligand field, the $d_{x^2-y^2}$ orbitals and d_{z^2} orbitals are destabilized more than the d_{xy}, d_{xz} and d_{yz} orbitals. This is because the former group of orbitals points along the Cartesian axes and interacts strongly with the ligands positioned at these axes, belonging to the group symmetry e_g. On the other hand, the latter group of orbitals points between the axes and interacts less with the ligands, resulting in lower energy and greater stabilization; these orbitals belong to the group symmetry t_{2g} [32], as depicted in Fig. 2.5b. The energy difference between the two sets of energy levels is defined as Δ_o, octahedral ligand field splitting, and the two sets are split with respect to the *Barycenter*, which is the raised energy level of the degenerate orbitals in a spherical ligand field .Thus, the e_g set is raised by 0.6 Δ_o and the t_{2g} set is lowered by 0.4 Δ_o.

On the other hand, the energy splitting in a square planar ligand field follows a different pattern. In this geometry, the d-orbitals split into four distinct symmetry groups: $a_{1g}(d_{z^2})$, $b_{1g}(d_{x^2-y^2})$, $b_g(d_{xy})$, and $e_g(d_{xz}, d_{yz})$, as shown in Fig. 2.5b. The ligands lie in the x-y plane along the coordinate axes. Therefore, the $d_{x^2-y^2}$ orbital is the most destabilized in this geometry because its lobes point directly along the x-y coordinate axes. The d_{xy} orbital, which lies between the x-y coordinates and has its lobes pointing between the axes, has the second highest energy. The d_{z^2} orbital is lower in energy than these two but higher than the d_{xz} and d_{yz} orbitals. This is because the d_{z^2} orbital has a ring of electron density in the x-y plane that interacts with the ligands, making it more destabilized than the d_{xz} and d_{yz} orbitals.

The energy splitting between the different *d*-orbitals depends on the strength of the ligand field which can be determined from the empirical spectrochemical series :

$$\mathrm{CO, CN^- > phen > bpy > NH_3 > H_2O > OH^- > Cl^- > SCN^- > I^-}.$$

If the ligand field lies in the right side of that series (weak ligand field) then the magnitude of the energy splitting, say Δ_o in octahedral ligand field, will be less than that generated by ligands on the far left side of the series (strong ligand field). Consequently, in some complexes with weak ligand fields with $d^4 - d^7$ electron configurations, it is more energetically favorable to fill the upper orbitals, e.g.: e_g orbitals in octahedral ligand field, rather than pair the electrons in the lower orbitals, e.g.: t_{2g} orbitals in octahedral ligand field, resulting in high-spin complexes with

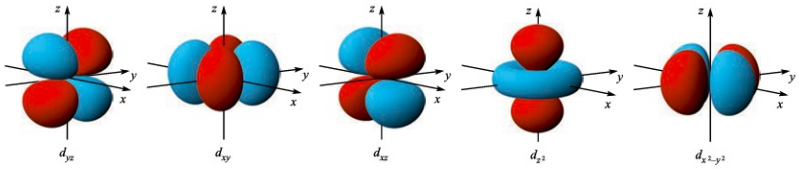

(a)

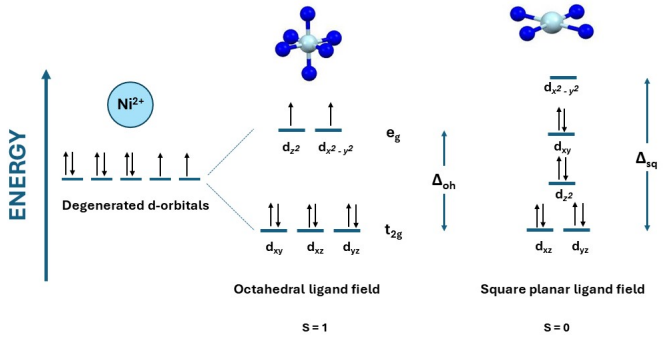

(b)

Figure 2.5: (a) Graphical representations of the five d-orbitals. (b) Schematic energy diagram of the d-orbitals of a hypothetical complex with a central Ni^{2+}ion in both octahedral (center) and square planar ligand field (right). In the octahedral ligand field, the complex results in a high-spin configuration (HS) with spin $S = 1$, whereas in the square planar ligand field, it results in a low spin (LS) configuration with spin $S = 0$. However, the square planar ligand field can also produce a high-spin complex if the ligands are weak enough, making it more favorable to fill the $d_{x^2-y^2}$ orbital rather than pairing the electrons in the d_{xy} orbital.

unpaired electrons. On the other hand, in strong ligand fields, it is more energetically favorable to pair the electrons in the lower orbitals rather than fill the upper orbitals, yielding low-spin complexes.

Magnetic Properties of coordination complexes

In the 1950s, Guha et al. observed paramagnetic behavior at low temperatures (below 80 K) in a **Cu(II) acetate** complex [47]. This magnetic behavior was attributed to superexchange interaction, with an exchange interaction of $J \sim -18.6$meV, between the two **Cu(II)** ions by *acetate* bridges within the complex. Subsequently, various magnetic orderings in polynuclear complexes have been reported at different temperatures, ranging from 5.5 K in the blue Prussian family complex $\mathbf{Fe_4[Fe(CN)_6]_3.xH_2O}$, to 60 K in $\mathbf{Ni_3[Cr(CN)_6]_2.9H_2O}$ (ferromagnet) [48], 125 K in $\mathbf{Cs_2Mn[V(CN)_6]}$ (ferrimagnet) [49], 240 K in $\mathbf{Cr_3[Cr(CN)_6]_2.10H_2O}$ (ferrimagnet) [50], and up to 376 K in $\mathbf{KV[Cr(CN)_6]_2.2H_2O}$ (antiferromagnet) [51]. The nature of the magnetic ordering in these complexes is determined by the symmetry of the interacting orbitals of both the ligand and the central metal ion. If the orbitals are symmetry-allowed, the interaction will be antiferromagnetic, whereas if they are symmetry-forbidden or orthogonal, the interaction will be ferromagnetic [52].

Later in the early 1990s, an unusual discovery in the coordination complex $\mathbf{[Mn_{12}O_{12}(OAc)_{16}(H_2O)_4]}$, commonly referred to as the $\mathbf{Mn_{12}Ac}$ cluster, opened new avenues in molecular magnetism research [43]. Sessoli et. al. observed a magnetic anisotropy in this cluster, leading to magnetic bistability at a low temperature of 4.4 K, which resulted in a pronounced hysteresis [43]. Consequently, the magnetization in this molecule experiences slow relaxation in the absence of a magnetic field. This retention of magnetization has become of great interest due to its potential applications in data storage and quantum computation [53–55]. This family of coordination complexes is known as single-molecule magnets (SMMs) [56–58].

The archetypical SMM $\mathbf{Mn_{12}Ac}$ skeleton consists of four internal Mn(III) ions with ground spin state, $S = 1/2$, and eight peripheral Mn(IV) ions with ground spin state, $S = 3/2$, in which they are antiferromagnetically coupled with each others resulting into total ground spin state of $S = 10$ leading to a ferrimagnetic spin arrangement. This "Giant Spin" has $2S + 1$ projections which are m_s microstates ranging from $S = -10$ to $S = +10$. The unperturbed Hamiltonian of this system includes the Zeeman energy, in the presence of an applied magnetic field along the molecule's unique axis H_z, and the crystal-filed splitting that lifts the degeneracy of the microstates in the absence of the magnetic field, known as Zero-field splitting (ZFS) [59]:

$$\hat{\mathcal{H}} = g\mu_B H_z S_z + D[S_z^2 - \frac{S}{3}(S+1)] \tag{2.8}$$

where g is the gyromagnetic ratio, μ_B is Bohr magneton, and D is the ZFS parameter. The corresponding energies of these microstates can be calculated from the Eq. 2.8 resulting into:

$$E(m_s) = D(m_s^2 - 110/3) + g\mu_B m_s H_z \tag{2.9}$$

where $-S \leq m_s \leq S$, and the two lowest microstates (most thermally stable states) are separated by an effective energy barrier. This energy barrier U_{eff} oc-

curs due to the easy axis magnetic anisotropy in this molecule, which means that the magnetization is preferentially oriented parallel to the z axis. For integer spin systems, it is equal to

$$U_{eff} = S^2|D|, \tag{2.10}$$

meanwhile, it is equal to

$$U_{eff} = (S^2 - \frac{1}{4})|D| \tag{2.11}$$

for half-integer spin systems. If $D < 0$, then the largest microstates $m_s = \pm 10$ lie lowest in energy in this molecule leading to depict the microstates states as two wells separated by an effective energy barrier and the separation between two subsequent microstates is equal to $|D|\,(2\,|m_s| - 1)$, as shown in Fig. 2.7. Below the blocking Temperature T_B in the absence of the magnetic field the molecules thermally populate the two lowest microstates equally, i.e.: $m_s = -10$ and $m_s = +10$, as shown in Fig. 2.7(a). If the magnetic field is applied parallel to the easy axis of the molecule with large value enough, the $m_s = -10$ state will be the only populated state, below T_B, where this projection is parallel to the applied field. Once the applied magnetic field is removed, the system relaxes back to its thermal equilibrium state as shown in Fig. 2.7(c). The magnetization relaxation decay exponentially, $M_z(t) = M_z(t = 0)\, exp(t/\tau)$, where τ is the relaxation time. The most sought goal of the researchers in the molecular magnetism community is to increase the magnetization relaxation time of such molecules at higher blocking temperature which might lead to use this kind of molecules as potential data storage mediums. The main source of this relaxation is the spin-phonon coupling which originates from the perturbation of the crystal field induced by lattice vibrations and it will be added to Eq. 2.8 to yield an effective Hamiltonian of the molecule, and it is known as Orbach relaxation process [60]. The spins lose energy during transitions between the microstates by emitting phonons, which excite vibrational modes of the lattice. Villain et al. demonstrated that the magnetization relaxation rate in such molecules follows the Arrhenius law [60]:

$$\tau = \tau_0\, exp(U_{eff}/k_B T) \tag{2.12}$$

The prefactor τ_0 is given by:

$$\tau_0 = \frac{2\pi}{3}\frac{\hbar^2 \rho c^5}{|V_{10}|}\left[\frac{S^2}{U_{eff}}\right]^3 \tag{2.13}$$

where ρ is the specific mass, c is the phonon velocity, and $|V_{10}|$ is the spin-phonon matrix elements of the last step to climb the energy barrier, which is the slowest and thus the most determinant transition for the relaxation rate. Also, alternative relaxation mechanisms can take place like: direct process and the Raman process, in which phonons can cause a "spin flip" within the ground doublet. These mechanisms will render the magnetization relaxation temperature independent in the low temperature regime [61]. For $Mn_{12}Ac$, $\tau_0 = 2.1 \times 10^{-7}$ s , and $U_{eff}/k_B = 62$ K yielding a relaxation time of 2 months at $T = 2$ K, and up to 50 years below $T = 1.5$ K [62]. As a matter of fact, another two relaxation mechanisms related to the

spin-lattice mechanisms takes place besides Orbach relaxation and QTM; i.e.: the Raman and direct processes. These relaxation mechanisms are beyond the scope of this study. Thus, the reader is refereed to Ref.[63] for further reading.

The magnetization of SMM molecules can experiences a quantum tunneling between two degenerate microstates on the sides of the well, known as "resonant tunneling states", without the need to overcome the energy barrier U_{eff} [59]. This tunneling occurs due to admixture of the states with some perturbation resulted from the transverse anisotropy in the x-y plane:

$$\hat{\mathcal{H}}' = E\,(S_x^2 - S_y^2) \tag{2.14}$$

where E is a the transverse anisotropy parameter with limits of $0 \leq |E/D| \leq 1/3$. As a result of the coexistence of these two phenomenon below T_B, the field-dependent magnetization, $M(H)$, of theses molecules shows a hysteresis loop with sharp transitions at some specific fields due to "short cuts" in the magnetic relaxation through the quantum tunneling magnetization [64], as shown in Fig. 2.6(c).

The main strategy to increase the energy barrier, besides the suppression of the zero-field QTM, was to increase the ground-state spin value S following the energy barrier equations 2.10,2.11 [44, 65]. Yet such strategy did not yield SMMs with larger U_{eff} that exceeds the one of the $\mathbf{Mn_{12}Ac}$ SMM. For example, the complex aggregate of $\mathbf{\{Mn_{12}^{III}Mn_{7}^{II}\}}$ has a spin ground state of $S = 83/2$, yet it does not show any hysteresis loop indicating to the absence of SMM behavior at low temperatures [66]. On the other hand, synthesizing complexes with large magnetic axial anisotropy, i.e.: large negative values of ZFS parameter D with small E values, can be more promising for larger U_{eff} [52]. Such approach can be challenging because a highly delicate control of the local coordination environment of the central metallic ions in the host molecules is required. Besides that, the $3d$ ions has quenched orbital magnetic moment which can not produce a sizable magnetic anisotropy.

Lanthanides (Ln) began to be incorporated into the synthesis of Single-Molecule Magnets (SMMs) due to their large spin and orbital magnetic moments. The unquenched orbital angular momentum in these ions leads to strong spin-orbit coupling, resulting in a total angular momentum J, which can be deduced from Hund's rules. The ground state of these ions is represented as $^{2S+1}L_J$, where S is the total spin angular momentum, L is the total orbital angular momentum, and J is the total angular momentum which is equal to $J = L + S$, if f-orbitals are more than half-filled and $J = L - S$ if f-orbitals are less than half-filled [69]. The spectroscopic notion (S, P, D, F, G, H, ...) is used to designate the total orbitals angular momentum of the ground state corresponding to the values (0, 1, 2, 3, 4, 5, ...). The 4f orbitals are localized and retain the ionic electronic structure within the molecules. Although the spin-orbit coupling in the ground state is smaller than the surrounding crystal field, the latter can be considered a significant perturbation, lifting the degeneracy of the ground state and yielding $2J + 1$ m_J projections (substates) ranging from $-J$ to $+J$ [61]. Including Ln in SMMs leads to significant magnetic anisotropy, introducing the concept of "single-ion" SMMs (SIMs). The first

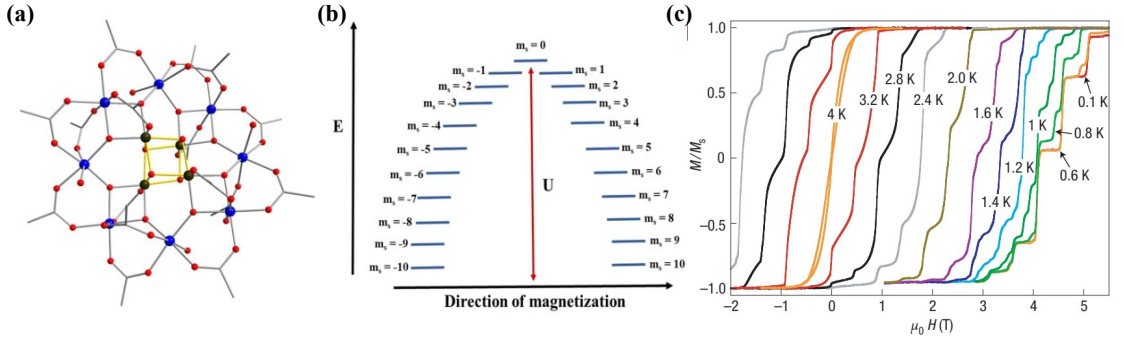

Figure 2.6: (a) Schematic representation of the molecular structure of the $Mn_{12}Ac$ cluster. Color scheme: Mn^{3+}(blue), Mn^{4+}(olive green), O (red), N (blue), C (grey), H atoms are omitted for clarity. (b) Energy barrier separating bistable magnetization direction (m_s ground microstates) $m_s = \pm 10$. (c) Isothermal field-dependent magnetization measurements at varying temperatures with constant field sweep rate of 2 mT/s of the SMM $Mn_{12}Ac$. The hysteresis loop opened below $T_B = 4\,K$ shows steps due to resonant QTM. The steps are getting sharper at lower temperatures and it becomes temperature-independent at T = 0.6 K. Images are taken from Ref.[67, 68].

known SIM was **$(Bu_4N)[TbPc_2]$**, where Pc^{2-} is the phthalocyanine ligand, which had an effective energy barrier of 28.52 meV (230 cm^{-1}), a record for several years [70]. Moreover, the blocking temperature of the slow relaxation of magnetization in SIMs exceeds that of SMMs, with the first reported SIM having a T_B of 40 K [70], compared to no SMM exceeding 8 K.

Most Ln-SIMs include **Tb(III)**, **Dy(III)**, **Er(III)**, or **Ho(III)** [61], due to their large ground m_J microstates. For example, Dy(III) ions, with a $4f^9$ electron configuration, have a ground state of $^6H_{15/2}$, with the second-lowest energy state $^6H_{13/2}$ about 372 meV (3000 cm^{-1}) above, providing stability and bistability for the lowest m_J in the molecule [71], as shown in Fig. 2.8(a). Similarly, **Tb(III)** ions have a ground state of $^7F_6$, with the separation between the lowest ground microstate $m_J = 6$ and the first excited state $m_J = 5$ around 49 meV (440 cm^{-1}) [72].

A notable strategy to achieve a large U_{eff} is the Reinhart model, which involves selecting the appropriate ligand field symmetry for the Ln central ion [73]. The $4f$-shell electron density distribution of Ln(III) ions exhibits strong angular dependence described by the quadrupole moment. The different occupation of these orbitals in the ground state of Ln (III) results into shape variation ranging from an oblate shape (equatorially expanded like donuts) to prolate shape (axially elongated like a cigar),

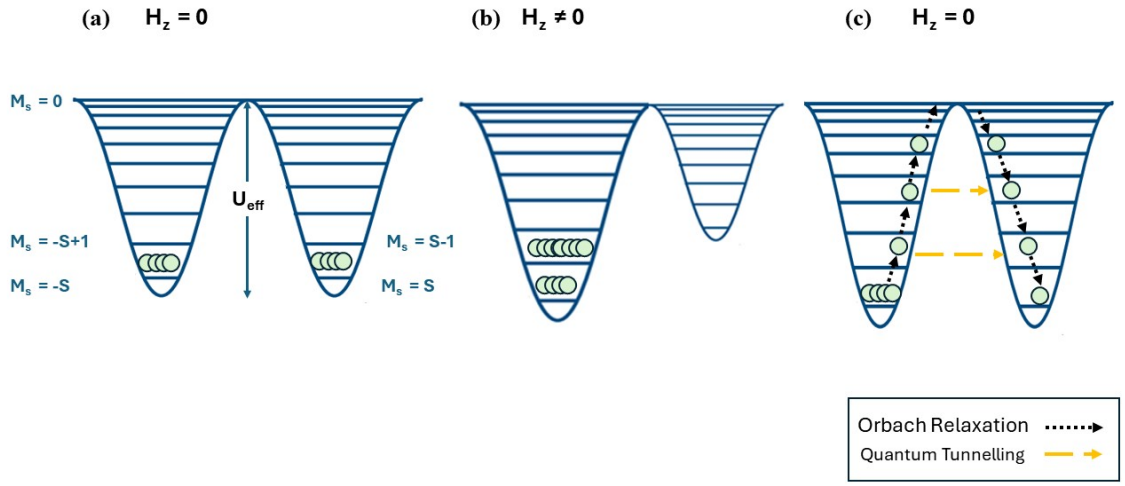

Figure 2.7: Schematic diagram of the two-well model of the magnetization relaxation. (a) In the absence of the magnetic filed, the two lowest microstates of the molecules $S = \pm 10$, separated by an effective energy barrier U_{eff}, are equally thermally populated below T_B. (b) In the presence of the magnetic field, the molecules starts to populate the lowest microstate aligned with the magnetic filed direction $S = -10$. (c) Once the applied magnetic field is removed, the magnetization of the molecules relax back slowly to the lowest state $S = +10$ by overcoming the energy barrier (black dotted arrow). It is possible a to observe QTM once the energy levels of the two microstates are degenerate (yellow dashed arrow).

as shown in Fig. 2.8(b). To prevent magnetization reversal, a ligand field should be created to minimize electrostatic repulsion at $m_J = \pm J$ and maximize it at other microstates, as shown in Fig. 2.8(c). SIMs with an Ln(III) ion with an oblate 4f-shell, such as **Ce(III)**, **Pr(III)**, **Nd(III)**, **Tb(III)**, **Dy(III)**, and **Ho(III)**, can achieve large anisotropy if the molecule's scaffold provides an axially symmetrical ligand field, as seen in **$(Bu_4N)[LnPc_2]$** [70], as shown in Fig. 2.8(d). Conversely, Ln(III) ions with a prolate 4f-shell prefer a circumferential ligand field. However, it should be noted that such straightforward approach is not working all the time, where the easy axis of magnetization may not always align with the molecular symmetry axis, and **Dy(III)**, being a Kramers' ion with an odd number of f-electrons, maintains the stability of the m_J ground state regardless of the ligand field symmetry [61].

A mixed $nd - 4f$ SMM has been reported in the literature as an attempt to mix the high spin S resulting from the magnetic exchange interaction of the nd ions and the large anisotropy of the Ln(III) [74, 75]. The potential application of such molecules in future data storage remains challenging due to several arising issues. Firstly, the low T_B presents a significant obstacle,where the record T_B is still slightly below the liquid nitrogen temperature 60 K . Additionally, QTM at zero field between the two lowest microstates hinders any bistability in these molecules.

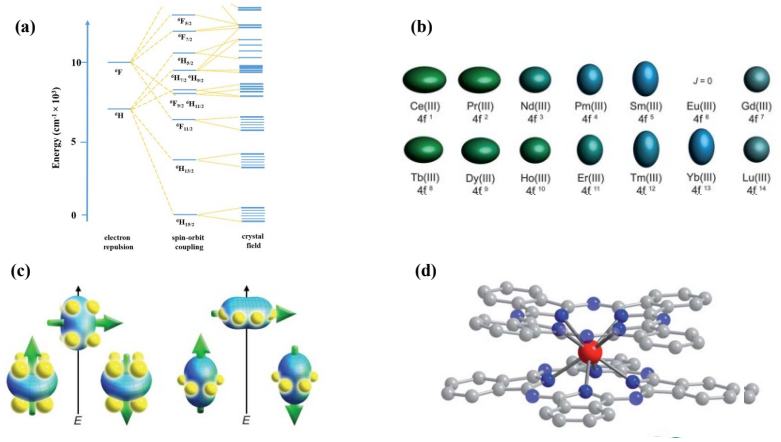

Figure 2.8: (a) Dy(III) free ion electronic structure diagram of low energy states in different perturbations: electron repulsion (left), spin-orbit coupling (middle), and crystal field (right). The spin-orbit coupling left the degeneracy of the ground state yielding multiplets with total angular momentum $|L+S| \leq J \leq |L-S|$. The crystal field lefts the degeneracy of the ground state ${}^6H_{15/2}$ into 2J+1 m_J substates, i.e. 16 m_J substates. Image is taken from Ref. [67]. (b) Ln(III) Quadrupole of the 4f-shell electron distribution. (c) Sketch of the low- and high-energy configuration of the oblate (left) and prolate (right) f-orbital electron density. Due to the strong spin-orbit coupling in Ln(III), S (green arrow) co-rotate with the electron density cloud. Thus, for the oblate electron density, the axial ''sandwich''- type crystal field minimizes the energy of the $m_J = J$ (high moment) microstates, and maximize the energy of the other intermediate microstates. Meanwhile, the equatorial electron configuration minimizes the energy of the high moment for the prolate electron density. (d) Structure of [$TbPc^2$] (Pc^{2-} =phthalocyanine) with red, blue, and gray spheres represent terbium, nitrogen, and carbon respectively. Hydrogen atoms have been removed for clarity.

However, some progress has been made in this direction, particularly by tuning QTM, as in the case of $\mathbf{Mn_4}$ SMM. These molecules do not exhibit zero-field QTM due to weak intermolecular antiferromagnetic exchange coupling within the molecule dimer, which shifts the resonance between the two lowest microstates and leads to the retention of magnetization upon the removal of the external magnetic field [76].

2.1.2 Molecule-surface interaction

To realize the potential applications of these molecules in advanced spintronics devices, it is essential to investigate their interactions with substrates at a fundamental level. This entails a comprehensive understanding of the adsorption mechanisms of the molecules, as well as the reciprocal modifications that occur, including changes to the local substrate at the adsorption sites and alterations in the electronic structure of the molecules themselves.

There are two primary adsorption mechanisms affecting molecules adsorbed on

a substrate: physisorption and chemisorption. In physisorption, the molecule binds weakly to the surface, resulting in minimal influence on the electronic structure of both the adsorbate and the substrate. Consequently, the discrete molecular orbitals are preserved, and the intrinsic molecular properties remain largely unchanged. In contrast, chemisorption involves the formation of new chemical bonds between the molecules and the substrate, leading to the emergence of an interface with altered electronic structures and properties. Such hybridization yields into broadening the electronic states of the molecules and shifting it with respect to the states in the gas phase [77], as depicted in Fig. 2.9(a).

In the gas phase, molecular states have longer lifetime, and their energies are precisely defined. However, upon adsorption on a metallic surface, the electron from the molecule has a finite probability of escaping to the surface. This interaction reduces the lifetime of the molecular states (τ) and increases the energy uncertainty, following the Heisenberg uncertainty principle, resulting in energy broadening with a finite width $\Gamma \approx \frac{\hbar}{\tau}$ [78]. The extent of this broadening can vary from meV to eV, depending on the density of states (DOS) of the metal and the interaction strength between the molecule and the surface [79].

In ferromagnetic metals, the spin-split DOS causes spin-dependent hybridization, lifting the degeneracy of the molecular electronic states and resulting in different energy shifts for different spin orientations [78]. This spin splitting can lead to various interface effects such as spin inversion [80], enhancement, or spin filtering [81]. The distinction among these effects is determined by the relative differences in broadening and shifting of the molecular orbitals occurring in the DOS of that spin-polarized interface, or spinterface, $\boldsymbol{D}_{\mathrm{int}}^{\uparrow(\downarrow)}(\mathrm{E})$ which is given by [78]:

$$\mathrm{D}_{\mathrm{int}}^{\uparrow(\downarrow)}(\mathrm{E}) \;=\; \frac{\Gamma^{\uparrow(\downarrow)}/2\pi}{(\mathrm{E}-\epsilon_{\mathrm{eff}}^{\uparrow(\downarrow)})^2+(\Gamma^{\uparrow(\downarrow)}/2)^2} \tag{2.15}$$

where $\Gamma^{\uparrow(\downarrow)}$ and $\epsilon_{eff}^{\uparrow(\downarrow)}$ is the spin-dependent molecular state broadening and the effective molecular level energy when coupled to the surface, respectively. The spin-polarization of the spinterface is defined as:

$$\mathrm{P}_{\mathrm{int}} \;=\; \frac{\mathrm{D}_{\mathrm{int}}^{\uparrow}-\mathrm{D}_{\mathrm{int}}^{\downarrow}}{\mathrm{D}_{\mathrm{int}}^{\uparrow}+\mathrm{D}_{\mathrm{int}}^{\downarrow}} \tag{2.16}$$

Spin-polarization inversion at the interface took place, i.e. $\mathrm{P}_{\mathrm{int}} = -\mathrm{P}_{\mathrm{FM}}$, when the broadening of the molecular state is larger than the shift of the molecular state with respect to the Fermi level, $\Delta\mathrm{E} = \mathrm{E}_{\mathrm{F}} - \epsilon_{\mathrm{eff}}$, i.e.: $\Gamma \gg \Delta E$. The DOS of the interface, expressed in Eq. 2.15, becomes $\mathrm{D}_{\mathrm{int}}^{\uparrow(\downarrow)} \approx \frac{1}{\Gamma^{\uparrow(\downarrow)}} \propto \frac{1}{\mathrm{D}_{\mathrm{FM}}^{\uparrow(\downarrow)}}$, where the broadening is proportional to the DOS of the ferromagnetic substrate. The larger the broadening the smaller the molecular DOS $\mathrm{D}_{\mathrm{int}}^{\uparrow(\downarrow)}$. Such spin-polarization inversion in the spinterface is expected to happen for intermediate to strong coupling between the molecule and the substrate. Atodiresei et al. observed local induced spin-polarization inversion near the Fermi level in the interface of H_2Pc molecules

adsorbed on two monolayers Fe/W(110) [80]. SP-STM microscopy measurements showed that the molecule has an opposite spin-polarization to the Fe substrate with significant positive spin-polarization at the carbon ring sites opposite to negative spin polarization for the Fe substrate but no significant polarization at the H atoms. This energy-dependent spin-polarization is attributed to the hybridization between the out-of-plane $\pi(p_z)$ and substrate's d-orbitals in what is known as $p_z - d$ Zener exchange mechanism [82].

The second case occurs at the other limit where the broadening is less than the shift of the MO energy levels, i.e.: $\Gamma \ll \Delta E$. From eq. 2.15 one obtains $\mathrm{D}_{\mathrm{int}}^{\uparrow(\downarrow)} \approx \frac{\Gamma^{\uparrow(\downarrow)}}{(\Delta \mathrm{E}^{\uparrow(\downarrow)})^2} \propto \frac{\mathrm{D}_{\mathrm{FM}}^{\uparrow(\downarrow)}}{(\Delta \mathrm{E}^{\uparrow(\downarrow)})^2}$, where the effective spinterface DOS $\mathrm{D}_{\mathrm{int}}^{\uparrow(\downarrow)}$ is proportional to the DOS of the ferromagnetic substrate with the broadening inverse as a prefactor. Thus, we expect an enhancement in the effective spinterface DOS when the MO energy levels (with small Γ) shifts away from the Fermi level of the ferromagnetic substrate (large ΔE). Based on that, the spin-polarization of the interface becomes larger than the ferromagnetic substrate, $\mathrm{P}_{\mathrm{int}} > \mathrm{P}_{\mathrm{FM}}$. This is more likely to occur for weak coupling where the broadening is small with respect to MO energy levels shift. Also, the spin-dependent shift of the effective molecular level energy coupled to the surface, ϵ_{eff}, makes this spinterface works as a spin-filter. Kawahara et al., using SP-STS, could detect spin-splitting of a LUMO derived molecular state of the molecule $\mathbf{C_{60}}$ adsorbed on different terraces with alternating in-plane magnetization directions of Cr(001) surface [83]. This molecular state close to the Fermi level can be used for energy-dependent spin-filtering, where the spin-up channel is separated from the spin-down channel by several meV and the tunneling magnetoresistacne (TMR) values achieved through these molecules can reach up to 100%. Both spin-polarization inversion and enhancement can take place in the same molecule as it is the case in **CoPc** molecules deposited on an Fe surface, where the carbon rings hosts the spin polarization inversion whereas the enhancement of spin polarization occurred on the cobalt center [84]. Fig. 2.9 (b), and (c) depicts the spin-polarization inversion and enhancement in the spinterface DOS, respectively.

Various other effects can occur when magnetic molecules are adsorbed on surfaces, including alterations in the molecules' magnetic anisotropy [85]. Stoll et al. observed an in-plane easy axis magnetic anisotropy in $\mathbf{Dy(tta)_3}$ complex deposited on an Au(111) surface. This anisotropy arises from the alignment of the molecule's easy axis parallel to the surface, caused by the chemisorption of two tta ligands to the substrate, which distorts the crystal ligand field around the **Dy(III)** ion. This behavior contrasts with other lanthanide-containing molecules, where the magnetic easy axis typically aligns perpendicular to the surface [86, 87]. Additionally, the magnetic anisotropy of some SMMs could be tuned by reduction or oxidation of the metallic surface which influences the mediating superexchange interaction between these molecules and the substrate [88–90].

On the other hand, the spin of the central transition metal in some molecules can be completely quenched due to interaction with the substrate, as seen in CoPc adsorbed on Fe [84]. Despite this quenching, the molecule still exhibits spin-polarization inversion and amplification. In CoPc, the unpaired electron in the out-of-plane

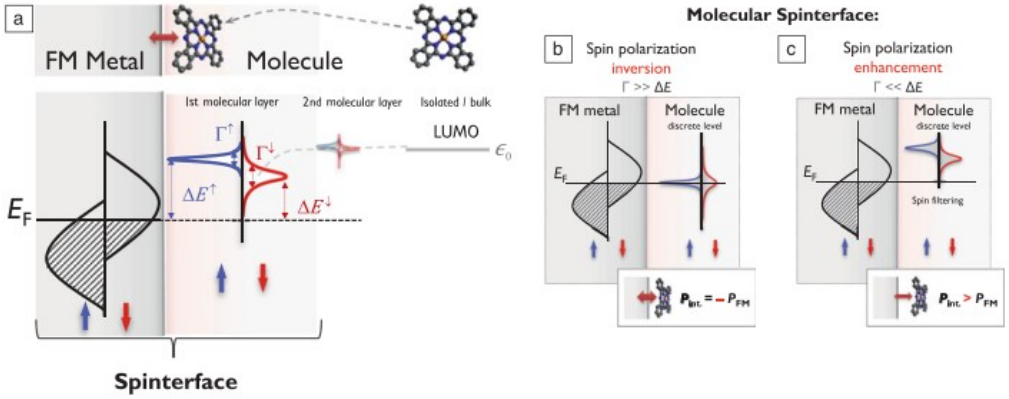

Figure 2.9: (a) The metallic substrate has a simple continuous spin-split $3d$ density of states (DOS), while the molecule in the gas phase features discrete MO, with only the LUMO illustrated. As the molecule nears the surface, the LUMO is altered through broadening, Γ, and shifting, $\Delta \mathrm{E} = \mathrm{E_F} - \epsilon_{\mathrm{eff}}$, due to hybridization at the interface. The spin-dependent MO shifting and broadening becomes smaller in the subsequent layers. (b) Spin-polarization inversion of the molecular DOS, $\mathrm{D}_{\mathrm{int}}^{\uparrow(\downarrow)}$, due to large broadening compared to the energy levels shifts $\Gamma \gg \Delta E$, as explained in the text. (c) Spin-polarization enhancement (spin-filter) of $\mathrm{D}_{\mathrm{int}}^{\uparrow(\downarrow)}$ occurs when $\Gamma \gg \Delta E$. Adapted from Ref. [78].

d_{z^2} orbital, located at the Co site, contribute to the total molecular spin yielding S=1/2. However, electron transfer from the substrate to this orbital leads to its occupation, thereby quenching the molecular spin [84]. Despite the spin quenching, spin-splitting of the hybridized density of states $\mathrm{D}_{\mathrm{int}}^{\uparrow(\downarrow)}$ is recovered due to the distortion of the molecular geometry upon adsorption. This distortion, along with van der Waals forces at the interface, generates locally varying electronic charges in the spin-up and spin-down channels within these hybridized states [84].

In contrast, electron transfer upon adsorption may either induce or leave the spin of the central atom unchanged, as observed in **NiPc** and **CuPc** adsorbed on Ag(100) [91]. Furthermore, when **CoPc** is deposited on different substrates, such as Co, the spin-polarization characteristics of the molecule vary significantly. For instance, **CoPc** on Co exhibits a spin-polarization resonance near the Fermi level, which is absent when the molecule is adsorbed on Fe. Moreover, the spin polarization in the molecular ligands of **CoPc**/Fe is stronger compared to **CoPc**/Co, likely due to the stronger interaction between the molecule and the Fe surface. This strong chemisorption results in a larger ΔE, leading to enhanced spin-polarization in the Pc ligands [92].

2.2 Molecules-Toolbox for Single-molecule Spintronics

Incorporating molecules into spintronic devices offers several distinct advantages over traditional inorganic spintronic systems. First, molecules can be synthesized and tailored to specific requirements, resulting in a vast array of functional molecules to meet diverse needs. Second, the use of light elements in molecular synthesis, which lack significant spin-orbit coupling and hyperfine interactions, enables long τ_s in the molecules. Third, the sharply defined electronic states of molecular orbitals (MOs) allow for precise quantum mechanical manipulation, introducing novel functionalities to the devices, such as quantum tunneling effects [30]. Molecular spintronic devices have been realized in various forms, including molecular spin valves [93], quantum-information buses [94], molecular spin transistors [95], and single-molecule magnets (SMMs) [43, 59, 68].

Single-molecule magnets (SMMs) have acquired significant attention in the molecular magnetism community due to their relatively long magnetization relaxation times below the blocking temperature, which for some SMMs can extend to years at temperatures below 2 K [44]. In this section, a literature review will be presented, focusing on various SMMs and the investigations related to them. Additionally, key findings from studies of SMMs on surfaces and other metallic-centered molecules will be discussed. It is important to note that this field is highly interdisciplinary, integrating synthetic chemistry, materials science, and physics. Consequently, this review will approach the topic from a physicist's perspective, emphasizing fundamental interactions within these molecules—such as spin-spin exchange interactions, substrate hybridization, and spectroscopic properties—rather than the synthetic development of these molecules, which can be explored in more specialized references [74, 96, 97].

SMMs exhibit a wide range of shapes, sizes, and compositions, with various guest ions and host complexes. The first discovered SMM was the $\mathbf{Mn_{12}Ac}$ complex, with an effective energy barrier U_{eff}= 6 meV (73.4 K) and a blocking temperature of T_B = 3K [44]. Subsequent discoveries of transition metal-based SMMs have been reported, but their U_{eff} and T_B values remain lower than those of the archetypal $\mathbf{Mn_{12}Ac}$ complex. One notable polynuclear transition metal SMM is the $\mathbf{\{Fe_8\}}$ cluster ($\mathbf{[Fe_8^{III}O_2(OH)_{12}(tacn)_6]^{8+}}$) [98]. However, this SMM also has a lower effective energy barrier than $\mathbf{Mn_{12}Ac}$ complex with U_{eff}= 2 meV (21.6 K) and T_B= 3 K. This molecule has exhibited intriguing quantum phenomena, such as quantum tunneling of magnetization at low temperatures (∼400 mK) [99], and quantum phase interference [100].

In 2003, the first mononuclear lanthanide single-ion magnet (SIM), $\mathbf{[TbPc_2]^-}$, showed an improved effective energy barrier of U_{eff}= 28 meV (330.9 K), setting a record at the time. However, the blocking temperature remained very low at T_B= 1.7 K [70]. This significant enhancement in lanthanide SMMs is attributed to the strong spin-orbit coupling and large unquenched orbital angular momentum of the

lanthanide ions, which lead to strong magnetic anisotropy. Phthalocyanine-based SIMs have been a particularly prolific research area in molecular magnetism studies [101], especially for surface deposition due to their planetary and chemical stability [102, 103]. Intensive research efforts have improved the energy barrier of these SIMs, reaching U_{eff}= 80 meV (938.1 K) with blocking temperature of T_B= 30 K [104].

A limitation of mononuclear 4f SIMs, however, is the weak exchange interaction between the spins in the well-shielded 4f orbitals and the surrounding ligands, which hampers spin manipulation—critical for potential molecular spintronics applications. Polynuclear 4f SMMs have shown improved U_{eff} values, such as $\mathbf{[Dy(\mu-OH)(DBP)_2(THF)]_2}$ with U_{eff}= 62 meV and T_B= 8 K [105]. This increase is due to the strong Dy-Dy dipolar magnetic coupling, although quantum tunneling of magnetization (QTM) causes a narrow hysteresis loop. To suppress QTM, the use of radical ligands between central Ln^{+3} ions is crucial, as their diffuse orbitals penetrate the outer shells of the $4f$ ions, resulting in strong magnetic coupling. An example is the SMM $\mathbf{\{[(Me_3Si)_2N]_2(THF)Ln)\}_2(\mu-\eta^2:\eta^2-N_2)^-}$, which shows an open hysteresis loop up to T_B= 8.3 K with a coercive field of 1.5 T [106]. That short axial bonds connecting the central Ln^{+3} ion to the ligand enhance the magnetic axiality and increases the magnetization energy barrier reversal.

Later developments involved incorporating both $3d$ and $4f$ ions into SMMs. The first mixed $3d-4f$ SMM, reported in 2004, was the tetranuclear $\mathbf{Cu_2Tb_2}$ complex, with U_{eff}= 2 meV (21.6 K) and T_B= 1.2 K [75]. A major breakthrough in SMM research occurred in 2018 when Layfield and colleagues judiciously designed a ligand framework for the dysprosium metallocene $\mathbf{[(Cp^{iPr5})Dy(Cp^*)]^+}$, resulting in an SMM with an effective energy barrier of U_{eff}= 191 meV (2217 K) and a robust magnetic hysteresis above liquid nitrogen temperature, with T_B= 80 K [107]. This enhanced performance is attributed to the strong cyclopentadienyl ($\mathbf{Cp}$) rings that provide strong magnetic axiality of the $\mathbf{Dy^{3+}}$ ions, with short $\mathbf{Cp-Dy}$ distance (2.296/2.284 Å) and a wide $\mathbf{Cp-Dy-Cp}$ angle (162.5°), as well as the constrained metal-ligand vibrational modes induced by the crystal field of the $\mathbf{Cp}$ rings. Numerous other polynuclear and mononuclear rare-earth SMMs have been explored in recent years, and additional reviews can be found in the literature [61, 74, 108, 109].

Another interesting class of SMMs that has recently garnered attention is metallacrowns (MCs) [110–113]. These multinuclear cyclic metal clusters feature a structure similar to organic crown ethers, consisting of repeating $\mathbf{[-M-N-O-]}$ units. The following chapter will delve into the details of metallacrowns, but here we will briefly review key results and progress. These complexes demonstrate high thermodynamic stability and structural integrity in solution, where the core motif of MCs offers a defined arrangement of metal ions. Furthermore, their flexibility arises from the ability to exchange guest metal ions, as well as bridging and secondary ligands, allowing for versatile molecular design and enabling surface-specific linkages [110].

Early investigations of heterovalent manganese-based MCs, such as,
$\mathbf{Mn(II)(OAc)_2[12-MC_{Mn(III)N(Shi)}-4](DMF)_6}$, revealed low effective energy

barriers due to the low-spin ground states resulting from intramolecular antiferromagnetic exchange interactions. Since a high-spin ground state is crucial for enhancing the energy barrier in $3d$ metal-centered SMMs [114], this low-spin preference was a limitation. To address this, Rentschler and colleagues introduced the "magnetic director" approach, which aims to enforce a high-spin ground state in these molecules [110]. This approach simplifies the exchange coupling into two distinct interactions: the radial coupling (J_1) between the central ion and the peripheral metal ions, and the tangential coupling (J_2) between the metal ions within the ring. The spin Hamiltonian's energy levels vary linearly with the J_1/J_2 ratio. By carefully tuning these couplings, a high-spin ground state can be achieved in 12-MC-4 complexes, such as homometallic **$CuCu_4$**, where a high-spin state emerges if the tangential exchange coupling exceeds a threshold ratio of $J_1/J_2 = 4$ [110].

This concept was later extended to heterometallic MCs, such as the 12-MC-4 **$CuFe_4$** complex, where the central **Cu(II)** ion (S = 1/2) aligns the peripheral **Fe(II)** ions (S = 5/2) in parallel, acting as a magnetic director and leading to a spin ground state of S = 11/2 [111], as shown in Fig. 2.10a. This alignment arises from strong radial exchange interactions between the central **Cu(II)** ion and the peripheral **Fe(II)** ions, facilitated by the antiferromagnetic exchange through the $d_{x^2-y^2}$ orbital. This orbital points directly toward the basal donor atoms, resulting in an antiparallel alignment of the central **Cu(II)** ion relative to the peripheral **Fe(II)** ions. This was confirmed through element-selective X-ray magnetic circular dichroism measurements, which verified the antiparallel alignment [115]. While these complexes do not exhibit slow magnetization relaxation, the magnetic director approach has successfully yielded SMM behavior in other systems, such as **$CoCo_4$** 12-MC-4 MC complexes. These systems demonstrate an energy barrier of 7 meV (78.9 K) with T_B= 8.5 K [110].

The development of mixed $3d-4f$ metallacrowns has also shown great promise as a pathway to novel molecular magnets, where the $3d$ metals serve as spin carriers and the unquenched orbital magnetic moments of $4f$ trivalent ions provide high magnetic anisotropy [67, 112, 113, 116, 117]. Notable examples include the **{$DyGa_8$}** double-decker 12-MC-4 complex, which exhibits an energy barrier of 3.5 meV (40 K), and the **{$TbNi_8$}** double-decker 12-MC-4 complex with energy barrier of 50.4 meV (585 K) [112]. Additionally, research on 15-MC-5 complexes has demonstrated improved energy barrier values. Examples include **$DyNi_5$** and **$TbNi_5$**, which were explored in this thesis and showed energy barriers of 28 meV (340 K) and 7 meV (85 K), respectively [118]. These advancements underscore the potential of mixed 3d-4f metallacrowns in enhancing the energy barriers and magnetic anisotropy of SMMs. Fig. 2.10b shows the most prominent chronological progress of the SMMs and their effective energy barrier.

Another key research question in the study of magnetic molecules involves investigating their behavior when deposited on different surfaces. The first attempt to organize single-molecule magnets (SMMs) into an ultrathin film was made by Clemente-León et al., using the Langmuir-Blodgett (LB) films technique [119]. However, this ambient approach did not see further development due to various limitations, such as the inherent instability of LB films [120]. Alternative deposition

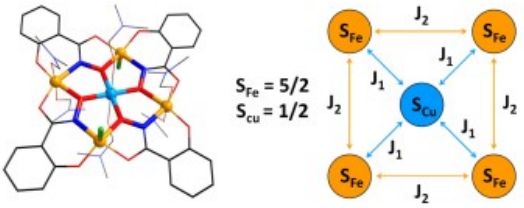

(a)

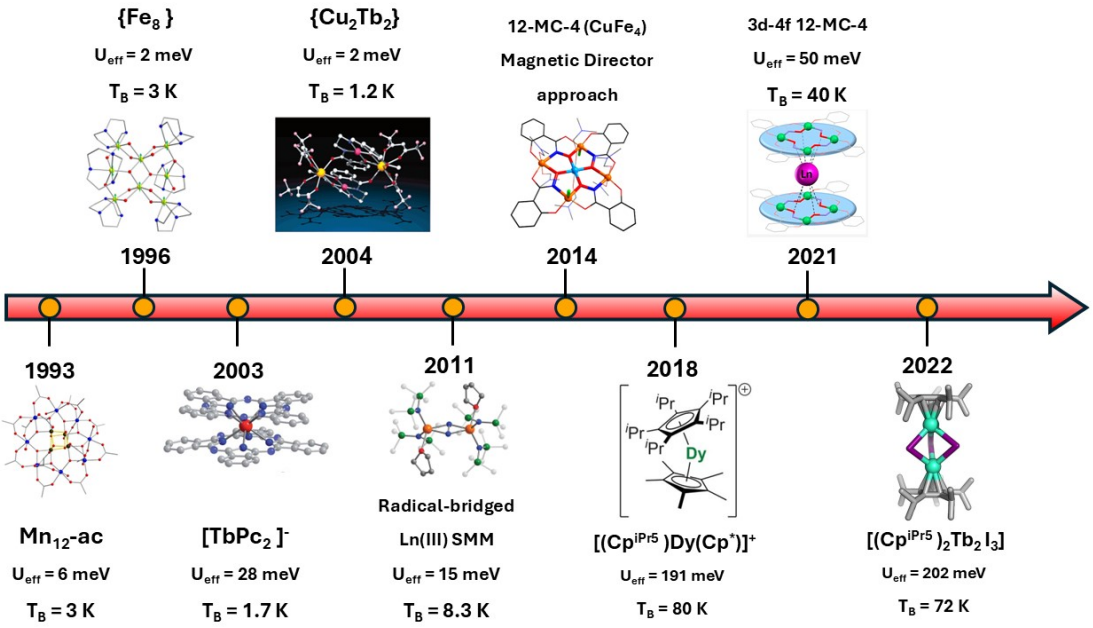

(b)

Figure 2.10: (a) Molecular structure of the $CuFe_4 12-MC-4$ complex (left) , Cu(II) (light blue), Fe(III) (gold), O (red), N (blue), C (black). Magnetic director approach in the square magnetic model of the molecule (right). (b) Chronological progress of the SMM U_{eff} and T_B mentioned in the text.

techniques have since been explored, including the self-assembly of functional monolayers (SAMs). In one such method, monolayers of $\mathbf{Mn_{12}Ac_{12}}$ SMMs were grafted onto gold substrates by immersing the substrate in a solution containing SMMs functionalized with sulfur groups (thiols) [121]. These functional peripheral ligands help preserve the magnetic properties of the SMM in the junction [122]. Other methods, such as stamp-assisted nanopatterning, have been employed to deposit hydrophobic $\mathbf{Mn_{12}}$ derivatives onto oxidized Si(100) substrates [123]. However, molecules deposited using this method are physisorbed on the surface and exhibit lower stability compared to covalently grafted layers. These gentler deposition techniques have proven reliable in maintaining the structural integrity of the molecules, as confirmed by X-ray photoelectron spectroscopy (XPS). Dunbar et al. successfully prepared thin films of $\mathbf{Mn_{12} - acetate}$ using moderate thermal evaporation methods like pulsed laser deposition (PLD) [124]. Additionally, several researchers have reported the deposition of SMMs on various surfaces through thermal evaporation using physical vapor deposition (PVD). For example, $NdPc_2$/Cu(100) [125] and $DyPc_2$/Au(111) [126]. For further details on other unconventional deposition and preparation techniques for SMMs and other magnetic molecules on surfaces, the reader is referred to the references [54, 127].

SMMs and metallic-centered molecules have been extensively studied using various complementary techniques. These molecules have been primarily investigated through SQUID magnetometry, which provides quantitative information on key properties such as the blocking temperature (T_B), the effective energy barrier (U_{eff}), and the relaxation time (τ). However, additional insights into the behavior and properties of SMMs can be obtained using other techniques. Neutron diffraction, for instance, offers valuable structural and magnetic information [128], while electron paramagnetic resonance (EPR) allows for the study of magnetic states and spin dynamics [129].

Moreover, β-nuclear magnetic resonance (β-NMR) provides information on local magnetic environments [130], and scanning tunneling microscopy / spectroscopy (STM/STS) enables atomic-level imaging and spectroscopy of the molecules on surfaces [102, 125]. Additional techniques such as resonant photoemission spectroscopy (RPES) [131] and X-ray magnetic circular dichroism (XMCD) [87, 132–136] have also been employed to further explore the electronic and magnetic properties of SMMs and metallic-centered molecules, providing a more comprehensive understanding of these systems.

In this review, we examine the microscopic magnetic behavior of single-molecule magnets (SMMs) and metallic-centered molecules deposited on surfaces, utilizing two high-resolution techniques: XMCD and STM. One of the initial research questions in this area was the preservation of magnetic integrity of SMMs once get deposited on surfaces, which is a critical factor for their potential use in future molecular spintronics devices. Mannini et al. reported the loss of magnetic remanence in $\mathbf{Mn_{12}}$ SMMs deposited on a gold surface, as observed from low-temperature XMCD measurements [132]. This loss was attributed to the partial reduction of $\mathbf{Mn^{3+}}$ ions to $\mathbf{Mn^{2+}}$, leading to structural rearrangement and, consequently, a loss of magnetic

hysteresis.

In a follow-up study, Mannini et al. demonstrated that the SMM behavior in **Fe_4** molecules, attached to a gold surface via sulfur-functionalized ligands, was preserved. A remnant magnetization and a butterfly-shaped open hysteresis loop at sub-Kelvin temperatures was observed, with a T_B of approximately 0.5 K [133]. This contrast in results was attributed to the superior redox stability and structural robustness of the **Fe_4** molecule. Other SMMs, such as Cr_7Ni/Au(111) [137, 138], $TbPc_2$/Cu(100)[135], $TbPc_2$/Au(111) [136], $TbPc_2$/graphite [139] and $TbPc_2$/HOPG [140], have also been shown to retain their SMM properties when deposited on surfaces. These findings suggest no fundamental limitation preventing the preservation of SMM magnetic properties on surfaces.

Moreover, XMCD studies of other paramagnetic molecules, which are not classified as SMMs, have revealed surface-induced magnetic ordering and hysteresis when deposited on ferromagnetic surfaces. For instance, Fe octaethylporphyrin (**OEP**) deposited on Co / Cu(100) [90] and Mn-porphyrin on Co / Au(111) [141] exhibited such behavior. The surface-induced ferromagnetic ordering in Fe(OEP)/Co/Cu(100) was attributed to an indirect superexchange interaction between the metallic center in the molecule and the magnetic substrate [90]. In this system, the Fe spin magnetic moment can be manipulated both in-plane and out-of-plane by adjusting the magnetization direction of the substrate.

Phthalocyanine molecules, a promising class of materials, have also been studied on various surfaces using element-selective XMCD technique. Stepanow et al. reported that **CuPc** molecules on Ag(100) surfaces not only retained their integrity but also exhibited a nine-fold increase in magnetic susceptibility compared to bulk **CuPc** powder. Angle-dependent XMCD measurements revealed a strong Cu spin dipole moment resulting from highly directional bonds and the local crystal field surrounding the metallic ion [134]. Despite the strong interaction between the planar molecule and the Ag(100) surface, a dramatic 500% increase in the orbital moment from in-plane to out-of-plane directions was observed in this hybrid system [134].

Further research on lanthanide-based phthalocyanine complexes, such as the double-decker **$TbPc_2$**, has highlighted the presence of strong anisotropic antiferromagnetic coupling between the molecule and ferromagnetic substrates [88]. In these systems, the ligand-mediated superexchange interaction can be tuned by doping the interface with electron donors or acceptors. Additionally, the magnetization of **$TbPc_2$** molecules can be aligned either parallel or antiparallel to the substrate's magnetization, paving the way for their potential application in spintronic devices, such as spin valves [88].

The investigation of single-molecule magnets (SMMs) on surfaces using scanning tunneling microscopy/scanning tunneling spectroscopy (STM/STS) necessitates specific conditions related to molecular deposition in ultra-high vacuum (UHV) and their conductive coupling to the substrate. As a result, the existing STM/STS studies on this class of molecules are largely confined to metal phthalocyanines (**MPc**), lanthanide phthalocyanines (**LnPc**), and double-decker phthalocyanines

(**LnPc$_2$**) [127]. The STS investigations of metallic-centered molecules can be categorized into two types, based on the energy range surrounding the Fermi level (E_F): (i) inelastic electron tunneling spectroscopy (IETS), which occurs within a narrow energy window (± 100 meV) around E_F and reveals two distinct phenomena—Kondo effects and spin excitations; and (ii) elastic electron tunneling spectroscopy, which occurs over a broader energy range (± 2 eV) around E_F and provides insights into the highest occupied molecular orbital-lowest unoccupied molecular orbital (HOMO-LUMO) gap.

Regarding the Kondo effect, the localized magnetic moment of the host molecules strongly interacts with the conduction electrons of the metallic substrate, forming a non-magnetic singlet state overall below a critical threshold known as the Kondo temperature (T_K) [142]. The onset of the Kondo effect is characterized by an increase in resistance as the temperature decreases, contrary to the expected behavior of metallic resistance. This phenomenon is reflected in the STS spectra as a resonance peak centered around E_F [142]. This peak corresponds to the ground state of the singlet state arising from the many-body interaction between the sea of Fermi electrons in the metal and the localized magnetic moment of the molecule. Various studies have reported elevated values of T_K in Phthalocyanines. For example, Zhao et al. found that the T_K of CoPc/Au(111) is approximately 208 K, and the Kondo resonance can be reestablished by removing eight hydrogen atoms from the molecule using voltage pulses from the STM tip [143]. Meanwhile, Gao et al. reported a significant dependence of the Kondo resonance on adsorption sites in FePc/Au(111) with a T_K exceeding room temperature (approximately 360 K) [144].

Fig. 2.11 illustrates the findings for TbPc/Au(111) reported by Katoh et al [145]. The **TbPc** molecule results from the fragmentation of the double-decker **TbPc$_2$**, leading to the loss of one **Pc** ligand upon adsorption [145]. STS spectra conducted on the central **Tb^{3+}** ion reveal a resonance peak with a width of approximately 20 meV, which is absent in the spectra taken over the **Pc** ligands, yielding a T_K of approximately 250 K. This observation is attributed to the strong coupling between the central Tb ion in the molecule and the STM tip. Additionally, the Kondo effect in these molecules requires more than just a localized magnetic moment; it also depends on the stability of the doublet ground state. For instance, in the case of the **Tb^{3+}** ion, the energy difference between the $m_J = \pm 6$ and the first excited state $m_J = \pm 5$ is greater than 50 meV, in contrast to the **Dy^{3+}** ion, where this energy difference is around 6 meV, thus resulting in the absence of a Kondo peak in the **DyPc** molecule [145]. For further information, readers are referred to more comprehensive reviews and articles on this topic [142, 146–151].

Another notable result from the IETS investigation of metallic-centered molecules is the measurement of spin-flip excitations. Chen et al. used spin-flip spectroscopy to explore the superexchange coupling between successive molecular layers of **CoPc** deposited on Pb(111) islands [152]. The first molecular layer exhibited neither Kondo resonance nor Zeeman splitting in the scanning tunneling spectroscopy (STS) spectra around the Fermi level, indicating a quenching of the molecular spin. This first layer acts as an insulating buffer between the Pb substrate and the subsequent molecular layers, allowing the magnetic moment of the second layer to survive. However,

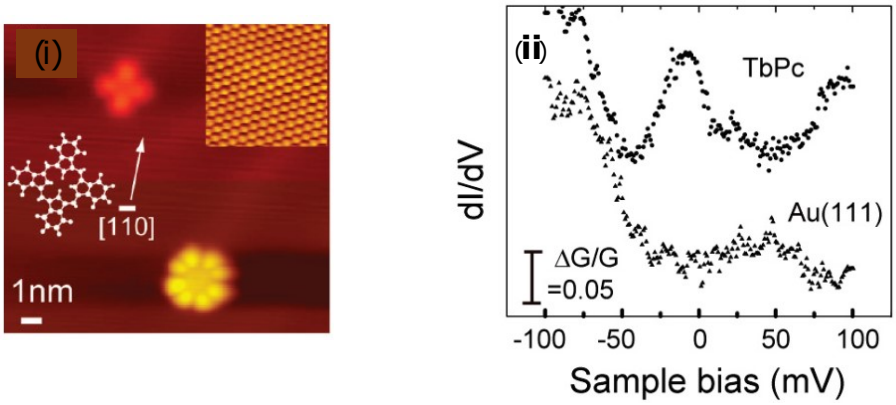

Figure 2.11: (i) Topographic images of TbPc molecules (top) and $TbPc_2$ molecules (bottom) deposited on /Au(111). (ii) dI/dV spectrum showing Kondo resonance peak around E_f of the TbPc molecule compared to the flat dI/dV spectrum of the bare surface of Au(111). Image is adapted from Ref. [145].

residual coupling between the substrate and the second layer screens the molecular magnetic moment, leading to the observation of a Kondo resonance peak with a Kondo temperature (T_K) of approximately 10 K at the second monolayer. Upon applying a magnetic field of 1.5 T, the superconducting state of Pb is quenched, causing the magnetic moment of the **CoPc** molecule to experience Zeeman splitting. The STS spectrum, shown in Fig. 2.12, was measured on the central $\mathbf{Co^{2+}}$ ion in the third molecular layer. A single IETS step at around 19 meV corresponds to a spin excitation from the singlet ground state to the triplet excited state, a result of antiferromagnetic exchange coupling between two adjacent **CoPc** molecules in the columnar chain. At higher magnetic fields, this single step is further split into three distinct steps due to the lifting of the degeneracy of the triplet state. By diagonalizing the Hamiltonian of the spin chain, Chen determined the exchange coupling constant to be around $J \sim 18$ meV. This antiferromagnetic ordering arises from superexchange coupling, where an electron from the π system of the **Pc** ring hops to the d_{z^2} orbital of the $\mathbf{Co^{2+}}$ ion. The remaining unpaired electron in the π-orbital then forms a direct exchange coupling with an electron in the d_{z^2} orbital of a neighboring $\mathbf{Co^{2+}}$ ion, as illustrated in the schematic diagram in Fig. 2.12.

The integration of spin-polarized scanning tunneling microscopy (SP-STM) and spectroscopy (SP-STS) into the study of molecules on surfaces has demonstrated the potential for spin transport through molecular systems. Iacovita et al. performed SP-STM and SP-STS on **CoPc** molecules deposited on Co nanoislands grown on a Cu(111) surface [153], as illustrated in Fig. 2.13. The Co nanoislands have a

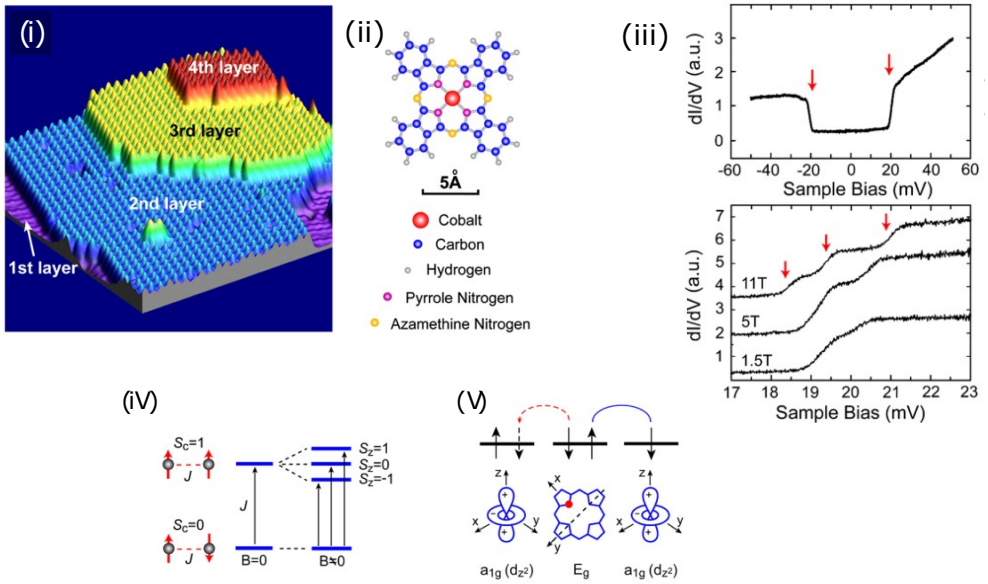

Figure 2.12: (i) STM topography image of Successive CoPc molecular layers deposited on Pd(111) islands (V = 0.9 V, I = 0.03 nA). (ii) CoPc molecular structure. (iii) IETS spectra acquired, at varying B-filed, on the top of central Co^{2+} ion in the third molecular layer. (iV) Schematic diagram of the spin transition from singlet ground state of the chain $S_c = 0$ to excited triplet state $S_c = 1$. (V) The superexchange mechanism between the electrons in the bridging N atom (red dot) of the Pc ligand and d_{z^2} orbitals of two central Co^{2+} ions. The red dashed line indicates the hopping and the solid blue line represents the direct exchange coupling. Image is adapted from Ref. [152].

perpendicular magnetization direction, which can be aligned collinearly with the out-of-plane magnetization component of the Co-coated metallic tips used in the experiment.

In this setup, the spin-dependent contribution to the differential conductance (dI/dV) varies with cosα, leading to different visualizations of the parallel ($\uparrow\uparrow$) and anti-parallel ($\uparrow\downarrow$) magnetization orientations between the tip and the Co nanoislands when in dI/dV mapping mode. Single-point spectroscopy (dI/dV vs V) on the Co nanoislands with different magnetization orientations shows a resonance peak with varying amplitudes at V = –0.28 V, as depicted in Fig. 2.13. Additionally, single-point spectroscopy at the center of the **CoPc** molecule reveals a resonance peak at V = –0.19 V, with different amplitudes for the ($\uparrow\uparrow$) and ($\uparrow\downarrow$) configurations of the nanoislands' magnetization (Fig. 2.13). The asymmetry of the dI/dV spectra for both the nanoislands and the molecules, defined as $\frac{dI/dV_{\uparrow\uparrow} - dI/dV_{\uparrow\downarrow}}{dI/dV_{\uparrow\uparrow} + dI/dV_{\uparrow\downarrow}}$, indicates ferromagnetic alignment between the molecule's spin orientation and the magnetization of the nanoisland over a specific energy range. This finding demonstrates the possibility of manipulating the molecule's spin by reversing the nanoisland magnetization, which is a promising mechanism for spin-dependent control in molecular electronics [153].

Further investigations of **CoPc** deposited on a different substrate, specifically a 1.8 monolayer (ML) of Fe, revealed spin-polarized tunneling through the molecule due to spin-split hybrid states formed between the molecule and the surface [84]. Brede et al. conducted energy- and site-dependent studies with intramolecular spatial resolution, showing the spin polarization transitions from inversion to amplification, despite the loss of the molecule's net spin due to the transfer of one electron from the substrate to the unoccupied d_{z^2} molecular orbital.

Although the spin quenching occurred, the observed spin-splitting in the hybridized molecule-substrate system is attributed to an imbalance in the occupation of the hybridized state within a specific energy range. The variation in contrast of the ligands on different magnetic Fe domains suggests that spin polarization inversion occurred at that site of the molecule, while the central Co ion exhibited no variation in contrast, as shown in Fig. 2.13. The spin polarization near the metallic Co ion ranges from inversion to amplification, depending on the energy interval. For more extensive STM investigations of metallic-centered molecules, additional studies can be found in the literature [80, 127, 154].

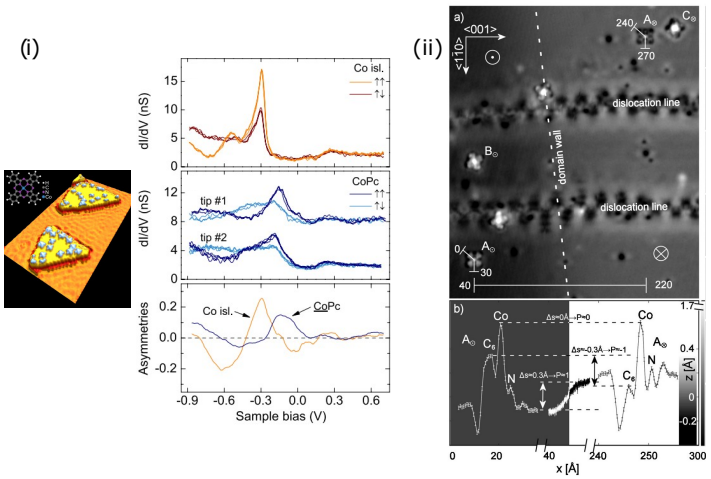

Figure 2.13: (i) CoPc molecules adsorbed on Co nanoislands grown on Cu (111) substrate; the inset shows structure model for CoPc molecule. STM image parameters (40×20 nm^2, 0.1 V, 0.5 nA) (left). Spin-polarized tunneling conductance through the nanoislands and CoPc molecule as explained in the text (right). Image is taken from ref. [153].(ii) SP-STM image of CoPc molecule deposited on Fe double layer of different magnetic domains (a). The scan line profile indicated in (a) is shown in (b) revealing the different contrasts of the molecule on different magnetic domains. Image is taken from ref. [84].

This PhD thesis centers on the investigation of **intramolecular spin-spin interactions** in **single-molecule magnets (SMMs)** based on **mixed 3d-4f metallacrown (MC) complexes** using element-selective XMCD magnetometry technique. The work aims to reveal detailed magnetic behaviors within these molecules that are not easily discerned with conventional macroscopic methods such as AC-susceptibility or SQUID magnetometry. Metallacrowns, such as 12-MC-4 and 15-MC-5, offer thermodynamically stable scaffolds for organizing spin centers, thus providing a promising avenue for designing SMMs with high spin ground states and substantial effective energy barriers. The inclusion of 4f ions, such as Tb(III) and Dy(III), enhances molecular magnetic anisotropy, leading to slower relaxation rates in the reversal of magnetization. This effect stems from the large orbital magnetic moments and strong spin-orbit coupling of the 4f ions.

The key research gap of this thesis addresses, is the accurate determination of the effective energy barrier (U_{eff}) of mixed 3d-4f MC-based SMMs using element-specific magnetometry. Traditional approaches, like AC-susceptibility or SQUID magnetometry [67, 112, 155, 156], are often hindered by the strong ligand field effects and the difficulty in fully saturating these complexes, particularly in the presence of substantial axial magnetic anisotropy. Additionally, these conventional methods often rely on the Arrhenius law to extract energy barriers, which does not account for the complex relaxation mechanisms that many of these systems exhibit [157]. XMCD, by contrast, provides a more refined analysis of the magnetic coupling between the $3d$ and $4f$ centers and can directly measure the individual contributions from each element in the molecule, allowing for a more accurate determination of magnetic anisotropy and relaxation processes.

A secondary goal of the thesis is to explore how interactions between $3d-4f$ magnetic center molecules and ferromagnetic substrates affect intramolecular exchange coupling, particularly for the rare earth magnetic moments in the $4f$ ions. Although initial attempts to deposit MC-based SMMs on ferromagnetic substrates proved challenging, the research pivoted to other mixed $3d-4f$ molecules. These molecules were successfully deposited on surfaces with alternating magnetization domains, and their spin properties were examined using spin-polarized scanning tunneling spectroscopy (SP-STS), which provided insights into the spin excitations in these heterometallic systems.

The literature review reveals significant gaps, particularly regarding the use of magnetic inelastic electron tunneling spectroscopy (IETS) for mixed $3d-4f$ center molecules on magnetic surfaces. While IETS has been extensively applied to heterometallic $3d$-center molecules on non-magnetic substrates (e.g., $CuFe_4$/Au(111) [158]) and monometallic $3d$ center systems like FePc / CuO / Cu(110) [159], Fe-porphyrine / Au(111) [160], and Fe_4H / graphene / Ir(111) [161]. Similarly, there have been IETS studies of monometallic 4f center molecules on non-magnetic surfaces, including $TbPc_2$ / Au(111) [162], $DyPc_2$ / Au(111) [126], $DyPc_2$ / Cu(001) [163], and $NdPc_2$ / Cu(100) [125]. Additionally, investigations of magnetic substrates have primarily focused on non-magnetic molecules, such as H_2Pc/ Fe / W(110) [80], or monometallic 3d molecules like CoPc / Fe / W(110) [84]. The investigation of mixed metallic center molecules on ferromagnetic surfaces remains underexplored, and further studies in this area could provide valuable insights, potentially opening new avenues in the field of magnetic molecules on ferromagnetic surfaces.

In conclusion, the literature review indicates the various strategies for designing magnetic complexes to achieve higher effective energy barrier and magnetization blocking temperatures. Two critical requirements for efficient single-molecule magnets (SMMs) are important: the presence of multiple spin-orbit doublets with strong angular momentum projections and the significant energy separation between them [164]. Achieving room-temperature data storage requires overcoming significant hurdles, as current SMMs cannot reach the necessary anisotropy barrier height, which is around 1.5 eV. Though progress has been made, particularly with lanthanide-based systems, the realization of polynuclear SMMs with strong magnetic anisotropy and exchange interactions remains complex. Future advancements may depend on synthesizing regular magnetic networks or polyatomic SMMs, potentially enabling room-temperature operation, although these approaches are still in their early stages. Furthermore, by extending SP-STS investigations to mixed metallic center molecules on magnetic surfaces, this work opens up new research avenues for spin transport and spin excitations in heterometallic molecules, which are of significant interest for future applications in molecular spintronics.

Chapter 3

Metal-centered Molecules

This chapter is dedicated to provide a glimpse on the investigated molecules in this thesis. Most of the presented material here are taken from the PhD Theses of our collaborators Dr. Athansopoulou [113], Dr. Völker [155], and Dr. Kredel [165] from AK Rentschler in the Institute of Inorganic Chemistry and Analytical Chemistry-JUG Mainz. This overview contains an introduction to the used metallacrown itself, their structure, and their magnetic properties.

3.1 Metallacrown complexes

Since their discovery in 1989, metallacrown (MC) complexes have emerged as a fascinating class of complexes [166]. MCs has been introduced as descendants of the macrocyclic crown ethers which selectively bind alkali and alkaline earth ions [167]. MCs possess high thermodynamic stability and structural integrity in solution, making them promising candidates for various applications such as molecular magnetism, molecular recognition, and the stabilization of unstable molecules [168].

The structure of MCs consists of a repeating unit of $-[M-N-O]_n-$ motifs arranged in a cyclic pattern. In this arrangement, the ring metal and nitrogen atoms replace the methylene carbon atoms in the motif of crown ethers $-[C-C-O]_n-$, hence the name "metallacrown", as shown in Fig. 3.1. The nomenclature for MCs is based on the number of atoms that make up the ring, the number of oxygen atoms within the ring, and the central metal ion. This naming convention follows the format [67, 168]:

$$M_1B[\text{ringsize} - MC_{M_2X(L)} - \text{oxygens of the rings}]Y$$

In this format:

- M_1 refers to the ring-cavity metal ion ($3d$ or $4f$) with its oxidation state,
- B refers to the coordinating ions,

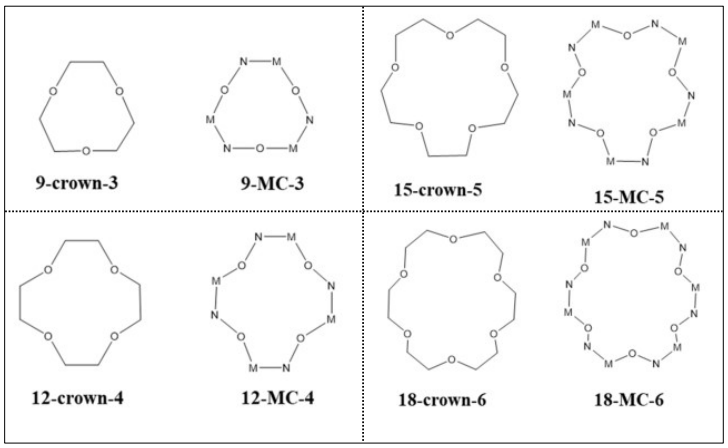

Figure 3.1: Schematic representations of different MC size motifs with their respecting crown ether analogue. Image is taken from Ref. [67]

- MC refers to the metallacrown,
- M_2 refers to the peripheral metal ring ions ($3d$) and its oxidation state,
- X refers to the third heteroatom of the ring,
- L refers to the ligand used,
- Yrefers to the non-coordinating ions.

Metallacrowns have different ring sizes and central and peripheral ions, but the used MCs in our investigations are the $3d-4f$ heterometallic $12-\mathrm{MC}-4$ and $15-\mathrm{MC}-5$. For $12-\mathrm{MC}-4$, MC is composed of 12-membered ring which is consisted of four repeating $-[\mathrm{M}-\mathrm{N}-\mathrm{O}]-$ units with 4 oxygen donor atoms. Meanwhile, the $15-\mathrm{MC}-5$ is composed of 15-membered ring consisting of five repeating $-[\mathrm{M}-\mathrm{N}-\mathrm{O}]-$ units with 5 oxygen donor atoms, as they are depicted in Fig. 3.1.

12-MC-4 Molecules

In our investigation of the magnetic properties of the $12-\mathrm{MC}-4$ molecules, we focused our experiments on two classes of molecules, shortly called: $\mathrm{REMn_4}$ and $\mathrm{RENi_8}$, where RE stands for trivalent rare-earth ions.

$\mathrm{REMn_4}$ Molecules:

The $\mathrm{REMn_4}$ molecule, $({}^{t}Bu_4N)[Mn_4^{II}Ln^{III}(O_2CBu^{t})_4][12-MC_{Mn(III)N(shi)}-4].5CH_2Cl_2$ where [Ln = Tb and Dy], was synthesized following the procedure outlined in Ref. [113].

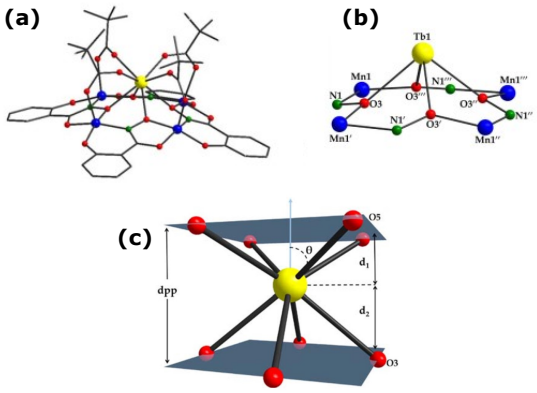

Figure 3.2: (a) Schematic representation of the molecular structure of $12-MC-4$ $TbMn_4$. (b) Labeled schematic representation of the complex core $\{Mn_4^{III}Tb^{III}(\mu-NO)_4\}^{11+}$. (c) Depiction of the interplanar distance (d_{pp}) between the two O_4-planes besides the distances between the central Tb^{III} ion with the upper and lower O_4-planes, d_1 and d_2, respectively. Color scheme represented as follow; yellow: Tb, red: Oxygen, green: Nitrogen, blue: Mn^{III},H atoms are omitted for clarity. Image is taken from Ref.[113].

By substituting the central rare earth ions, two distinct molecules, $TbMn_4$ and $DyMn_4$, were obtained. Single-crystal diffraction studies revealed that these compounds are isostructural, crystallizing in the P4/n tetragonal space group. The core structure of these compounds, illustrated in Fig. 3.2, features a square pyramidal topology with the Tb^{III} at the apex and the Mn^{III} ions forming the base. The core has a C_4 symmetry axis passing through the central Tb^{III} ion. The central Tb^{III} ion is coordinated by eight oxygen atoms, with the $Tb^{III}-O$ bond forming an angle of 56.15° relative to the four-fold symmetry axis, resulting in a slightly distorted square antiprismatic geometry (axially compressed), as shown in Fig. 3.2 (c). The lower 4 oxygen atoms binds with the basal Mn^{III} through the $Mn-N-O-Mn$ unit , which exhibits a torsion angle of 173.3(4)° and $Mn\cdots Mn$ separation of 4.642(9) Å. This near-ideal linear torsion angle (180°) ensures the planarity of the Mn_4^{III} basal plane. The Tb^{III} ion is positioned 1.789(8) Å above the basal Mn_4^{III} plane. The interplanar distance between the upper and lower O_4-planes (d_{pp}) is 2.639(0) Å, while the distances between the central Tb^{III} ion and the upper and lower O_4-planes (d_1 and d_2 , respectively) are 1.103(4) Å and 1.535(6) Å.

The isothermal field-dependent magnetization measurements, M(H), exhibit a rapid linear increase below 1 T, followed by a slow, nearly linear rise without reaching saturation, as shown in Fig. 3.3(a). This behavior suggests the presence of magnetic anisotropy, in this molecule, that prevents saturation at higher magnetic field values. Furthermore, the temperature-dependent magnetic susceptibility indicates antiferromagnetic exchange interactions both between the central Tb^{III} ion and

the peripheral Mn_4^{III} ions of the basal plane, and among the Mn_4^{III} ions themselves, as shown in Fig. 3.3(b) [113]. To achieve quantitative insights into the intermolecular exchange interactions and the effective energy barrier within the molecule, it is necessary to use element-specific magnetic techniques rather than macroscopic SQUID magnetometry [85, 87]. This line of investigation is detailed in Chapter 6 of this thesis using the synchrotron-based X-ray magnetic circular dichroism method.

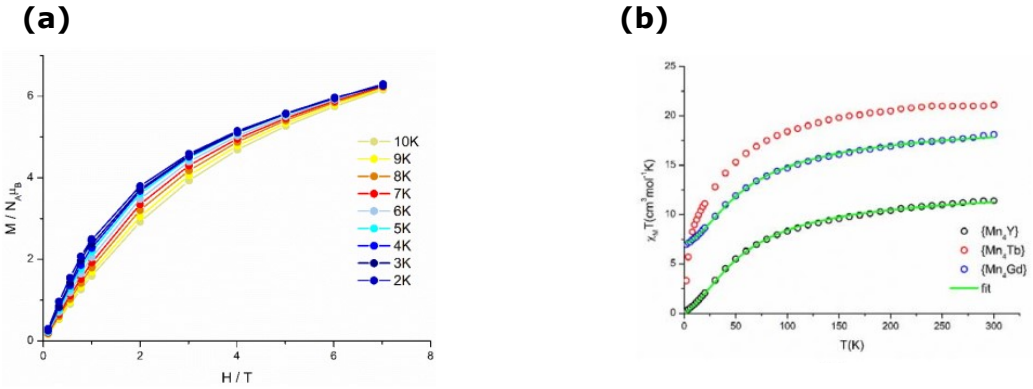

Figure 3.3: (a) Field-dependent magnetization measurements, M(H), at varying temperatures (2-10 K) over the range of 0 – 7 T for the $TbMn_4$ molecules. (b) Temperature-dependent magnetic susceptibility of the $TbMn_4$ molecules (red open circles). Green solid line represents the simulation of the spin Hamiltonian, as mentioned in the Ref.[113]. The measurements of the YMn_4 molecule (black open circles), with diamagnetic central Y^{III} ion, ensures the antiferromagnetic exchange interaction between the Mn_4^{III} ions of the basal plane. The figure is taken from Ref. [113].

Double-Decker Sandwich $RENi_8$ Molecules:

The molecules $(Hpip)_6RE(III)[12 - MC_{Ni(II)N(shi)} - 4]_2(Hsal)$, shi = salicylhydroxamic acid (in short $\{RENi_8\}$), with RE = Gd and Tb, was synthesized following the procedure outlined in Ref. [165]. The isostructural molecules crystallize in triclinic space group $\bar{1}$ [155]. The Tb(III) central ion in the molecule is sandwiched by two $[12 - MC_{Ni(II)N(shi)} - 4]$ planes with D_{4d} symmetry, where the distance separating the two planes is equal to 3.05 Å, with the Tb(III) ion being closer to the metallacrown with additional morpholin coordination at a distance of 1.39 Å. Similar to

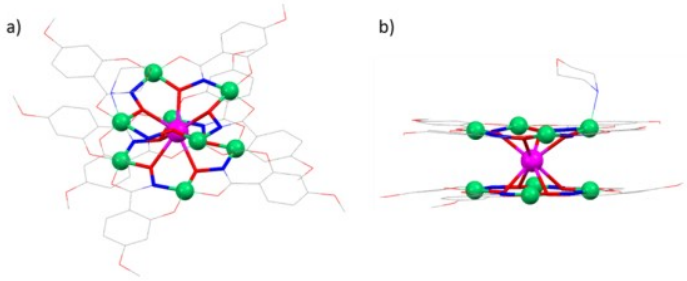

Figure 3.4: Molecular structure of the 12-MC-4 complex $RENi_8$ is shown in top view (a) and side view (b). The central MC structure motif is $-[M-O-N]-$. Color scheme represented as follow ; Magenta: Tb^{III}, Green: Ni^{II}, Red: Oxygen, Blue: Nitrogen, Grey: Carbon, H atoms are omitted for clarity. Image is taken from Ref. [155].

the previous molecule, the central Tb(III) is eight-fold coordinated by eight oxygen atoms, with the $Tb^{III}-O$ bond forming an angle of 49,30° relative to the four-fold symmetry axis, resulting in a slightly distorted square antiprismatic geometry, as shown in Fig. 3.4.

15-MC-5 Molecules

The molecules $RE(III)[15-MC_{Ni(II)N(picha)}-5](\mu_2-NO_3)(\eta^1-NO_3)(py)_8$ (referred to as $\{RENi_5\}$, RE = Sm, Tb, Dy) were synthesized following the procedure outlined in Ref.[42]. These molecules are crystallized in C_2/c space group [169]. The central RE(III) ion is eight-coordinated, bonded to five hydroxamate oxygen atoms and three oxygen atoms from coordinated nitrate ions. Four of the peripheral nickel(II) ions are coordinated by eight axial pyridine molecules, each exhibiting distorted octahedral geometry, with the two axial pyridine molecules at each high-spin nickel(II) ion being nearly parallel. The fifth nickel(II) ion, however, has a square-planar ligand field and does not bind to any axial pyridine ligands, forming a low-spin square-planar nickel(II) configuration [42]. Fig. 3.6 depicts the molecular structure of $RENi_5$ molecules.

The field-dependent magnetization measurements of $SmNi_5$ shows a paramagnetic behavior, as shown in Fig. 3.6(a). Conversely, the field-dependent magnetization measurement of $TbNi_5$ and the $DyNi_5$ molecules displays a linear increase with

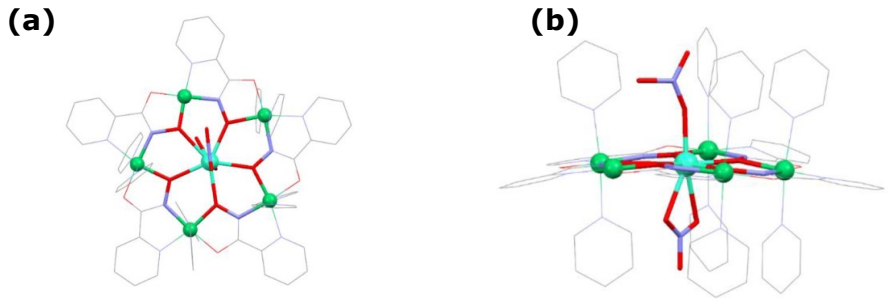

Figure 3.5: Molecular structure of the 15-MC-5 complex $RENi_5$ is shown in top view (a) and side view (b). Color scheme represented as follow ; Turquoise : RE^{III}, Green: Ni^{II}, Red: Oxygen, Blue: Nitrogen, Grey: Carbon, H atoms are omitted for clarity.

a temperature-dependent slope at low magnetic fields, which becomes temperature-independent at higher fields without reaching saturation, as depicted in Fig. 3.6(b) and (c). This suggests a magnetic anisotropy energy barrier similar to that of the previously mentioned $REMn_4$ molecules. The χ_mT vs T measurements for both $TbNi_5$ and $DyNi_5$ molecules indicate weak antiferromagnetic exchange interactions. Element-selective measurements are required to determine whether these interactions occur among the peripheral ions or between the central ion and the peripheral ions. These measurements are thoroughly examined in Chapter 6 of this thesis.

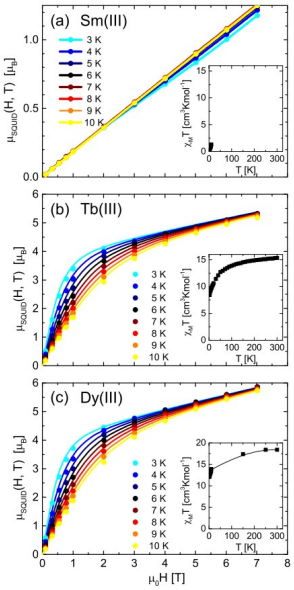

Figure 3.6: Field-dependent Molecular magnetic moment μ_{SQUID} measurements of (a) $SmNi_5$, (b) $TbNi_5$, and (c) $DyNi_5$ molecules. The isothermal measurement (dots) were running at variyng tempeeratures from 3 K to 10 K in AK Rentschler group. Full lines in (a) represent a guide to the eye, meanwhile for (b) and (c) it represents a spin-Hamiltonian fitting model. The insets show experimental results for $\chi_{\mathrm{m}}\mathrm{T}$ vs T.

3.2 $TbNi_2$ mixed $3d-4f$ metallic-centered molecules

This molecule was synthesized by our collaborator, Dr. Athanasopoulou, in the AK Rentschler group at JGU-Mainz. Unfortunately, the measured crystal was of low quality, Thus, the model could be refined only with isotropic displacement parameters and no solvent molecules or counter ions could be identified properly. The chemical formula of the core part is $[TbNi_2(HL)_2(H_2L)_4]^-$, where the ligands are $HL^{2-} = C_{13}H_9NO_3$ and $H_2L^- = C_{13}H_{10}NO_3$. Shortly, the molecule can be named with its mixed $3d-4f$ core structure as $TbNi_2$. It is crystallized in the C_2/c space group, where the core exhibits a C_2 symmetry axis passing through the central Tb^{III} ion, as shown in Fig. 3.7. The Ni^{III} ions are 6.91 Å apart, with the Tb^{III} positioned halfway at a distance of 3.57Å. The central Tb^{III} ion is eight-coordinated with oxygen atoms, featuring a $Tb^{III}-O$ bond length of 2.36 Å. The two Ni^{III} ions are situated in an octahedral ligand field, suggesting a high-spin state configuration. Although this molecule does not exhibit any single-molecule magnet (SMM) behavior, it is of interest for studying spin excitations on ferromagnetic surfaces, as will be discussed in Chapter 5 of this thesis.

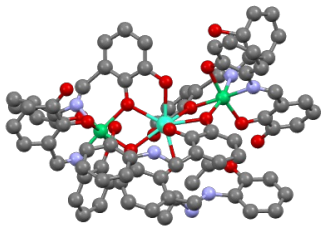

Figure 3.7: Molecular structure of the complex $TbNi_2$. Color scheme represented as follow; Turquoise: Tb^{III}, Green: Ni^{II}, Red: Oxygen, Blue: Nitrogen, Grey: Carbon, H atoms are omitted for clarity.

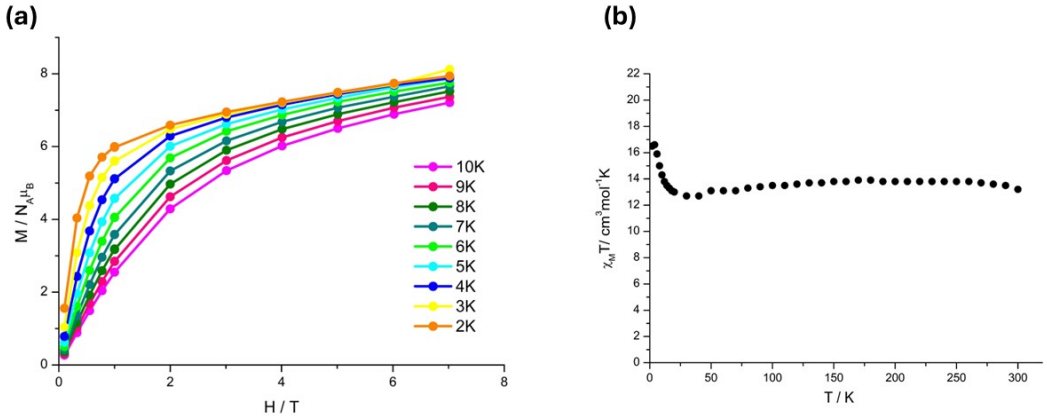

Figure 3.8: (a) Field-dependent magnetization measurements, M(H), at varying temperatures (2-10 K) over the range of 0–7 T for the $TbNi_2$ molecules. (b) Temperature-dependent magnetic susceptibility of the $TbNi_2$ molecules.

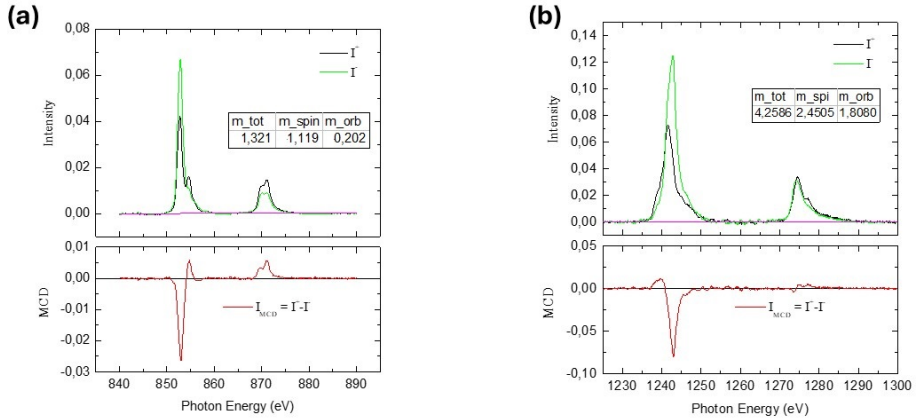

Figure 3.9: X-ray circular absorption and the corresponding XMCD measurement measured at the Ni $L_{2,3}$ edges (a) and at the Tb $M_{4,5}$(b) edges for the $TbNi_2$molecule. I^+ and I^- denotes the total photoemission yield measured for external field parallel (black solid) and anti-parallel (green solid), respectively.

The isothermal field-dependent magnetization behavior M(H), is similar to the previous Tb^{III}-containing molecules, and shows a rapid temperature-dependent linear increase below 1 T, followed by a slow, nearly linear rise without reaching saturation, as shown in Fig. 3.8(a). This indicates magnetic anisotropy in the molecule that hinders the magnetization saturation to occur. The χ_mT vs T measurements shows a constant value at higher temperatures (around 13 $cm^3mol^{-1}K$) but it increases at low temperatures range below 25 K, as shown in Fig. 3.8. Tentatively, this can be attributed to ferri-/ferromagnetic ordering between the magnetic centers as shown in other mixed $3d-4f$ metallic center molecules, especially that the element-selective XMCD measurements shows a parallel orientation between the Ni(II) and Tb(III) ions, as shown in Fig. 3.9.

Chapter 4

Experimental Methods

4.1 Scanning Tunneling Microscopy (STM)

The ongoing trend to miniaturize devices in several fields such as microelectronics, optoelectronics, and spintronics has highlighted the need for understanding structural and electronic properties on an atomic scale. Consequently, there is a demand for high atomic spatial resolution microscopy, insightful local spectroscopy, and the capability to manipulate individual atoms to tailor the engineering of atomic landscapes. The arena where such physics takes place is called "Surface Science," where the sample surface is defined as the region of the outermost layers exhibiting properties distinct from those of the bulk material [170].

Certainly, the advancement in surface science is closely linked to the development of surface instrumentation. Over the past decades, surface characterization techniques have undergone significant improvement, leading to the development of more than 50 different measurement techniques tailored for various surface characterizations. These techniques are collectively known as Scanning Probe Microscopy (SPM) [171].

Amid the SPM family the Scanning Tunneling Microscopy (STM) raises as a pivotal player in the surface characterization field. In 1981, G.Binnig and H.Roher published their seminal paper of the feasibility of obtaining an externally controllable vacuum tunneling junction with an exponential-dependence of the resistance from the surface distance with a stabilization distance around 10**Å**.[172] The ingenuity of Binnig et al. was the fabrication of a compact unit with a suppressed external noise vibration and a meticulous coarse/fine control technique. They could eliminate external noise (coming from the building) by installing the unit on inflated rubber tubes and then they exploited the magnetic levitation to get rid of the internal vibrations. The unit had a permanent magnet and an external lead bowl surrounded with cryogenic tubes to get the bowl into the superconductivity state.

To provide the unit with a high-spatial resolution control, they mounted the electrodes (W tips and Pt plate) on two separated Piezodrives. The Tungsten-tip piezoplate can move step-wise down to 100**Å** using Piezoplate fixed with three feet on

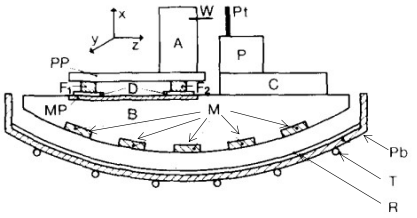

Figure 4.1: Schematic of Binnig STM unit and magnetic levitation. The letters denote the component of the system as follow: W : Tungsten-Tip, Pt: Platinum plate, A: W-tip support, P: Platinum plate piezodriver, PP: Piezoplate of W-tip support, F_1& F_2: PP feet, D: Dielectric materials clamps the feet to metallic plate (MP), M: permanent magnet, Pb: Lead bowl, R: Eddy-current metallic damper, T: Cryogenic cooling tubes. [172]

a metallic sheet and the Platinum-plate can move up some thousands of angstroms with a sensitivity of 2 $\mathbf{\mathring{A}/V}$, as shown in Fig. 4.1.

This result has been used in the next year for studying the topography of the solid surfaces. They could obtain topographic images of $CaIrSn_4$ (110) surface, with values of Ir (110) planes spacing heights of 6.7 Å, which has a very good agreement with the crystallographic x-ray diffraction measurements [173]. Later on, Binnig and his colleagues started tackling some problematic surfaces like Au (110) and Si (111) rather than just mapping surfaces' monosteps. They could observe missing rows leading to 1 x 2 and 1 x 3 surface reconstructions of Au (110) surface [174], and with that they weighed in the missing-row model in favour of other propsed models to describe such surface reconstructions after long debate amongst the surface community regarding this surface [175].

The technologically important Si (111) 7 x 7 surface reconstruction, which can be easily observed using low energy electron diffraction (LEED), initially sparked conflicting models due to its large unit cell before scanning tunneling microscope (STM) data became available. Binnig was able to spatially resolve the unit cell of this surface using STM and observed 12 topographical peaks corresponding to Si adatoms located at deep holes in the corners of the unit cell, which corresponds to empty adatom positions in a rhombohedral unit cell [176]. This auspicious debut of STM, pioneered by G. Binnig and H. Rohrer, marked a promising future for this instrument. Consequently, they were jointly awarded the Nobel Prize in Physics after

a remarkably short time, only four years following its first successful demonstration [177].

De facto the advent of STM could not only transfer our knowledge of the surface from speculation to certainty, but also gives us the opportunity to get some other surface-related insights, to name a few:

- Tunneling spectroscopy has been proven to be a powerful experimental method to probe the spatial distribution of electronic states on semiconductor surfaces and to determine the surface density of states in some energy range around the Fermi level.[178]
- Chemical-selective imaging can be performed by selecting an appropriate sample bias voltage.[179]
- Atomic manipulations. [180]
- Customized local functional spectroscopy, such as: Electron Paramagnetic Resonance with a single-spin sensitivity [181] , and studying the ultrafast transient dynamics in atomic landscapes by coupling optical pump probe with STM microscopy.[182]

Additionally, this genuine technique could circumvent the limitation of optical microscopy to see small details, i.e.: the Abbe diffraction limit [183], where the minimum spatial resolution between two points is given by:

$$d = \frac{\lambda}{2nsin\theta} \tag{4.1}$$

where : λ: optical wavelength, n : medium refractive index, θ: half the angle of diffracted beam.

By considering green light with $\lambda \approx 550\,nm$ and $nsin\theta = 1$, the minimum resolution we can get is $d = 0.275\,\mu m$. This value is relatively large for any atomic landscape, whereas STM spatial resolution is measured in angstroms. However, STM also has its own set of limitations, where the technique requires operation under ultra-high vacuum conditions ($10^{-10} - 10^{-12}$ mbar), in order to prevent rapid surface contamination. Furthermore, STM is primarily suitable for studying metals and semiconductors but not for insulating materials. Another significant challenge with STM measurements is the need to minimize external and internal vibrations, in addition to the time-consuming data acquisition during experiments.

4.1.1 Quantum Tunneling Effect: Observations and Models

In 1924, the french physicist Louis De Broglie could incorporate Einstein ideas about relativity, mass, and the limiting light velocity to justify Bohr's stability conditions of electrons in atom's orbitals by using moderate math treatments [184]. His endeavors

introduced us what he called " the coexistence of the wave and of the corpuscular aspects that Einstein had introduced for photons in his theory of light quanta in 1905" [185].

Based on his hypotheses, one could deduce the famous simple matter-wave formula:

$$\lambda = \frac{h}{p} = \frac{h}{mv} \tag{4.2}$$

where : λ is particle's wavelength , h is Planck's constant and it equals $6.626 \times 10^{-34} m^2 kg/s$, m is particle's mass , and v is particle's velocity.

This opened the door for E.Schrödinger, in 1926, to introduce his bold contribution about " *Wave Mechanics*" to the physics community [31]. Starting from the fact that the probability density of finding a photon is proportional to the square amplitude of its associated electromagnetic radiation ($\frac{Probability}{V} \propto \frac{N}{V} \propto I \propto E^2$), Schrödinger followed the hypothesis of De Broglie and worked out the wave function of the particle $\psi(\overrightarrow{r}, t)$. Later Max Born added his contribution about the probability of finding this particle based on the square of the associated wave function $\|\psi(\overrightarrow{r}, t)\|^2$[186]. The time-independent one-dimensional wave function of a free particle can be written as follow:

$$\psi(z) = A\, e^{ikz}, \tag{4.3}$$

where A is a constant amplitude, and $k = \frac{2\pi}{\lambda}$ is angular wave number of the particle's wave. The particle's wave function depends mainly on the system (which interacts with the particle) and the boundary conditions of this system rather than on the particle solely. This concept will be shown later when we deal with the tunneling problem. Schrödinger started to deal with the quantum system as an eigenvalue problem with a Hamiltonian (H = T+ U) that describes the energy of the quantum system, and he could derive his well-known time-independent Schrödinger equation, which in 1D has the following form:

$$\left[-\frac{\hbar}{2m_e}\frac{d^2}{dz^2} + U(z)\right]\psi(z) = E\,\psi(z), \tag{4.4}$$

where the wave function $\psi(z)$, Eq. 4.3, is the Ansatz which solves this equation.

This new paradigm could be put into a practice to explain some baffling observed phenomena. One of those puzzling observations for scientists, in the end of 19^{th} Century, was the sparks between two cold electrodes in vacuum at high voltages which has been reported by R.W. Wood in 1897 [187]. Lothar Nordheim embraced this paradigm in explaining this emission of electrons at high voltages [188, 189]. He worked on the electrons' reflection/transmission at vacuum-metals interfaces in a semi-classical approach, where he considered the potential energy at the interface as a step potential, with modified rounded edges, and the electrons must have sufficient energy to overcome this energy barrier to get emitted, Fig.4.2. Based on

Sommerfeld's model of the metals, Nordheim could anticipate the required electric field intensity at which the emission starts but with values one order of magnitude larger than the experimental deduced values ($\sim 10^5$ kV/m). He also worked out the corresponding formula: $I = CF^2 e^{-\frac{\alpha}{F}}$, where I defines the emission current, C the proportionality constant, α the thermionic work function-related constant and F is the Field Strength. Yet he did not deal with any kind of emission at lower voltages.

On the other hand at lower voltages, many researchers observed an electrical current between two electrodes with very small separation-distance. Giaver conducted a series of experiments to measure the tunneling current between superconductors thin films (e.g.: Pb at 7.2 K and Al at 1.2 K) separated by insulating oxide layers [190]. He could record different characteristic I-V curves for these thin films for the metallic and superconductors phases apart. Once these curves are attributed to the assumption of the existence of a tunneling current, which depends on the density of the states of both layer, he could determine the superconductivity gap from these curves directly which matches very well with the superconductivity gap of these materials measured by other methods. Additional experiment was done by him, as well, on metal- insulator -metal junction [191] where his experiment has showed inevitably that the observed current can not be explained by other than a tunneling current penetrating the oxide insulating layer [191].

These observations can be explained within the framework of different theoretical models employing various approximations. The first model is the ideal 1D square barrier, which considers incident and reflected wave functions at the barrier borders. This model focuses on a single energy level and serves as a foundation for understanding tunneling phenomena, although it does not account for potential differences influencing tunneling. The second approach, proposed by Bardeen [192], treats the problem as a scattering problem with a weak perturbation. Finally, Tersoff and Hamann introduced an approximation that relates the tunneling current to the surface density of states of the sample [193, 194], based on the idea that only electrons near the Fermi level contribute to the tunneling current.

One-Dimensional square potential barrier

This ideal model consider a potential barrier U(z) with height U_0 relative to the zero level in the region between $z = 0$ and $z = d$, as shown in Fig. 4.3. The solution of the time-independent Schrödinger, eq.4.4, provides us with the wave function of the electron, $\psi(z)$, at any region, as shown in Fig. 4.3. This wave function can be used to calculate the probability of finding the electron in each respective region of Fig. 4.3 and the corresponding probability current density $\boldsymbol{j}(\boldsymbol{z},t)$. Following the Ansatz of eq. 4.3, the solutions of an incoming wave, traveling from left to right, in the three regions are:

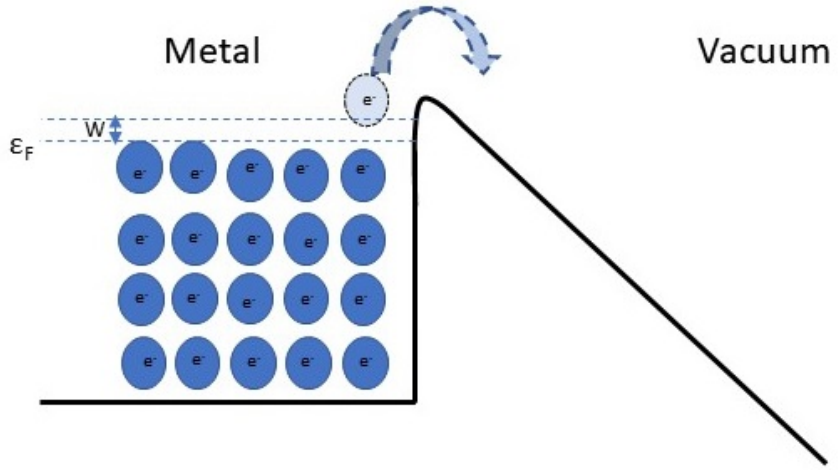

Figure 4.2: Nordheim' approach to explain electron emission at high voltages based on Sommerfeld's metals model where electrons are filled up to certain energy level called Fermi Energy Level, ε_F, and the transmitted electrons have kinetic energy, W, that enable them to overcome the barrier. Original sketch is adapted from Ref. [189].

$$\psi(z) = \begin{cases} A_1 e^{ikz} + B_1 e^{-ikz} & z < 0 \ (region\,\mathrm{I}) \\ A_2 e^{-\kappa z} + B_2 e^{\kappa z} & 0 < z < d \,(region\,\mathrm{II}) \\ A_3 e^{ikz} & d < z \ \ (region\,\mathrm{III}) \end{cases}, \tag{4.5}$$

where the parameters A_{1-3} describe the incoming waves meanwhile the parameters B_{1-2} describe the reflected parts of the wave function at the barrier borders. All parameters are complex numbers except the amplitude of the incoming wave A_1 which can be considered unity for the sake of simplicity. The wave numbers k and κ determine the wave function behavior outside and inside the energy barrier, respectively. One obtains for k

$$k = \sqrt{\frac{2m}{\hbar^2}[E - U(z)]}, \tag{4.6}$$

where $U(z) = 0$ in both regions I and III, thus rendering $k = \sqrt{\frac{2m}{\hbar^2}E}$.

This leads to an oscillatory wave function solution, as shown for those regions in eq. 4.5. Meanwhile, the region inside the barrier has potential of $U(z) = U_0$, with $E - U_0 < 0$. Hence, eq. 4.6 becomes a complex number with real and imaginary parts and one can re-write it as $k = i\kappa$, where κ is the real part, called decay constant, and can be expressed as

$$\kappa = \sqrt{\frac{2m}{\hbar^2}[U_0 - E]}. \tag{4.7}$$

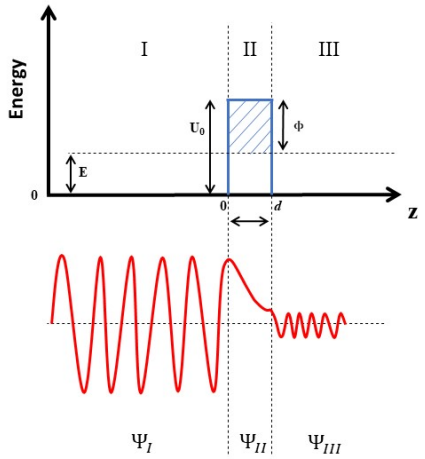

Figure 4.3: Ideal 1D square potential barrier for the metal-vacuum-metal tunneling junction.

The Ansatz, eq. 4.3, for the wave function inside the barrier becomes $\psi_{\mathrm{II}} = e^{-\kappa z}$ as shown in eq. 4.5. This is a real exponential function describing the decay of the wave function inside the barrier once the electron's energy is less the energy barrier. This implies that there is some probability of finding the electron on the other side of the barrier if the barrier width is narrow enough to not kill the wave function completely. This is called the 'quantum tunneling' which is counter intuitive classically yet possible quantum mechanically. Following the exponential dependence of this current, the intensity of this current drops one order of magnitude once we increase the barrier width with 1 Å at standard tunneling conditions (i.e. $U_0 - E \approx 1\,eV$, $d \approx 5\,\text{Å}$).

The amplitude of the tunneling wave function to the incident wave function, $|\psi_{\mathrm{III}}(d)|^2$, reflects the tunneling transmission

$$T = \frac{|A_3|^2}{|A_1|^2} = \frac{16k^2\kappa^2}{(k^2+\kappa^2)^2}\, e^{-2\kappa d} = \frac{16E(U_0-E)}{U_0^2}\, exp\,[-2d\sqrt{\frac{2m}{\hbar^2}\phi}], \tag{4.8}$$

where $\phi = U_0 - E$ is the work function. Both, the transmission factor, T, and the tunneling current decreases exponentially in terms of the barrier width, d, hence the tunneling current at some fixed energy level. Another related parameter worth of mention is the probability current density $\boldsymbol{j}(\boldsymbol{z},t)$. It can be calculated from

$$\boldsymbol{j}(\boldsymbol{z},t) = \frac{-i\hbar}{2m}\,(\psi^*\frac{\partial\psi}{\partial z} - \psi\frac{\partial\psi^*}{\partial z}). \tag{4.9}$$

The probability current density of the third region wave function is equal to $j = |A_3|^2 v$, where v is the electron's velocity. Thus, One can deduce that the flux

density (probability current) takes place for the tunneling particle and the particle is in motion although that wave function is stationary. More discussion of this model can be found in refs. [195, 196].

Bardeen Model

The previous ideal model describes the electron tunneling from one energy level and no voltage biased was considered. These conditions are not suitable for describing the tunneling current observed by many authors, at that time, for the metal-vacuum-metal junction [190, 197]. Thus, Bardeen had introduced his model [192] to provide some explanation for the tunneling current in such systems long before the invention of the STM itself. He considered the junction as two subsystems: the first one is the metal electrode and the second one is the upper metallic layer. The tunneling of the electrons between these two subsystems can be treated as a scattering problem with the first subsystem is considered as the initial states and the second subsystem contains the final states. In this approach, the transition rate between these two subsystems, $\omega_{i\to f}$, can be mathematically treated via the time-dependent perturbation theory assuming a weak coupling between them

$$\omega_{i\to f} \;=\; \frac{2\pi}{\hbar}\sum_{i,f}|M_{fi}|^2\delta(E_f - E_i), \tag{4.10}$$

where $\hbar$ is the reduced plank constant, and M_{fi} is the matrix element of the transition from one initial state to a final one. The summation runs over all contributing states in the tunneling process. The Dirac delta function ensures the conservation of energy in this transition, i.e. $E_i = E_f$, where only elastic tunneling is considered. By applying this approach to the electron tunneling from the tip (initial states) to the sample (final states), as shown in Fig. 4.4, one can find the tunneling current by multiplying eq. 4.10 with the absolute value of electrical charge and consider the spin degeneracy, to get

$$I \;=\; 2e\,\omega_{i\to f} \;=\; \frac{4\pi e}{\hbar}\sum_{i,f}|M_{fi}|^2\delta(E_{sample,\,f} - E_{tip,\,i}), \tag{4.11}$$

and the matrix elements can be written as follow:

$$M_{fi}(\psi^*_{sample,\,f}(\boldsymbol{r}),\,\psi_{tip,\,i}(\boldsymbol{r})) \;=\; \frac{\hbar^2}{2m}\int_{S_{tip/sample}} [\psi_{tip}(\boldsymbol{r})\nabla\psi^*_{sample}(\boldsymbol{r}) - \psi^*_{sample}(\boldsymbol{r})\nabla\psi_{tip}(\boldsymbol{r})].dS \tag{4.12}$$

As a matter of fact, in Bardeen approach the matrix elements are energy-dependent since the energy is an eigenvalue of the wave function of the states. Thus, one can re-write Eq. 4.12 in terms of the energy of the initial and final states instead of the wave functions, $M_{fi}(\psi^*_{sample,\,f}(\boldsymbol{r}),\,\psi_{tip,\,i}(\boldsymbol{r})) \;=\; M_{fi}(E_f,\,E_i)$.

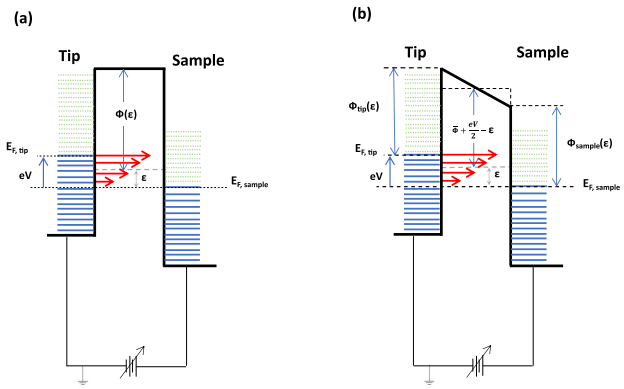

Figure 4.4: (a) Schematic Energy diagram of the tip and sample occupied (solid blue) and unoccupied (dotted green) states. Applying positive bias voltage to the sample decrease the $E_{F,\,sample}$ states by eV and increase $E_{F,\,tip}$ by the same amount. The electron tunnels elastically (red arrows) from the tip to the sample in the energy window eV between $E_{F,\,tip}$ and $E_{F,\,sample}$. The work function of an electron with energy ε is $\phi(\varepsilon) = V_0 - \varepsilon$. (b) The tip and sample have different work functions leading to a trapezoidal energy barrier approximated with an effective square energy barrier with an average height of both work functions, $\overline{\phi} = \frac{\phi_{tip}+\phi_{sample}}{2}$. For an energy state of ε the effective energy barrier changes by $\overline{\phi} = \bar{\phi} + \frac{eV}{2} - \varepsilon$. The tunneling current in both cases decreases exponentially due to the transmission factor $T(\phi, d)$.

Introducing these energy-dependent matrix elements into the transition rate equation, eq. 4.10, lead to[1]

$$\omega_{tip\to sample} \;=\; \frac{2\pi}{\hbar}\int_{E_{F,sample}}^{E_{F,tip}} |M(\varepsilon)|^2 \sum_i \delta(\varepsilon - E_i) \sum_f \delta(\varepsilon - E_f)\, d\varepsilon, \tag{4.13}$$

and following the definition of the density of states for discrete states,

$$\rho(E) \;=\; \sum_n \delta(E - E_n), \tag{4.14}$$

the transition rate can be expressed in terms of the density of states of both the tip and the sample

$$\omega_{tip\to sample} \;=\; \frac{2\pi}{\hbar}\int_{E_{F,sample}}^{E_{F,tip}} |M(\varepsilon)|^2\, \rho_{tip}(\varepsilon)\, \rho_{sample}(\varepsilon). \tag{4.15}$$

If we set the sample Fermi energy level as the reference level, then the Fermi energy level of the tip is equal to eV. Then, the tunneling current between the tip and the sample is the convolution of the density of states of the tip and the sample, in the energy window up to eV,

$$I \;=\; 2e\,\omega_{tip\to sample} \;=\; \frac{4\pi e}{\hbar}\int_0^{eV} \rho_{tip}(\varepsilon - eV)\, \rho_{sample}(\varepsilon)\, |M(\varepsilon)|^2\, d\varepsilon. \tag{4.16}$$

One can calculate the energy-dependent matrix elements in eq.4.16 from eq. 4.12 in 1D at some certain tip-sample separation, z_s, with suitable wave function of tip and sample states, $\psi_{tip}(z) \;=\; \psi_{tip}(0)\, e^{-\kappa z}$, $\psi_{sample}(z) \;=\; \psi_{sample}(0)\, e^{-\kappa(z-d)}$, respectively. As a result of that, one can find that the matrix element is distance-independent and only energy-dependent, $M(\varepsilon) \;\propto\; e^{-\kappa d}$, and $|M(\varepsilon)|^2 \propto\; e^{-2\kappa d}$ which is nothing but the transmission factor $T(\phi, d)$ obtained by the first ideal model based on the matching of the wave function in eq. 4.8. Thus, in this approach for 1D one can approximate the matrix elements $|M(\varepsilon)|^2$ with an exponential function representing the transmission factor in the data analysis of the acquired tunneling current. Therefore, the tunneling current, eq. 4.16, can be simply written as

$$I \;=\; \frac{4\pi e}{\hbar}\int_0^{eV} \rho_{tip}(\varepsilon - eV)\, \rho_{sample}(\varepsilon)\, T(\varepsilon,\, V,\, d)\, d\varepsilon. \tag{4.17}$$

Thus, the states close to the Fermi level experience a lower effective energy barrier and contribute most to the tunneling current more than the ones far from the Fermi level, as shown in red arrows in Fig.4.4. If the work functions of the tip and the sample are different, the square energy barrier is replaced by a trapezoidal effective energy barrier approximated with a square barrier with average height of both work

[1]Using the following identity for Dirac delta function: $\int_{-\infty}^{\infty} f(\epsilon)\, \delta(\epsilon - E_f)\, d\epsilon \;=\; f(E_f)$, and setting $f(\epsilon) \;=\; |M(\epsilon)|^2\, \delta(\epsilon - E_i)$

function, $\overline{\phi} = \frac{\phi_{tip}+\phi_{sample}}{2}$, as shown in Fig. 4.4(b), where all the aforementioned equations are applied in this case as well.

In conclusion, Bardeen approximation provides us with a reliable way to obtain information about the density of states of either the tip or the sample if we could deconvolute the tunneling current and get rid of the exponential contribution of the transmission function which might mask the features of DOS of the sample. Thus, this approach has its own limitations like the unknown density of stats of the tip which keeps changing during the course of the STM experiment. Detailed derivations and further reading can be found in the following ref.[196, 198].

Tersoff-Hamann approach

In 1985, Tersoff and Hamann introduced their theory to explain the tunneling current between a probe tip and real surface and its implications in the STM [193, 194]. Based on Bardeen formalism of the transition rate in the first-order-perturbation theory, eq. 4.13, one can re-write the tunneling current, eq. 4.16, in terms of Fermi-Dirac distribution $f(E)$

$$I = \frac{4\pi e}{\hbar} \sum_{\mu,\nu} f(E_\mu)[1 - f(E_\nu + eV)] \, |M_{\mu\nu}(E)|^2 \, \delta(E_\mu - E_\nu), \tag{4.18}$$

where E_μ and E_ν are the Eigenenergy of the eigenstate of the tip, ψ_μ, and the sample surface, ψ_ν, respectively. The matrix element $|M_{\mu\nu}(E)|$ is energy-independent and it is evaluated at the limit of small voltages in Tersoff-Hamann approach. This means that the energy window around the Fermi energy level will be very narrow, in which one can consider the energy of the electrons equal to the Energy of the Fermi level itself and the tunneling current at this limit will be

$$I = \frac{4\pi e^2 V}{\hbar} \sum_{\mu,\nu} |M_{\mu\nu}(E)|^2 \, \delta(E_\nu - E_F)\delta(E_\mu - E_F). \tag{4.19}$$

The matrix elements can be calculated from Eq.4.12 using a plane wave expanded in terms of Fourier expansion for the wave functions of the sample surface states, $\psi_\nu(\overrightarrow{\boldsymbol{r}}) = \Omega_{sample}^{-\frac{1}{2}} \sum_G a_G \, exp[(\kappa^2 + |\overrightarrow{k}_{||} + \overrightarrow{G}|^2)^{\frac{1}{2}}.\overrightarrow{\boldsymbol{r}}] \, e^{i\overrightarrow{k_G}.\overrightarrow{\boldsymbol{r}}}$, where Ω is the volume, $\overrightarrow{k}_{||}$ is the surface Bloch wave vector of the state and $\overrightarrow{G}$ is the surface reciprocal-lattice vector. Meanwhile, the tip in Tersoff-Hamann is approximated to a simple spherical local potential with radius of curvature of R centered at r_t, as shown in Fig. 4.5. Thus, the tip wave function is introduced as an asymptotic spherical wave $\psi_\mu(\overrightarrow{\boldsymbol{r}}) = \Omega_t^{-\frac{1}{2}} \frac{c_t \, \kappa \, R \, e^{\kappa R}}{\kappa \, |\overrightarrow{\boldsymbol{r}} - \overrightarrow{\boldsymbol{r_0}}|} \, e^{|\overrightarrow{\boldsymbol{r}} - \overrightarrow{\boldsymbol{r_0}}|}$, where c_t is determined by the tip geometry and electronic structure, and its Fourier expansion [2] is substituted into Eq. 4.12. The

[2]The Fourier expansion of the spherical wave $\frac{1}{\kappa \, r} \, e^{-\kappa \, r}$ is $\int dq^2 \, b(\overrightarrow{q}) \, exp[-\sqrt{|\kappa^2 + q^2|} \, |z|] \, exp(i \, \overrightarrow{q} \, . \, \overrightarrow{x})$ where the expansion coefficient is $b(\overrightarrow{q}) = \frac{1}{2\pi \, \kappa^2} \, (1 + {}^{q^2}/_{\kappa^2})^{-1/2}$

integration is done over an arbitrary plane within the vacuum barrier. Then, the tunneling current will be expressed as

$$I = \frac{32\pi^3}{\hbar}\left(\frac{e\,R\,\phi}{\kappa^2}\right)^2 V\,\rho_{tip}(E_F)\,\rho_{sample}(E_F+eV,\,\overrightarrow{\boldsymbol{r_t}})\,e^{-2\kappa d}. \tag{4.20}$$

It is clear from Eq. 4.20 that the tunneling current is dependent linearly on bias voltage but has exponential dependence on the distance between the sample and the surface. Based on that, at fixed bias voltage and distance (z_0) the tunneling current is dependent on LDOS of the sample, if we considered the tip DOS constant, $I \propto \rho_{sample}(E_F,\,z_0)$. This approximation provides a simple interpretation of the tunneling current at different locations on the surface for a rastering tip across the surface. Then, the tunneling current values is nothing but a contour plot image of a constant LDOS at the Fermi level of the surface at the tip position.

This approximation is valid as long as the tip wave function is approximated by an s-wave function, hence spherical wave function. The lateral resolution of the STM based on this model is in the range of 5 Å for typical metals with values of z_0= 15Å and $R = 9$ Å[193]. As a matter of fact, STM can resolve atom-sized features down to 2 – 3Å on some close-packed surfaces [199] which is beyond Tersoff-Hamann model. Thus, many authors started to overcome the simplifications adapted by Tersoff-Hamann model. Nougera et al. suggested that the strong interaction between the tip and the sample due to the short tip-sample distance, leaves the perturbation Ansatz used by Tersoff-Hamann not valid anymore [200, 201]. Instead, they tried to obtain an exact expression for this problem with a theoretical framework based on the Green's functions formalism with boundary conditions of matching the wave functions at the interfaces between the vacuum and the two electrodes apart. As a result of that, their calculations showed that the tunneling current is no longer proportional to LDOS although they are related and a straightforward answer could not be achieved. On the other hand, Chen et al. could present a straightforward theory to calculate the STM images, where the tunneling matrix elements could be derived based on Green formalism for the angular momentum of the orbitals of the tip states [202, 203]. As a matter of fact, the DOS at the Fermi level of the widely used STM tips (W, Pt , or Ir inter-metallic alloys) has a large contribution of d-orbitals which has an angular momentum on contrary to the s-orbital [204].

In addition to that, the existence of localized surface states near E_F in W (100) surfaces is proven theoretically [205] and experimentally [206]. Such surface states located 0.3 eV below E_F (0.4 eV width) and it has d_{z^2} orbital character. Due to the small decay constant of these states, their tail extend much further in the vacuum more of the $5d$ and $6s$ orbitals. Thus, it has been suggested that these localized surface states in the tip play an important role in explaining the atomic resolution for the STM images recorded with these tips [207]. Based on that, Chen et al. [202, 203] could find an enhancement of the tunneling current due to d_{z^2} tip states by a factor of 11 on close-packed metal surface, which can give some explanation of the enhanced atomic resolution of the STM with these tips. Although, this approach is more microscopic, yet one can recover the matrix elements derived by Tersoff-

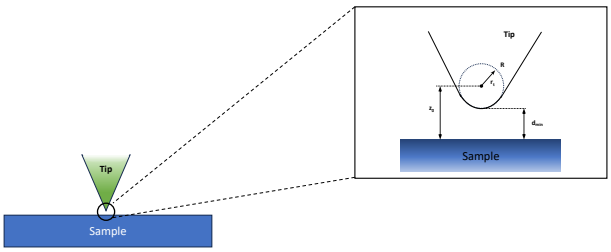

Figure 4.5: Schematic diagram of STM tip approaching the sample till distance d_{min}. In Tersoff-Hamann model, the tip is approximated as a spherical local potential with radius of curvature of R centered at r_t. Following the approximation, the tunneling current is due to the LDOS of the sample surface at the tip center located at z_0 above the sample, $\rho_\nu(E_F, z_0)$. [193]

Hamann results for s-orbitals, $l = 0$, which is a macroscopic approach for the tip with a spherical potential well. Other approaches for the STM theory has been introduced where the reader is refereed to their corresponding sources [208–211]

4.1.2 STM Operation: Topographic imaging and Spectroscopy Measurements

The initial STM prototype developed by Binnig and Rohrer in the 1980s has undergone relatively few changes compared to contemporary STM devices [212]. The main components of the STM can be grouped into three parts: (i) The scanning unit which includes the metallic probe tip and the sample holder. (ii) The electronic control unit containing amplifiers, Analog-to-Digital converters and Feedback loop controller. (iii) The vibration damping system. In the following section, we will provide a technical overview of the STM apparatus employed in the experiment. Additionally, we will delve into the two measurement modes, namely topography imaging and spectroscopy measurements.

4.1.2.1 Technical Features

The STM apparatus and the tip employed in these experiments is produced by Scienta-omicron company. The apparatus is made out of two main UHV chambers, along with an additional load-lock chamber for introducing the sample into the UHV chambers. The first chamber is designated for the STM measurements, while the

second one is equipped with PVD thermal evaporator combined with Low energy electron diffraction (LEED) apparatus for surface studies, as shown in Fig. 4.6.

The STM chamber is provided with an inner and outer cryostat tanks, each with a volume capacity of 3.5 L enabling low temperature working environment down to 4.7 K. To achieve high spatial resolution in STM, a tip-sample spacing stability at the level of pm is required[3]. Thus, one can reach such high degree of stability by a combination of active and passive vibration isolation along with the STM instrument itself where the resonance frequency of the instrument will be higher than the building vibrations low frequency. Therefore, the design of the STM unit needs to be simultaneously rigid and compact [214].

The instrument is located in the first floor of the building and this makes it more susceptible to the building vibration which is in the low frequency range of 10 Hz. Hence, the STM head is suspended freely with three soft springs to avoid any contact with the inner walls of the UHV chamber. Although the metal springs have lower resonance frequency (2 Hz), it provides little damping due to the vibration of the suspension itself. Thus, it is combined with other passive damping systems to intercept these vibrations like eddy current retarder at the bottom part of the measuring chamber. One can switch back and forth between these two modes: suspended mode (measurement mode) and locked mode (cooling mode) by a locking mechanism with a handle via a Feedthrough as shown in Fig. 4.7. Besides that, an active damping system was introduced beneath the microscope, resulting in approximately a tenfold reduction in the background noise, not shown in Fig. 4.6. Fig. 4.7 depicts a schematic representation of the STM chamber, highlighting its main components.

The fundamental operational concept of the STM is outlined in Fig. 4.8. In our apparatus, the sample is grounded and a bias voltage is applied to the tip, typically between mVs and several volts. The tunneling current is measured and converted into proportional voltages with a pre-amplifier with a gain of $10^7 - 10^9$V/A. The feedback controller for the z-piezo drive in the STM consists of a combined proportional controller and Integral controller (PI controller) with adjustable gains through the software. The tunneling current signal, I_{tunnel}, is compared with the set current, I_{set}, typically ranging between several picoamperes up to 333 nA. The error signal ($I_{set} - I_{tunnel}$) is then fed into the PI amplifiers. The proportional amplifier generates a control signal that is proportionate to the error signal and it reacts to the fast deviations of the tunneling current from the set point value like atomic corrugation or step edges in the sample topography [196]. Hence, if the proportional gain K_P is large, it may lead to overshooting and oscillations in the tip, affecting the ongoing measurement. Consequently, the integral controller produces a control signal proportionate to the accumulated deviations from the set-point over a specified time interval, with a proportional gain K_I. Therefore, the careful selection of suitable values for K_P and K_I is crucial for optimal performance.

[3]In our instrument the z-resolution of 10 pm can be achieved

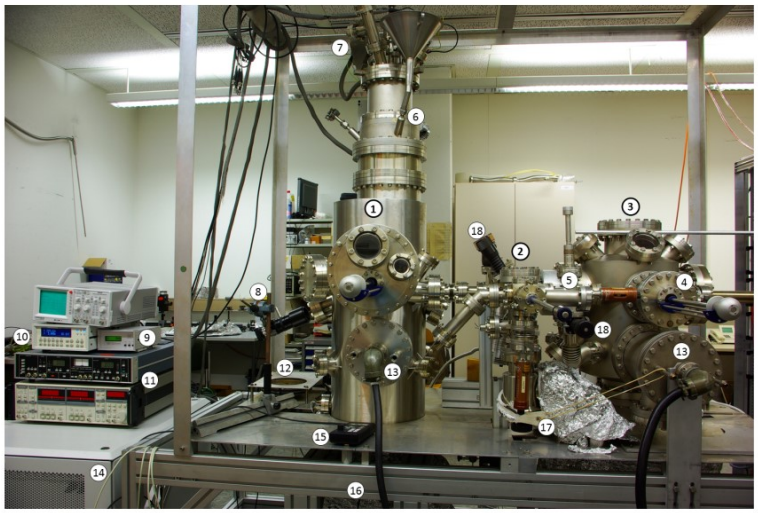

Figure 4.6: a photo of Omicron LT-STM used in the experiment showing the parts of the instrument labeled as follow: (1) STM main chamber. (2) Load-lock chamber including molecule evaporator and cutting pliers pumped by Turbo-molecular pump at the bottom. (3) Preparation chamber pumped by HV Ionic gitter pump at the bottom, it includes metal evaporator, substrate heater, mass spectrometer and LEED. (4) Sample transfer wobble stick. (5) The adjustment-screw of the cutting pliers. (6) Liquid Nitrogen inlet for the outer thermal shield. The outlet is in the rear side of the chamber (not shown).The inlet and the outlet of the liquid He at the top (not shown). (7) The electronics Feedthrough of the instrument including the sample heater, the temperature sensor, and the tunneling current signal preamplifier and voltage converter. (8) camera provides optical access to the sample and the tip during the coarse approach and retract. (9) Helium filling level meter device. (10) Thermometer for the STM main chamber temperature. (11) Lock-in amplifier. (12) A heater fan for baking out the system, this system has another one (not shown). (13) Ti-sublimation pump. (14) The commercial electronic measurements box, "Matrix" produced by Scienta Omicron. (15) Control Unit of the coarse approach/retract of the tip. (16) HV ionic getter-pumps for the STM main chamber. (17) The Turbo-molecular pump valve (black,left) and the exhaust port (right) wrapped with aluminum foil covering the heating tapes. (18) UHV bakable valves separating the load-lock chamber from the rest of the system. Image is taken from Ref. [213]

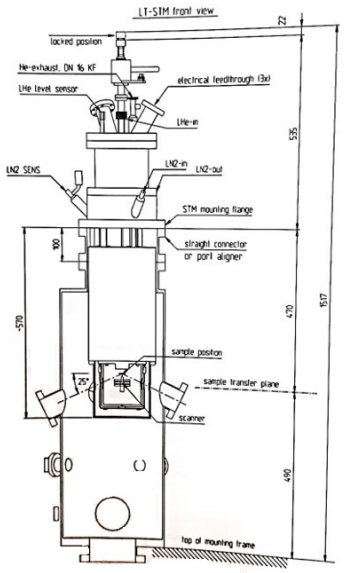

Figure 4.7: CAD sketch of the STM chamber in our apparatus. Image is taken from the manual guide of the instrument.

The output signal undergoes conversion to a digital signal through a suitable Analog-to-Digital Converter (ADC) and is subsequently processed by a digital signal processor (DSP). The DSP forwards the tip height data to the computer, facilitating the display of the topography image in grayscale as a function of x and y. The digitized measured signal is then transformed back into an actual voltage by a Digital-to-Analog Converter (DAC). Following this, High-voltage amplifiers boost the voltage up to ± 140 V before applying it to the piezo tube electrodes. This leads to the re-adjusting of the tip height along z-cooridantes in order to keep the tunneling current at the set value, I_{set}.

At liquid helium temperature, the x- and y-piezo electrodes exhibit a sensitivity within the range of 3.6 nm/V, while the z-piezo electrode demonstrates a sensitivity of approximately 1.2 nm/V. These sensitivities enable high resolution in smaller scanning areas. Together, these electrodes constitute the tube scanner, which plays a crucial role in finely controlling the motion of the tip during the scanning procedure. Meanwhile, for the coarse approach this scanner is driven by a linear piezo motor, as shown in Fig. 4.9.

A saw-tooth voltage with small slope followed by a steep slope is applied to a shear piezos (mover part) in the motor which holds piezo tube scanner (slider part) with a magnet resulting with the stick/slip effect [4]. These voltages are responsible for the coarse forward/backward movements to the tube scanner, in which the small slope voltage lead to small movement of both the mover and slider part due to the magnetically coupling between them (stick) and the steep slope voltage will decouple the mover and slider part due to the inertia of slider's mass (slip) [196].

[4]It is known as well as riding/sliding effect, for further details the reader is refereed to the following reference [196].

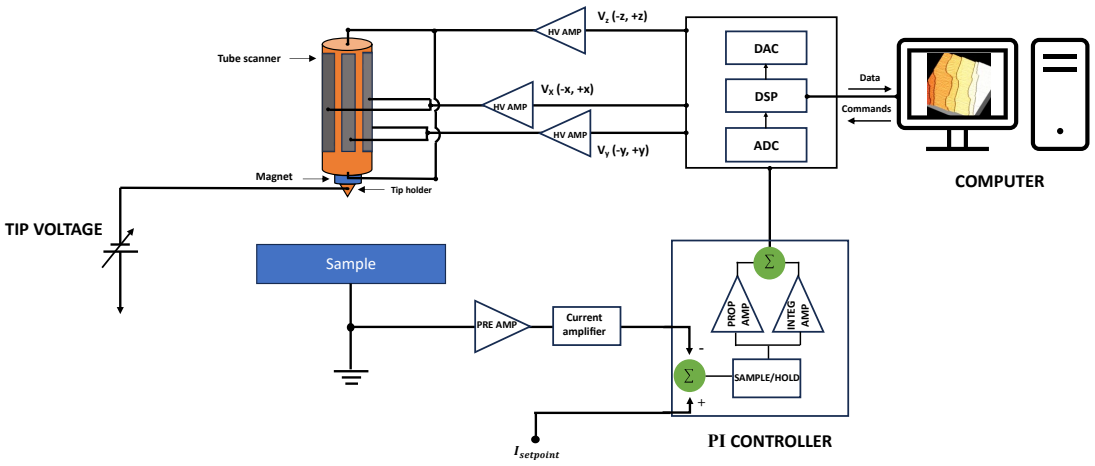

Figure 4.8: The Sketch of the STM basic operation. The tip is hold by a magnet in the tip holder and attached to the piezo tube scanner. The tip is biased with a voltage and the sample is grounded. The tunneling current is collected from the sample and amplified before being compared with the I_{set} in the PI controller. A sample/hold amplifier nullify the error signal leading to no change of the control signal applied on the z-piezo electrode. This enable the user to ramp the voltage and detect the corresponding tunneling current in the spectroscopy mode without changing the tip height. The control signal is fed to HV amplifiers to re-adjust the tip height. The feedback loop is connected to the PC via DSP card and enable the data/Commands connections.

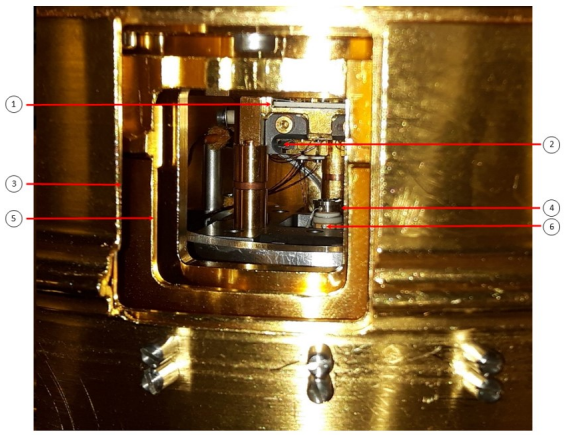

Figure 4.9: a photo of Omicron LT-STM stage showing the main parts labeled as follow: (1) The sample heater regulating the temperature down to 4.7 K. (2) The sample holder. (3) The outer cooling shield connected to the outer LN_2 tank. (4) The magnetic tip holder at the top of the tube scanner. (5) The inner cooling shield attached to the inner LHe tank. (6) The piezo tube scanner. Image is taken from Ref. [213]

The frequency of this saw tooth voltage must not exceed the resonance frequency of the piezo element and it is bounded by the bandwidth of the high-voltage amplifiers (<10 kHz).

Initial monitoring of the coarse approach for the tip can be achieved visually through a CCD camera, utilizing the side view port. Meanwhile, the other view port illuminated by a light source as shown in Fig. 4.6 and Fig. 4.7. Once the mirror image of the tip is observed on the sample surface, the coarse approach is halted, and the automatic approach takes over.

Due to the small values of the tunneling current (nA-pA), the current is occasionally superimposed with background noise. This noise can, sometimes, impede the extraction of meaningful spectroscopic information. Thus, the Data acquisition procedure of the tunneling current can be complemented by a Lock-in amplifier, as shown in Fig. 4.6.

The Lock-in amplifier used in this experiment is MODEL SR830 DSP Lock-In Amplifier, manufactured by Stanford Research Systems [215]. The basic idea of this amplifier is to lock the phase of the measured signal with another reference signal (external or internal), hence the name Lock-on amplifier or phase-sensitive detection. The measured signal is modulated with an AC signal, i.e. multiplied by an AC reference signal with known frequency and stable phase. The product of the modulated and reference signal (phase shifted) yield with an AC signal with two frequency components, one at the sum frequency ($\omega_{ref} + \omega_{sig}$) and the other at the

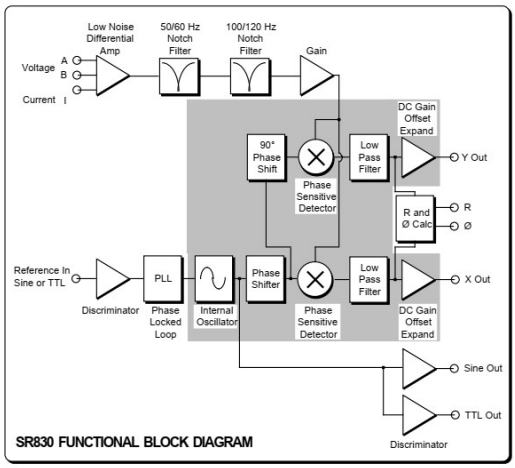

Figure 4.10: Block Diagram of Lock-in Amplifier: The tunneling current undergoes excitation with a reference signal having a frequency higher than the grid frequency (50/60 Hz or 100/120 Hz) to pass through Notch Filters. The output labeled (Sine Out) provides this excitation, resulting in a modulated signal fed back to the Lock-in amplifier through the Input labeled (Current I). In this scenario, no Phase-Locked Loop is required, as the reference signal and the excited signal come from the same internal oscillator. The modulated tunneling current signal is then multiplied with the reference signal after being phase-shifted to nullify the phase difference between the two signals. The Low-pass filter time-averages all AC components and eliminates them, yielding the X-component of the signal, proportional to $cos(\Delta\theta)$. Another signal can be measured, if the reference signal is shifted by 90° and that is the Y-component, i.e. proportional to $sin(\Delta\theta)$. The digital outputs of the Lock-in amplifier are generated by the DSP (gray square).

difference frequency $(\omega_{ref} - \omega_{sig})$:

$$V_{Lock-in} = \frac{1}{2} V_{sig} V_{ref} \{cos([\omega_{ref} - \omega_{sig}]t + \theta_{sig} - \theta_{ref}) + cos([\omega_{ref} + \omega_{sig}]t + \theta_{sig} + \theta_{ref})\}. \quad (4.21)$$

If $\omega_{ref} = \omega_{sig}$, then the first component of Eq. 4.21 will result in a DC component. When the AC signal ($V_{Lock-in}$) passes through a low-pass filter, the remaining AC component will be eliminated by time averaging the signal and we end up with a DC signal proportional to the measured signal amplitude, $V_{Lock-in} = \frac{1}{2} V_{sig} V_{ref} \, cos(\theta_{sig} - \theta_{ref})$. By adjusting the phase of the reference signal, θ_{ref}, one can make the phase difference equal zero and hence $cos(\theta_{sig} - \theta_{ref}) = 1$. Fig. 4.10 shows the block diagram of the used Lock-in amplifier. The importance of Lock-in amplifier is to provide noise-free $I-V$ and dI/dV spectra for various investigations.

The thin films are prepared in a separated preparation chamber, as shown in Fig. 4.6. The thermal evaporator consists of six water-cooled beryllium crucibles, each containing various metal powders or chunks. These crucibles are connected to a power supply, enabling the heating of the specific crucible needed for preparing the required thin film. Meanwhile, the molecules powder is loaded in an another water-cooled thermal evaporator in the load-lock chamber to deposit the molecules on the substrate. The substrate used in this experiment is single crystal W(110) fixed on standard Omicron sample holder.

4.1.2.2 Topography

The tunneling current flowing between the sharp tip and the sample can be used to map the surface of the sample. As stated earlier, the density of states of the sample and the tip are convoluted in the tunneling current, thus the recorded tunneling current as a function of the lateral $x\,y$-position on the surface can yield with an image of surface of constant DOS. Thanks to the Digital-to-Analog converters (DAC), the height of the tip (z-output signal) will be represented by varying gray levels, around 256 levels for 8-bit DACs [5], which get displayed as images with 512 × 512 pixels. There are two measurement modes for recording the topography of the surface: (i) Constant current mode and (ii) Constant height mode.

1. Constant current mode (CCM):

   In this measurement mode, the tunneling current between the tip and the sample is set to a fixed nominal value as well as the applied bias voltage (ΔU) before the scanning takes place. The feedback loop keeps readjusting the tip separation of the sample to retain the set-point value of the tunneling current, as shown in the schematic diagram of Fig. 4.11. The change in the tunneling current is due to the modulation of the sample's local DOS(E_F+ΔU). Hence, the positions where LDOS is high (e.g.: atoms, terraces, adsorbates, ... etc) are represented with brighter gray levels (close to the white) due to the large applied piezo voltage to retract the tip. On the other hand, the low LDOS (e.g.: absence of atoms, misfit locations, ... etc) shows darker gray levels. This contour of constant LDOS images the topography of the surface. Yet, one should be careful about the direct interpretation of the contour of CCM as the topography of the surface.
   If the LDOS of the adsorbates are less than the LDOS of the substrate, e.g.: CO molecules on metallic bare Cu surface [216], the molecules will be represented as depressions rather than hills in contrast to the "real topography" of the surface. Utilizing the Feedback loop in practice results in a drawback of a slower scanning, which could be viewed as a disadvantage in specific situations.

[5] For 8-bit DAC, gray levels are 256 levels ranges from 0 (black) to 255 (white). For 16-bit DAC, this increases to 65,000 levels which enhance the image resolution.

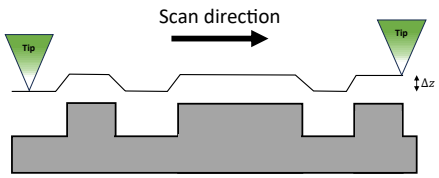

Figure 4.11: Schematic diagram of STM topography scan in constant-current mode. The tip retracts/extends according to the hills/vacancies on the surface in order to keep the set tunneling current fixed. The feedback loop parameters affects the tip response to the change of the topography of the surface

When the scanning process is sluggish, there is a potential for the scanning tip to undergo alterations, and in such instances, there is a risk of debris falling during the process. Also, the piezo creep and thermal drift might lead to some distortions in the scanned images. At low temperatures, such effects are negligible and one can get stable images after few scanning measurements on the same region. Conversely, the advantage of implementation of CCM is the constant resolution of the image. Furthermore, another feature of the constant-current mode is the capability for element-specific scanning similar to what is seen in resolving the morphology of GaAs(110) surface [217]. This scanning is achieved by changing the polarity of the applied bias voltage and choosing proper voltages, hence, probing the occupied and unoccupied states of the surface.

2. Constant height mode (CHM):

Another operating mode in STM is the constant height mode (CHM). In this configuration, the feedback loop is disabled, and the probe is moved across the surface at a fixed height while monitoring the tunneling current. Following Tersoff-Hamann approach, the tunneling current can directly capture the variations in the Local Density of States (LDOS), while maintaining a constant height, as indicated in Eq. 4.20. Although it is straightforward in its approach, it is not advisable to employ this measurement mode for scanning purposes. One reason of that is the crash of the tip itself if the surface is not flat enough atomically. Two atomic steps might lead to undesirable tip-sample contact. Thus, to mitigate the risk of the contact between the tip and the sample one tends to compromise the resolution of the sample by adjusting the height [218, 219]. Also, thermal drift and piezo creep make it challenging to maintain the scanner stably at constant height above the surface. CHM allows for relatively

high scanning speeds because data acquisition, in this mode, is unrestricted by the feedback loop.

4.1.2.3 Spectroscopy

I(V)-Spectroscopy

The STM's spatial atomic resolution facilitates local spectroscopy on specific atoms or molecules, distinguishing it from area-averaged sampling spectroscopy techniques like Photoemission Spectroscopy (PES) [220]. Additionally, the STM can provide highly energy-resolved spectroscopic data down to several meVs. This capability enables the detection of various excitations, including spin flip excitations [221] and vibrational modes of a molecule [222]. However, it's important to note that a limitation of scanning tunneling spectroscopy (STS) is its lack of chemical sensitivity.

The STS monitors the variation of the tunneling current while ramping the applied tip-sample bias voltage at a locally determined point in the topography image. As expressed in Eq. 4.17, the integrand is proportionate to the sample Local Density of States (LDOS), assuming energy independence for both the tip Density of States $\rho_{tip}(\varepsilon - eV)$, and the transmission factor $T(\varepsilon, V, d)$, which can be justified at low temperatures:

$$\frac{dI}{dV} \propto \rho_{sample}(eV), \tag{4.22}$$

where the contribution to the tunneling current dI is coming from the states between the Fermi levels of the sample and the tip, as shown in Fig.4.4.

In practical terms, the tip-sample distance is maintained constant at the desired lateral position with a stabilized tunneling current and bias voltage. This is achieved by the sample/hold amplifier in the feedback loop, which disables the feedback loop, as depicted in Figure 4.8.

The voltage ramps from initial to final values, as set by the STM software, and the tunneling current is recorded. The dI/dV spectrum can be calculated numerically using data analysis software. Alternatively, the dI/dV spectrum can be obtained directly using the Lock-in amplifier. The bias voltage (DC signal) is modulated by an AC signal, $\mathrm{V_m cos(\omega t)}$, with a voltage amplitude V_m leading to a modulated tunneling current, I_m. The amplitude of the modulated tunneling current I_m is proportional to the dI/dV around each voltage bias values. Thus, to detect the small features in the $I - V$ curve, the modulation voltage V_m should be smaller than that of these characteristic spectral features under investigation, as shown in Fig. 4.12.

To record the dI/dV spectrum (or generally the nth derivative), it is enough to record the AC amplitude of the signal at n-times the modulation frequency. This stems from the Taylor expansion of the modulated AC tunneling current, $I = f(V + V_m \cos \omega t)$, around the voltage V as a polynomial function of the modulation

Voltage:

$$I = \sum_{k=0}^{\infty} \frac{V_m^k}{k!} \frac{d^k f(V)}{dV^k} cos^k \omega t = [f(V) + \frac{d^2 f(V)}{dV^2} \frac{V_m^2}{4} + \cdots] + V_m cos\omega t \, [\frac{df(V)}{dV} + \frac{d^3 f(V)}{dV^3} \frac{V_m^3}{8} + \cdots] + \frac{1}{4} V_m^3 cos 2\omega t \, [\frac{d^2 f(V)}{dV^2} + \frac{d^4 f(V)}{dV^4} \frac{V_m^4}{12} + \cdots] + \cdots . \quad (4.23)$$

It is evident from the above expansion that the nth derivative of the signal, $f(V)$, is proportional to the signal with nth multiples of the modulation frequency, $n\omega t$, if we neglect the higher-order terms in each harmonic term. Therefore, measuring the signal with the nth harmonic of the original signal will yield the spectra of the nth derivative, and this can be accomplished using the Lock-in amplifier. The oscillator reference signal generated internally in the Lock-in amplifier, as shown in Figure 4.10, is multiplied n-times based on the nth derivative required. Following that, this multiplied reference signal is shifted to compensate for any phase shift. Subsequently, it is multiplied by the modulated tunneling current signal and passes through a low-pass filter to get the desired $\frac{d^n I}{dV^n}$ DC voltage.

The Lock-in amplifier provides us with good signal-to-noise ratio, a benefit not easily achieved with conventional data analysis procedures such as smoothing spectra. Consequently, longer averaging times during the measurement result in reduced spectral noise. On the other hand, using the Lock-in amplifier in the experiment extends the overall experiment time, which is unfavorable due to the potential drift that alters the tip-sample distance and, consequently, the tunneling current. Thus, reproducing the same spectra would be favorable and it would increase the credibility of the obtained results.

The energy resolution of the STS measured via Lock-in amplifier, at low voltages, is determined by the applied modulation voltage V_m (instrumental broadening) and the thermal broadening, ΔE_{therm}. The total energy resolution of the experiment, ΔE, is given by [196]:

$$\Delta E = \sqrt{\Delta E_{therm}^2 + \Delta E_{mod}^2} \approx \sqrt{(0.28\, meV/K \,.\, T)^2 + (2 * eV_{mod})^2}. \quad (4.24)$$

Consequently, there is an upper temperature limit if high energy resolution is desired. Therefore, both the temperature and the modulation voltage must be minimized to increase energy resolution. At 4 K, the energy resolution in STS related to the thermal broadening is around 1.2 meV. Additionally, at higher voltages, the transmission coefficient $T(\varepsilon, V, d)$ dictates the energy resolution, which may be in the hundreds of meV range [196].

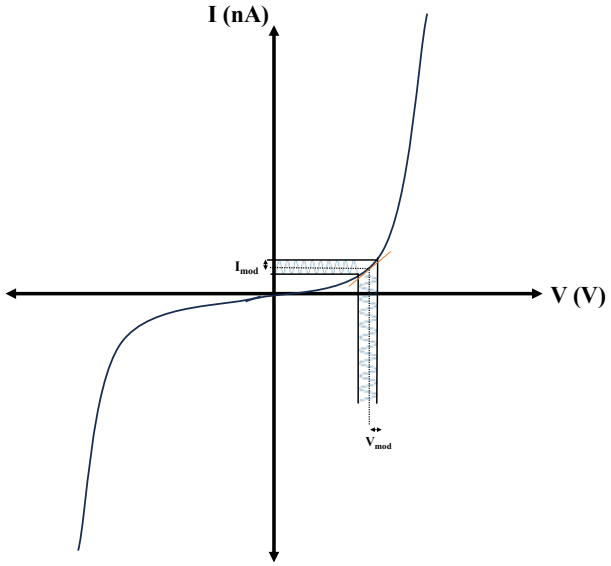

Figure 4.12: Modulated hypothetical I-V curve.

I(z)-Spectroscopy

In this kind of spectroscopy, the lateral position of the tip is held constant, and the feedback loop is switched off. Meanwhile the voltage is applied to the z-piezo drive and the tunneling current is measured while the relative distance between the tip and the sample is changing, I(z). As indicated in Eq.4.17, the transmission coefficient $T(\varepsilon, V, d)$ introduces an exponential dependence on the tunneling current, in which

$$T(\varepsilon, V, d) \propto exp(-2z\sqrt{\frac{2m}{\hbar^2}\overline{\phi}}), \tag{4.25}$$

where $\overline{\phi} = \frac{\phi_{tip}+\phi_{sample}}{2}$ is the effective energy barrier. At low bias voltage ($\overline{\phi} \gg V$), this transmission coefficient is constant. Hence, the effective energy barrier $\overline{\phi}$ can be extracted from the proportionality constant of the curve $\ln \mathrm{I}(z)$ vs z.

Spin-Polarized Spectroscopy (SP-STS)

The tunneling current between the tip and the sample can have spin-dependent contribution I(ϕ, V, s) as well, which so far is not accounted for the spin-averaged tunneling current. Spin-polarized electrons are a prerequisite for this, and they can be achieved through extrinsic factors, such as GaAs tips being optically pumped with circular light, resulting in a spin polarization of around 43% [223] or intrinsic factors, like the spin-polarized d-band splitting in ferromagnetic tips [224]. The spin polarization degree of the electrons in those tips depend critically on the tip preparation procedure [214].

Ferromagnetic materials are best described by the Stoner model [225] wherein the density of states spontaneously undergoes spin-splitting to minimize energy. The

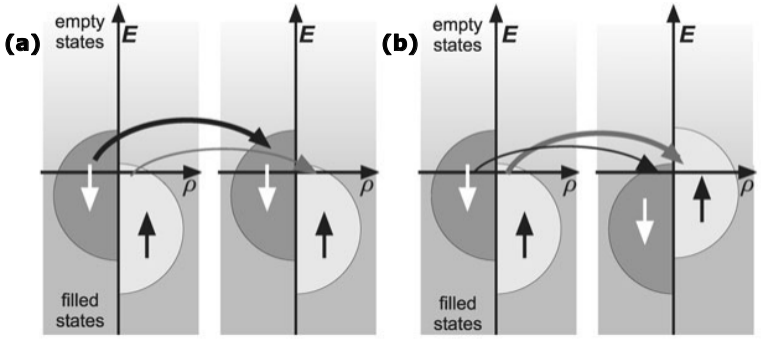

Figure 4.13: Principle of spin-polarized tunneling between magnetic electrodes showing (a) parallel and (b) antiparallel magnetization. In the case of elastic electron tunneling, spin is conserved. Thus, spin-up electrons tunneling out of the occupied states of electrode A can only enter empty spin-up states of electrode B.[226]

two resulting sub-bands are occupied by electrons with definite spin orientations, giving rise to majority and minority sub-bands, as shown in Fig.4.13. The exchange correlation between the itinerant electrons lead to different values of density of states at the Fermi level of either the tip or the sample, $\rho_{t.s}^{\uparrow\downarrow}(E_f)$, resulting in a spin-polarization $P(E_f)$ [214]:

$$P_{t,s}(E_f) = \frac{\rho_{t.s}^{\uparrow}(E_f) - \rho_{t.s}^{\downarrow}(E_f)}{\rho_{t.s}^{\uparrow}(E_f) + \rho_{t.s}^{\downarrow}(E_f)}. \tag{4.26}$$

In experiment one can calculate the polarization with the tunneling current signal:

$$\mathrm{P_{t,s}(E_f)} = \frac{\mathrm{I^{\uparrow\uparrow} - I^{\uparrow\downarrow}}}{\mathrm{I^{\uparrow\uparrow} + I^{\uparrow\downarrow}}}, \tag{4.27}$$

where $I^{\uparrow\uparrow}$, $I^{\uparrow\downarrow}$ refer to the tunneling current between the tip and the sample with parallel and anti-parallel magnetization direction, respectively.

This spin-polarization affect the tunneling process between two ferromagnetic electrodes as observed by Jullière in the Fe-Ge-Co planar tunneling junctions [10] which could be explained by Slonczewski theoretical work [227]. It deduced the cosine dependence of the tunneling current, I_{sp}, on the relative alignment of the two magnetization directions of the two electrodes:

$$I_{sp} = I_0(1 + P_t.P_s cos\theta). \tag{4.28}$$

The maximum contrast of the tunneling current can be obtained when the relative magnetization directions of the electrodes are parallel and anti-parallel for a collinear orientation, corresponding to $\theta = 0°$ and 180°, respectively. Thus, this

tunneling junction behaves as magnetic valve. In the limit of the low bias voltage, the tunneling current is dominated by elastic processes. Hence, the spin-flip of the tunneling electrons is not permissible. For the sake of simplicity, if we consider a tunneling junction consisting of two electrodes of the same material, the elastic tunneled electrons will tunnel between the same spin-polarized sub-bands of the opposite electrodes, as depicted in Fig.4.13. Since the tunneling current in the tunneling junction depends on density of states at Fermi level, as expressed in Eq. 4.20, the tunneling current will be higher in the case of parallel relative magnetization direction between the two electrodes and will be lower in the anti-parallel configuration. This will add additional contribution to the topography of the magnetic sample in the constant current mode, I_{SP}, [228]:

$$I(\overrightarrow{r_t},\, V,\, \theta) \;=\; I_0(\overrightarrow{r_t},\, V) \;+\; I_{SP}(\overrightarrow{r_t},\, V), \tag{4.29}$$

$$I(\overrightarrow{r_t},\, V,\, \theta) \;\propto\; \rho_t.\tilde{\rho}_s(\overrightarrow{r_t},\, V) + m_t.\tilde{m}_s(\overrightarrow{r_t},\, V)\, cos\theta(\overrightarrow{r_t}), \tag{4.30}$$

where $\rho_{t,s}$ is the LDOS of either the tip or the sample at the tip position $\overrightarrow{r_t}$ and $\tilde{\rho}_s$ is the energy integrated LDOS of the sample in the energy interval $[E_f;\, E_f + eV]$. $m_t, \tilde{m}_s$ are the vector local magnetization DOS of the tip and the energy-integrated vector local magnetization DOS of the sample in the energy interval $[E_f;\, E_f + eV]$, respectively. One can also image the magnetic domain with high spatial resolution in the SP-STM, as shown in ref. [229–231], by recording the differential of the tunneling current simultaneously to the topographic constant current mode, as expressed in the following equation:

$$dI/dV(\overrightarrow{r_t},\, V,\, \theta) \;\propto\; \rho_t.\rho_s(\overrightarrow{r_t},\, E_f + eV) + m_t.m_s(\overrightarrow{r_t},\, E_f + eV)\, cos\theta(\overrightarrow{r_t}). \tag{4.31}$$

The differential tunneling current in the SP-STM mode, Eq. 4.31, is directly proportional to the density of states of the sample ρ_s, and to the vector local magnetization DOS of the sample m_s at the energy $E_f + eV$. The optimum bias voltage V can be chosen wisely to obtain the maximum value of m_s over the former parameter ρ_s by running a SP-STS measurement on different regions.

On the other hand, the constant current mode, expressed by Eq. 4.30, is dependent on the energy integrated LDOS $\tilde{\rho}_s(\overrightarrow{r_t},\, V)$ and the energy-integrated vector local magnetization DOS of the sample $\tilde{m}_s(\overrightarrow{r_t},\, V)$. These parameters are energy-dependent, thus $\tilde{\rho}_s(\overrightarrow{r_t},\, V)$ always increase as the bias voltage V increases, meanwhile, the parameter $\tilde{m}_s(\overrightarrow{r_t},\, V)$ may stay constant or even decrease if the integration is carried out over states of opposite spin-polarization. Therefore, the constant current mode of the SP-STM yields minimal magnetic contrast among distinct magnetic domains as I_0 predominantly influences the tunneling current.

The magnetic spin-polarized tip can be made of either bulk material as in the case of CrO_2[232], $in - situ$ prepared CoCr [233] or from deposited thin films on non-magnetic tips like W- tips, e.g.: 3–10 ML Fe which is almost always sensitive

to the in-plane component of the magnetization of the sample. Meanwhile, the tip prepared with deposited thin films of 7–9 ML Gd, 10–15 ML $Gd_{90}Fe_{10}$, and 25–45 ML Cr are usually sensitive to the perpendicular out-of-plane magnetization component at low temperatures [226].

Inelastic Electron Tunneling Spectroscopy (IETS)

The tunneling current between two electrodes in the tip-vacuum-sample tunneling junction mainly experiences elastic tunneling. However, once the electron tunneling current passes through certain adsorbates, such as adatoms or molecules, some inelastic tunneling events may occur with a low probability of 1-10% [214, 234, 235].

The inelastic electron scattering occurs, once the energy of the tunneling electron exceeds some excitation energy in the adsorbate, i.e.: $eV \geq h\nu$, where h is Planck constant and ν is the excitation's frequency. At these excitation energies, a new tunneling channel is open and there will be some enhancement in the conductivity, which is shown as steps in the dI/dV vs V spectra and as peaks in d^2I/dV^2 vs V spectra at the corresponding energies, as shown in Fig. 4.14. The increase in conductivity occurs because a portion of the tunneling current's energy is transferred to the adsorbate, and it still reaches a state above the Fermi energy of the corresponding electrode. This, in turn, contributes to the tunneling current as part of an inelastic current added to the total tunneling current [236].

The enhancement in conductivity can be utilized as a reference point for distinguishing between various excitations observed in the adsorbates. While vibrational IETS typically results in modest increases in conductance, usually not exceeding 10%, magnetic IETS often leads to substantial changes, sometimes exceeding 100% [236]. In some cases, smaller changes, around 20%, have also been documented for magnetic excitations [221, 237, 238]. This disparity in behavior between vibrational and magnetic IETS can be attributed to the differing strengths of the interactions involved: electron-vibration couplings tend to be weak, whereas electron-spin couplings are typically very strong [236]. Additionally, it's worth noting that the energy range of the molecules' vibrations differs from that of spin excitations. For instance, spin excitations can occur up to ± 200 meV around the Fermi energy (E_F) [159, 221], while vibrations such as C-H stretching energies are typically around 359 mV [239]. Thus, IETS is a special kind of local electron energy loss spectroscopy with a high spatial resolution.

The high-spatial resolution of the STM enables IETS to probe the local vibrational properties of the adsorbates, e.g.: single molecule bond active sites, or the influence of the surface defects on the vibrational modes [222, 234, 240, 241]. Such capability of local study of the adsorbates is of particular importance since it is believed that, in numerous catalytic reactions, only a few active sites are present on the surface, serving as the locations for crucial chemical reactions [235].

Moreover, IETS can be used to detect magnetic excitation, e.g.: magnetic excitations on a single magnetic atom [242], spinwave excitation [243] and itinerant magnetism [244]. IETS measurements have been carried on magnetic molecules to

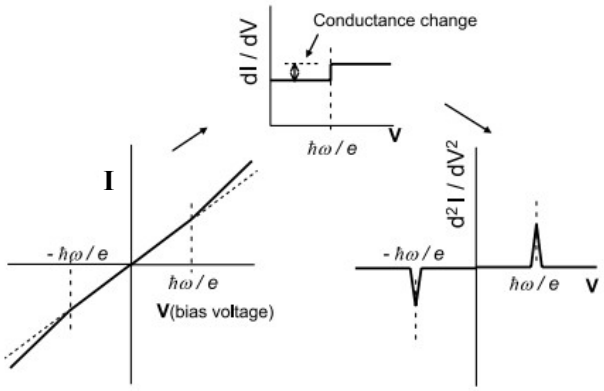

Figure 4.14: The I-V tunneling current experiences a slight change at some energy, $\hbar\omega/e$. This slight variation is attributed to inelastic tunneling events due to some excitations in the tunneling junction at the threshold energy. The excitations are shown in the conductivity spectrum as steps and in the dI^2/dV^2 curve as peaks and dips [240].

measure the magnetic anisotropy parameters and the switching of the spin states, like the work of Tsukahara et al. on iron(II) phthalocyanine molecule (FePc) deposited on an oxidized Cu(110) Surface [159]. Depositing these molecules on non-conducting layer rendered the molecules with its free molecule character where the charge transfer with the substrate will be hindered. However, IETS measurements on this system showed that the two possible orientations of the molecules on this surface have a different magnetic anisotropy. Moreover, the magnetic anisotropy of the molecule itself has been changed from easy plane, in the free gas molecules, to the out-of-plane easy axis in the adsorbed molecules [159]. Such change has been accompanied with switching of the spin states from singlet (S=0) on metallic surface to triplet (S=1) on oxidized surface [159].

Magnetic IETS can be used, as well, on full-stacked molecular monolayers as done by Chen et al. on cobalt phthalocyanine (CoPc) molecules [152], where they could probe the antiferromagnetic superexchange interaction mediating the molecules chains in the thin film in the top layers. Another powerful application of the magnetic IETS is the applicability of the charge states identification in CoPc single molecules as demonstrated in Fu et al. work [245]. The energy of the LUMO state of CoPc molecule could be varied by controlling the tunneling separation gap voltage between the tip and the molecule. The electrostatic effect causes this variation leading to the shift of the LUMO below E_F and charging the molecule with spin state $S = 1/2$. The vibronic LUMO state can be detected via the IETS and the magnetic IETS can be used to distinguish between the neutral and charged molecule. The main difference between the two cases is the shift of the magnetic

IETS steps to higher energies at higher magnetic field in the charged molecules. This is a consequence of the spin-flip inelastic electron tunneling into charged molecules Zeeman split states.

Magnetic IETS could also measure the decay rate of some excited magnetic states, as demonstrated by Loth et al. in their study on single Mn atoms adsorbed on CuN/Cu(100) [246]. In such investigations, the tunneling current intensity of a spin-polarized tip is controlled, where at low current levels, each successive tunneling electron interacts with the spin in its ground state due to the higher frequency of spontaneous relaxation compared to the excitation by tunneling current. Meanwhile, at sufficiently high current levels, it is more probable for the successive tunneling current to interact with the spins at the excited states. They found that the spin lifetime in this regime is in the sub-nano-second range. However, as demonstrated by Khajetoorians et al., the hybridization of the states of the magnetic Fe adatoms with the Cu(111) metallic substrate continuum electrons causes the spins in magnetic adsorbates on metallic substrates to have a shorter life in the range of 200 fs [244].

The hybridization of the orbitals of the deposited molecules with the electronic continuum of the metallic substrates can influence magnetic (IETS) and give rise to another phenomenon known as the Kondo effect which was first described in 1964 [247]. Instead of displaying symmetric steps around the Fermi energy (E_F) as seen in IETS, the conductance spectra exhibit zero-bias anomalies, which are characteristic signatures of the Kondo effect in STM experiments. This zero-bias resonance peak occurs due to the screening of the spin of the magnetic moment of the impurity by the conduction electrons of the substrate, involving spin-flip scattering of the substrate conduction electrons at no energy cost.

This phenomenon was observed in adsorbed molecules in some investigations done by Komeda et al. on the double-decker bis(phthalocyaninato)terbium(III) complex ($TbPc_2$) adsorbed on an Au(111) surface [162]. This resonance in these molecules is observed on the lobes of the top Pc ligands but not on the central Tb^{+3} ion, as shown in Fig. 4.15. The reason for this is the localization of $4f$ orbitals hosting the magnetic moment of the lanthanide ion, so no screening takes place for the magnetic moment of the central ion. Moreover, the strong magnetic anisotropy of the Tb^{+3} ion leads to left the degeneracy of the spin states of the central Tb^{+3} ion, which hinders the Kondo resonance. On the other hand, the unpaired spin in the π-orbital of the phthalocyaninato (Pc) ligands occupies p-orbitals with a degenerate spin state, $S = 1/2$, which can be screened with the substrate conduction electrons due to the ligand's sizable coupling with the substrate. Thus, Kondo peaks in this molecule originates from the Pc ligands rather than the central ion.

Many theoretical approaches were introduced to explain the magnetic IETS that correspond to the spin excitation in magnetic molecules and adatoms. Hirjibehedin et al. presented an empirical theoretical approach to explain the conductance spectra of adsorbed magnetic Fe and Mn on the insulating layer CuN/C(110) [248]. Depending on the spin Hamiltonian in an anisotropic environment,

$$\hat{\mathrm{H}} = \mathrm{g}\mu_{\mathrm{B}}\overrightarrow{B}.\overrightarrow{\hat{S}} + \mathrm{D}\hat{\mathrm{S}}_{\mathrm{z}}^{2} + \mathrm{E}\,(\hat{\mathrm{S}}_{\mathrm{x}}^{2} - \hat{\mathrm{S}}_{\mathrm{y}}^{2}), \tag{4.32}$$

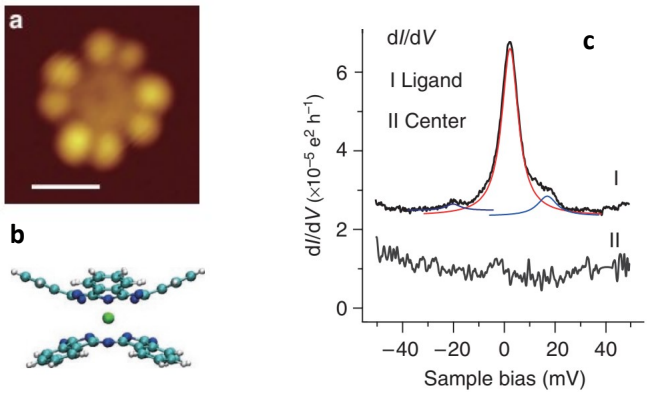

Figure 4.15: (a) Topography of $TbPc_2$ single molecule on Au(111) surface. The four bright (dark) lobes are the upper (lower) Pc ligands of the double-decker $TbPc_2$-molecule. The upper and lower deckers are shifted by 45° with respect to each others. (b) Side view of the double-decker $TbPc_2$-molecule showing the central Tb^{+3} ion and the upper and lower Pc ligands. (c) dI/dV spectra measured at the Pc ligand (I) and at the Tb^{+3}central ion (II). The spectra demonstrate unequivocally the zero-bias peak (ZBP) attributed to Kondo resonance at the ligand but the absence of such anomaly on the center of the molecule. The images are adapted from Ref. [162].

the excitation energy spectrum can be calculated by the diagonalization of Eq. 4.32, where g is the gyromagnetic ratio of the spin, D and E are the axial and transverse magnetic anisotropy, respectively. Their phenomenological model is based on (i) a voltage-independent elastic conductance and (ii) the thermally broadened IETS transition weighted with the spin transitions between the spin eigenstates of the three orthogonal spins, $I_{i\to f} = \sum_{j=x,y,z} | < \psi_f|\hat{S}_j|\psi_i > |^2$, and Boltzmann population of the filled and initial states.

Lorente et al. introduced a more rigorous theoretical framework to explain the spin transitions in IETS [249]. In his theoretical approach, he excluded the perturbation theory which introduced incomplete theories as in the work of [250–252] which failed to renormalize for the elastic channels and it exaggerated of the inelastic tunneling contributions. Lorente et al. calculated the branching ratio between the elastic and the inelastic channels in the tunneling process [249]. They based their calculation on the fact that during the very short collisional time between the tunneling electron and the magnetic adsorbate, the interaction with the adsorbate environment can be neglected, i.e. perturbation can be overlooked. This strong coupling between the tunneling electron and the adsorbate forms a transient collisional intermediate state. These collision tunneling channel can be included in calculating the transition rate and reproduce the conductance steps at the threshold voltages of the spin excitations in the experimental results in former work [248, 253]. Further details on the theoretical investigations of the IETS can be found in Ref. [236, 254, 255].

4.1.2.4 Molecule and metallic thin films deposition

The molecules and metallic thin films were evaporated *in-situ* using the physical thermal deposition technique (PVD) within a separate preparation chamber, as illustrated in Fig. 4.6.

Fig. 4.16 provides a schematic representation of the operational principles of this deposition method. A crucible containing the powdered molecules is heated until the powder sublimates, creating vapor pressure. The crucible is heated using a wrapped tungsten wire connected via an electrical feedthrough to a power supply. Temperature regulation is achieved through a PID controller, which adjusts the heating power based on the difference between the measured temperature and the desired setpoint. This precise temperature control is essential to reach the desired temperature without overshooting, particularly the sublimation temperature, thereby preventing uncontrolled deposition of thin films. Additionally, by regulating the current, one can prevent the dissociation or carbonization of the molecule powders by avoiding heating them beyond the sublimation temperature.

The target coverage of the molecules on the substrate is to have single scattered molecules within each scan frame of the substrate ($500 \times 500\ nm^2$). Thus, the trial-and-error approach was used to decrease the coverage as much as possible. After each evaporation attempt, an STM scan measurement was conducted to measure the coverage. The trials revealed that by evaporating Ni_2Tb molecules at their sublimation temperature, i.e.: 120 °C, and exposing the sample to the molecular beam for around one second, individual scattered molecules could be obtained in each frame. Throughout the molecular evaporation process, the pressure was consistently maintained at approximately 10^{-9} mbar, except during the initial evaporation trials, which involved the degassing of the molecules.

The metallic thin layers were prepared in the other preparation chamber in the STM shown in Fig. 4.6. The thermal evaporator used for this purpose is similar to the previous one but lacks a temperature controller. As a result, the sublimation temperature cannot be precisely regulated; however, the deposition process can be monitored using a quartz crystal. The deposition rate of the Fe layers were in the range of 0.12 – 0.15 ML/min. The sample holder within the preparation chamber has the capability to heat the sample using a filament positioned behind the sample, enabling electron beam heating. The temperature is monitored using a radiation thermometer (Pyrometer). The heating filament can reach very high temperatures to cleanse the sample, desorbing any adsorbates on the surface through brief flashes lasting less than 10 seconds.

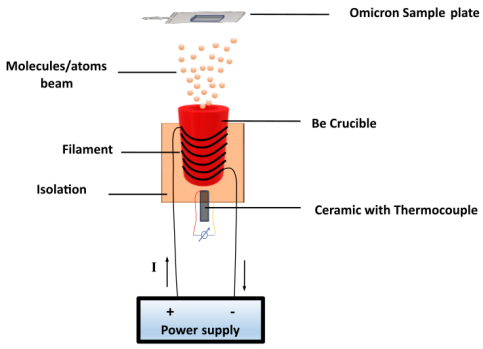

Figure 4.16: Sketch depicts the setup of the PVD thermal evaporator.

4.2 Low- Energy Electron Diffraction (LEED)

Low-energy electron diffraction (LEED) is a highly effective technique for surface crystallography, wherein electrons undergo elastic scattering off a surface. When a beam of electrons impinges upon a surface with a periodic two-dimensional structure, a diffraction pattern emerges due to the wavy nature of electron wavefunctions, introduced by Eq. 4.2, similar to the phenomenon observed with electromagnetic radiation[6] [256].

Because of the extended mean free path of electrons in ultra-high vacuum (UHV), the LEED technique enables $in-situ$ investigations of the surface, both before and after surface preparation. In the energy range of 50-100 eV, electrons have a minimized penetration depth into solids (5 – 10 Å), which makes them optimal for probing surface layers [257]. These characteristic features give the technique its name, hence Low-energy electron diffraction.

Figure 4.17 illustrates the operational principle of the LEED technique [258]. An electron gun emits an electron beam from a hot filament, which is then accelerated toward the sample. Upon interaction with the surface, the incident electrons undergo both elastic and inelastic scattering processes. To filter out the inelastically scattered electrons, the diffracted electrons pass through several grids positioned between the sample and the fluorescence screen, as depicted in Fig. 4.17. The first grid, located near the sample, is grounded to isolate the field from the space surrounding the sample, thereby ensuring that the energy of the diffracted electrons remains unchanged. The two following grids are known as suppressors, and they are maintained at a variable negative potential to block low-energy electrons. The

[6]For low-energy electrons, approximately 100 eV, the wavelength is around 1.22 Å, which is comparable to the lattice constants in solids.

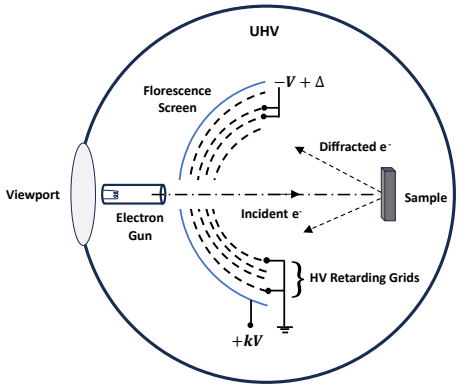

Figure 4.17: Schematic illustration of LEED system. The electrons are emitted from the electron gun and impinge upon the surface. The diffracted electrons are reaching a florescence screen after passing high-voltage retarding grids preventing lower energy electrons creating the reciprocal lattice point of the surface structure.

final grid is employed to measure the draining current of the fluorescence screen, effectively assessing the intensity of the diffracted electrons relative to the energy of the electron beam. The positively biased florescence screen display the diffraction spots, enabling a qualitative description of the surface and its symmetry.

The diffraction pattern displayed on the florescence screen directly represents the reciprocal lattice of the surface in k-space. These intensity maxima fulfill 2D Laue conditions

$$\begin{aligned} \Delta k \,.\, a &= 2\pi h \\ \Delta k \,.\, b &= 2\pi k. \end{aligned}$$

In this context, $\Delta k = k_f - k_i = G_{hk}$, where $G_{hk} = ha^* + kb^*$ represents a reciprocal lattice vector, and $a^*, b^*$are the primitive reciprocal lattice vectors corresponding to the real lattice vectors a and b.

Considering the elastic scattering of incident electrons with the surface, the wave-vector magnitudes of the incident and diffracted electrons are equal, i.e., $|k_i| = |k_f|$. Consequently, the incident and diffracted wave vectors define a sphere, with its origin at the tail of the incident wave vector and its head pointing to the (0,0) point in reciprocal space. The intensity maxima occur at points on the sphere satisfying $\Delta k = k_f - k_i$, as depicted in Fig. 4.18. These scattering vectors, Δk, correspond to the reciprocal lattice points (h, k).

The size of Ewald's sphere, and thus the number of diffraction spots on the screen, is determined by the energy of the incident electrons. The central point of the patterns denotes by (0,0) which is the primary incident electron beam. The reciprocal lattice structure can offer qualitative insights into the surface and its periodicity, as they mirror each other. Thus, in case of surface reconstruction one can

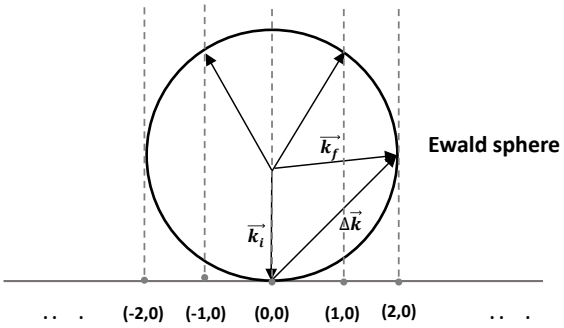

Figure 4.18: The Ewald 2D circle of a electron elastic diffraction with radius of $|\vec{k_i}|$.The reciprocal lattice point rods (h, k) intersect the circle at the points that satisfy Laue condition $\Delta k = G_{hk}$.

observe additional reciprocal lattice points on the florescence screen [259], as shown in Fig. 4.19. The superimposed overlayer, influenced by the surface reconstruction, is related to the surface's real lattice constant with an integer multiple; $a^{'} = na$ and $b\prime = mb$.

A quantitative analysis can be conducted by examining the I-V curve, which entails measuring the intensity of the diffracted electrons versus the incident electron energy. To enhance our understanding of the diffracted beam's intensity, it's essential to explore a theoretical framework beyond the kinematic theory of single scattering to calculate the intensities of diffraction of an electron beam impinging on a surface as accurately as possible, where the scattered electron undergoes multiple scattering events, which must be accounted for in the theoretical model. Therefore, the recorded I-V curves are compared with calculated curves obtained from dynamical LEED multiple scattering calculations [260].

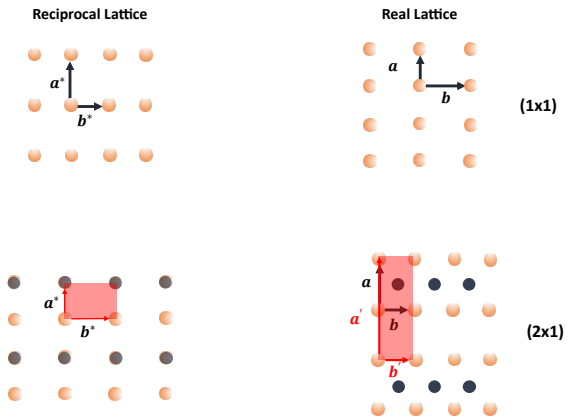

Figure 4.19: Schematic diagrams of reciprocal and real lattices with their lattice constant, $a^*, b^*$and a, b, respectively.

4.3 X-Ray Magnetic Circular Dichroism (XMCD)

Since their discovery in the late 19th century by Wilhelm Röntgen in 1895, X-rays have played an indispensable role in advancing various scientific and technological disciplines, including medicine, materials science, and chemistry. Their significance in material analysis stems from their unique properties.

Firstly, X-rays possess energy-dependent penetration depths, allowing for non-invasive examination of samples. This versatility enables scientists to probe both the inner and outer surfaces of materials based on photon energy and sample electron density. Additionally, high-energy X-ray photons ($\sim$ KeV) exhibit wavelengths comparable to the interatomic distances in solids, facilitating diffraction experiments that elucidate the crystalline structure of materials. Conversely, soft X-rays ($<$ 2 KeV) can be used at probing electronic transitions from core states to valence shells, offering insights into the electronic and magnetic properties of materials.

X-rays can be generated in several ways either naturally or artificially. Synchrotrons are considered powerful sources of X-rays that can generate X-rays with a tunable energy range and different polarization, offering enhanced versatility in experimental setups.

In this section, we will briefly cover synchrotron facilities and the emitted radiation and its properties. Then, we will introduce the main concepts in X-ray absorption by matter. Finally, we will delve into one of the soft X-ray techniques used for probing the magnetic properties of samples, known as X-ray Magnetic Circular Dichroism (XMCD). The sum rules quantifying this effect to measure the total number of valence holes, spin, and orbital magnetic moment will be explored in this subsection.

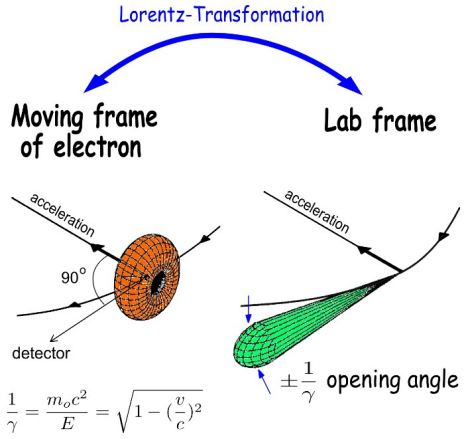

Figure 4.20: Sketch of the synchrotron radiation cone emitted by the accelerating electrons. The moving electrons generate the conventional dipole field in their own frame of reference (left).As the electron is accelerated, the dipole field becomes distorted and appears as a cone in the observer's frame of reference, with the indicated half-opening angle. [262]

4.3.1 Synchrotron radiation

The moving electrons with constant velocities, with respect to the observer, are emitting electromagnetic (EM) field, characterized by field lines that mainly radiate outward radially. Yet, the accelerating electrons with relativistic velocities, with respect to the observer, emanate distorted EM field with an electric field component parallel to the acceleration direction. This component is called the EM radiation and it travels away of the accelerating electron and falls off with the distance r from the particle as 1/r [69]. This radiation is focused into a forward cone tangent to the trajectory of the moving electron, with a half-opening angle ranging from 0.1 to 1 mrad, depending on the energy of the electrons, as shown in Fig. 4.20, and it is known as Synchrotron radiation.

This energy can be determined by the inverse Lorentz factor, $\gamma^{-1} = E_0/E$, where E represents the actual energy of the electron and E_0 is the rest energy of the electron, which equals 0.511 MeV. The total radiation power P_{rad} of a traveling electron of energy E around an orbit with radius R in a magnetic field B is [261]:

$$P_{rad} = \frac{e^2 c}{6\pi\epsilon_0}\frac{1}{R^2}\left(\frac{E}{E_0}\right)^4, \tag{4.33}$$

e is the electron charge, c is the speed of light, and ϵ_0 is the vacuum permittivity.

The synchrotron radiation is very intense and extends over a broad energy range in electromagnetic spectrum, starting from infrared through ultraviolet and visible to soft and hard x-ray regions. Such radiation can be generated either from cosmic sources, like pulsars, or from man-made sources, like: large electron-accelerators facilitates. Nowadays, there are over 50 synchrotron facilities worldwide, spanning various generations [263].

Figure 4.21 illustrates the fundamental configuration of a synchrotron facility. Initially, electrons are emitted from an electron gun and accelerated to relativistic velocities in a **linear accelerator (LINAC)** until their energy reaches several MeV. Subsequently, the accelerated electrons are injected into a **booster ring** to further increase their energy to the GeV range. These highly energetic electrons are then injected into a larger **storage ring**, where they are constrained to follow a circular path due to the magnetic field generated by the bending magnets [264]. The storage ring contains quadrupole magnets in addition to the bending dipole magnets. The quadrupole magnets are used to focus and defocus the electron beam within the ring. The RF cavities are installed in some parts of the ring to replenish the energy of the electrons after they have lost a portion of it. The **insertion devices (ID)** are responsible for generating the synchrotron radiation cone from the storage ring.

The first generation of the synchrotron was not dedicated solely to synchrotron radiation; rather, it was a byproduct of high-energy experiments, where the radiation emitted from the bending magnets was considered as energy loss and heat. This led to the development of dedicated synchrotron facilities, marking the second generation of synchrotron facilities where the **bending magnet** themselves became as a source of the synchrotron radiation, as shown in Fig. 4.22(a), and some tangential **beam lines** with an experimental end-station for running the experiments where established. The third generation of the synchrotron facilities further optimized insertion devices, incorporating Wigglers and Undulators installed in straight portions of the storage ring.

The insertion devices consists of a periodic arrangement of magnets (N magnetic poles) that produce an alternating perpendicular magnetic field, inducing the traveling electrons to oscillate in the horizontal plane of their motion, with period of length λ_μ, as shown in Fig. 4.22(b). The oscillating motion generates multiple radiation cones at each "wiggle", contributing to a cone with higher intensity overall. A key distinction between wiggler and undulator insertion devices (IDs) is the wiggling angle, which is larger for wiggler IDs than for undulators, as shown in Fig. 4.22(c). This difference impacts the interference pattern of the emitted radiation cones. In undulators, the cones add up coherently, resulting in an intensity increase proportional to N^2, where N represents the number of magnetic poles. Conversely, in wiggler IDs, the intensity is proportional to $2N$.

The parameter K, defined as $K = \alpha\gamma$, relates the wiggling angle deviation to the natural angular aperture of the synchrotron radiation cone, $1/\gamma$. It serves to differentiate between wigglers and undulators, where for wigglers, $K >> 1$, and for undulators, $K << 1$. Another defining parameter that sets apart the various generations is the spectral brilliance, which quantifies the number of photons emitted per second per unit area within a spectral bandwidth $\Delta E/E = 0.1\%$ into a unit solid angle [265].

Figure 4.22(d) provides a comparison of brilliance among different synchrotron radiation sources. It's worth noting that Free Electron Lasers (FELs) are not included in this comparison, as they fall outside the scope of this thesis.

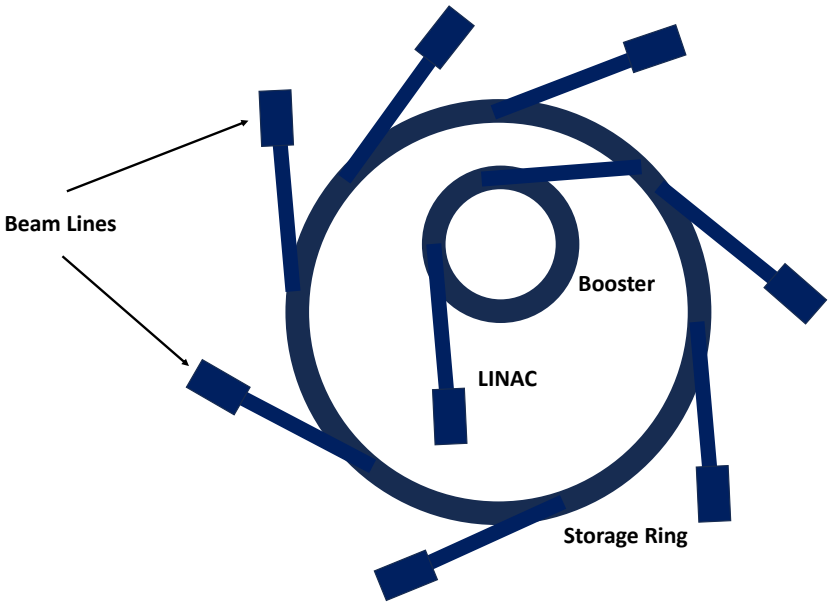

Figure 4.21: Sketch of Synchrotron main parts as described in the text.

The synchrotron radiation emitted is predominantly linearly polarized when observed in the horizontal plane of the traveling electrons. This polarization occurs because the electric field aligns parallel to the plane of the electron orbit. However, at vertical angles above that plane, there exists a polarization component perpendicular to the plane of the orbit. Thus, it is meaningful to define the degree of linear polarization as

$$P_{linear} = \frac{I_{//} - I_{\perp}}{I_{//} + I_{\perp}}, \tag{4.34}$$

where the linear polarization decreases as one moves off the axis. Above and below the orbital plane there is a constant phase difference between both components, leading to right circular polarization above the orbital plane and left circular polarization below. The degree of polarization

$$P_C = \frac{I_R - I_L}{I_R + I_L} = \frac{\pm 2\sqrt{I_{//}\, I_{\perp}}}{I_{//} + I_{\perp}}, \tag{4.35}$$

where I_R and I_L are the intensities of right and left polarized light and the sign $\pm$ corresponds to the positive and negative values of the half-opening angle [264]. Further technical details about the beamline PM2 VEKMAG in the Bessy II synchrotron, where we conducted our measurements are covered in chapter 6.

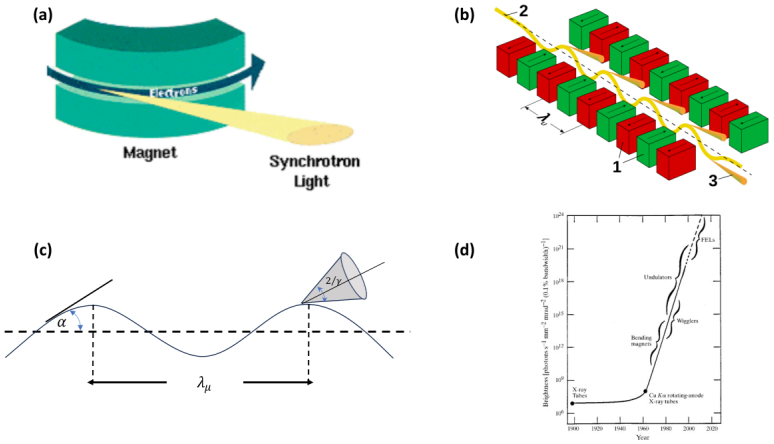

Figure 4.22: (a) First and second generation of synchrotrons produce synchrotron radiation out of dipole bending magnets [266]. (b) The wigglers and undulators are used in the third generation to produce intense synchrotron radiation. The gap between the magnetic poles (1) is tunable in undulator and this make the wiggling electrons (2) produce more radiation cones (3) leading to more intense radiation [266]. (c) Schematic view of the "wiggler" regime, where α represents the wiggling angle and λ_μ represents the period of the oscillations. (d) Brilliance (Brightness) of several storage rings in different synchrotron generations in the last 100 years [267].

4.3.2 X-ray absorption in matter

Electromagnetic radiation interacts with matter through various mechanisms such as reflection, refraction, and absorption, and X-rays follow the same principles. In the case of X-rays, reflection and refraction occur via scattering and the emission of radiation by scattering elements, typically the electron cloud. This scattering can either occur at the same frequency (Thomson elastic scattering) or at a reduced frequency (inelastic Compton scattering).

In most synchrotron radiation applications (below 1 MeV), the Compton scattering cross-section is negligible due to insufficient energy to eject bound electrons. Additionally, for interactions involving photons with energies less than 3 keV, the Thomson scattering cross-section remains constant but it is orders of magnitude smaller than the photoabsorption cross-section [268, 269].

The photoabsorption cross-section is both material- and energy-dependent, typically varying approximately as Z^4, where Z is the atomic number of the element, and decreasing with increasing photon energy following E^{-3}, as depicted in Fig. 4.23(a). The atomic photoabsorption cross-section, σ_a, is directly related to the absorption coefficient, denoted as μ, which quantifies the rate at which radiation is attenuated within the material, with the attenuation length being the distance at which the initial intensity drops to $1/e$. This relationship is expressed as $\sigma_a[cm^2g^{-1}] = \frac{\mu}{\rho_m}$, where ρ_m is the mass density.

At some specific energies, a sudden sharp increase occurs due to a resonance

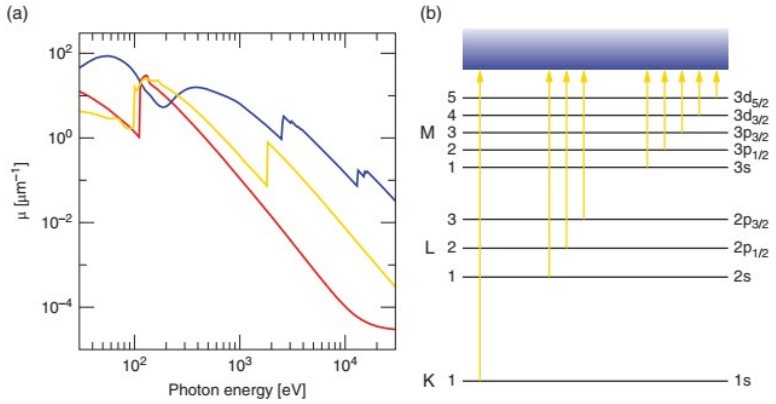

Figure 4.23: (a) X-ray absorption coefficient as a function of incident photons energy for Be (red), Si (yellow), and Pb (blue). (b) The absorption edges depicted in (a) correspond to the excitation of electrons from different orbitals to the continuum. Excitation from orbitals with principal quantum numbers n = 1, 2, 3 correspond to absorption edges labeled as K, L, M, respectively. Image is taken from Ref. [268].

between the x-ray photons energy and the binding energy of electrons in their orbital in the atom, leading to their excitation either to the continuum or to the upper valence shell. These peaks are known as "absorption edges" and are labeled according to the orbitals from which the electrons are excited, as illustrated in Fig. 4.23(b). With the exception of the K-edges, all absorption edges feature multiple closely spaced "sub-edges" linked to nondegenerate quantum states of the localized core states which are split due to spin-orbit coupling by 10 eV [69]. Consequently, one can find a one K-peak, three L-peaks ($L_{1,2,3}$-edge), and five M-peaks ($M_{1,2,3,4,5}$-edge) in an absorption spectrum. For transition metals the magnetism originates from the 3d-orbitals meanwhile for the rare-earth metals the 4f-orbitals are the source of the magnetism. Therefore, examining the $L_{2,3}$-edges for the transition metals and $M_{4,5}$-edges provides valuable insights into the magnetic properties of the material.

Generally speaking, any interaction of radiation with matter leads to attenuation of the radiation within the material. The intensity of transmitted X-rays through a slab of certain thickness decreases exponentially as a function of the absorption coefficient, as expressed in the Beer–Lambert equation: $I = I_0 exp(-\mu(E).z)$, as depicted in Fig. 4.24. The linear absorption coefficient parameter is of central importance in the X-ray Absorption Spectroscopy (XAS). This coefficient for a material can be understood within the single-particle approximation, where one photon is absorbed, causing an electronic transition from the occupied initial state $|i>$ with an energy E_i to the unoccupied final state $|f>$ with an energy E_f, according to

Fermi golden rule:

$$\mu \propto \sum_{i,f} | < f|\hat{H}|i > |^2 \, \rho(E_f)\rho(E_i)\delta(E_f - E_i - \hbar\omega) \tag{4.36}$$

where $\hat{H}$ is the Hamiltonian interaction between the x-ray EM-wave and the electrons, $\rho(E)$ is the electronic density of states, and the Kronecker delta function ensures the conservation of energy in this transition. The matrix elements of the transition is proportional to the amplitude of the dipole operator transition $| < f|\hat{\epsilon}.\overrightarrow{r}|i > |^2$ (in the simplest case)[7]. This amplitude has non-zero values if the integrand is as symmetric as possible, which occurs when the orbital overlap$< \psi_f|\psi_i >$ is antisymmetric, as the dipole operator $\hat{\epsilon}.\overrightarrow{r}$ is antisymmetric. This implies that the orbitals of the initial and final states must have different symmetry to allow this transition. Therefore, the difference in orbital angular momentum must be $\Delta l = \pm 1$, and there must be no spin flip, meaning $\Delta s = 0$ and the total angular momentum difference $\Delta j = 0, \pm 1$. Such considerations are known as *selection rules* and they are the governing rules in the dipole transition.

Following this approach, an electron can be elevated to an unoccupied bound valence state, selectively probing the valence shell. For transition metals, where magnetism originates from the 3d-orbitals, investigating the $L_{2,3}$-edges involves exciting electrons from the $p_{1/2,3/2}$-orbitals to the d-orbitals. Conversely, for rare-earth metals, where magnetism arises from the $4f$-orbitals, examining the $M_{4,5}$-edges involves exciting electrons from the $d_{3/2,5/2}$-orbitals to the f-orbitals. Such investigations can be performed using tunable synchrotron radiation, making the synchrotron a versatile tool for various spectroscopic techniques.

The absorption spectrum can be directly measured using the Beer-Lambert law by comparing the initial X-ray intensity to the transmitted intensity through the sample in transmission geometry. Alternatively, it can be indirectly measured by detecting either emitted fluorescence photons or secondary (Auger) electrons, which arise from the two main de-excitation processes: (i) emission of characteristic fluorescence photons or (ii) radiationless ejection of Auger electrons.

When an X-ray photon is absorbed, it creates an electron-hole pair. The electron may transition to higher energy shells or escape into the continuum. In fluorescence emission, the core-hole is filled by an outer-shell electron, emitting a characteristic X-ray photon with energy corresponding to the difference between the two states, following selection rules. This occurs on a femtosecond timescale, with the emitted photon having slightly lower energy due to nonradiative relaxation.

On the other hand, in Auger emission, the core-hole is filled with electrons from the outer shell, and the excess energy is released by emitting electrons from the outer shells whose binding energy is less than that of the excess energy. These

[7]The dipole ($| < f|\hat{\epsilon}.\overrightarrow{r}|i > |^2$) and quadrupole terms ($| < f|(\hat{\epsilon}.\overrightarrow{r})(\overrightarrow{k}.\overrightarrow{r})|i > |^2$) of the matrix elements are originated from the expansion of the Hamiltonian interaction of the EM plane wave with the electron $\hat{H} = \hat{\epsilon}.\overrightarrow{r}e^{i\overrightarrow{k}.\overrightarrow{r}}$, where for the heavier atoms the later is not negligible anymore [270].

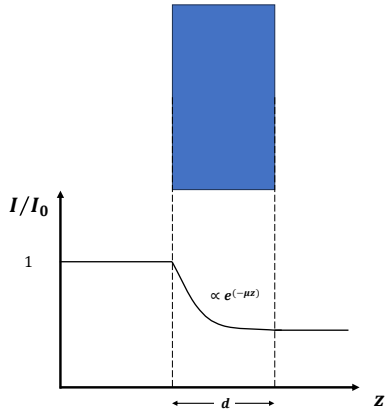

Figure 4.24: The intensity of the x-ray through a material falls off exponentially depending on the thickness and the absorption coefficient of the material.

two processes compete [271], with fluorescence favored in heavier atoms due to larger energy differences between states, and Auger emission more common in lighter atoms.

As the energy differences between the states increase, the probability of Auger emission decreases, while fluorescence emission increases. Consequently, for heavier atoms where the nucleus charge is large and the energy differences between adjacent states are significant, especially those close to the nucleus, electrons are bound more tightly by the nucleus charge. Thus, for heavier atoms, it is more probable to emit fluorescence photons (K-line) than Auger electrons, whereas for lighter atoms, the Auger electron yields exceed the fluorescence yield.

The quantity of emitted Auger electrons correlates directly with the absorption cross-section in the surface region, thereby facilitating a reliable measurement of the material's absorption coefficient. In contrast, fluorescence yield primarily applies to thin samples, as thicker samples can experience self-absorption of emitted photons [272], requiring corrections detailed in Section 6.3 of this thesis.

4.3.3 X-ray Magnetic Circular Dichroism (XMCD): Sum Rules

The use of linearly and circularly polarized radiation produced by synchrotron insertion devices, as described in Section 4.3.1, provides critical tools for investigating various electronic and magnetic properties of materials. The changes in the polarization of the X-ray photon electric field can markedly influence the material's X-ray absorption intensity.

The XAS resonance intensity must be independent of the sample's orientation to yield information on the charge and the magnetic moments in the sample. The

orientation-averaged XAS intensity can be defined following the polarization of the incident X-ray photons, their propagation direction, the symmetry of the sample's lattice structure and whether the sample is magnetic or non-magnetic [69].

For the XMCD measurements of polycrystalline magnetic samples one should first eliminate any magnetic effects by saturating the sample's magnetization with an external magnetic field parallel and antiparallel to the x-ray propagation direction, and one measurement along some direction parallel to the prorogation direction will be sufficient to obtain the orientation averaged isotropic XAS

$$< I_{iso} >= I^{+} + I^{0} + I^{-} \tag{4.37}$$

where I^{+} (I^{-}) denotes the right (left) circular polarized photons and I^{0} denote the linear polarized photons which can be approximated by $I^{0} = \frac{(I^{+}+I^{-})}{2}$. Note that the three propagation directions are fixed all along the same certain direction. The orientation-averaged x-ray resonance absorption intensity is directly proportional to the total number of the valence holes, e.g.: 3d states in the transition metals. This has been shown for various 3d-transition metals as shown in Fig. 4.25(a) where the white line intensity [8] decreases with increasing atomic number along the periodic table series. This observation can be explained by the fact that in such metals, the d-valence shells are filled with one electron per atom along the series leading to the decrease of the empty valence states. The number of holes corresponds to the energy-integrated density of states above the Fermi level, $N_h = \int_{E_f}^{\infty} \rho(E) dE$. Therefore, the greater the number of empty states above the Fermi level, the higher the x-ray absorption intensity. Theoretical calculations of the hole number for 3d metals plotted against the integrated resonance intensity (the shaded peak area shown Fig. 4.25 inset) reveal a linear relationship with a strong correlation, as depicted in Fig. 4.25 (b).

This lead to the first sum rule which states that **the total intensity of core to valence shell transition with angle-averaged XAS is directly proportional to the total number of the empty states above Fermi level**.

In the one electron picture, the dipole operator, $P^{q}_{\alpha} = \hat{\epsilon}.\overrightarrow{r}$, does not act on the spin, since the only allowed transitions are the ones that preserve the spin, but it acts on the angular part of the orbital wave function [69]. Hence, there is no allowed spin flip transition but the allowed transitions are the one that obey the transition selection rules between orbitals, e.g.: $\Delta l = \pm 1$. Also, the dipole operator can be written in terms of Racah's tensor, $C^{(l)}_{m} = \sqrt{\frac{4\pi}{2l+1}} Y_{l,m}(\theta, \phi)$ of rank $l = 1$, $P^{q}_{\alpha}/r = \sum_{p=0,\pm 1} e^{q}_{\alpha,p} C^{(1)}_{m}$. This can be useful to derive the sum rules by applying the sum rules of Racah's spherical tensor operator.

The $\boldsymbol{k}$-dependent generic l-orbital wavefunction of atoms in solids is

[8] The term "white line intensity" is often used interchangeably with absorption intensity. This terminology stems from early methods of recording x-ray intensity on photographic film, where areas of increased absorption appeared as "white lines" due to their higher absorption strength.

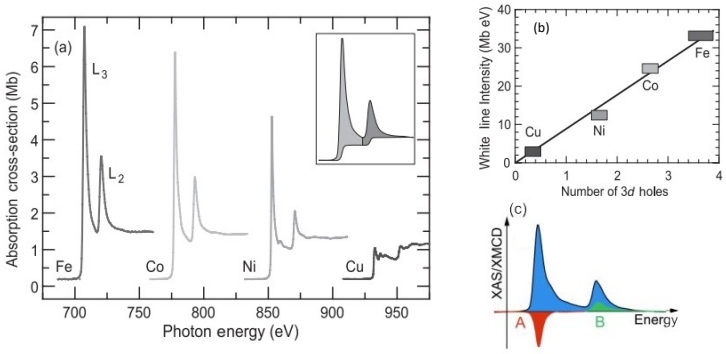

Figure 4.25: (a) The plots of XAS absorption cross section at L-edge for 3d metals Fe, Co, Ni and Cu. The inset shows the shaded peak areas corresponding to the energy-integration of the XAS intensity at the $L_{3,2}$-edge. (b) The correlation between the theoretical values of the $3d$ hole and the values obtained from the first sum rule. The theoretical values used for the holes are 1.5–1.78 for Ni, 2.5–2.80 for Co and 3.4–3.93 for Fe. (c) The average XAS of Fe (blue) and the XMCD peaks at L_3 edge (red) and at L_2 edge (green). Images are taken from Ref. [69, 273].

$$|\phi_l(\boldsymbol{k},r)> = R_{n,l}(r)\left(\sum_{m_l=-l}^{l} a_{m_l}(\boldsymbol{k})\,|Y_{l,m_l}\chi^{+}> + b_{m_l}(\boldsymbol{k})\,|Y_{l,m_l}\chi^{-}>\right) \tag{4.38}$$

where $R_{n,l}(r)$ is the radial part of the orbital wave function, and $Y_{l,m}$ is the spherical harmonics, and $\chi^{\pm}$ is the spin part. The coefficients a_m and b_m satisfy the normalization condition $\sum_m |a_m|^2 + |b_m|^2 = 1$. The intensity of XAS of solids can be obtained by calculating the amplitude of the matrix elements of the dipole operator transition from core to valence shell ($c \rightarrow L$)

$$\begin{aligned} I^q_\alpha &= \mathcal{A}\sum_{\substack{E_i>E_F\\ i,\boldsymbol{k},m}} |<\psi_i|P^q_\alpha|\phi_j>|^2 \\ &= \mathcal{A}\mathcal{R}^2\sum_{\substack{E_i>E_F\\ i,\boldsymbol{k},m}}\sum_{p,M}[|a_{i,M}(\boldsymbol{k})|^2 + |b_{i,M}(\boldsymbol{k})|^2]\,|e^q_{\alpha,p}|^2\,|<L\,M|C^{(1)}_p|c\,m>|^2 + \\ &\quad \mathcal{A}\mathcal{R}^2\sum_{\substack{E_i>E_F\\ i,\boldsymbol{k},m}}\sum_{\substack{p\neq p'\\ M\neq M'}} e^q_{\alpha,\,p}(e^q_{\alpha,\,p'})^*<L\,M|\,C^{(1)}_p\,|c\,m><L\,M'|\,C^{(1)}_{p'}\,|c\,m>^* \\ &\qquad\qquad \times\,[a_{i,M}(\boldsymbol{k})(a_{i,M'}(\boldsymbol{k}))^* + b_{i,M}(\boldsymbol{k})(b_{i,M'}(\boldsymbol{k}))^*]. \end{aligned} \tag{4.39}$$

where the first term represents the diagonal terms and the second term represents the cross terms and the dipole operator has been written in terms of Racah's tensors. The orientation-average of Eq.4.39 can be done by summing either over polarization states $q = 0, \pm 1$ or crystallographic direction. In both cases the cross terms in Eq.4.39 vanishes because $\sum_q e^q_{\alpha,\,p}(e^q_{\alpha,\,p'})^* = \sum_\alpha e^q_{\alpha,\,p}(e^q_{\alpha,\,p'})^* = 0$. The polarization averaged intensity is given by

$$\begin{aligned} <I> &= \frac{1}{3}(I^{-1}_\alpha + I^0_\alpha + I^{+1}_\alpha) \\ &= \mathcal{A}\mathcal{R}^2\sum_{\substack{E_i>E_F\\ i,\boldsymbol{k},m}}(|a_{i,M}(\boldsymbol{k})|^2 + |b_{i,M}(\boldsymbol{k})|^2)\sum_{p,M}|<L\,M|C^{(1)}_p|c\,m>|^2\sum_q|e^q_{\alpha,p}|^2 \\ &= \mathcal{A}\mathcal{R}^2\frac{L}{3(2L+1)}\,N_h \end{aligned} \tag{4.40}$$

where $\sum_{\substack{E_i>E_F\\ i,\boldsymbol{k},m}}(|a_{i,M}(\boldsymbol{k})|^2 + |b_{i,M}(\boldsymbol{k})|^2) = N_h$, $\sum_{p,M}|<L\,M|C^{(1)}_p|c\,m>|^2 = \frac{L}{2L+1}$, $\sum_q|e^q_{\alpha,p}|^2 = 1$, $\mathcal{A} = \frac{4\pi\hbar\omega}{137}$ and $\mathcal{R}$ is the radial matrix element. That was the first sum-rule which directly relates the total number of valence holes N_h in the electronic ground state to the average-orientation XAS intensity.

This sum rule suggests that if we could make the absorption spin-dependent, then we could probe holes with different spin polarizations, i.e.: spin-up and spin-down holes. Consequently, the corresponding intensity difference could yield information

about the magnetic moment of the atoms, where magnetism originates from the valence shells. This intensity difference is what leads to the Dichroism effect in circular-polarized XAS and forms the basis of X-ray Magnetic Circular Dichroism (XMCD) spectroscopy. The XMCD effect is maximized when the sample's magnetization direction is collinear with the angular momentum of the incident photons. Therefore, the intensity difference is measured by changing the magnetization direction to be either parallel or antiparallel to the incident photon's angular momentum, represented as $\Delta I = I^{\uparrow\downarrow} - I^{\uparrow\uparrow}$. This intensity difference at the two edges L_3 and L_2 yield two areas denoted by $\boldsymbol{A} = \int_{L_3} XMCD\, dE$ and $\boldsymbol{B} = \int_{L_2} XMCD\, dE$ as shown at Fig. 4.25(c). Carra et al. [274] and Thole [275] derived the second and the third XMCD sum rules which results the spin and orbital magnetic moment from different linear combinations of the integrated regions of $\boldsymbol{A}$ and $\boldsymbol{B}$ in the XMCD spectrum. The *spin sum rule* yield the spin magnetic moment in the atom and it can be expressed as follow

$$m_{spin} = -\frac{3\, N_h\, \mu_B}{P} \frac{\boldsymbol{A} - 2\boldsymbol{B}}{\int_{L_{2,3}} I_{iso} dE}, \tag{4.41}$$

where N_h, μ_B, and P are the number of holes in the valence shells, the Bohr magneton and the polarization degree of the X-ray photons, respectively. On the other hand, the *orbital moment sum rule* yield the orbital magnetic moment of the atom and it can be expressed by

$$m_{orb} = -\frac{3\, N_h\, \mu_B}{P} \frac{\boldsymbol{A} + \boldsymbol{B}}{\int_{L_{2,3}} I_{iso} dE}, \tag{4.42}$$

The above spin sum (Eq. 4.41) rules has been derived solely to the $3d$ transition metal ions based on three main assumptions: (i) atomic-like model rather than a solid-state band energy model (ii) negligible core-valence coulomb interaction, and (iii) large spin-orbit coupling of the initial core-states leading to distinct spin-orbit-split core-states. However, these assumptions can introduce deviations in the results, necessitating correction when applying this sum rule in practice. As a result, the late 3d ions in the series , relevant to this thesis, exhibit an error of approximately 10% [276].

For 4f elements, the orbital moment and spin sum rule are expressed by

$$m_{spin}^{eff} = \frac{3\, N_h\, \mu_B}{P} \frac{\boldsymbol{A} - \frac{3}{2}\boldsymbol{B}}{\int_{M_{4,5}} I_{iso} dE}, \tag{4.43}$$

$$m_{orb} = -\frac{3\, N_h\, \mu_B}{P} \frac{\boldsymbol{A} + \boldsymbol{B}}{\int_{M_{4,5}} I_{iso} dE}, \tag{4.44}$$

where $\boldsymbol{A} = \int_{M_5} XMCD\, dE$ and $\boldsymbol{B} = \int_{M_4} XMCD\, dE$. The effective spin magnetic moment in Eq. 4.43 has two intricate ground state expectation values;

the first one is the the expectation value of the spin magnetic moment, m_{spin}, i.e. $< S_z >$, and the second one is the magnetic dipole operator, i.e. $< T_z >$.

In atoms, when considering the spin magnetic moment, it's important to account for the coupling between spin and charge of valence electrons. The magnetization distribution resulting from infinitesimal charge distribution in the atom (or ions in transition-metal complexes) lacks spherical symmetry. Therefore, the common pictorial idea of the spin magnetic moment as a rotating charged sphere, akin to a dipole, is somewhat misleading, especially when seeking element-wise information about spin- and orbital-magnetic moments. To describe the magnetization (or spin density within atomic volume) more accurately, we can use a multipole expansion including monopole $(1/r)$, dipole $(cos(\theta)/r^2)$ and quadrapole terms $(\sum_{\alpha,\beta} Q_{\alpha,\beta} r_\alpha r_\beta / r^3)$. Here $Q_{\alpha,\beta}$ represents a symmetric second-rank tensor of charge, which can be expressed in terms of Legendre polynomials in spherical coordinates to yield:

$$Q_{\alpha,\beta} = \begin{pmatrix} 1 - 3\ sin^2\theta\ cos^2\phi & -3\ sin^2\theta\ sin\phi\ cos\phi & -3\ cos\theta\ sin\theta\ cos\phi \\ -3\ sin^2\theta\ sin\phi\ cos\phi & 1 - 3\ sin^2\theta\ sin^2\phi & -3\ cos\theta\ sin\theta\ sin\phi \\ -3\ cos\theta\ sin\theta\ cos\phi & -3\ cos\theta\ sin\theta\ sin\phi & 1 - 3\ cos^2\theta \end{pmatrix}. \quad (4.45)$$

In magnetostatic physics, the monopole term is always absent, and the first two surviving terms are the dipole and quadrupole terms[9]. The quadrupole terms, described by its tensor (Eq. 4.45), contribute to anisotropy in the spin magnetic moment. They can be considered as the coupling parameter between the spin magnetic moment (generated from the isotropic spin of perfect spherical charge distributions) and the charge density distribution, resembling a dipole. The term that relates this spin and charge coupling is called the intra-atomic magnetic dipole operator T_α in the spin sum rules, and it can be expressed as part of the multipole expansion:

$$T_\alpha = \sum_\beta Q_{\alpha,\beta}\ S_\beta, \quad (4.46)$$

Thus, the coupling along the $z-$axis , considering the $z-$axis to be the quantization axis of the spin magnetic moment, under investigation :

$$T_z = Q_{zz}\ S_z = \ S_z(1 - 3\ cos^2\theta). \quad (4.47)$$

If the spin-orbit-coupling is significant then this term is important and it shows up in the sum rules for calculating spin magnetic moment but if the spin-orbit coupling is negligible (like in $3d$ metals) then the spin will follow the charge density. In other words, the spin charge coupling will dominate and take the lead. In that case, it can be eliminated by running three- orthogonal measurements since $< T_z > + < T_x > + < T_y > = 0$ and this stems from the properties of the quadrapole

[9]For a complete and rigorous derivation of the multipole expansion in magnetostatics, interested readers are referred to more specialized textbooks like "Classical Electrodynamics" by Jackson[277].

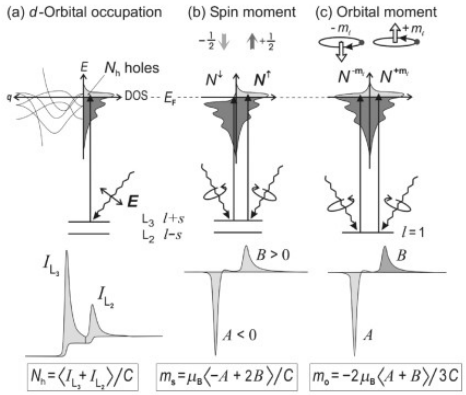

Figure 4.26: Schematic summarizes the three XMCD sum rules. (a) Charge sum rule: the polarization-averaged (or linear polarization) XAS probe the number of valence holes. (b), (c) Spin and Orbital moment sum rule: two circular polarized XAS yield different transitions leading to XMCD signals at $L_{3,2}$-edges, $\boldsymbol{A}$ and $\boldsymbol{B}$ respectively. The proportionality constant $\boldsymbol{C}$ in all the sum rules is nothing but the one written explicitly in Eq. 4.40.

tensor which is a traceless tensor, i.e. $Q_{xx} + Q_{yy} + Q_{zz} = 0$, as we can see above in Eq.4.45. The expectation value of this dipolar operator $< T_z >$ is the intra-atomic magnetic dipole moment[278]:

$$m_D^z = -\frac{7}{\hbar} < T_z > \mu_B, \tag{4.48}$$

which is the anistropy contribution to the spin magnetic moment. This leads to measure the effective spin magnetic moment for $4f$ ions using Eq. 4.43, which equals to $m_{spin}^{eff} = m_{spin} + 7 < T_z >$. This term becomes non-zero in anisotropic bonding environments and with the polarized X-ray photons generated in the synchrotrons one can probe the angular distribution of spins within the atomic volume, whereas conventional magnetometry only assesses the integrated number of spins. The spin sum rule for rare-earth ions deviates systematically from the actual value of the spin magnetic moment along the the $4f$ series, starting from 60% for Ce reaching up to 230% for Sm and drops to less than 10% for Gd and heavier rare-earth ions [279]. Fig. 4.26 summarizes the XMCD sum rules.

Chapter 5

Spin-excitations of mixed 3d-4f metallic centered molecules

Magnetism in low-dimensional structures exhibits distinct properties compared to their three-dimensional counterparts. This is evident in various magnetic parameters, such as Curie temperature [280, 281], magnetic anisotropy [282] and remnant magnetization [283], among others. The dimensional reduction leads to a decrease in coordination numbers and induces interfacial stress, which affects the density of states near the Fermi level. According to the Stoner-Wohlfarth criterion, an increase in the density of states near the Fermi energy may introduce ferromagnetic order, which might be absent in bulk materials [225]. Such avenue provide us with several playground to investigate magnetic adsorbates on magnetic surfaces.

One promising substrate for molecular spintronics is Fe/W(110), due to its thermodynamic stability and controlled pseudomorphic growth. This surface allows for both in-plane and out-of-plane magnetization orientations below 2 monolayers (ML), making it an ideal platform to study single metallic-centered molecules across different magnetic regions under identical experimental conditions using STM's high spatial and energy resolution.

The first section of this chapter focuses on the presentation of STS spectra, along with topographical and conductivity mapping STM images of the Fe(110)/W(110) surface. Meanwhile, the second section delves into SP-STS spectra and SP-STM topographical and conductivity mapping images of the metallic-centered $\mathbf{TbNi_2}$ deposited the on the first and second ML of Fe.

5.1 Fe/W(110) substrate

5.1.1 W(110) substrate

Tungsten is a metallic transition element that crystalizes in the body centered cubic (bcc) crystal configuration with lattice parameter of 3.165 **Å** [284]. Large Tungsten crystals are grown by melting and recrystallization using a seed crystal. Then,

the single crystals are oriented using Laue diffraction and cut in thin plates with the chosen surface. Finally polishing and annealing forms a flat surface with large terraces. This refractory material has a high durability with the highest melting point of all pure metals which is around 3700 K at atmospheric pressure [285]. Besides that, Tungsten crystals show low thermal expansion and low degassing rate in vacuum. Thus, it is a good substrate choice for surface experiments on metallic layers in UHV regime. In addition to that, single crystals of W is a non-magnetic material and this makes it suitable for studying magnetic layers like Fe [286–293].

Usually, Tungsten surface can grow thin oxide layers at ambient temperature and pressure [284], which can get removed by flashing the substrate to high temperature around 2000 K in UHV chambers. Dedicated studies on W surface using several complement techniques, like LEED equipped with residual gas analyzer [294, 295], showed the existence of carbon impurities at W crystal surface even after several prolonged flashing cycles. This is attributed to the diffusion of carbon atoms from the bulky interior regions towards the surface.

Consequently, another surface treatment was introduced by Bode to improve the quality of this surface by cyclic annealing of the surface at temperature of 1500 K for time duration of 30 mins with O_2 gas exposure [296]. The O_2 pressure gradually get reduced by 30% – 50% between the annealing cycles, starting from 10^{-6} mbar down to 10^{-8} mbar, subsequently the substrate got flashed off at high temeprature $\geqslant$ 2000 K to desorpe CO adsorpates and another residual molecules from the surface.

According to our best knowledge, that was the optimum method to prepare a clean W(110) surface as much as possible, yet a complete removal of impurities from the surface was not possible as our experiments and earlier experiments in literature have shown [286]. Thus, we adopted this cleaning procedure to clean the W(110) surface in this thesis.

Figure 5.1 shows a clean surface of W(110) substrate following the cleaning procedure mentioned above using STM. The image background is subtracted with relative to the lower plane in the figure. Thus, the lower part of the figure has darker color comparing to the upper part of the figure following the fire palette color code shown at the far-right corner of the figure.

The root-mean square (rms) roughness measured on the lower part of the figure is around 0.1 Å as shown in Fig. 5.1 (b-c). This rms roughness is comparable to the rms of the tunneling current recorded via point-measurment at this experiment[1]. Since the tip is still and fixed to one point, then the changes in the tunneling current are not attributed to any changes in the topography of the sample. Instead, it is attributed to the background noise affecting the tip itself and leads to some oscillations.

This rms value is different in each experiment and it can be added as an error source in each corresponding measurement. The step edge is in order of 2.0 $\pm$ 0.1 Å, as shown in the height profile (Fig.5.1 (d)) of the line across the step edge in Fig.

[1]In the point-measurement, the tip is fixed at some specific point in the image rather than being laterally rastered and the tunneling current is measured for long time.

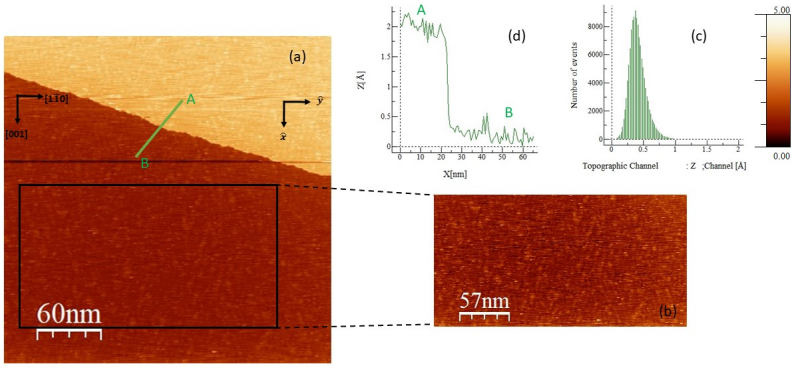

Figure 5.1: (a) Constant-current image of W(110) clean surface, of 300 x 300 $\mathbf{nm^2}$ size, recorded after several annealing cycles following the cleaning procedures mentioned in Ref.[296]. The crystallographic directions are depicted on the right-corner of the figure. The central abrupt line depression is attributed to tip change during the scanning. (b) The black rectangle region extracted from (a) of 285 x 171 $\mathbf{nm^2}$ size. (c) Histogram profile of region in Fig. (b) showing average height of 0.4 **Å** with roughness average of 0.1 **Å**. (d) Height profile of the green line in Fig.(a) showing the step edge of 2 **Å** which corresponds to the difference between (110) planes in W. The height color code between 0 – 5 **Å** is shown in the figure. STM image parameters: $I_T = 100\text{pA}, V_{Bias} = 1\,\text{V}$, 4.6 K. The image has been processed by WSXM software[297] .

5.1 (a) (green line segment $\overline{AB}$). This height is close to the inter-planar spacing distance of {110} planes in bcc crystal of Tungsten $\frac{a}{\sqrt{2}} = \frac{3.165}{\sqrt{2}} = 2.3\,\text{Å}$.

Figure 5.2(a) shows LEED pattern of diffracted electrons with energy of E = 96 eV from a clean W(110) surface at room temperature in 10^{-12} mbar pressure range. This pattern matches well with other LEED patterns in several references [294, 298] featuring a rectangle reciprocal unit cell.

The LEED pattern in Fig. 5.2(a) shows sharp spots with some blurry due to some small unexpected movements of the recording camera. Also, it is possible that some dirt got accumulated during running the LEED measurement yet no surface reconstruction or superstructures were observed. This ties well with the surface free energy calculations which hints to the unreconstructed surface of W(110) bcc crystal as the stable surface with minimum surface energy [299] .

A sketch of the LEED pattern is shown in Fig. 5.2(c) with fcc reciprocal lattice to the bcc real lattice of the W. The central spot in this pattern is the due to the incoming beam and it is the origin of the reciprocal space (0,0) and the corner spots are the the corner lattice points of the plane along [110] direction in fcc reciprocal lattice. Due to the inverse relationship between the reciprocal and real lattices, the real lattice spacings will have opposite lengths to the ones of the reciprocal lattice, as shown in Fig. 5.2(b). The crystallographic directions of the (110) plane according to the lab frame of reference can be seen in Fig. 5.2(b). Based on these observation

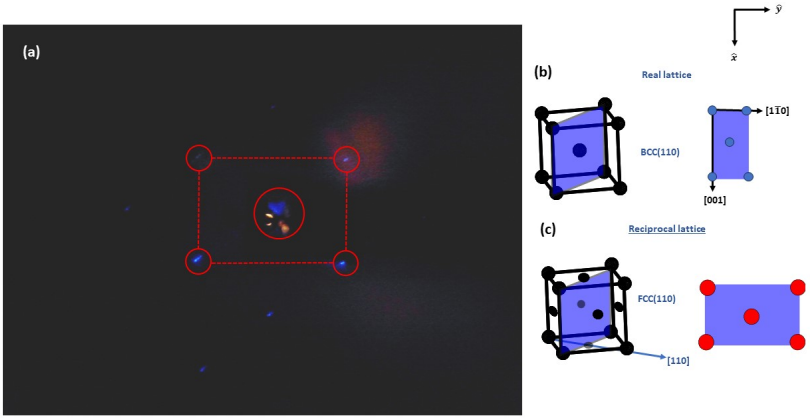

Figure 5.2: (a) LEED pattern of clean surface of W(110) substrate. The central spot is the reflection (0,0) of the incident electron beam. The other four spots are first unit cell of the reciprocal fcc lattice. (b) Sketch of real bcc lattice of W with (110) plane shown in blue. The crystallographic directions [1$\bar{1}$0] and [001] determine the width and the the height of the lattice, respectively. (c) Sketch of reciprocal fcc lattice and the lattice points along [110] direction which depicts the LEED pattern in (a).

we can conclude that this surface is clean and can be used for further depositions of Fe monolayers (MLs) and the targeted molecules.

5.1.2 1.5 ML Fe/W(110)

Iron monolayers on W(110) substrate has been studied thoroughly in the last years using several surface techniques, e.g.: LEED [286, 300, 301], Auger electron spectroscopy [301], conversion electron Mössbauer spectroscopy [302, 303], magneto-optical Kerr effect measurements [289–291], and scanning tunneling microscopy and spectroscopy [229, 287, 304–307]. This intensive investigation endeavors provide us with rich information about this surface including its growth mechanism, electronic and magnetic properties.

Growth mechanism

Iron has surface energy ($\gamma_{\mathrm{Fe}} = 2.9$ J/m^2) lower than the one of W(110) single crystal ($\gamma_{\mathrm{W}} = 3.5$ J/m^2) [308]. Thus, the iron monolayers on W(110) surface is thermodynamically stable [308, 309]. Both metals have similar crystal structure, i.e. bcc, with moderate lattice mismatch, $\frac{a_{\mathrm{W}} - a_{\mathrm{Fe}}}{a_{\mathrm{W}}} = 9.4\%$, where $a_{\mathrm{W}} = 3.165$Å and $a_{\mathrm{Fe}} = 2.866$Å. This mismatch creates some strain affecting the topography of the surface and the related magnetic and electronic properties as well. As a result, this leads to a pseudomorphic growth of the first monolayer of Fe following the lattice constant of the W(110) substrate and its 2D translational symmetry [286].

The first deposited Fe monolayer obeys Frank–van der Merwe mechanism of

layer growth (layer-by-layer growth) where the Fe atoms are more attracted to the W(110) substrate than being attracted to each others [301]. Thus, the second deposited monolayer start growing after the complete growth of the first layer [229, 304]. The temperature of annealing (either during or post deposition) affects the morphology of the grown Fe monolayers. At elevated substrate temperature (T > 570 K), the first monolayer start growing from the W(110) step-edges in a step-flow growth mode forming a long continuous stripes [287]. On contrast, depositing Fe at room temperature yields scattered nucleated islands with varying sizes which start to coalesce near $\theta \approx 0.6$ ML with dendritic tendencies till the ML cover the substrate completely [287]. For detailed information regarding the growth of Fe pseduomorphic monolayer ($0 < \theta < 1$) the reader is referred to the following reference [287].

The second layer starts growing preferably along the [001]-direction in two different ways following the orientation of the step edges [291–293]. If the step edges of the substrate are oriented along the [001] direction, then Fe coverage show smooth edges and adapt "nanowires" shapes along this direction in the vicinity of the step edges. On the other hand, if the step edges are along $[1\bar{1}0]$-direction then the Fe coverage start to grow non-uniformly in [001]-direction and can even have triangular islands shapes as shown in Ref. [293]. The adapted growth by the second layer is Stranski-Krastanov growth mode where some third layer contributions are observed for $\theta \geq 1.7$. The second ML grow pseudomorphically on the first ML following its lattice constant (which is the lattice constant of the W substrate) till it got relaxed by developing dislocations lines in the second layer along [001]-direction [288], as shown in Fig. 5.3.

Figure 5.3(a) shows a topography STM image of Fe coverage $1.3 \leq \theta \leq 1.5$ deposited at hot surface around 670 K and post annealed at the same temperature for 5 minutes. During the deposition process, the preparation chamber pressure was kept below 10^{-12} mbar, and the deposition rate was around 0.3 ML/min. The deposition was monitored by 10 MHz quartz crystal and calibrated by STM scanning measurement at the beginning of the very first experiment. The non-uniform growth of the Fe atoms in the vicinity of the W(110) step edges reflecting the step-flow growth mode of the Fe monolayers. The Fe monolayers has height of 2 Å which corresponds to the inter-planar distance of Fe(110), as shown in Fig. 5.3(d). The terrace width (w_0) of W(110), shown in Fig. 5.3(a), is of the order of 50 nm which corresponds to $w_0/\sqrt{2}\,a_w = 112$ atomic rows. The dislocation lines developed on the second monolayer has separations of around 10 nm, as it is shown on Fig. 5.3(c).

On the other hand, depositing Fe at room temperature lead to the formation of 3D nanoislands with elongation along [001] islands as reported in Ref. [288]. The nanoislands start to coalesce once the coverage is between $1.4 \leq \theta \leq 1.7$ [288]. Any coverage below this shows isolated nanoislands as shown in Fig. 5.4. Although, the sample shown in Fig. 5.4 is prepared on hot surface yet the low coverage, which is estimated $\theta \leq 1.25$ ML, prevents any coalescence between the 3D nanoislands with varying sizes ranging from 250 – 900 nm^2 as expected in Ref. [288].

During the course of the experiments, the heating filament has been changed

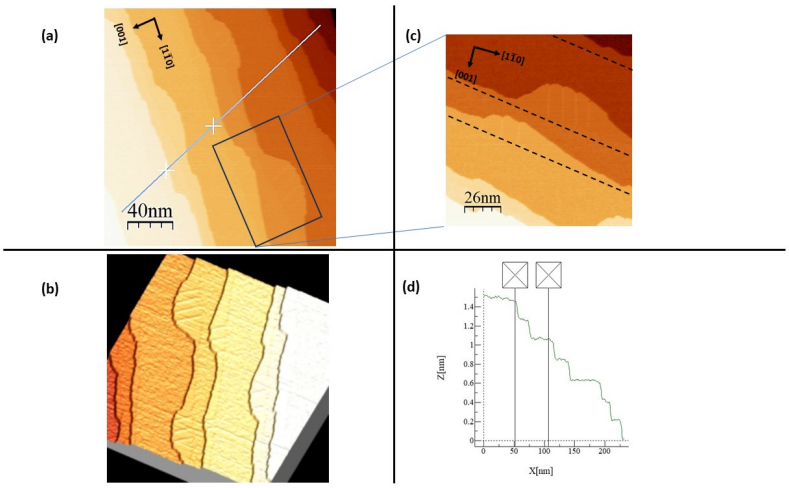

Figure 5.3: (a) STM topography image of Fe coverage estimated by $\theta \leq 1.5$ ML on W(110). The Fe stripes grow in vicinity of the W(110) step edges which propagate along $[1\bar{1}0]$-direction, and dislocation lines on the Fe double layer start to grow along [001]-direction. Image size: 200 × 200 nm^2, STM parameter: $V_{bias} = 1$ V, $I_{set} = 0.5$ nA (b) 3D perspective representation of the same region of (a) rotated counter-clock wise. (c) Zoomed-in region of figure (a) showing the non-uniform nanostripes and the dislocation lines clearly. The dashed lines are the W(110) step edges. Image size: 120 × 120 nm^2, STM parameter: $V_{bias} = 1$ V, $I_{set} = 0.1$ nA. (d) Profile height of the line drawing diagonally across the step edges in figure (a). It is clear the varying Fe coverages on each step-edge in which one can estimate the coverage $1.3 \leq \theta \leq 1.5$.

several times rendering the preparation of nanostripes not possible, thus we decided to deposit the molecules on the nanoislands and investigating them. All layers above the second layer following Stranski-Krastanov growth mode where they start growing before the previous layer is completed. Fe grows with its bulk lattice constant starting from the fourth layer. More detailed discussion about the layers above the second layer is beyond the scope of this work and can be found in Ref. [125, 310].

Electronic and magnetic properties

The Fe monolayers on W(110) at room temperature exhibit rich magnetic behavior following their coverage amounts. Investigations using SPLEED [287] showed that the Fe films are nonmagnetic for coverage $\theta \leq 0.58$. Meanwhile, there is a clear presence of remnant magnetization for a coverage of $0.58 \leq \theta \leq 1.2$ with a Curie temperature up to $T_c = 230$ K. Abruptly, this remnant magnetization vanishes for $1.2 \leq \theta \leq 1.48$ which is attributed to some magnetic frustration due to the quasi-antiferromagnetic frustrating interaction between the superparamagnetic

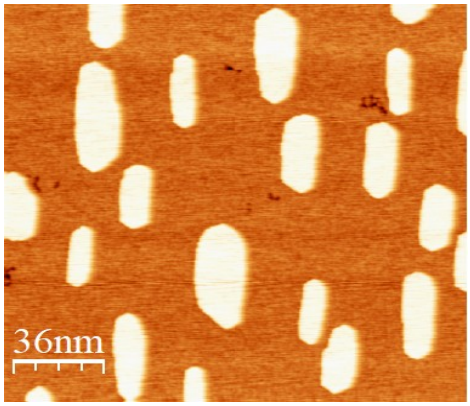

Figure 5.4: STM topography image of Fe coverage estimated by $\theta \leq 1.25$ ML on W(110). The Fe nano islands grow along [001]-direction. Image size: 150 × 150 nm^2, STM parameter: $V_{\text{bias}} = 1$ V, $I_{set} = 0.1$ nA.

double layer nanoislands [288, 311]. The remnant magnetization get resurrected once the coverage exceeds $\theta \geq 1.48$ but with higher cure temperature, around $T_c \geq 300$ K and it reaches 450 K in coverage $\theta = 2$ [288].

These results were obtained using spatially averaging methods which do not provide high spatial resolution. Wiesendanger et al. [230, 312, 313] reported the imaging of the real-space for different Fe coverages between $1.2 \leq \theta \leq 2.1$ using SP-STM. The DL shows a periodic out-of-plane magnetic domains structure, pointing up and down, separated by 180° in-plane domain walls in case of nanostripes [314] and single domains in case of non-coalesced island with opposite magnetization direction. Meanwhile, the magnetization direction in the first monolayer is along the [1$\bar{1}$0]-direction in the plane of the surface (in-plane) [287, 289]. Further research showed that this spin reorientation in the Fe double layer takes place due to the existence of some complicated features governed by Dzyaloshinskii–Moriya interaction (DMI) which favors a perpendicular orientation of spins as shown in Ref.[290, 291, 315].

The preparation of the Fe second layer has its own limitations which should be taken into consideration. The second layer shows a spin-reorientation towards the film plane when it is exposed to residual gas for a long time, which is 1 Langmuir or more [316]. In our case, this corresponds to around 4 hrs in the pressure of 8.5×10^{-11} mbar.

For non-magnetic STM tips, e.g.: W tips, ML and DL spectra exhibit characteristic peaks at U = +400 mV and U=+690 mV, respectively [312], which can be observed with magnetic tips as well.

Figure 5.5(a) shows a SP-STM topography image for Fe coverage of $1.3 \leq \theta$

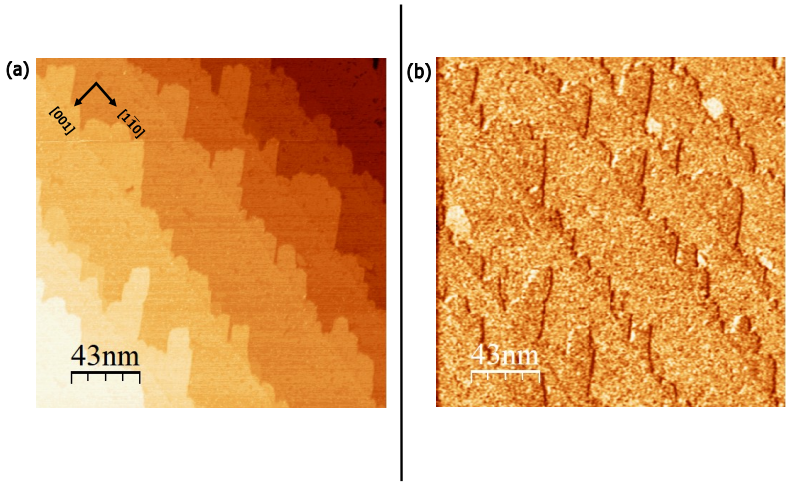

Figure 5.5: (a) Constant current STM image of Fe/W(110) with coverage of $1.3 \leq \theta \leq 1.5$, with parameters: I_{set} = 1.1 nA, U = 100 mV, and image size: 213 nm × 213 nm. (b) The simultaneous recorded dI/dU map of the same region of (a) at a bias voltage image of U = 100 mV.

$\leq$ 1.5 recorded using a spin-polarized tip made out of 30 ML Cr/W tip. The DL stripes have darker contrast than the ML due to the different electronic properties at U = 100 mV as shown in Fig. 5.6.

Figure 5.5(b) reveals the magnetic contrast in dI/dU mapping. The dislocation lines start to show up at coverage θ = 1.6 ML as deduced from previous systematic research [312] and this explains the absence of them in our experiment. The nanowire extended along the step-edge is formed due to a chain of coalesced islands. It shows only a definite out-of-plane magnetization orientation with the absence of alternating magnetization direction, which can be observed at a larger Fe coverage as in Ref. [230].

The constant height spectroscopy of the DL Fe regions, shown in Fig. 5.6, shows the typical surface states located at U= -90 ± 60 meV and 640 ± 60 meV which can be attributed to d_{z^2}-states as mentioned in Ref. [226, 229, 230, 317, 318]. The additional prominent peak at 250 ± 60 meV shown in Fig. 5.6 can be attributed to tip states. The spectrum has been normalized to the tunneling probability function as mentioned in Ref. [319, 320]. The fitting curves and parameters can be seen in the Appendix.

The DOS of the first layer Fe/W(110) around the Fermi level features a peak at 440 ± 60 meV, as indicated by the green line in Fig. 5.6. This value aligns well within the error range with the 400 meV reported in the literature [229]. Additionally, the same tip peak appears again but it is shifted to a lower energy of 120±60 meV, likely due to changes in the tip during the experiment. According to first-principles calculations [321], this peak originates from highly spin-polarized anti-bonding s, p_z, and d_{z^2} orbitals, which can exhibit nearly 100% spin polarization. These calculations indicate that this spin-polarized state primarily arises from

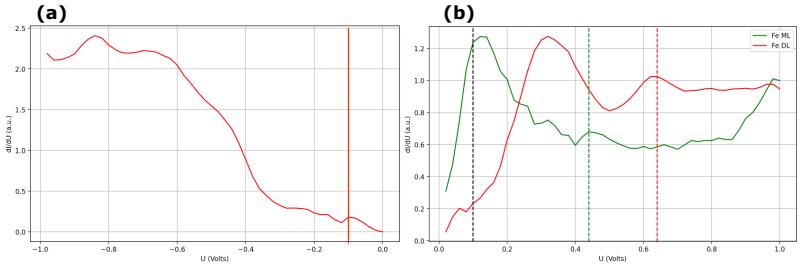

Figure 5.6: (a) dI/dU spectra of DL Fe/W(110) showing unoccupied surface states located at -90 mV (orange line). (b) dI/dU spectra of DL Fe/W(110) (red solid line) and dI/dU spectra of ML Fe/W(110) (green solid line). The occupied surface states of DL Fe are located at 620 mV (dashed red line), and those of the ML Fe are located at 440 mV (dashed green line). The dashed black line indicates the voltage bias at which the dI/dU mapping of Fig.5.5 performed.

majority-spin electrons. Meanwhile, the two Fe surface states at $V_{bias} = -90 \pm 60$ mV and 640 $\pm$ 60 mV are of minority spin character [318], which may explain the significant intensity difference observed in the corresponding peaks.

The observed narrow width of the Fe DL in our experiment, shown in Fig. 5.5, likely prevents the formation of multiple domain walls in that layer, contrasting with previous findings [313]. The critical width for misfit dislocation formation in Fe DLs is 9 nm [230], exceeding the DL width in our experiment. When this threshold is surpassed, nanowires can exhibit alternating magnetic domains with widths up to 100 nm. These domains typically adopt antiparallel alignment with adjacent domains to minimize magnetic stray fields, producing a "terrace-wise antiferromagnetism" pattern along the step edges of the W(110) substrate [230].

Interestingly, once these alternating domain walls form, they can be observed even without spin-polarized tips. The spin-orbit interaction (SOI) within this layer induces a mixing of the d_{xy+xz} and d_{z^2} states at the domain walls. This mixing results in localized changes to the DOS, which can be visualized using conventional dI/dU mapping at $V_{bias} = 50$ mV.

5.2 $TbNi_2$ adsorbed on 1.5 ML Fe

5.2.1 Topography

Fig. 5.7 (a) shows the constant current topography image of single scattered $TbNi_2$ molecules on the 1.5 ML Fe(110) surface. The molecules have a length of 18.56 Å± 2.19 Å and a height of 1.42 Å± 0.29 Å, as indicated by the histograms in Fig. 5.7 (b). The measured length of the molecules matches well the length of the molecule in the gas phase as determined by the Mercury software as shown in Fig. 5.8. This suggests that the molecules remain intact upon evaporation and deposition on the surface. Additionally, previous studies have shown that the Fe surface preserves the integrity of thermally evaporated molecules [125], so we expect the molecules to retain their bulk shape as in the gas phase.

The Fe islands grow along the [001] direction, as previously discussed. Concurrently, adsorbed molecules exhibit a preferential orientation on the first Fe monolayer, aligning along an axis approximately 45° relative to the [001] crystallographic axis, as depicted in Fig. 5.7(a). This preferential orientation can be further elucidated through first-principles DFT calculations of optimized molecule-surface geometries, similar to approaches used in prior studies with other molecules [84, 90, 237]. This well-defined adsorption position of these molecules after several scans suggests, tentatively, that the molecules are chemisorped on the surface, leading to the formation of bonds between them. This happens on contrary to some molecules adsorbed on other surfaces, e.g.: Au(111) , where the molecules can mobilize with the tip during scanning and get accumulated at the step edges [125]. On the other hand, the molecules on the double-layer Fe island are get accumulated on the edge of the Fe islands. Further DFT calculations are needed to provide us with insightful details about the adsoprtion optimized geometry of the molecule on the substrate.

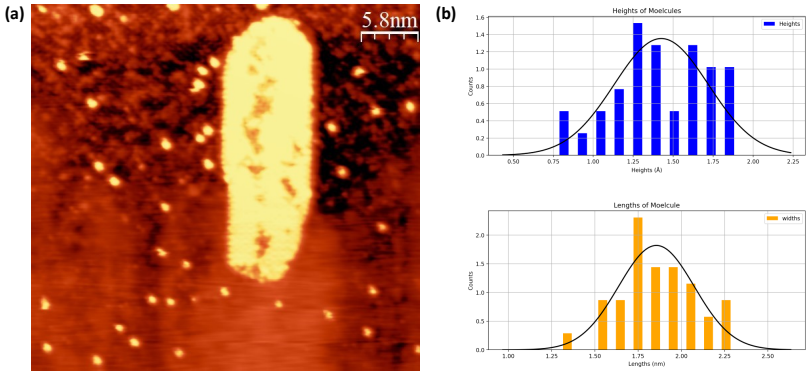

Figure 5.7: (a) Constant current spin-averaged STM topography image of $TbNi_2$ molecules deposited on 1.5 ML Fe DL island. The molecules on the first Fe ML has some preferential orientation. STM image parameters: $I_T = 100pA, V_{Bias} = 1\,V, T = 4.6\,K$. (b) Histogram plots of the heights (Top) and the lengths (Bottom) of the scattered molecules in image (a). The mean height of the molecules is 1.42 Å ± 0.29 Å and for lengths 18.56 Å ± 2.19. These values are obtained from the Gaussian distribution fitted to the heights and lengths values.

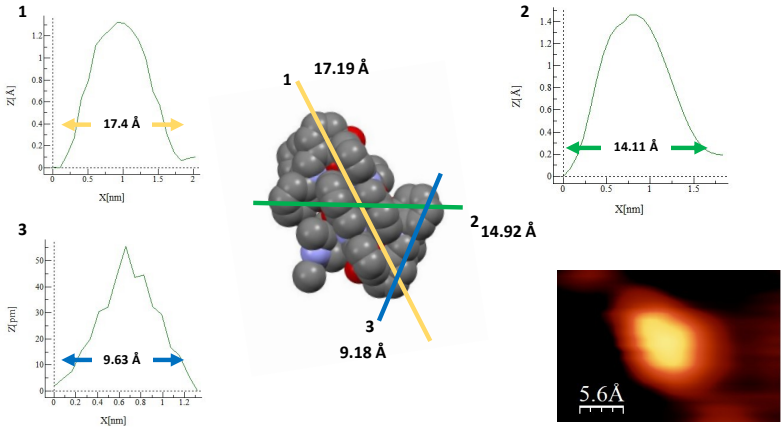

Figure 5.8: Central image: A 3D sketch of the molecule in the gas phase with color-coded directions for measurements. The surrounding color-coded line profiles were obtained from the STM image of the deposited molecule (bottom right corner) and correspond to the distances indicated by the same colors in the sketch.

5.2.2 Spectroscopy

Spin-averaged and spin-polarized STS measurements were conducted on $TbNi_2$ molecules deposited on first and second Fe monolayers. These spectroscopic measurements were performed at a low temperature of 4.7 K, within a narrow energy range around the Fermi level, $E_f \pm 150$ meV, where inelastic tunneling events can be observed using inelastic spin-flip spectroscopy.

The spin-polarized spectroscopy measurements were conducted with an out-of-plane magnetized Cr tip (approximately 30 ML thickness) [226]. After several pulses and measurements additional 10 ML were deposited on the tip to ensure the out-of-plane magnetization of the tip. Due to time constraints, each molecule was measured five times, and the results were averaged. Tunneling current was recorded using a Lock-in amplifier (Stanford Research Systems, Model SR830) with modulation parameters U_{mod}= 6 mV – the smallest achievable modulation voltage for this device – and f_{mod}= 616 Hz. The first derivative of the tunneling current signal, dI/dU , is acquired simultaneously with the Lock-an amplifier, meanwhile the second derivative d^2I/dU^2 is calculated numerically afterwards. To minimize noise from minor fluctuations in dI/dU affecting the second derivative, a simple moving average filter with a window size of 11 meV was applied to the first derivative spectrum before the numerical differentiation.

Fig. 5.9 presents line spectroscopy measurements taken across $TbNi_2$ molecule deposited on Fe DL island. The distinct S-shape of the I(V) curve becomes more pronounced as the measurement points approach the molecule's center, as illustrated by the differing curve shapes at point 1 in comparison to point 7 in Fig. 5.9(b). This can be attributed tentatively to an increase in the inelastic tunneling cross section, likely resulting from additional excitations occurring near the center of the molecule. Possible excitation types include vibronic excitations of the ligand, Coulomb blockades, or spin excitations of the metallic centers.

Identifying specific excitations among these options would require supplementary techniques and methods, such as IR spectroscopy and DFT calculations [159, 236, 238, 255]. However, the observed variation in spectral features for the same molecule in regions with differing magnetization orientations suggests magnetic spin excitation as a likely cause.

Fig. 5.10 reveals such variations of spin-averaged STS of $TbNi_2$ molecules where d^2I/dU^2 spectra of molecules deposited on Fe DL shows symmetric peaks around Fermi level which are missing in the molecules deposited on Fe ML.

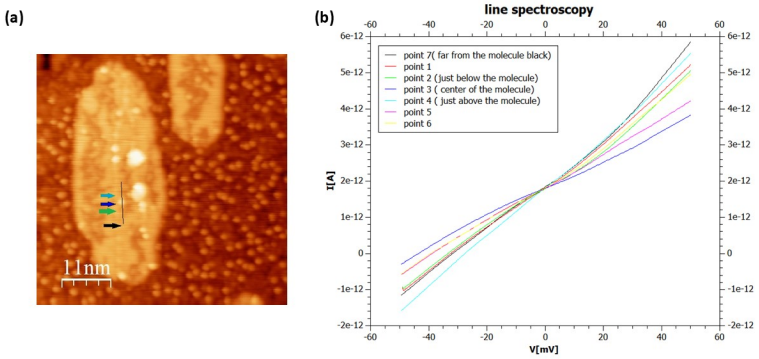

Figure 5.9: (a) Spin-averaged constant current STM topography image of $TbNi_2$ molecules deposited on a Fe island. Image dimensions: 56.8 nm × 56.8 nm. (b) Line spectroscopy across the $TbNi_2$ molecule shown in (a), with measurement points indicated by colored arrows corresponding to their respective spectra. The STM current has an offset of approximately 2 pA. STM image parameters: $U_{gap} = 1$ V, $I_{set} = 100$ pA.

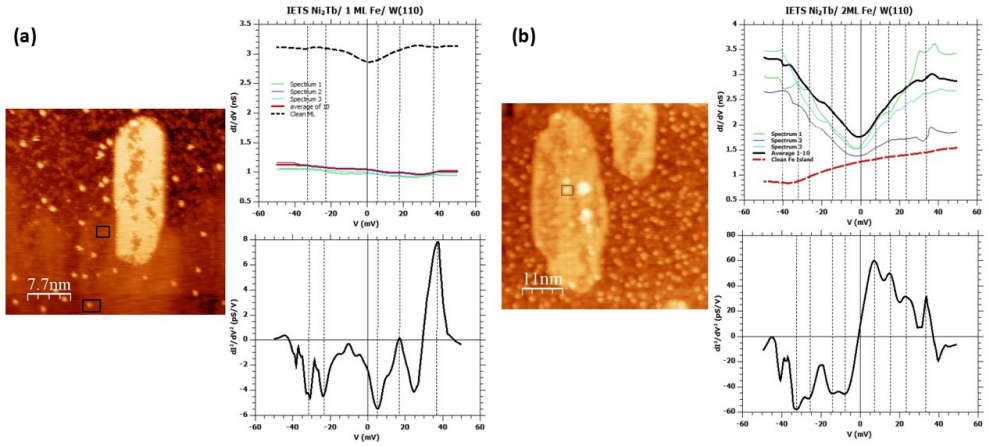

Figure 5.10: Spin-averaged IETS spectra of $TbNi_2$ molecules deposited on the first Fe ML (a) and Fe DL island (b). Each measurments were 10 times repeated yet here only 3 spectra are shown.

On the other hand, the differential conductance dI/dU on top of the molecules, measured with a with spin-polarized tip, features symmetric features, on both Fe ML and DL, around the Fermi energy which becomes more obvious as prominent peaks in the numerically second derivative spectrum d^2I/dU^2.

The deposited $TbNi_2$ molecules on the Fe ML reveal a single excitation at U = 14 meV and –11.5 meV, as shown in Fig. 5.11. Meanwhile, the d^2I/dU^2 spectrum of the deposited molecules on Fe DL shows an additional peak located at U = 48 meV and –45.5 meV besides the one of the molecules deposited on Fe ML, as shown in Fig. 5.12. The existence of other excitation peaks at higher energies can not be excluded, since lower modulation voltages might reveal additional features in dI/dU spectra with lower amplitudes, as shown in other works like in Ref. [159, 238]. Further discussion of the results will be introduced in the upcoming subsection.

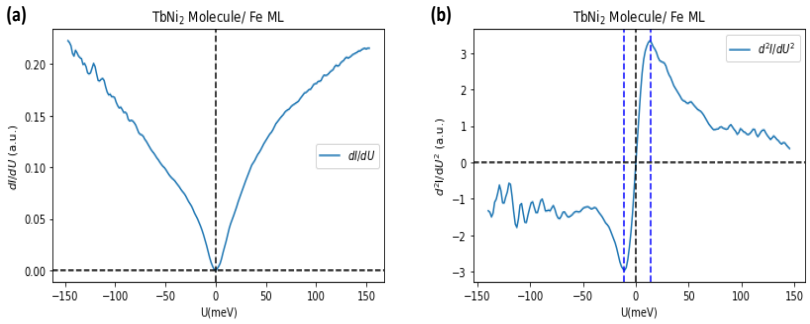

Figure 5.11: SP-IETS measurement of $TbNi_2$ molecule on Fe ML using ∼30 ML Cr tip. (a) Experimental dI/dU spectrum measured on the center of the $TbNi_2$ molecule. (b) d^2I/dU^2 spectrum derived numerically from the experimental spectrum. The spectrum shows a solely spin excitation at U = 14 ± 12 meV and –11.5± 12 meV. STS parameters: Temp. = 4.7 K, U_{mod}= 6 mV, f_{mod}= 616 Hz, I_{set} = 1 nA, U_{gap}= 200 mV.

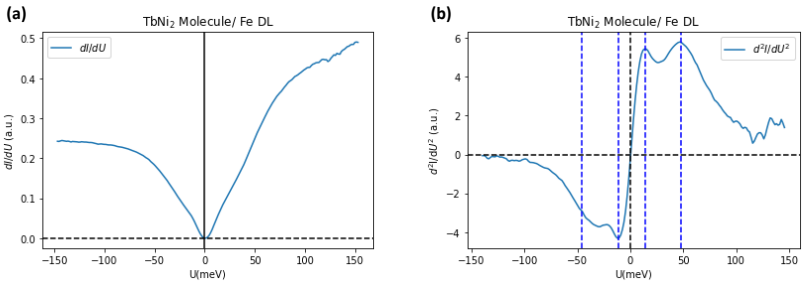

Figure 5.12: SP-IETS measurement of the $TbNi_2$ molecule on the Fe DL using ∼30 ML Cr tip. (a) Experimental dI/dU spectrum measured on the center of the $TbNi_2$ molecule. (b) d^2I/dU^2 spectrum derived numerically from the experimental spectrum. First spin excitation occurs at 14 ± 12 meV and – 11.5 ± 12 meV , meanwhile the second excitation at 48 ± 12 meV and –45.5 ± 12 meV . STS parameters: Temp. = 4.7 K, U_{mod}= 6 mV, f_{mod}= 616 Hz, I_{set} = 1 nA, U_{gap}= 200 mV.

5.2.3 Discussion

The first point in discussing the results is to identify the inelastic tunneling excitations whether they are spin excitations. The excitations in the dI/dU spectrum are detected when the energy of the tunneling electrons are large enough to excite some excitation energies in the adsorbate, as it has been elaborated previously in section 4.1.2.3.

The stretching vibrational modes of functional groups in molecules generally exhibit energies above 180 meV (1500 cm^{-1}), with C–H bond vibrational modes, in particular, commonly found in the range of 335 – 460 meV [222, 240, 322]. Metal-oxygen bonds, however, may show vibrational modes at lower energies, around 25 meV, as evidenced by the Mn–O bond measured through Raman spectroscopy in $Mn_{12}-$acetate [323]. Thus, we expect the Ni–O bond to vibrate at lower frequencies; since Ni atoms are heavier than Mn atoms. Consequently, we cannot completely exclude the excitations observed in our d^2I/dU^2 spectra below 50 meV as potential vibrational stretching excitations. Nonetheless, the observed differences in the d^2I/dU^2 spectra of the molecule on the DL and ML surfaces, as presented in Figures 5.11 and 5.12, call this interpretation into question.

Additionally, at lower energy levels, intramolecular vibrational excitations may become magnetic field-dependent due to possible vibrational and spin degree coupling, as seen in other magnetic molecules like $Mn_{12}-$acetate [324]. However, SQUID measurements for the $TbNi_2$ molecule do not show slow magnetization relaxation, leading us to tentatively discount vibrational excitation at these energies. Therefore, without far-infrared or Raman vibrational spectroscopy data and DFT calculations, it remains challenging to entirely rule out vibrational excitations of this nature [323–325].

Another excitation type to discuss is the Coulomb blockade energy. At low temperatures, the electrostatic energy in the tunneling junction, which is confined between the STM tip and the adsorbate, exceeds the thermal energy, k_BT. Thus, an electron must get a threshold energy once get transported through this confined region, which is equal to $E_C = \frac{e^2}{2C}$; where C is the capacitance of the tunneling junctions and e is the elementary charge of electron.

A rough estimate of the tip-sample distance in our tunneling junction can be derived from previous measurements conducted by Chen et al. using a W-tip [198] , which suggest a distance of approximately 0.4 nm for tunneling junction resistance R_T in the range of $100 - 200\,M\Omega$. By modeling the tip-sample tunneling junction as a parallel-plate capacitor, the capacitance can be determined using the formula $C = \epsilon_0 \frac{A}{d}$, where $\epsilon_0 = 8.85 \times 10^{-12}\,F/m$ represents the vacuum permittivity, A is the effective area of the tip approximated as a spherical cap with a radius "R" in nm , $A = \pi R^2$, and d is the tip-sample distance estimated by 0.4 nm. This calculation yields a tunneling junction capacitance of approximately $C \sim 0.7 \times 10^{-19}F$, corresponding to a Coulomb energy of around 1.14 eV , which significantly exceeds the energy range covered by our IETS measurements, and it ties well with values of Coulomb blockade energies of other metallic-centered molecules investigated by

IETS [238].

In studying 3d–4f metal-centered molecules with IETS, it is critical to first assess whether tunneling electrons can interact with the electrons of both $3d$ and $4f$ metallic centers. Such an investigation could help resolve ambiguities regarding the nature of the inelastic excitations observed in the conductivity spectra presented in Fig. 5.11 and Fig. 5.12 without delving into further calculations of the energy levels splitting in the $4f$ ion as introduced in Ref. [72, 326].

The ability to probe or excite electrons within the 4f orbitals is a topic of debate in the literature. Fahrendorf et al. demonstrated the ability to access the $4f$ orbitals of the Nd(III) ion in the metal-centered SMM $NdPc_2$ adsorbed on Cu(100) surface [125, 327]. This capability is attributed to the more extended nature of the $4f$ orbitals in Nd compared to the later Lanthanides such as Tb(III) or Dy(III), whose $4f$ orbitals are deeper in energy and more spatially localized around the nucleus, preventing them from participating in charge transport. In fact, this makes $4f$-states in early Lanthanides closer to the Fermi level than the ones in the later Lanthanides; allowing for potential hybridization with the ligand's molecular orbitals.

In contrast, Stoll et al. provided evidence that 4f orbitals are challenging to access [85]. They investigated two structurally and electronically similar molecules, $Dy(tta)_3$ and $Gd(tta)_3$, adsorbed on Au(111) surface using IETS measurements. Although both molecules exhibit similar adsorption configurations, $Dy(tta)_3$ demonstrates notable magnetic anisotropy due to ligand field distortion and the unquenched orbital magnetic moment of the Dy(III) central ion. This results in an energy separation of 9.5 ± 2.1 meV between the ground and first excited states. In contrast, $Gd(tta)_3$ shows negligible anisotropy owing to the Gd(III) ion's zero orbital magnetic moment, which arises from a quenched orbital magnetic moment and the absence of spin-orbit coupling. Thus, spin-related excitations are not expected in the $Gd(tta)_3$ molecule. However, both molecules exhibited inelastic excitations at the same energy, prompting the authors to dismiss the possibility of $4f$ orbital electron excitation and instead attribute the observation to some possible ligand vibrations. This conclusion was supported by the shielding effect of the $4f$ orbitals by the $5s$,$5p$, and $5d$ orbitals, which contribute to the molecule's coordination bonds. Consequently, the tunneling pathway is dominated by molecular states, precluding any significant exchange coupling with $4f$ electrons [85].

Further evidence comes from Steinbrecher et al., who definitively demonstrated the absence of exchange interactions between tunneling electrons and localized $4f$ orbitals [328]. Through multiple IETS measurements with varying microtips and modulation voltages, they studied single Ho ($4f$) and Fe ($3d$) atoms adsorbed on a Pt(111) surface at very low temperatures (approximately 0.3 K). Their results revealed inelastic excitations in the Fe spectra but no such signals in the Ho spectra. Additionally, distance-dependent IETS measurements between Fe and Ho atoms showed no change in the Fe spin excitations in the respective spectra. These findings led to the conclusion that 4f orbital electrons exhibit weak exchange interactions with their surroundings, making it difficult to access their magnetic moments through direct tunneling or indirect exchange pathways.

Based on these findings, it is reasonable to conclude that, in the studied molecule, the Tb(III) ion does not contribute directly to the tunneling pathway. Consequently, the observed inelastic excitations are unlikely to originate from spin excitations in the 4f center.

On the other hand, IETS of spin excitation from $3d$ atoms either adatoms [210, 242, 246, 329–331] or as a metallic center in adsorbed molecule [152, 158, 221, 238] is prevailed in the literature.

To gain qualitative insights into the magnetic exchange interactions within the investigated molecule, we consider its thermal behavior as reflected in the$\chi_{\mathrm{m}}\mathrm{T}$ vs T plot (Fig. 3.8 and the element-selective XMCD measurements (Fig. 3.9).

The $\chi_{\mathrm{m}}\mathrm{T}$ product exhibits a slight decrease below 50 K, stabilizing at approximately 13 $\mathrm{cm}^3.\mathrm{K.mol}^{-1}$. This behavior is tentatively attributed to antiferromagnetic interactions or, more likely, the thermal depopulation of the excited states of the Tb(III) ion within this temperature range [332]. Below 20 K, the $\chi_{\mathrm{m}}\mathrm{T}$ product rises again, reaching 17 $\mathrm{cm}^3.\mathrm{K.mol}^{-1}$, indicating a high-spin ground state and ferromagnetic interactions between the metallic centers (Ni – Tb – Ni). Furthermore, XMCD measurements reveal that the magnetic moments of the Ni ions are aligned parallel to those of the Tb(III) ions, as shown in Fig. 3.9. Therefore, one can weigh in the ferromagnetic exchange interaction as the prevailing intramolecular exchange interaction at low temperature.

Antiparallel alignment has been observed in rare-earth adatoms on Fe islands [333], extending a phenomenon previously reported in higher-dimensional 3d–4f alloy structures [334–337]. The model proposed to describe such kind of exchange interaction in alloys was introduced by Campbell, in which the $5d$ orbitals of the rare-earth atoms hybridize with the $3d$ orbitals of the transitions metal atoms resulting in antiparallel spin coupling. Meanwhile, the local spins of $4f$ and $5d$ in the rare-earth atoms are ferromagnetically exchange-coupled.

A similar qualitative mechanism for mixed 3d–4f metallic-centered molecules was proposed by Gatteschi and Kahn [338, 339]. They identified competing ferromagnetic (J_F) and antiferromagnetic J_{AF} exchange contributions to the net interaction between the transition metal (TM) and lanthanide (Ln) ions, as illustrated in Fig. 5.13. The J_F contribution arises from both the spin polarization of the 4f orbitals toward surrounding 5d, 6s, and 6p orbitals and charge transfer from the 3d orbitals of the TM ion to the vacant 5d orbitals of the Ln ion. Conversely, the J_{AF} contribution originates from overlap between the 3d orbitals of the TM ion and the 4f orbitals of the Ln ion. The dominant contribution determines the net **J** value and its sign [340–342].

Although the 4f orbitals are highly localized and do not participate directly in coordination bonding, a nonzero overlap probability exists between the more delocalized 3d orbitals and the localized 4f orbitals. $Ab-initio$ calculations, such as those in Ref. [341], are required to quantify the strength of J_{AF}. In most cases, J_F dominates because the 4f orbitals are spatially and energetically localized, leading to minimal overlap with the 3d orbitals. However, structural features such as the

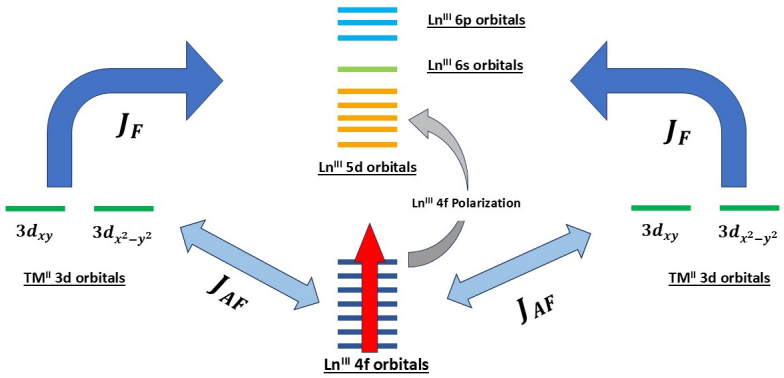

Figure 5.13: $3d-4f$ intramolecular exchange interaction mechanism as introduced by ref.[341]. The large magnetic moment of the Ln(III) $4f$ shielded orbitals polarize the $5d$ orbitlas of the Ln(III) ion. This in turn experiences a ferromagnetic exchange coupling with the delocalized $3d$ orbitals of the TM(II) ions via the charge transfer which determines the J_F contribution to the net exchange interaction. Meanwhile, the J_{AF} contribution originates from the overlapping strength between the delocalized $3d$ orbitals of the TM(II) ions and the localized $4f$ orbitals.

angle $\sphericalangle$ TM–O–Ln significantly influence the balance between J_F and J_{AF}. Larger angles favor J_F by promoting σ-type charge transfer, while acute angles suppress charge delocalization from 3d orbitals (e.g.: $3d_{x^2-y^2}$ orbital in Ni(II)) to vacant 5d orbitals in the Ln(III) ion, thereby reducing J_F and enhancing J_{AF}.

For the investigated molecule, the wide $\sphericalangle$ Ni–O–Tb angle and strong 4f spin polarization of the Tb(III) ion's 5d orbitals suggest that J_{AF} contributions are weak. This inference aligns with theoretical studies of similar 3d–4f systems, where J_{AF} contributions are typically smaller than the thermal energy at 4.7 K (approximately 0.4 meV) [340, 341, 343]. Consequently, it is reasonable to conclude that any spin excitation detected via IETS in this molecule originates from the 3d orbitals and their associated polarized bonds.

To comprehensively elucidate these excitations, further $ab-initio$ calculations are necessary, such as broken-symmetry DFT (BS-DFT), molecular orbital (MO) analyses, and natural bond orbital (NBO) calculations. These methods can help disentangle complex exchange interactions in mixed 3d–4f systems, including long-range dipolar interactions and short-range exchange couplings [340, 341, 344].

Chapter 6

Intramolecular Exchange Interaction of $3d-4f$ Metallacrowns

This chapter summarizes the XMCD results of element-specific magnetic properties of several $3d$-$4f$ metallacrowns obtained with the Bessy II synchrotron-based VEKMAG end station of the PM2 beamline [345]. The investigated molecules are $\mathbf{RENi_5}$ ($\mathbf{RE}$ = $\mathbf{Sm(III)}$, $\mathbf{Tb(III)}$, $\mathbf{Dy(III)}$) [169], $\mathbf{RENi_8}$ ($\mathbf{RE}$ = $\mathbf{Tb(III)}$,$\mathbf{Gd(III)}$) [165], and $\mathbf{REMn_4}$ ($\mathbf{RE}$ = $\mathbf{Tb(III)}$,$\mathbf{Dy(III)}$). Their chemical structure and magnetic properties have been discussed in chapter 3. X-ray absorption (XAS) and X-ray magnetic circular dichroism (XMCD) spectra for each molecule are shown in section 6.1, 6.2 and 6.3 accompanied with discussions and simulations based on charge transfer multiplet calculations.

Section 6.1 is dedicated to the results of $\mathbf{RENi_5}$ metallacrowns. In addition to that, a phenomenological model is used to determine the magnetic anisotropy energy barrier of the molecules from their orbital magnetic moments and their effective spin moments. This model will be used for the next sections, too.[118]

Besides that, section 6.2 reports a spin crossover in $\mathbf{RENi_8}$ metallacrowns deduced from XMCD-calculated spin magnetic moments of the $3d$ ions in the molecule. This spin crossover is attributed to re-coordination of $\mathbf{Ni(II)}$ ions when getting dissolved in methanol leading to a re-arranging of $3d$-states and creating a surrounding tetrahedral ligand field rather than the square planar ligand field of the isolated molecule. Simulated XAS and XMCD spectra based on charge-transfer multiplet calculations justify this claim.[346]

Finally, in section 6.3 we examine the magnetic anisotropy of rare-earth ions in a single crystal of $\mathbf{REMn_4}$ metallacrowns. XAS spectra, reported in this section, were acquired via fluorescence yield (FY) rather than the conventional total electron yield mode (TEY) used for the spectra in the previous two sections. A combination of FY signal correction and XAS simulation using the crystal-field multiplet calculations is necessary to calculate the spin and orbital magnetic moments correctly. Angular-dependent measurements showed a decrease of the magnetic moments at $\theta = 45°$ for $\mathbf{DyMn_4}$ indicating to a fourth-order anisotropy. A simple model based on electrostatic Coulomb interaction between the $4f$ anisotropic charge distribution

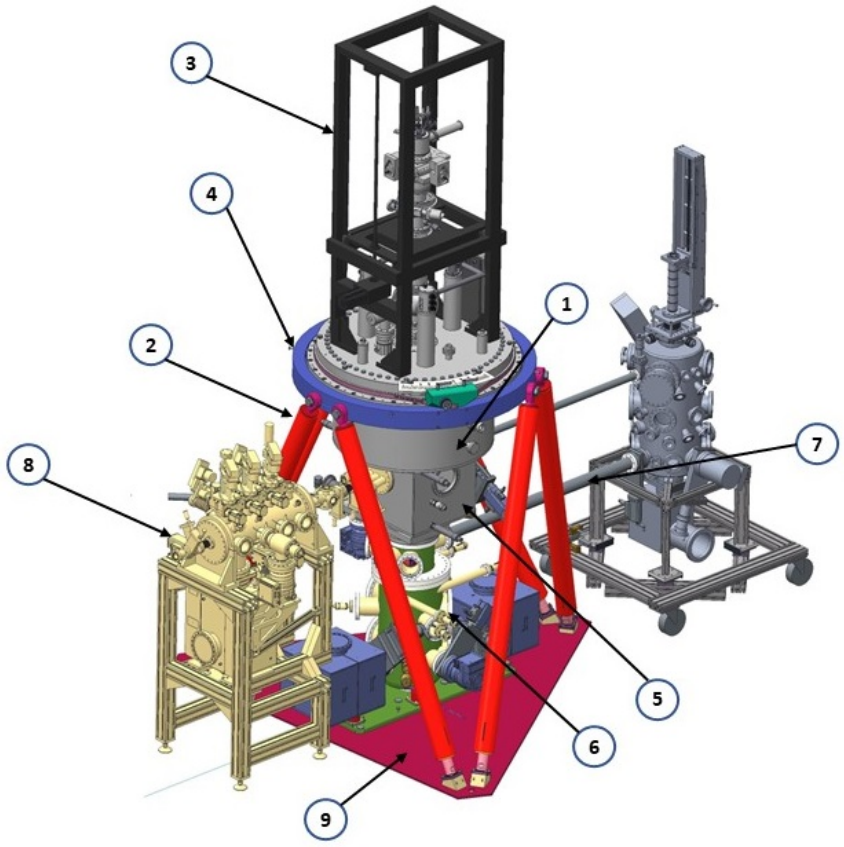

Figure 6.1: CAD schematic diagram of VEKMAG end-station at the synchrotron radiation source BESSY II of the Helmholtz-Zentrum Berlin. Additional details can be found in the corresponding reference [345]. 1- Vectormagnet chamber. 2- Hexapod frame of vector magnet chamber. 3- Sample z-manipulator. 4- Motorized rotation ball bearing. 5- Measurments chamber. 6- Sample exchange manipulator and chamber. 7- X-ray Beamline. 8- Preparation chamber. 9- Base Plate.

and the ligand field explains this anisotropy. [347]

6.1 Magnetic Anisotropy in Metallacrowns: Element-Specific Measurements

6.1.1 Experimental Procedure

This experiment has been performed at the synchrotron radiation source BESSY II of the Helmholtz-Zentrum Berlin at the VEKMAG end-station (Fig. 6.1) with the assistance of the beamline scientists F. Radu and C. Luo. The mechanical design of the end-station can be found in Ref. [345]. A brief explanation of the synchrotron facility has been given in section4.3.1 of this thesis.

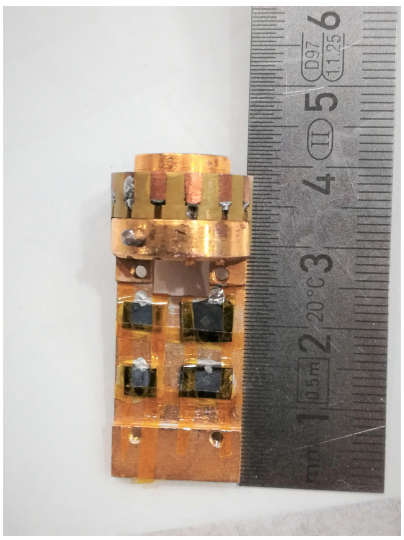

Figure 6.2: Pieces of a Si wafer mounted on a copper sample holder with a conducting silver paste to collect the generated photoelectrons. The tape stripes are used to fix the samples tightly on the sample holder. The ruler shows the size of the sample holder.

$\mathbf{RENi_5}$ molecules – $\mathbf{RE[15-MC_{Ni(II)N(picha)}-5(\mu^1-NO_3)(py)_8]}$, $\mathbf{RE=Sm(III)}$,$\mathbf{Tb(III)}$,$\mathbf{Dy(III)}$ – were synthesized by C. Gamer, A. Rauguth, L. Völker and A. Athanasopoulou in the group of Prof. Rentschler, in the chemistry department of Mainz University, based on the synthetic method described in Ref. [42]. The molecules have been dissolved in methanol and then using a pipet, a drop from the solution was deposited on a rinsed Si-wafer (drop-cast method). The methanol evaporates at ambient pressure after a couple of minutes and once it is inserted into the UHV chamber no liquid remains. The molecules remain on the surface forming small crystallites. Their direct contact to the conducting surface enables the emission of photo-excited electrons, which is the precondition for the total electron yield method. The Si-wafers are mounted on a sample holder with a conducting silver paste to enhance the drain current signal, see Fig.6.2. Electrospray ionization mass spectrometry performed in the group of Eva Rentschler confirms the chemical integrity of the molecules after getting dissolved in methanol. Besides that, atomic force microscopy and x-ray diffraction data performed in the group of Eva Rentschler as well, indicate a random orientation of the molecular crystallites after the drop cast procedure. [169].

Due to the non covalent bonding between the molecules and the Si-wafer, we expect that van der Waals interactions (vdW) are the dominating interactions, that bind the crystallites to the substrate surface. For two-dimensional layers separated by inter-layer separation (D) ranging from 2 – 15 nm, vdW interaction's inverse power law results in dependence on D ranging from D^{-4}– $D^{-3.5}$. For Si-bulk one finds a polarizability of 25 $bohr^3/atom$[1] resulting in forces on the order of pN [349,

[1]The polarizability parameter (usually denoted by α) reflects the tendency of matter to form induced dipole moments (μ_{ind}) upon exertion of E-field(E); $\alpha = \frac{\mu_{ind}}{E}$. Its SI units are $A^2.S^4.Kg^{-1}$[348].

350]. Such a weak interaction is still large enough to fix the molecular crystallites on the surface. On the other hand it is weak enough to result in physisorbed molecules which assures that no electronic re-configuration between the molecules and substrates takes place. Hence, we measure the properties of isolated pristine molecules. To prevent the accumulation of charges, caused by Auger electrons that left the sample surface, the Si surface has been contacted to the copper frame by silver paste.The diamagnetic behavior of the Si-wafer does not contribute to the magnetic measurements. Further details about physisorption of molecules can be found in Ref. [351–355].

The bending magnet beamline P2 provides a circular polarization of 77% at Fe L-edge and at the Gd M-edge. The experiment were performed at low temperature of around 7 K. A superconducting magnet located in a cryostat L-He tank provides an adjustable magnetic filed up to ± 7 Tesla in the direction of the incident X-ray beam, which is perpendicular to the sample holder (No.1, Fig. 6.1). The photon flux intensity of the X-ray beam is in the range of $\sim 5 \times 10^9$ photons/sec and has a beam size of $800\,\mu$m $\times$ $800\,\mu$m with 6 mrad and 10 mrad horizontal and vertical divergence, respectively. This photon flux is generated from nominal electron current of 300 mA with 1.7 GeV energy in the storage ring with a duration of light pulse of around 20 ps and separation time of nano seconds. After the beam leaves the insertion device from the storage ring, it travels through the beam line PM2 in UHV regime generated by several ion-getter pumps and other auxiliary pumps.

The beam line consists of four main UHV chamber which provide controllability of the radiation beam. These four chambers are: pre-monochromator chamber, monochromator chamber, focusing chamber, and refocusing chamber. The selection of the desired wavelength, which corresponds to the desired energy scan range, is done by the user at the end-station by virtue of two grating monochromators: the first one located in the "Pre-Monochromator chamber" which enables a rough filtration of the radiation beam, and the second one is a servo-motor-controlled grating located in the "Monochromator chamber" which provides a fine-tuning of the selected wavelength. Curved Mirrors in the focusing and re-focusing chamber bundle the diffracted beam and a slit located in the focal point of the mirror selects the desired wavelength. The slit width of the exit slit determines the energy resolution. Usually, the energy resolution is set to 100 meV. Fig.6.3 shows the PM2 line section between the insertion device outlet until the user end-station.

The sample holder is introduced into the load-lock chamber and it can be inserted into the measurement chamber using manipulators (No. 5, Fig.6.1). To find the samples' coordinates inside the measurement chamber, one moves the sample holder in-situ using the x- and y- motorized stage with a z-manipulator (No. 4 & No. 3, Fig.6.1, respectively).

Firstly, an energy scan along the range of the two edges ($M_{4,5}$-edges for 4f ions, $L_{2,3}$-edges for 3d ions) of one of the constituting element of the first sample is done along z-axis to look for the first sample on the holder. Once a TEY signal with good signal-to-noise ratio is recorded by the ammeter, one can use these coordinates for the sample. Based on the dimensions of the sample holder and the relative positions

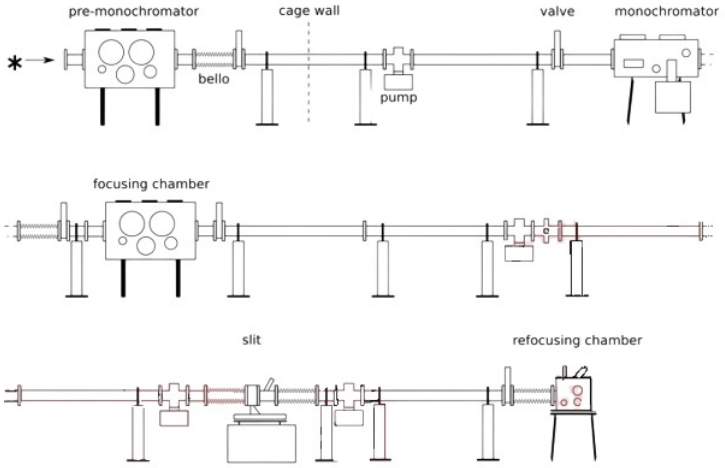

Figure 6.3: PM2 beamline section between the outlet of the storage ring until the VEKMAG end station (not shown here). The Pre-Monochromator chamber located behind the cage wall of the radiation-controlled zone, meanwhile, the other chambers located outside this zone. Image adopted from Ref. [356]

of the different samples on the sample holder, an educated guess for the relative coordinates of the other samples can be taken and move the stage accordingly. We run an energy scan with the corresponding energy range of the constituting elements of each sample separately. The coordinates with the highest signal-to-noise ratio will be used to acquire the data. In addition to that, a quick scan for the whole energy range of the two edges will be done again before commencing the experiment to double check the quality of the signal.

All XAS spectra in this section and the next section are obtained with normal incidence of x-ray photons at TEY acquiring mode, as shown in Fig.6.4. TEY is considered to be the most suitable detection method for XAS in the soft x-ray energy regime, due to the emission of many secondary electrons (Auger decay and the correspondingly easy method of detection). Those electrons can be measured as a drain current which is proportional to the absorption coefficient $\mu(\omega)$ of the sample[2]. The electron yield can thus be described according to: $I_{TEY} = C\mu L/cos\theta$, if the absorption depth is larger than the electron‘s escape depth(L) [357, 358].

To obtain the XAS spectra with parallel and anti-parallel orientation of external field and polarization direction, we switch the magnetic field or the polarization of the incident x-ray photons. The spectrum obtained at parallel magnetic field direction will be denoted, in this thesis, by I^+ and for anti-parallel magnetic field will be denoted by I^-.

We measure the pair of XAS spectra twice for each element in each sample to check the integrity of the molecules under x-ray beam incidence. During the course

[2]The term absorption coefficient ($\mu(\omega)$) is used loosely to indicate to the x-ray photoelectric absorption events in the sample. As a matter of fact, the incident x-ray has other several interactions with the matter but with less occurrence probability, e.g.: coherent (elastic) scattering and incoherent (inelastic) scattering. Thus, it is more accurate to use “ *linear attenuation coefficient* “ instead, and it is expressed by: $\mu = \rho\sigma$, where ρ is the density of the sample, and σ is cross section of all the events,$[\mu] = m^{-1}$.[270]

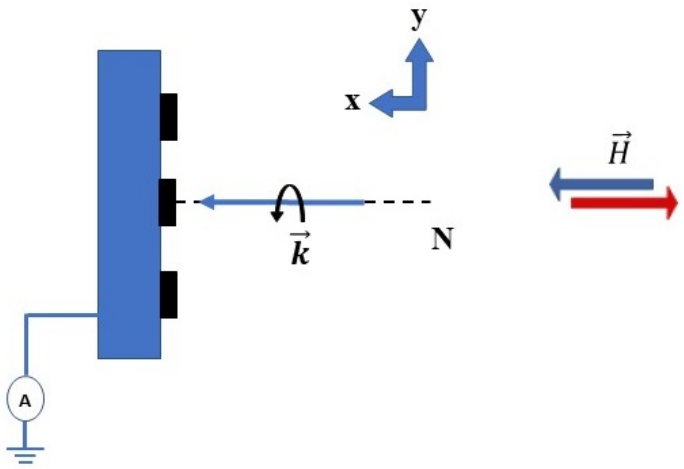

Figure 6.4: Top View: Sketch of sample holder holding Si-wafers pieces (black squares) as substrates of drop-cast molecules. The propagation of incident X-ray photons ($\overrightarrow{k}$) is parallel to the normal of the surface (N). The photons have left-circular polarization as shown from the helicity along the propagation direction. The upper right arrows shows the Lab-frame coordinates (x,y) where magnetic field direction ($\overrightarrow{H}$) is applied along ±x-directions. The generated photo-electrons are acquired as a drain current from the sample holder using an ammeter (TEY mode).

of the experiment we did not detect any change of the characteristic XAS of all the molecules which indicates that no damage of the molecules takes place. This observation agrees well with previously published results on molecules investigated by the same technique [88, 90, 103].

The incident x-ray intensity varies during the data acquisition due to the top-up operation of the storage ring. Therefore, the intensity of the x-ray beam in the beamline is monitored by Au-grid. Fig.6.5 shows the TEY drain current signal of the Au-grid. Since all the absorption edges of Au, see Table 6.1, do not lie in the soft x-ray energy range (<2000 eV), we can assume that the TEY signal of the Au grid in Fig.6.5 represents the incident X-ray intensity. The data shown in Fig.6.5 have been recorded from left to right with increasing photon energy. The step-like increases occurring in regular intervals correspond to the top-up events where additional electrons are injected into the synchrotron ring to replace the electron losses in the normal operation. The typical lifetime describing the exponential intensity decrease is 5 hours while the top-up event occur every minute. The gradual decrease of the intensity observed in Fig.6.5 is caused by the transmission function of the monochromator. All obtained XAS spectra in this thesis are normalized to this signal before running any further analysis.

Because two XAS spectra of opposite field directions, I^+ and I^-, are measured one after the other, surface contamination of the sample, deflection of electrons by the magnetic field, and small changes of the position during recording the data can

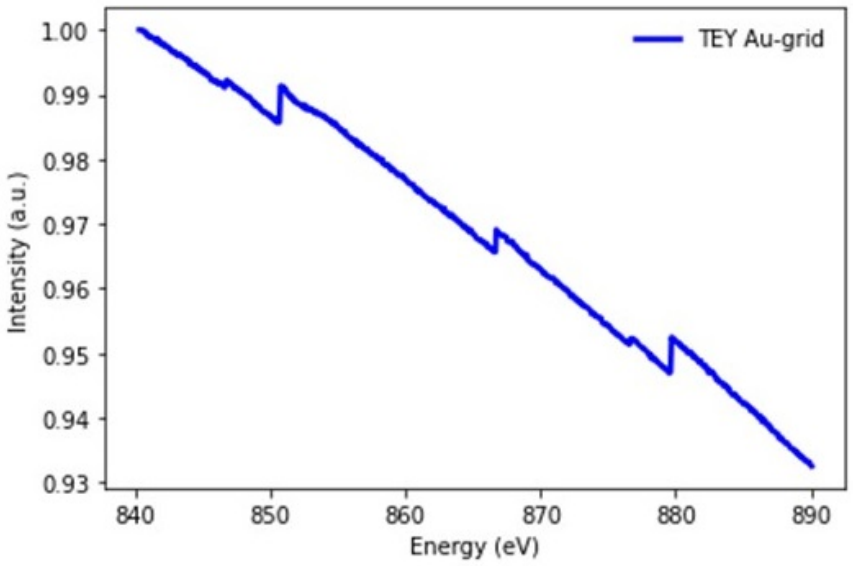

Figure 6.5: TEY drain current signal of the Au-grid monitoring the intensity of x-ray in the Beamline. This signal has been acquired in the energy range of $L_{2,3}$-edges of $Ni(II)$ ions. The signal is normalized to its maximum value just for the purpose of demonstration in the thesis, but not during the data analysis.

Edge	Energy (KeV)
K_1	80.722
L_1	14.352
L_2	13.732
L_3	11.918

Table 6.1: Au X-ray absorption Edges[359]

lead to differences in the recorded spectra where no changes are expected. Therefore, we fit the pre-edge and post-edge region of the spectra with a polynomial function. The polynomials are then used to normalize the spectra. This is justified because all the mentioned experimental artifacts are multiplicative. For practical reasons, the data evaluation process is as follows: we divide one spectra by the other one, $I_r = \frac{I^+}{I^-}$. Then we perform a linear fit, I_{r_0}, through the pre- and post-edge region. Finally, we multiply one of the spectra with I_{r_0} function yielding $I^{-'}=I^- \times I_{r_0}$. This guarantees that the pre- and post-edge regions on both I^+ and I^- spectra are equal. A background linear function was generated from the average of pre- and post-edges of both intensity spectra, I^+ and I^-, $I_{backgrd.} = \frac{I^+ + I^-}{2}$, and then subtracted from each spectrum. Finally, all spectra were normalized to the pre-edge values.

6.1.2 Results

A script of commands was used to apply the XMCD sum rules that allow to calculate the effective spin-magnetic moments, m_{spin}^{eff}, and orbital-magnetic moments, m_{orb}, of each element, respectively [274, 275].

XMCD sum rules for $3d$-ions are:

$$m_{orb} = -\frac{3n_h\mu_B}{P}\ \frac{\int_{L_{2,3}} \mu_{MCD}\ dE}{\int_{L_{2,3}} I_{iso} dE}, \tag{6.1}$$

$$m_{spin}^{eff} = -\frac{3n_h\mu_B}{P}\ \frac{\int_{L_3} \mu_{MCD}\ dE\ -\ 2\int_{L_2} \mu_{MCD}\ dE}{\int_{L_{2,3}} I_{iso} dE}, \tag{6.2}$$

and for trivalent $4f$-ions:

$$m_{orb} = -\frac{3n_h\mu_B}{P}\ \frac{\int_{M_{4,5}} \mu_{MCD}\ dE}{\int_{M_{4,5}} I_{iso} dE}, \tag{6.3}$$

$$m_{spin}^{eff} = \frac{3n_h\mu_B}{P}\ \frac{\int_{M_5} \mu_{MCD}\ dE\ -\ \frac{3}{2}\int_{M_4} \mu_{MCD}\ dE}{\int_{M_{4,5}} I_{iso} dE}, \tag{6.4}$$

where n_h, P and μ_B stand for the number of holes in the valence shells, the degree of polarization, which is around 0.77, and the Bohr magneton, respectively.

Element		Edge	Energy(eV)
$3d$	**Mn(II)**	L_3	637
		L_2	648
	Ni(II)	L_3	852
		L_2	870
$RE(III)$	**Sm(III)**	M_5	1076
		M_4	1100
	Dy(III)	M_5	1291
		M_4	1328
	Tb(III)	M_5	1238
		M_4	1272
	Gd(III)	M_5	1182
		M_4	1212

Table 6.2: Soft XAS energy edges of several $3d$ and $RE(III)$ elements used in this Thesis. L_3 and L_2 edges correspond to inter-atomic electronic transitions of $2p_{3/2} \rightarrow 3d_{5/2}$ and $2p_{\frac{1}{2}} \rightarrow 3d_{\frac{3}{2},\frac{1}{2}}$ orbitals, respectively. Meanwhile, M_5 and M_4 edges correspond to the transitions of $3d_{\frac{5}{2}} \rightarrow 4f_{\frac{7}{2},\frac{5}{2},\frac{3}{2}}$ and $3d_{\frac{3}{2}} \rightarrow 4f_{\frac{1}{2},\frac{3}{2},\frac{5}{2}}$ orbitals, respectively.

$\mu_{MCD} = I^+ - I^-$ is the XMCD signal which must be integrated at the energy edges of the corresponding electronic transitions. For $3d$-ions, L_2 and L_3 edges correspond to $2p_{\frac{1}{2},\frac{3}{2}} \rightarrow 3d_{\frac{1}{2},\frac{3}{2},\frac{5}{2}}$ electronic transitions, respectively. In the case of M_4 and M_5 edges in the trivalent $4f$-ions the electronic transition are $3d_{\frac{3}{2},\frac{5}{2}} \rightarrow 4f_{\frac{3}{2},\frac{5}{2},\frac{7}{2}}$, respectively. Table 6.2 lists some energies of the resonance absorption-edges of the elements relevant for this thesis.

The integral is normalized to the isotropic absorption signal, $I_{iso} = < I > = I^+ + I^- + I^0$, which is the average of all the dipole transitions intensities in the sample coming from all polarization components of x-ray beam for some certain propagation direction. It includes the absorption of circular polarized, I^+ and I^-, and linear polarized x-ray photons, I^0, which can be calculated according to: $I^0 = \frac{I^+ + I^-}{2}$. This is important to find the $angular-averaged$ intensity which is the related XAS intensity to the sum rules. Since the molecules on the Si wafer form random microcrystals, averaging over 3-polarization components along fixed directions will be sufficient to find the angular-averaged intensity [69].

We set the number of d-holes for **Ni(II)** to $n_h = 2$ according to the charge transfer multiplet calculations [276]. Due to the localization of 4f-orbitals, one can set the number of 4f-orbitals holes similar to the ones of the ionic values calculated according to Hund's Rules: **Dy(III)** = 5, **Tb(III)** = 6, and **Sm(III)** = 9. As a matter of fact Eq.6.1 and Eq.6.3, yield a direct result for the ground-state expectation value of the orbital angular momentum $< \boldsymbol{L_z} > = -m_{orb}/\mu_B$, whereas Eqs.6.2, and 6.4, include two intricate ground-state expectation values, namely $< \boldsymbol{S_z} >$ and $< \mathbf{T_z} >$, which stand for the expectation value of the spin magnetic moment, m_{spin} and the magnetic dipole operator, T_z. Thus, the effective spin magnetic moment for 3d-ions

is:

$$m_{spin}^{eff} \;=\; m_{spin} + 7 < \mathbf{T_z} >, \tag{6.5}$$

and for 4f-ions:

$$m_{spin}^{eff} \;=\; m_{spin} + 6 < \mathbf{T_z} > . \tag{6.6}$$

The expectation value of the magnetic dipole operator, $< \mathbf{T_z} > = \; T_z$, is not easy to calculate since it depends on the environment surrounding the magnetic atom in the $3d$-transition metals. Therefore, it is better to get environments where such T_z is negligible such as octahedral ligand fields O_h with negligible spin-orbit coupling as introduced in Ref.[274]. Crocombette et al. have calculated T_z for several ions in O_h ligand filed configuration at varying temperatures to scrutinize the above mentioned claim [360]. He found that at both low and room temperature T_z term is close to zero, even in the case of small spin-orbit coupling, like in **Ni**(**II**) ions with d^8- configuration , $T_z/S_z \;\approx\; 0.1\%$. So Eq.6.5, in the case of 3d ions, can be reduced to:

$$m_{spin}^{eff} \;=\; m_{spin}. \tag{6.7}$$

On the other hand for 4f ions, the T_z term contributions originates from the spin-orbit splitting of the 4f orbitals rather than the crystal field splitting, since the latter one is relatively smaller than the former one due to the localization of 4f-orbitals and not having bonding contributions. The large spin-orbit splitting leads to a large contribution from the $< T_z >$ term, which might even surpass the contributions of $< S_z >$ itself, and any kind of ignoring of this term leads to a large relative error in spin sum rules, which may reach around 30% [361]. So Eq.6.6 must be applied including the dipole operator. This is not the only obstacle in using the spin sum rule where several research papers discussed the validity of the spin sum rules itself and the necessity to include some correction factors due to the ideal assumptions in deriving the spin sum rule reported by Carra et al. [274]. Thus, one should correct for the spin magnetic moment calculated by the sum-rules by multiplying Eq. 6.4 with a correction factor. The correction factor for rare-earth trivalent ions are adopted from Ref.[279] as follows: it is 2.3 for **Sm**(**III**) and equlas to 1 for **Dy**(**III**) , **Tb**(**III**). Meanwhile, **Ni**(**II**) has a correction factor around $\sim$1 according to Ref.[276]. On the other hand, the orbital sum rules have been confirmed and accepted in the magnetism community theoretically [362] and experimentally [363] for $3d$-transition metals and for $4f$-rare earth ions [364]. Eqs.6.1 and 6.3 are used directly to calculate the orbital magnetic moments. More details have been already discussed in section 4.3.3.

The transitions from the $3d$- and $4f$-states in **RE**(**III**) are considered strong correlated systems, which means that the interaction between the electrons and the core-holes after the absorption process is important and can not be neglected. Thus, the one-electron approximation, where all the interactions are negligible, does not hold. Theoretical atomic multiplet calculations are required to calculate all possible electronic transitions between the initial $3d^{10}4f^n$ and final $3d^9 4f^{n+1}$ configurations that obey the dipole selection rules, $\Delta J \;=\; 0, \pm 1$ [365]. The calculated XAS spectra

of **RE**(**III**) ions for opposite circular polarization are compared with experimental spectra Ref.[366, 367].

6.1.2.1 XAS & XMCD of $SmNi_5$ Molecules

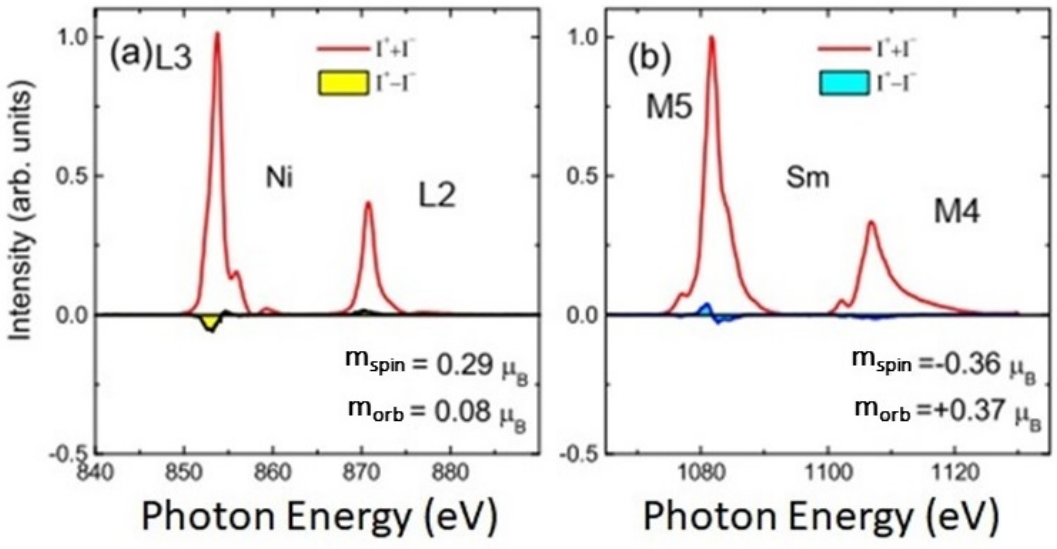

Figure 6.6: (a) Measured XAS (red) normalized to the maximum absorption and XMCD (yellow) spectra for **Ni**(**II**) $L_{3,2}$ edges. (b) Measured XAS (red) normalized to the maximum absorption and XMCD (blue) spectra for **Sm**(**III**) $M_{5,4}$ edges for $\mathbf{SmNi_5}$ 15-MC-5 metallacrowns.[118]

Figure 6.6 shows XAS and XMCD spectra for $\mathbf{SmNi_5}$ 15-MC-5 metallacrowns. For XAS spectra, the **Ni**(**II**) spectrum (Fig.6.6(a), red) has two distinct peaks due to spin-orbit splitting of core p shells, namely $2p_{\frac{3}{2}}$ (L_3 edge) and $2p_{\frac{1}{2}}$(L_2 edge). The spectrum has two small additional satellite peaks ∼4 eV and ∼6 eV higher than the energy of the absorption maximum of L_3 edge, which is 851 eV. The theoretical results indicate that these satellite peaks are due to the mixture of several configurations $3d^{10}, 3d^9$ and $3d^8$ with different weights in the ground state of **Ni**(**II**) ions [368]. The peak intensity changes with the crystal field acting on the $3d$ orbitals. This is observed in the figures of the three molecules, Fig.6.6 – Fig.6.8, where the intensity of this satellite peak slightly decreases with increasing atomic number of the **RE**(**III**) ion, indicating a change of the ligand field strength. Meanwhile, the L_2 edge at 870 eV shows a single peak with relatively constant height for different central **RE**(**III**) molecules. These features are characteristic for a **Ni**(**II**) ion within an octahedral ligand field as determined by the charge transfer multiplet calculations in Ref.[369].

The **Sm**(**III**) XAS spectrum (Fig.6.6(b), red) shows the typical ionic XAS spec-

trum indicating the absence of any mixed valence states or bonding with neighboring atoms due to the localization of 4f-orbitals [366, 367]. The larger absorption maximum peak at lower photon energy corresponds to the M_5 edge resulting from the inter-atomic transitions from $3d_{\frac{5}{2}}$, meanwhile the peak at higher photon energy, M_4 edge, indicates the transitions from $3d_{\frac{3}{2}}$ core states. The separation of these two peaks is correlated with the spin-orbit splitting of the $3d_{3/2} - 3d_{5/2}$ core states. Thus, one can see that this separation increases from around 23 eV in the **Sm**(**III**) in Fig.6.6 to around 34 eV for **Dy**(**III**) in Fig.6.8. The reason for the different peak heights at the two edges is the relative weight of the initial $3d_{\frac{5}{2}}$ and $3d_{\frac{3}{2}}$ which is around 3:2, yet the selection rules of $\Delta J = \pm 1$ lead to different peak ratios of each element, which is in good agreement with charge transfer multiplet calculations. Such calculations show that the peaks ratio for **Sm**(**III**) is around 0.44 which is a comparable to the one in the experimental spectrum [366].

By assuming the fact that at low temperatures only low-lying energy states will be populated, one can say that the ground state of **RE**(**III**) can be determined according to Hund's rules. Thus, the ground-state of initial configuration $3d^{10}4f^5$ of **Sm**(**III**), is ${}^6H_{\frac{5}{2}}$[3]. Meanwhile, the final configuration $3d^9 4f^6$ can have thousands of ground states following the multiplicity of the possible combinations of the terms of $3d^9$ (10 combinations) and $4f^6$ orbitals (3003 combinations). Of course, the selection rules will reduce these combinations, yet simple spectra will not be obtained and all the multiplet lines will be grouped in two groups around M_5 and M_4 edges. The M_4 edge in all the measured **RE**(**III**) ions [**RE**(**III**) = **Sm**(**III**), **Tb**(**III**), and **Dy**(**III**)] has a single peak with asymmetric shape followed by an extended tail at higher energies. At first glance, this can be attributed to some multiplet lines with low weight at these higher energies. Nevertheless, some argue that these transitions can be attributed to excitation from $3d$ or $5p$ core states to the continuum [371].

The XMCD **Ni**(**II**) spectrum (Fig.6.6(a), yellow) shows a negative maximum at the L_3 edge with a small positive peak at the L_2 edge. This will be discussed in detail in the upcoming section in terms of spin-splitting and branching ratio of the intensities $I(L_3)$ and $I(L_2)$ of the two spin-orbit split $2p$ absorption edges, since in complexes with significant ligand fields it is not clear whether Hund's rules apply. The spin magnetic moment of **Ni**(**II**) is expected to be close to the saturated value of 2 μ_B, yet the spin and orbital magnetic moments obtained via XMCD sum rules, Eq.6.1 and Eq.6.2, are far from this value. Similar smaller magnetization has been reported by others Ref.[372]. The charge transfer multiplet calculations reported in Ref.[372] discards the hypothesis of the hybridization between the **Ni**(**II**) ions and the neighboring Nitrogen atoms regarding the reduction of the spin magnetic moment in **Ni**(**II**) ions. Instead, the reduction is tentatively attributed to the surface anisotropy acting in the powder crystallites. In our case, where the sample is prepared using the drop-cast method one can exclude such an explanation. Due to the coordination of the **Ni**(**II**) ions with one another in the metallacrown, one can

[3]The ground-state term notation based on Russel-sander, LS, Coupling is written as ${}^{2S+1}L_J$, where $2S+1$ is the multiplicity, L is the total angular momentum which is written with the spectroscopic notation S,P,D,F,G,H,.. for numbers 0,1,2,3,4,5,.. , and J is the total angular momentum [370].

attribute this magnetization reduction to an antiferromagnetic exchange coupling between the **Ni**(**II**) ions in the molecule.

The **Sm**(**III**) XMCD spectrum (Fig.6.6(b), blue) shows a positive small peak at the M_5 edge indicating a negative spin magnetic moment, which in turn points to anti parallel alignment with the **Ni**(**II**) spin moments. The spin- and orbital-magnetic moments of **Sm**(**III**) calculated from the sum-rules have comparable values with opposite signs leading to a vanishing total magnetic moment, as expected from ionic values.

6.1.2.2 XAS & XMCD of $TbNi_5$ Molecules

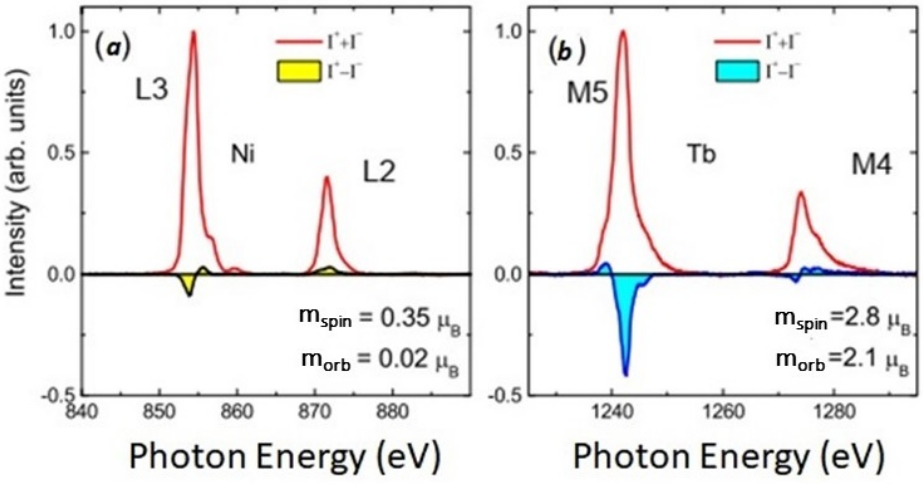

Figure 6.7: (a) Measured XAS (red) normalized to the maximum absorption and XMCD (yellow) spectra for **Ni(II)** $L_{3,2}$ edges. (b) Measured XAS (red) normalized to the maximum absorption and XMCD (blue) spectra for **Tb**(**III**) $M_{5,4}$ edges for $\mathbf{TbNi_5}$15-MC-5 metallacrowns. [118]

Figure 6.7 shows XAS and XMCD spectra for $\mathbf{TbNi_5}$ 15-MC-5 metallacrowns. The **Ni(II)** XAS spectrum has similar features as the previous $\mathbf{SmNi_5}$ spectrum. Yet, the satellite peak intensity at the L_3 edge is slightly decreased indicating a change of the ligand field strength. The **Tb(III)** XAS spectrum shows the typical characteristic ionic spectrum and is compared to the atomic multiplet calculations with a comparable peaks ratio, around 0.35 [366]. The spectra correspond to the multiplet transitions from the ground-state $^7F_6$ to the final states of electronic configuration $3d^9 4f^9$.

The **Ni(II)** XMCD spectrum is again similar to the one shown in Fig.6.6, yet the XMCD peak at L_2 edge is increased. The spin magnetic moment is increased

by 17% compared to the **Ni(II)** spin magnetic moment in **$SmNi_5$**, yet it is still far from the saturated value of 2 μ_B. The orbital magnetic moment is decreased by 75%. The **Tb**(**III**) XMCD Spectrum shows a negative peak at the M_5 edge resulting in a positive spin magnetic moment which indicates a parallel alignment with the **Ni(II)** spin moments. The **$TbNi_5$** molecule shows similar XAS and XMCD spectra to other SMM molecules containing **Tb**(**III**) ions [87, 140, 373].

The spin magnetic moment of **Tb(III)** calculated from the sum-rules has the value of 2.8 μ_B, which is smaller than the ionic value, 6.9 μ_B. Meanwhile, the orbital magnetic moment has the value of 2.1 μ_B, which is close to the the ionic value of 3.4μ_B. Such discrepancy will be discussed later in terms of magnetic anisotropy energy barrier in the discussion part of this section.

6.1.2.3 XAS & XMCD of $DyNi_5$ Molecules

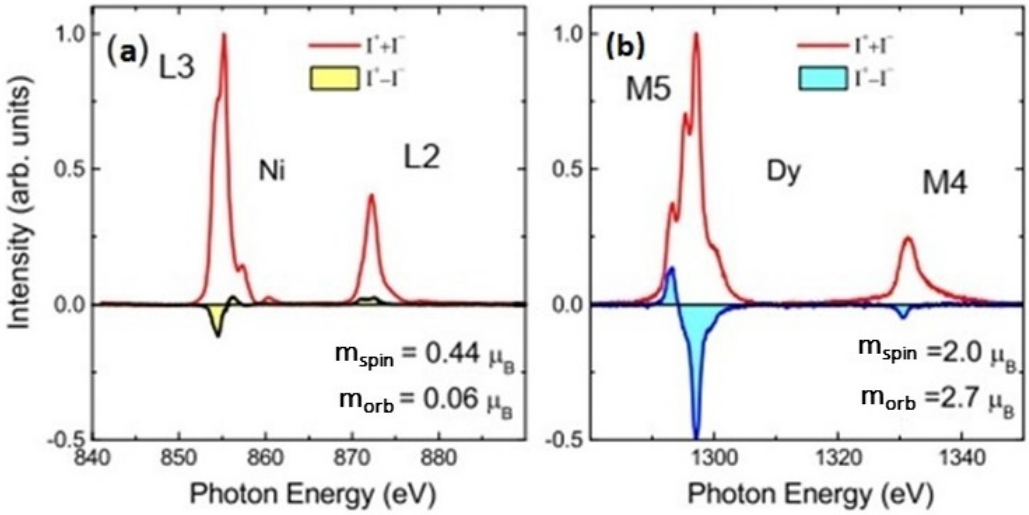

Figure 6.8: (a) Measured XAS (red) normalized to the maximum absorption and XMCD (yellow) spectra for **Ni(II)** $L_{3,2}$ edges. (b) Measured XAS (red) normalized to the maximum absorption and XMCD (blue) spectra for **Dy**(**III**) $M_{5,4}$ edges for **$DyNi_5$** 15-MC-5 metallacrowns. [118]

Figure 6.8 shows the XAS and XMCD spectra for **$DyNi_5$** 15-MC-5 metallacrowns. The **Ni(II)** XAS spectrum has similar features to the previous two molecule spectra. Besides that, the **Dy**(**III**) XAS spectrum shows also its typical ionic XAS spectrum due to the localization of 4f-orbitals [366]. The peak at M_5 edge is a linear combination of three peaks which corresponds to the electronic transitions from the ground state ${}^6H_{\frac{15}{2}}$ to the various final state energetic levels. Multiplet calculations show that the peaks within the M_5 edge stand for the transitions with $\Delta J = +1, 0, -1$, respectively [374].

The **Ni(II)** XMCD spectrum is not different from the previous one shown in Fig.6.7. Yet, the spin magnetic moment is increased by 25% of the**Ni(II)** spin magnetic moment but it is still far from the saturated value, $2\mu_B$, meanwhile the orbital magnetic moment is increased by a factor of three. The **Dy**(**III**) XMCD spectrum shows a negative peak at the M_5 edge yielding a positive spin magnetic moment which indicates to a parallel alignment with **Ni(II)** spin moments similar to the case of **Tb**(**III**) 15-MC-5. The spin magnetic moment of **Dy**(**III**) calculated from the sum-rules has the value of 2.0 μ_B, which is smaller than the ionic value, 5.9 μ_B. The orbital magnetic moment has the value of 2.7 μ_B, which is half of the the ionic value, 5.4 μ_B. This discrepancy will be discussed in terms of the magnetic anisotropy energy barrier in the discussion part of this section.

	Ni(II) [μ_B]		RE(III) [μ_B]										Molecular moments [μ_B]	
	m_{spin}^{eff}	m_{orb}	m_{spin}^{eff}	m_{orb}	m_{spin}^{*}	m_{orb}^{*}	m_{spin}^{Hund}	m_{orb}^{Hund}	S [$\hbar$]	L [$\hbar$]	J [$\hbar$]	g_J	T_z/S_z	μ_{mol}	μ_{SQUID}
$SmNi_5$	**0.29(2)**	**0.08(1)**	**-0.8(2)**	**0.8(2)**	**N.A.**	**N.A.**	**N.A.**	**N.A.**	**5/2**	**5**	**5/2**	**0.28**	**−0.231**	**N.A.**	**1.2**
$TbNi_5$	**0.35(2)**	**0.02(1)**	**2.8(2)**	**2.1(1)**	**6.2(6)**	**3.0**	**6.92**	**3.46**	**3**	**3**	**6**	**1.5**	**−0.111**	**8.4(6)**	**5.3**
$DyNi_5$	**0.44(3)**	**0.06(1)**	**2.0(2)**	**2.7(1)**	**6.0(6)**	**5.0**	**5.91**	**5.48**	**5/2**	**5**	**15/2**	**1.33**	**−0.133**	**8.2(6)**	**5.9**

Table 6.3: m_{spin}^{eff} and m_{orb} represent effective spin magnetic moment and orbital magnetic moment measured from XMCD sum-rules at 7 K for a field of 7 T, respectively. m_{spin}^{*} and m_{orb}^{*} represent the spin and orbital magnetic moment calculated from the model as mentioned in the text. $S[\hbar]$, $L[\hbar]$, $J[\hbar]$, g_J, and T_z/S_z stand for the different angular momenta , the Lande g-factor, and the ratio of dipole and spin operators for the ground state of RE(III) ions, respectively. The molecular moments μ_{mol} calculated from XMCD results are compared to the magnetization measured by SQUID magnetometry for the same temperature and magnetic filed for each molecule. $SmNi_5$ SQUID Data is not available. The statistical error of sum rules values given in the table is in most cases less than 10%. The total error is dominated by systematic errors of the common factors polarization, n_h, and the error due to subtraction of transitions into continuous states. We estimate the total error to be on the order of 20%.

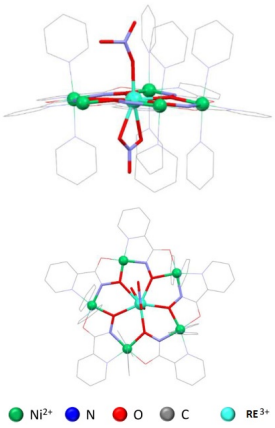

Figure 6.9: Molecular structure of $RE(III)[15-MC_{Ni(II)N(picha)}-5(\mu^1-NO_3)(py)_8]$ where molecule, where $\boldsymbol{RE = Sm(III), Tb(III), Dy(III)}$. The colors code of the Elements is shown in the figure. The depicted molecular structure has been created using Mercury Software [376].

6.1.3 Discussion

For 3d-ions, the magnetism originates from the 3d-orbitals [278]. In contrast to the delocalized spin-polarized electronic states in metals comprising Ni, which are described by the Stoner model [225], the Ni 3d-states in molecules are localized. The size of the local magnetic moments derived from these localized states can be deduced from crystal field theory (CFT). CFT provides a framework to describe the magnetism in transition-metal coordinated complexes based on coulomb repulsion between the transition-metal 3d-orbitals and the surrounding ligands [375]. Four out of five **Ni(II)** ions, in the investigated $\mathbf{RENi_5}$ molecules experience an octahedral ligand fields due to their sixfold coordination and the fifth one has a square planar ligand field due to the fourfold coordination as shown in Fig. 6.9.

According to CFT, **Ni(II)** in octahedral ligand field has a high-spin configuration with the spin ground state S = 1. In contrast, the square planar ligand field endows **Ni(II)** ions with a low-spin ground state of S = 0. This is a result of the minimization of the repulsive energy of the d-orbitals with surrounding ligands as discussed briefly in section 2.1.1. Fig. 6.10 summarizes the spin states configurations of both geometries.

XAS provides us with an experimental evidence of the spin ground state of the transition metal ions in complexes with ligand fields. The question whether they have a high-spin or low-spin can be deduced from the branching ratio $I(L_3)/[I(L_2)+I(L_3)]$, i.e.: the fraction of the total transition probability which goes into the $2p_{3/2}$ manifold [377]. This happens because the XAS is governed by dipole transitions where the spin is conserved, $\Delta S = 0$. Thus, the branching ratio will depend on the spin distribution over the core-hole manifolds. High-spin states complexes have holes with determined parallel spins in the e_g orbital group, as shown in Fig. 6.10. This will lead to a preferential excitation of the core electrons. Due to the spin-orbit splitting of the core electrons, electrons occupying the $2p_{3/2}$ orbital has parallel spin and

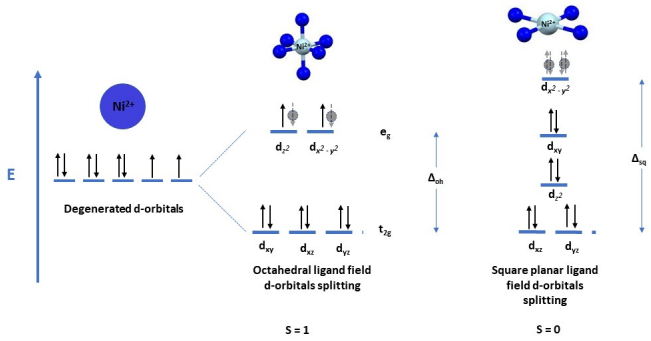

Figure 6.10: The 3d-orbitals splitting of **Ni(II)** ions in d^8configuration (light blue) in several ligand field geometries approximated by point charges (dark blue). The spherical ideal ligand-field geometry does not lift the degeneracy of the 3d-orbitals and shifts their energy up relative to the free ion (left). In octahedral (middle) and square planar (right) ligand fields, the electrostatic interaction lifts the degeneracy of the 3d-orbitals according to the shape and the angular distribution of d-orbitals along the principal axes with an energy difference between excited and ground state of ΔO_h (or $10D_q$) and Δ_{sq}, respectively. In O_h ligand field, the holes of e_g orbitals (gray circles) are spin-polarized which affects the branching ratio of XAS spectra. In contrast, for square ligand fields there is no preferential spin excitation into the excited states.

orbital angular momenta ($j = L + S$) whereas the $2p_{\frac{1}{2}}$ orbital has anti-parallel spin and orbital angular momenta ($j = L - S$). Thus, the final states spin in the valence 3d-orbitals and the spin-flip forbidden dipole transition selection rule, $\Delta S = 0$, will prefer exciting electrons from one core spin-split state more than the other. Based on that, the high spin complexes will have, on average, a larger branching ratio than the low-spin ground state, where low-spin ground state complexes lack holes with the corresponding spin. Branching ratios obtained for **Ni(II)** have a value of 0.72, which indicates a high-spin ground state as calculated in Ref.[377]. The high-spin state also agrees with the fact that five- and sixfold coordinate Ni(II) typically shows a high spin configuration. In the present case, one of the **Ni(II)** ions is fourfold coordinated and could indeed be in the low spin state. Thus the spin state for four out of five **Ni(II)** ions is expected to be S = 1 and the corresponding spin moment should be close to the saturated value of 2 μ_B. Instead, the observed spin moment is considerably smaller. This fact indicates an antiferromagnetic exchange coupling between the **Ni(II)** spin moments.

On the other hand, one expects the spin and orbital magnetic moments values of **RE(III)** ions in the molecules to be close to the values calculated by Hund's Rules, due to the localization of 4f orbitals in **RE(III)** ions. Yet, spin (m_{spin}^{eff}) and orbital magnetic moments (m_{orb}) shows some deviations of the ones calculated by Hund's rules, as shown in Table 6.3. The localization of 4f-orbitals lead to the assumption of the large spin-orbit coupling comparing to the negligible crystal field. According to Hund's rules, One can determine the total magnetic moment in case of non-quenching orbital magnetic moment for the ground-state from the following formula:

$$m_J^{Hund} \;=\; g_J \mu_B \sqrt{J(J+1)}, \tag{6.8}$$

where : J is the total angular momentum of the ion and it can be written as $J \;=\; \mid L \pm S \mid$ depending on the half-shell occupancy of the valence shells of the ions. L and S stands for the total orbital and spin angular momenta of the valence shells, respectively. g_J is the Lande g-factor [370], which is expressed by:

$$g_J \;=\; \frac{3}{2} \;+\; \frac{S(S+1) - L(L+1)}{2J(J+1)}. \tag{6.9}$$

The spin and orbital magnetic moments can be calculated using the following equations [370]:

$$m_S^{Hund} \;=\; 2\ \mu_B \sqrt{S(S+1)}, \tag{6.10}$$

and

$$m_L^{Hund} \;=\; \mu_B \sqrt{L(L+1)}. \tag{6.11}$$

By comparing the experimentally determined spin- and orbital-magnetic moments with the ones calculated by Hund's rules, we see that the experimental values are smaller. Since our experiment was carried out at low temperature, around 7

K, we expect that the thermal energy has a smaller value ($K_BT \approx 0.6\ meV$) comparable to the Zeeman energy (several $meVs$ in the range of 7 $Tesla$). Therefore, one does not expect a strong temperature dependence, especially at lower magnetic fields.

SQUID magnetometry measurements carried out by our collaborators confirmed this claim. Fig. 6.11 shows the isothermal molecular magnetic moment $\mu_{SQUID}(H,T)$ as a function of external magnetic field for varying temperatures in the range of 3 K to 10 K. Figure 6.11(a) displays a temperature-independent paramagnetic behavior of **$SmNi_5$** molecule. Meanwhile, Figure 6.11(b) and (c) reveal a linear increasing magnetic moment for small fields with a slope strongly dependent on temperature for **$TbNi_5$** and **$DyNi_5$** molecules, respectively, but for larger fields $\mu_{SQUID}(H,T)$ becomes temperature independent. The molecular magnetization does not saturate with increasing the magnetic field, and this is another indicator to the existence of a magnetic anisotropy energy barrier that hinders a saturation of the magnetization in **$TbNi_5$** and **$DyNi_5$** molecules. The source of this magnetic anisotropy can be thought of as a combination of spin-orbit coupling in **RE(III)** central ion and the electrostatic potential of crystal field which will be added as a perturbation due to the localization of the $f-orbitals$. The multiplicity of the total angular momentum of the ground state, $2J+1$, has a large value of **Dy(III)** (**Tb(III)**) which is around 16 (13), and this lead to a zero-field splitting (ZFS) of the ground state ${}^6H_{15/2}$ (${}^7F_6$). This phenomena is know as single-ion magnet (SIM) rather than the widely spread used one of single-molecule magnet (SMM), where one obtains the magnetic behavior from the exchange interaction of the spin ground-state of the different metallic ions in poly-nuclear complexes [71]. $\mu_{SQUID}(H,T)$ can been fitted using the SIMPRE software[108] by the crystal-field Hamiltonian:

$$H_{CF}(J) = \sum_{k=2,4,6} \sum_{q=-k}^{k} B_k^q O_k^q, \tag{6.12}$$

where H_{CF} is the crystal-field Hamiltonian which can be modeled in terms of corrected electrostatic point charges and can be written in terms of what is called extended Stevens operator O_k^q, as defined by Ryabov in terms of the angular momentum operators $J_\pm$ and J_z, and k is the operator order (also called rank or degree) and q is the operator range that varies between k and $-k$ [378]. For another Dy(III)-centered metallacrown molecule, namely **$DyGa_8$**, synthesized by Angeliki Athanasopoulou, in AK Rentschler in Uni Mainz, the fitting of $\mu_{SQUID}(H,T)$ with Eq.6.12 results in a very good agreement with small relative error of 1.2×10^{-4}. Moreover, the magnetization measurements at the magnetic field of 7 Tesla is comparable to the magnetization measurements obtained in **$DyNi_5$** molecule which is around 5.92 μ_B regardless of the different surrounding ligands. Thus one might think that in our case the exchange interaction among the **Ni(II)** moments is not significant and does not contribute to the magnetization or the magnetic anisotropy to the molecule in total. But if we take a look on Fig. 6.11(a) one can find that the measured magnetic moment of the whole **$SmNi_5$** molecule is close to the summation of the five XMCD **Ni(II)** magnetic moments, which adds up to the fact that the total XMCD magnetic moment of **Sm(III)** is close to zero, to conclude that in **$SmNi_5$** molecule

the main magnetic contribution is coming from the transition metal ions **Ni(II)**, which increases linearly with the applied magnetic field. This linear increase, instead of a Brillouin function for paramagnetic behavior, might be explained by an antiferromagnetic coupling between neighboring **Ni(II)** spins. This result suggests that **Ni(II)** ions must be included in any fitting to the SQUID measurements to calculate the magnetic anisotropy energy in these molecules where Fig. 6.11(b) and (c) shows that there is a good agreement between the spin exchange Hamiltonian and the measured data of $\mathbf{TbNi_5}$ and $\mathbf{DyNi_5}$ molecules. Besides that, the change of **Ni(II)** XMCD spin- and orbital-magnetic moments in each case of $\mathbf{RENi_5}$ as shown in Table 6.3 might indicate a kind of weak $3d-4f$ exchange interaction which should be considered. Therefore it is not possible to deduce the anisotropy parameter from the magnetometry data alone and one need an element-specific approach.

In such mixed $3d-4f$ molecules one expects a strong magnetic anisotropy that forces the orbital magnetic moment along the molecular symmetry axis depending on the strength of the uni-axial anisotropy energy. Due to LS coupling in rare-earth ions, the spin and orbital moments will be aligned parallel to each other. The orientation of the total magnetic moment, at some constant temperature and applied magnetic field, will be determined once the enthalpy of the molecule is minimized. The enthaply energy of the molecule results from the summation of two terms: the first one is the Zeeman energy applied by the magnetic field on the magnetic moment to rotate it, and the second term is the magnetic anisotropy energy which keep the magnetic moment pointing along some certain preferable direction:

$$G \;=\; -m^*_{RE} B\; cos\vartheta \;+\; K_{RE}\; cos^2(\theta-\vartheta), \tag{6.13}$$

where K_{RE} is the anisotropy energy constant, and $m^*_{RE} = m^*_{spin} + m^*_{orb}$ is the corresponding absolute total value of the magnetic moment of the central rare earth ion. The angle θ denotes the angle between the applied magnetic field, $\mathbf{B}$, and the molecular symmetry axis. Meanwhile, the angle ϑ refers to the subtended angle between the total magnetic moment m^*_{RE} and the applied magnetic field, as shown in Fig. 6.12.

Note that we exclude the exchange energy between 3d-ions and 4f-ions in equation 6.13. Ref.[343] showed that such exchange energy between some 3d and 4f ions, namely Dy(III) and Cr(II), does not exceed 0.02 meV. Meanwhile, Ref.[340] calculated the exchange interaction of $Ni(II)-O-Ln(III)$ $[Ln = Dy, Gd]$, based on DFT and ab-initio calculations, and they found that the exchange energy does not exceed 0.1 meV for several$\sphericalangle$ $Ni(II)-O-Ln(III)$ bond angle values. This linker's angle affect the charge transfer between orbitals which in turn affects the exchange interaction strengths. Yet, this energy value is small compared to the thermal energy at 7 K ($K_BT \approx 0.6\ meV$). As calculated in ref. [340], one can assume that the 3d-4f exchange interaction in our molecule is ferromagnetic, based on the wide angle of the linker $\sphericalangle$ $Ni(II)-O-Ln(III)$ which is around 126.05°. Then, it will just add up to the Zeeman energy. However, Fig.6.11 insets shows a monotonous decrease of χT with decreasing the temperature, which can be thought of an indicator to an antiferromagnetic exchange interaction within the molecule.

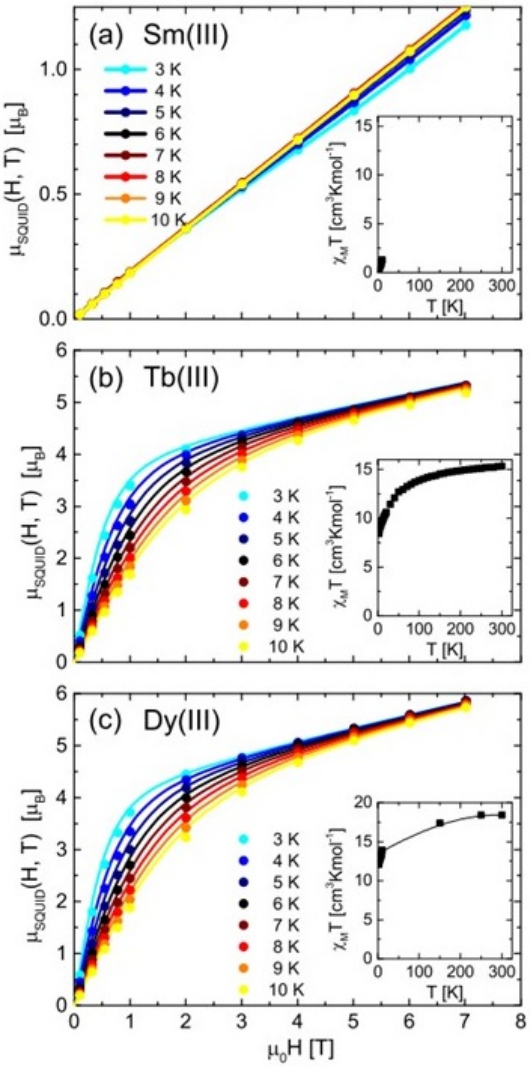

Figure 6.11: Molecular magnetic moment μ_{SQUID}(H, T) of $\mathbf{RENi_5}$(a) $\mathbf{SmNi_5}$, (b) $\mathbf{TbNi_5}$ and (c) $\mathbf{DyNi_5}$ molecule as a function of external field for temperatures in the range of 3 K to 10 K (dots). Full lines in (a) are a guide to the eye, whereas in (b) and (c) full lines represent fits by a spin-Hamiltonian model with g and a temperature-independent paramagnetic component as fit parameter. The insets show experimental results for the magnetic susceptibility multiplied by temperature, χT .

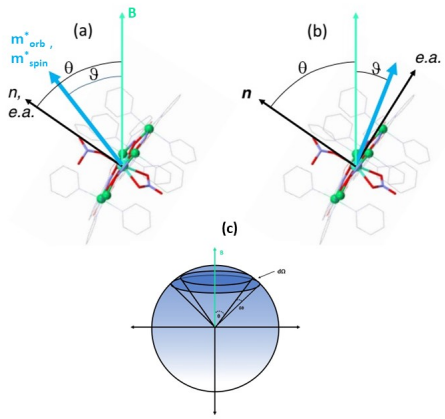

Figure 6.12: Sketch of the rare-earth central ion magnetic moment orientation (blue), in the magnetic anisotropy intermediate case, with angle ϑ with respect to an external applied magnetic field (green). The molecular symmetry axis (black) have an angle θ relative to the applied magnetic field. The molecule's magnetic anisotropy is assumed to have two possibilities: (a) easy axis along the molecular symmetry axis, and (b) an easy plane anisotropy [118]. Figure (c) shows a sketch of the projected magnetic moments lying on the surface of a cone with an opening angle of 2θ and $2(\theta + \delta\theta)$, within an element area of $d\Omega$, in spherical polar coordinates.

Yet, elaborate calculations, as done in ref.[340], is necessary to reach a decision on this issue.

The arbitrary angular distribution of the crystallites, resulting in a random distribution of magnetic anisotropy axes, should be taken into consideration for the calculation of the magnetic anisotropy energy in the single molecule. Thus, the conventional direct method of calculating the uni-axial anisotropy energy used in single crystals or epitaxial layered thin films can not be used here [282]. Thus, to minimize the free enthalpy of the molecule, we are going to introduce a tuning parameter for the ratio between the anisotropy and Zeeman energy, i.e.: $r = \frac{K_{RE}}{m^*_{RE}\,B}$, and find the average orientation of the ensemble as a functional of this parameter. For some given r value, and hence for some anisotropy energy value, the magnetic moments which make angle θ with $\mathbf{B}$ direction are forming a surface of a cone with opening angle of 2θ, see Fig.6.12(c). The trapped area between two cones separated by an incremental angle $\delta\theta$ is given by $d\Omega = 2\pi\ sin\theta\ d\theta$. This area encloses magnetic moments equal to $m^*_{RE}\ d\Omega$ and since we are interested in the magnetic moments lying along the $\mathbf{B}$ direction then the average projected magnetic moments will be the summation of the cones between angle 0 and $\pi/2$ divided by $\int_0^{\frac{\pi}{2}} d\Omega$, as follows:

$$< m_{proj}(r) > = \frac{\int_0^{\frac{\pi}{2}} m^*_{RE}\ cos\ \vartheta\ (r)\ sin\ \theta\ d\theta}{\int_0^{\frac{\pi}{2}} sin\ \theta\ d\theta}. \tag{6.14}$$

If $r = 0$, i.e. vanishing anisotropy, one expects the full ionic orbital moment

to be measured, i.e. $m_{proj} = m^*_{RE}$. Meanwhile, for infinitely strong anisotropy, $r \to \infty$, the ensemble average over all orientations would result into a value half of the nominal theoretical value,$< m_{proj}(\infty) > = \int_0^{\pi/2} m^*_{RE}\ cos\ \theta\ sin\ \theta\ d\theta / \int_0^{\pi/2} sin\ \theta\ d\theta = \frac{1}{2}\ m^*_{RE}$, note that at high anisotropy energy values, both angles θ and ϑ coincide. Only at intermediate values of r the magnetic moment has finite values of angle ϑ, as written in Eq. 6.14 and shown in Fig. 6.12.

Fig. 6.13(a) shows the result of the calculation of Eq.6.14 for **RENi$_5$** molecules with an easy-axis anisotropy along the molecular symmetry axis, which reflects our own considerations for the extreme cases. Alternatively, one can assume an easy plane anisotropy instead of easy axis anisotropy, as shown in Fig.6.12(b). This calculation results in value of the projected magnetic moment of 0.78 of the total magnetic moment, $< m_{proj}(\infty) > = \int_0^{\pi/2} m^*_{RE}\ sin^2\ \theta\ d\theta / \int_0^{\pi/2} sin\ \theta\ d\theta\ = 0.78\ m^*_{RE}$. This means that the experimental value of the orbital magnetic moment, for Dy(III) in our molecule for example, should be around 7.63 $\mu_B$which is much larger than the obtained experimental value. Based on these calculations, one concludes that the molecule **DyNi$_5$** exhibits an easy axis anisotropy. Since **Dy(III)** and **Tb(III)** have a similar asymmetric shape of the 4f electron density, one can say that the same conclusion can be extended to the **TbNi$_5$** molecule. Note that these considerations are valid only for the case of the orbital magnetic moment.

The measured effective spin moment is smaller than the true spin moment because of the negative sign of dipole operator T_z, even when the spin moment is aligned along the molecular symmetry axis, as one can see in Eq.6.6, which can be written as follows: $m^{eff}_{spin} = 2 < \mathbf{S_z} > + 6 < \mathbf{T_z} >$. If the direction of the spin moment deviates from the molecular symmetry axis by an angle $\delta = \theta - \vartheta$, the expectation value is given by $T_{\boldsymbol{z}}(\delta) = T_{\boldsymbol{z}}(3\ cos^2\delta - 1)/2$. For negligible anisotropy, one obtains $\delta = \theta$ and the powder average results in a vanishing T_z contribution. For finite anisotropy, we can calculate the projected effective spin moment with respect to the absolute spin moment in the same approach used for Eq. 6.14, to obtain:

$$m^{eff}_{spin}/m^*_{spin} = \int_0^{\pi/2} (1 + 3\frac{T_z}{S_z}) \frac{3\ cos^2[\theta - \vartheta(r)] - 1}{2}\ cos\vartheta(r)\ sin\theta\ d\theta. \qquad (6.15)$$

The ratio of the expectation values of the dipole operators T_z and the spin angular momentum S_z of **RE(III)** ions mentioned in Eq. 6.15 can be calculated from Eq. 6.16:

$$< T_z > / < S_z > = (l - n + \frac{1}{2}) 2J(J+1). \\ \frac{3(S-J)^2(S+J+1)^2 - L(L+1)[L(L+1) + 2S(S+1) + 2J(J+1)]}{2(2l+3)(2l-1)(2L-1)SJ(J+1)[J(J+1) + S(S+1) - L(L+1)]} \qquad (6.16)$$

where l and n stands for the vacant orbital shell quantum number and the number of vacant holes, respectively [274]. Table 6.3 listed the values of T_z/S_z

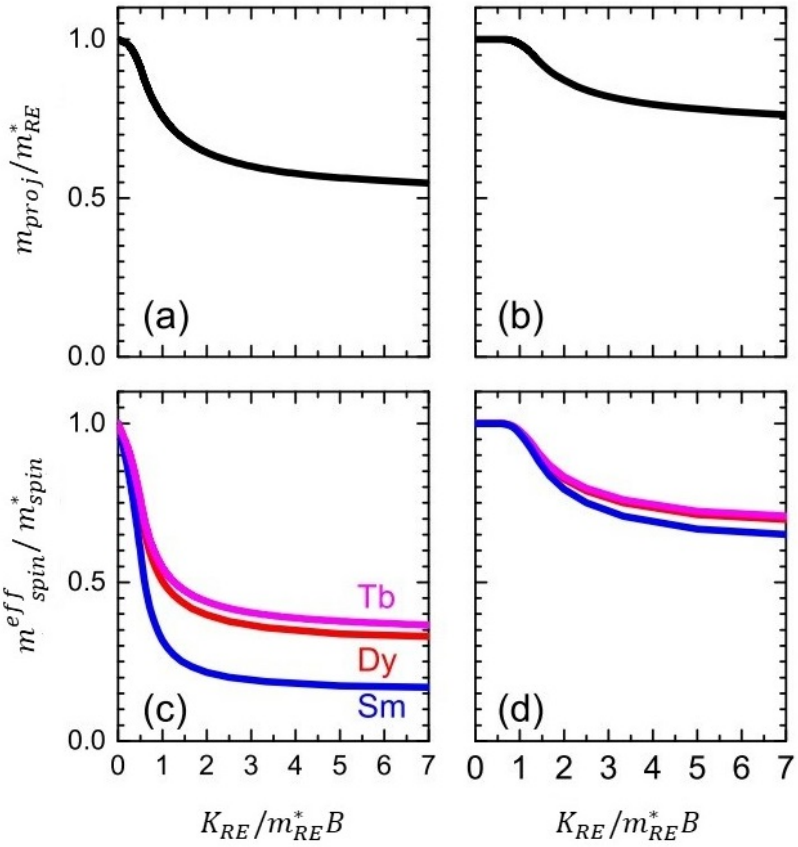

Figure 6.13: Calculation of the projected magnetic moment along the external field axis normalized to the absolute moment as a function of the ratio of anisotropy constant and Zeeman energy, r, for the case of easy axis anisotropy (a), and easy plane anisotropy (b), respectively. (c) and (d) show the effective spin magnetic moment along the external field axis normalized to the absolute moment as a function of the ratio r for the case of easy axis and easy plane anisotropy, respectively. The contribution from the T_Z term is considered according to the exact ionic value for the indicated rare earth ions. [118]

ratios for **RE(III)** ions used in this thesis. Eq.6.16 was derived by Carra et al. [274], based on ideal assumptions, which led to some deviations of the XMCD spin sum rule if calculated by atomic multiplet calculations. Teramura et al have calculated this deviation and found that for heavy **RE(III)**, like **Dy(III)** and **Tb(III)**, this deviation is just around $\backsim 10\%$, meanwhile it can reach more than 230% for less than half-filled **RE(III)** ions like in **Sm(III)** [279]. This deviation can be attributed to many factors, e.g.: the core-valence exchange interaction inside **RE(III)** ion itself and the finite spin-orbit splitting of the core $3d$ states. Since we are not interested in $\mathbf{SmNi_5}$ molecules due to the paramagnetic behavior and since the deviation of the XMCD spin sum rule (Eq.6.4) is not significant for **Dy(III)**and **Tb(III)**, we use Eq.6.16 to calculate the ratio $< T_z > / < S_z >$. The result of the calculation of Eq.6.15 is shown in Figs.6.13(c) and 6.13(d) for the case of an easy axis and easy plane anisotropy, respectively.

One can use the result of Fig.6.13 to obtain (i) the magnetic anisotropy energy constant K_{RE} and (ii) the correction of the spin magnetic moment m^*_{spin} for **RE(III)** ions in $\mathbf{RENi_5}$, for Dy and Tb, where the external magnetic field of 7 Tesla is sufficient to saturate the magnetic moments against thermal fluctuations. The ratio of the projected orbital magnetic moment to the ionic value, $m_{proj}(r)/m^*_{RE}$, for **Dy(III)** is around 54%, which corresponds to $r = 7(3)$, and for **Tb(III)** the ratio is around 70% which corresponds to $r = 1.3(3)$. Based on these values one can determine the magnetic anisotropy constant for the **RE(III)** ions in each molecule according to $r = \frac{K_{RE}}{m^*_{RE}\, B}$. For **Dy(III)**, the absolute total magnetic moment m^*_{RE} is around 10 μ_B, hence the magnetic anisotropy constant is $K_{RE} = 28(12)\ meV$. For **Tb(III)**, m^*_{RE} is around 9.72 μ_B, and $K_{RE} = 6.5(2.0)$ meV. Thus both molecules have a remarkable magnetic anisotropy energy barrier, and it even exceeds room temperature in thermal units, *i.e.* 25 meV, for the case of Dy.

Fig.6.13 (c) justifies our model assumptions: The spin orbit coupling aligns both the spin and orbital moment, thus the ratio r obtained for the **RE(III)** ions for the orbital magnetic moment holds for the spin moment, too. Consequently, for this ratio one can obtain the m^*_{spin} value, which we already know from Hund's rule, and by comparing we can get a correction factor. Accordingly, the spin moment of **Dy(III)** is given by $m^*_{spin} = 6.0\ \mu_B$, which equals the expected value 5.9 μ_B. For the case of **Tb(III)** one obtains a spin moment of m^*_{spin}= 6.2 μ_B, being close to the expected value of 6.92 μ_B. The agreement of the spin moments with the corresponding ionic values justifies the model assumptions. The error margin of the XMCD orbital and spin moments of about 20% results in a considerable change of the T_z correction factors and thus may explain part of the discrepancy between molecular magnetic moment μ_{mol} values obtained from SQUID and XMCD magnetometry measurements.

In Summary, the magnetic moments of both the $3d$ and $4f$ elements in heterometallic 15-MC-5 $\mathbf{RENi_5}$ metallacrowns could be measured in an element-specific manner using the XMCD technique. The comparatively small **Ni(II)** moments demonstrated that the intramolecular exchange interaction between the **Ni(II)** ions is dominated by an antiferromagnetic exchange interaction. The exchange inter-

action between the $3d$ and $4f$ elements is an antiferromagnetic in **$SmNi_5$** where **Sm(III)** magnetic moment align antiparallel to the **Ni(II)** magnetic moment. On contrary to that, both **$TbNi_5$** and **$DyNi_5$** shows parallel alignment between the circumstantial **Ni(II)** ions and the central **RE(III)** ion. In addition to that, we observed a discrepancy between the measured magnetic moments of **RE(III)** ions and the expected ones calculated by Hund's rule. An explanation to such disagreement could be attributed to the existence of a large magnetic anisotropy. A simple phenomenological model based on the ratio of the experimentally determined rare earth moment and the expected ionic value has been used to deduce the anisotropy energy barrier considering the random orientation of the easy axis in the powder. This results in a magnetic anisotropy of 28 meV (340 K) in the case of **Dy(III)** and 7 meV (85 K) in the case of **Tb(III)**. This approach in calculating the magnetic anisotropy of $3d-4f$ heterometallic SMMs in powder samples is desirable for any future work where there is no need to grow any highly oriented single crystal to measure the anisotropy.

6.2 Solvent-Induced High Spin Transition in Double Decker 3d-4f Metallacrowns

6.2.1 Experimental Procedure

The procedures of this experiment are the same as the previous ones regarding the beamline end-station parameters, preparation of the samples, temperature measurements, measurement modes (TEY mode), X-ray normal incidence, and the data analysis procedures, see section 6.1.1.

The investigated samples discussed here are powders of metallacrown molecules $(Hpip)_6\left\{(RE(III)[12-MC_{Ni(II)N(shi)}-4]_2\ (Hsal)\right\}$, RE = Gd(III), Tb(III), shortly called $RENi_8$. The molecules were synthesized by L. Völker, C. Gamer, A. Rauguth, and A. Kredel in the group of Prof. Rentschler, in the chemistry department of Mainz University, based on the synthetic method mentioned in Ref. [165].

Several preparation methods were used in this experiment. The first method was gluing the powder directly to the Si-wafer using a mixture of graphite powder and a xylol (a conductive carbon cement). The insulating powder crystals get charged and this charging affects the signal quality in TEY mode leading to a reduced current in the range of 0.1 pA. Hence, a long exposure time is needed to reduce the signal noise. Thus, this method has been abandoned. The other approach was the drop-cast method, where the molecules were dissolved in dichloromethane (case A) and methanol (case B) solutions separately and then drop casted on different Si-wafers substrates on the sample holder. The drop-cast method showed more promising results regarding signal-to-noise ratio in XAS spectra which make this method more preferable than the previous one.

6.2.2 Results

The orbital-magnetic moments, m_{orb}, and the effective spin-magnetic moments, m_{spin}^{eff}, of each element is calculated using XMCD sum rules of Eqs. 6.1 – 6.4 [274, 275] similar to what is mentioned in section 6.1.2.

The number of d holes in **Ni(II)** ions has been set according to the charge-transfer multiplet calculations, $n_h = 2$. For **Gd(III)** and **Tb(III)** ions one can use the number of holes for the ionic electronic configuration due to the localization of the $4f$-orbitals, $n_h = 7$ for **Gd(III)** and $n_h = 6$ for **Tb(III)**. The correction factors for **Ni(II)** is equal to 1 according to Ref. [276]. The XMCD spin sum rules holds for **RE(III)** ions with more than half-filled shells occupancy like **Gd(III)** and **Tb(III)**. Thus, the correction factor for both elements is around 1 as calculated in Ref. [279]. The calculated XAS spectra of **RE(III)** ions for opposite circular polarization are compared with experimental spectra Ref.[366, 367, 379].

6.2.2.1 XAS & XMCD of $GdNi_8$ Molecules

Figure 6.14 shows XAS and XMCD spectra for {**$GdNi_8$**} 15-MC-5 metallacrowns drop-casted from both a dichloromethane solution **CH_2Cl_2** (panels (a) – (b), case A), and from a methanol solution **CH_3OH** (panels (c) – (d), case B). The **Ni(II)** XAS spectrum has two satellite peaks at 2 eV and 5 eV higher than the L_3 edge of 853 eV in both cases [Figs. 6.14(a) and 6.14(c)] with varying heights. For case A, the satellite peak is at 855 eV and it is smaller than the one in case B. The shift of the first satellite peak from the main peak in case A is larger (2 eV) compared to case B (1.8 eV). This shift leads to a clear satellite peak in case A, whereas in case B the main peak rather has a shoulder on the high-energy side. Both cases, A and B, exhibit another deviation of each others at the **Ni(II)** XAS L_2 edge of 870 eV. For case A we observe a narrow peak almost half the size of peak L_3 edge. In contrast, case B reveals a smaller maximum peak value with an enhanced width. The measured XAS spectra of **Gd(III)** in both cases [Figs. 6.14(b) and 6.14(d)] are similar and show the typical characteristic ionic spectrum according to the atomic multiplet calculations [366].

This reflects the localization of $4f$-orbitals and the absence of a chemical bonding between the surrounding $3d$-ions and the $4f$-orbitals of the central **RE(III)** ion. Both **Gd(III)** XAS spectra show a single narrow peak at the M_5 edge of 1185 eV preceded by a shoulder peak on the low-energy side and followed by a satellite peak around ∼5 eV on the high-energy side. Ref.[366, 379] show that this resonance absorption corresponds to the multiplet transitions from the ground-state of $3d^{10}4f^7$, $^8S_{7/2}$, to the final states of the electronic configuration of $3d^9 4f^8$, ^7F mixed with many multiplets, mainly $^8P_{5/2}$. On the other hand, the M_4 edge at 1215 eV shows a split peak with two comparable intensity peaks.

The experimental XAS and XMCD spectra of **Gd(III)** in {**$GdNi_8$**} is similar

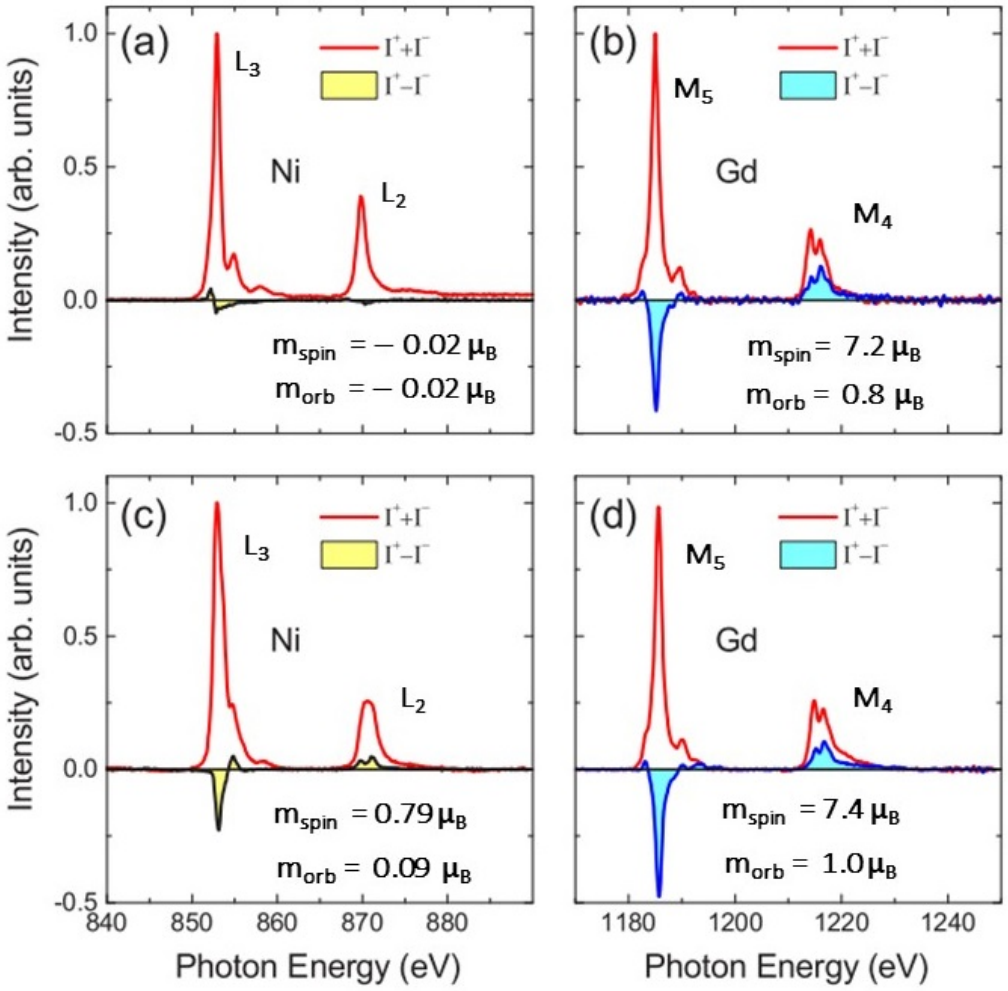

Figure 6.14: The panels (a) – (b) show both the measured XAS (red) normalized to the maximum absorption and XMCD (yellow) spectra for **Ni**(**II**) $L_{3,2}$ edges and for **Gd**(**III**) $M_{5,4}$ edges for **GdNi$_8$** metallacrowns deposited by drop-casting from a solution in dichloromethane. The panels (c) – (d) show both the measured XAS (red) normalized to the maximum absorption and XMCD (yellow) spectra for **Ni**(**II**) $L_{3,2}$ edges and for **Gd**(**III**) $M_{5,4}$ edges for **GdNi$_8$** metallacrowns deposited by drop-casting from a solution in methanol. The spin and orbital magnetic moments calculated from XMCD sum rules for each element, are given in each figure respectively. [118]

to other spectra obtained from materials containing **Gd(III)** and **Ni(II)** ions [380–382]. This confirms the localization of $4f$-orbital and the ionic electronic configuration of the **Gd(III)** ion in our molecule.

The **Ni(II)** XMCD spectra of both cases have discernible features at both energy edges. In case A, the XMCD signal is very small and it reveals a plus/minus feature at the L_3 edge (853 eV). Instead, case B results in a prominent negative peak at the L_3 edge and a positive peak at the L_2 edge. Thus, the XMCD signal indicates a prevailing spin moment parallel to the external applied magnetic field.

The XMCD sum rules, Eq.6.1 and Eq.6.2, yield a vanishing orbital and spin magnetic moment for **Ni(II)** ions in the molecules drop-casted from dichloromethane (case A), but for the other case **Ni(II)** ions show a considerable orbital and spin magnetic moment values, as shown in Fig.6.14. Drop-casting from methanol (case B) results in a significant increase of the spin magnetic moment to almost 0.8 μ_B per **Ni(II)** ion. This is a significant value where the magnetic moment amounts to around half the maximum possible value for the **Ni(II)** $3d^8$configuration, i.e. 2 μ_B per ion. Yet the orbital magnetic moment does not show such an increase as a result of the vanishing orbital contribution to the ionic magnetic moments in $3d$ ions.

On the contrary, the XMCD spectra of **Gd(III)** ions shows similar features in both cases as expected from the localization of the $4f$-orbitals. The prominent negative XMCD peak at the M_5 edge (1185 eV) and the positive peak at the M_4 edge (1220 eV) indicate a large spin moment parallel to the external field. The total moment of **Gd(III)** ions, $m_{tot} = m_{spin}^{eff} + m_{orb}$, calculated by XMCD sum rules, Eq.6.3 and Eq.6.4, show a small increase by 5% for the molecules drop-casted from methanol solution (case B) in comparison to the total moment for the molecules drop-casted from dichloromethane solution (case A).

For the **Gd(III)** ion the total magnetic moment has a spin contribution solely since the orbital angular momenta is canceled out according to Hund's rules, S=7/2 and L=0. This renders the $4f$-orbitals in this ion spherical which leads to a negligible T_z term. Thus, one can write Eq.6.6 simply as $m_{spin}^{eff} = m_{spin}$. The spin magnetic moment experimental values are close to the ones calculated from Hund's rules, Eq. 6.8–6.11, which has the value of $\mathbf{m_{spin}^{Hund}} = 7.94\,\mu_B$**,** see Table 6.4.

Surprisingly, the orbital magnetic moment of **Gd(III)** ions in {**GdNi$_8$**} metallacrowns does not vanish in both cases. This is also shown in other research papers like in Ref.[380]. This can be attributed to some limitations in the sum rules themselves, since they were derived based on ideal assumptions. The total molecular moment, $\mu_{mol} = 8\,\mu_{tot}$(**Ni(II)**) + μ_{tot}(**Gd(III)**), of {**GdNi$_8$**} metallacrown molecules got doubled when the drop-casting solution is exchanged from dichloromethane (case A) to methanol (case B). Table 6.4 summarizes the different magnetic moments for each element of both cases.

6.2.2.2 XAS & XMCD of TbNi$_8$ Molecules

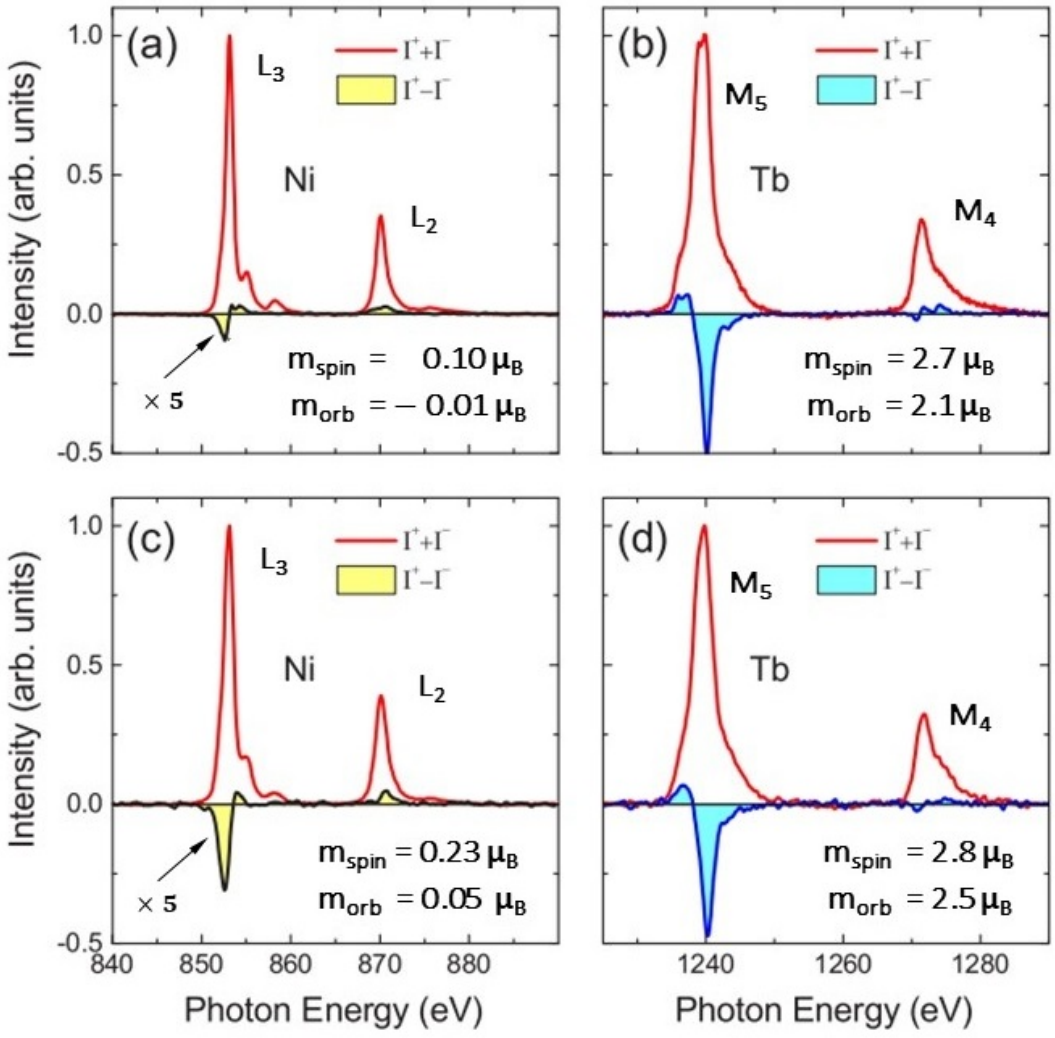

Figure 6.15: The panels (a) – (b) show both the measured XAS (red) normalized to the maximum absorption and XMCD (yellow) spectra for **Ni**(**II**) $L_{3,2}$ edges and for **Tb**(**III**) $M_{5,4}$ edges for $\mathbf{TbNi_8}$ metallacrowns deposited by drop-casting from a solution in dichloromethane. The panels (c) – (d) show both the measured XAS (red) normalized to the maximum absorption and XMCD (yellow) spectra for **Ni**(**II**) $L_{3,2}$ edges and for **Tb**(**III**) $M_{5,4}$ edges for $\mathbf{TbNi_8}$ metallacrowns deposited by drop-casting from a solution in methanol. The **Ni**(**II**) XMCD spectra [panels (a) and (c)] are magnified by a factor of 5. The spin and orbital magnetic moments calculated from XMCD sum rules, for each element, are given in each figure respectively. [118]

Figure 6.15 shows XAS and XMCD spectra for $\{\mathbf{TbNi_8}\}$ 15-MC-5 metallacrowns drop-casted from both a dichloromethane solution $\mathbf{CH_2Cl_2}$ (panels (a) – (b), case A), and from a methanol solution $\mathbf{CH_3OH}$ (panels (c) – (d), case B). The **Ni(II)** XAS spectra in both cases [Figs. 6.15(a) and 6.15(c)] show similar features regarding the two satellite peaks at 2 eV and 5 eV higher than the L_3 edge of 853 eV in comparison with Fig. 6.14. However, there is small deviation in the satellite peak located at 855 eV. For case A the satellite peak is smaller than the one seen in case B, and the separation of this satellite peak from the main peak is larger in case A than the one in case B by 0.2 eV. Both cases do not exhibit any deviation of each others at the **Ni(II)** XAS L_2 edge of 870 eV, where both spectra show a narrow single peak with comparable width and height.

The XAS spectra measured at the **Tb(III)** $M_{5,4}$ edges in both cases [Figs. 6.15(b) and 6.15(d)] look almost identical to each other for the same reason as for the spectra of **Gd(III)**, i.e. the localization of the $4f$-orbitals. However, a closer look at the maximum of the M_5 edge reveals a slightly more pronounced double peak for case A in comparison to case B. This issue can be described in details in terms of the charge-transfer multiplet calculations in the discussion part of this section. The discussion of the **Tb(III)** XAS spectra is the same for the one of $\{\mathbf{TbNi_5}\}$ mentioned in the previous section 6.1.2.2.

The **Ni(II)** XMCD spectra in case A [Fig. 6.15(a)] shows a small negative peak at the L_3 edge and a small positive peak at the L_2 edge. This is contrary to the vanishing peaks in $\{\mathbf{GdNi_8}\}$ drop-casted from dichloromethane solution [Fig. 6.14(a)]. For case B the **Ni(II)** XMCD spectra show similar features to case A but with larger values. Both cases reveal a prevailing spin moment parallel to the applied external field. The total magnetic moment of **Ni(II)** ions in $\{\mathbf{TbNi_8}\}$, calculated by the XMCD sum rules, Eq.6.1 and Eq.6.2, shows an increase by a factor of three in the sample drop-casted from a methanol solution comparing to the sample drop-casted from dichloromethane solution.

The XMCD spectra of **Tb(III)** ions for both cases, depicted in Figs. 6.15(b) and 6.15(d), display a negative peak at M_5 edge with a vanishing peak at M_4 edge. This hints to a parallel spin alignment with respect to the external applied field similar to the **Ni(II)** ions. The orbital- and spin-magnetic moment calculated by the XMCD sum rules, Eq. 6.3 and Eq. 6.4, deviates from the ones calculated by Hund's rules, Eq. 6.8 – 6.11, in both cases.

By assuming a powder average of the molecules in both cases one can apply the phenomenological model developed in the previous section 6.1 on the **Tb(III)** ions in $\{\mathbf{TbNi_8}\}$ metallacrowns. This results in ratios $r = 0.7$ and $r = 0.83$ for cases A and B, respectively. Following the procedures mentioned in section 6.1 one obtains the magnetic anisotropy constants in both cases $K_{RE}\mathbf{(Tb)} = 5.1$ meV for case A and $K_{RE}\mathbf{(Tb)} = 2.9$ meV for case B. The expected ionic values of the spin- and orbital magnetic moments has the ratio of 2:1 following $2S = 6$ and $L = 3$. But we notice that this ratio is 1:1 in both cases for the **Tb(III)** ions in $\{\mathbf{TbNi_8}\}$. To recover this ratio one should deduce a correction factor for the T_z component of the effective spin moment from the calculated ratio r. This results in $\mathbf{m^*_{spin}} = 3.8\,\mu_B$

and $\mathbf{m^{*}_{spin}} = 3.9\,\mu_B$ for **Tb(III)** ion in $\{\mathbf{TbNi_8}\}$ metallacrowns drop-casted from dichloromethane and methanol, respectively. This correction restores the expected spin- and orbital-moment ratio for **Tb(III)** ions.

Considering all ionic moments contributing to the molecular moment one find that the total molecular moment for $\{\mathbf{TbNi_8}\}$ metallacrowns drop-casted from methanol solution, $\mu_{mol} = 8\,\mu_{tot}(\mathbf{Ni(II)}) + \mu_{tot}(\mathbf{Tb(III)})$, increases by a factor of approximately 1.5 in comparison to the sample drop-casted from a dichloromethane solution. Table 6.4 summarizes all the magnetic moments and related parameters for both metallacrown molecules in this section.

	Ni(II) [μ_B]			RE(III) [μ_B]										Molecular moments [μ_B]
	$\mathbf{m_{spin}^{eff}}$	$\mathbf{m_{orb}}$	$\mathbf{m_{tot}}$	$\mathbf{m_{spin}^{eff}}$	$\mathbf{m_{orb}}$	$\mathbf{m_{spin}^{*}}$	$\mathbf{m_{spin}^{Hund}}$	$\mathbf{m_{orb}^{Hund}}$	**S** [$\hbar$]	**L** [$\hbar$]	**J** [$\hbar$]	$\mathbf{g_J}$	$\mathbf{T_z/S_z}$	μ_{mol}
{GdNi$_8$}	**–0.02(2)**	**–0.02(2)**	**–0.04(4)**	**7.2(2)**	**0.8(2)**	–	**7.94**	**0**	**7/2**	**0**	**7/2**	**2**	**0**	**7.8(4)**
{GdNi$_8$}.CH$_3$OH	**0.79(2)**	**0.09(2)**	**0.88(4)**	**7.4(2)**	**1.0(2)**	–	**7.94**	**0**	**7/2**	**0**	**7/2**	**2**	**0**	**15.4(4)**
{TbNi$_8$}	**0.10(2)**	**–0.01(2)**	**0.09(4)**	**2.7(2)**	**2.1(2)**	**3.8**	**6.92**	**3.46**	**3**	**3**	**6**	**1.5**	**–0.111**	**6.4(4)**
{TbNi$_8$}.CH$_3$OH	**0.23(2)**	**0.05(2)**	**0.29(4)**	**2.8(2)**	**2.5(2)**	**3.9**	**6.92**	**3.46**	**3**	**3**	**6**	**1.5**	**–0.111**	**8.9(4)**

Table 6.4: m_{spin}^{eff} and m_{orb} represent effective spin magnetic moment and orbital magnetic moment measured from XMCD sum-rules at 7 K for a field of 7 T, respectively. m_{spin}^{*} and m_{orb}^{*} represent the spin and orbital magnetic moment calculated from the model as mentioned in the text. $S[\hbar]$, $L[\hbar]$, $J[\hbar]$, g_J, and T_z/S_z stand for the different angular momenta , the Lande g-factor, and the ratio of dipole and spin operators for the ground state of RE(III) ions, respectively. The molecular moments calculated from XMCD results, $\mu_{\mathbf{mol}} = \mathbf{8m_{tot}(Ni) + m_{tot}(RE)}$, are reported for each molecule. **{RENi$_8$}** denotes case A of the samples drop-cast from a dichloromethane solution, and **{RENi$_8$}.CH$_3$OH** indicates case B of the samples drop-cast from a methanol solution. The total **Ni(II)** magnetic moment results from $\mathbf{m_{tot} = m_{spin}^{eff} + m_{orb}}$. The total error is dominated by systematic errors of the common factors polarization, n_h, and the error due to subtraction of transitions into continuous states. We estimate the total error to be on the order of 20%.

6.2.3 Discussion

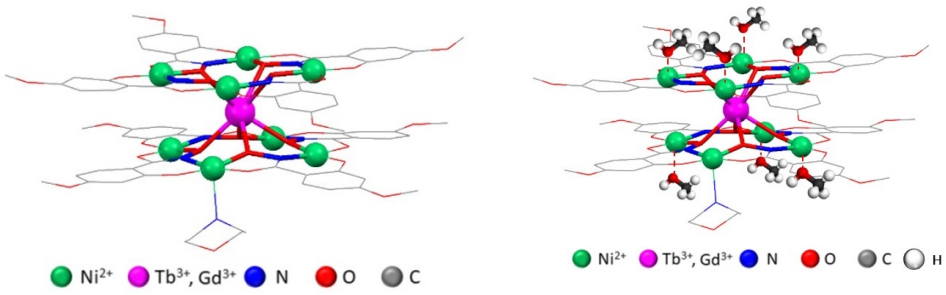

(a) (b)

Figure 6.16: (a) Molecular structure of the pristine {**RENi$_8$**} metallacrown, **RE** = **Tb(III)**, **Gd(III)**, case A. (b) The assumed molecular structure of the {**RENi$_8$**} metallacrown after **Ni(II)** ions coordinated with the methanol molecules, **CH$_3$OH**, upon drop-casting from methanol solution, case B. Color code in both images shows the corresponding elements in the molecular structures. The depicted molecular structure has been created using Mercury Software.[376] [346]

The experimental magnetic moments of **Ni(II)** ions in {**RENi$_8$**} metallacrowns drop-casted from different solutions show different values in contrast to the unchanged **RE(III)** magnetic moments. The different polarity of the used solvents, the dichloromethane and methanol, gives raise to the hypothesis of the change of the ligand filed of **Ni(II)** ions due to an additional coordination with the methanol molecules in case B. In order to test this hypothesis, we carried out charge-transfer multiplet calculations on {**TbNi$_8$**} metallacrowns in different ligand field environments. A good agreement between the simulated XAS and XMCD of **Ni(II)** and **Tb(III)** with the experimental ones supports this hypothesis.

The pristine molecular structure obtained from the x-ray diffraction of a single crystal shows that the eight **Ni(II)** ions sandwich the **Tb(III)** central-ion in a form of double-decker structure, Fig. 6.16(a). Seven of the eight **Ni(II)** ions have four nearest-neighbor atoms, three oxygen and one nitrogen atom, arranged planar. The remaining **Ni(II)** ion has an additional covalently bonded morpholin ligand. As a result of such coordination, at least seven **Ni(II)** ions have a square planar ligand field environment which in turn leads to a low-spin state, i.e. $S = 0$.

It is noteworthy first to mention that the experimental XAS and XMCD of small single crystals of {**TbNi$_8$**} metallacrowns is identical to the ones obtained for dissolved {**TbNi$_8$**} metallacrowns in the non-coordinating solvent dichloromethane, case A of Fig. 6.15 (a) – (b). Thus, one can consider the experimental XAS and XMCD of case A as a representative of the pristine molecules and we can compare the

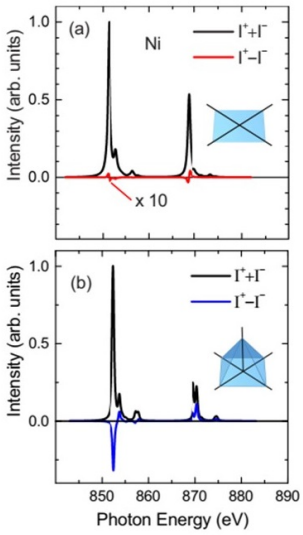

Figure 6.17: **Ni(II)** XAS (solid black) and XMCD (solid red) spectra simulated by charge transfer multiplet calculations [383]. Panel (a) shows the calculation done for **Ni(II)** ions in a square planar ligand fields, as shown in the inset, with parameters values of $10D_q$= 1.8 eV, D_s= 0.6 eV and D_t= 0.1 eV. Panel (b) shows the same calculation done for **Ni(II)** ions but in extended tetragonal ligand field environment, as shown in the inset of the same figure, with parameters values of $10D_q$= 1.8 eV, D_s= 0.0 eV and D_t= 0.0 eV. [346]

result of the charge-transfer multiplet calculation with this spectrum as a reference spectra for our investigation.

Fig. 6.17(a) shows the XAS and XMCD simulated spectra of a square-planar ligand field with the following ligand filed parameters: $10D_q = 1.8\,eV$, $D_S = 0.6\,eV$, and $D_t = 0.1\,eV$. These values represent the splittings of $d-$orbitals in a ligand field of square planar geometry. The parameter $10D_q$ (or ΔO_h) is the energy separation between the $d_{x^2-y^2}$ and d_{xy} states, and it has the same value as it would for the same ligands in an octahedral geometry. Whereas the parameter D_S stands for the energy separation between the d_{xy} and d_{z^2} and the parameter D_t refers to the energy separation between the states of d_{z^2} and the group $d_{xz}\,, d_{yz}$, as depicted in Fig. 6.19. The simulated XMCD spectra of this case vanishes yielding vanishing spin and orbital magnetic moments as well (note the 10x magnification factor shown in the figure). This is an indication of the low-spin of **Ni(II)** ions in case A as expected. Besides that the simulated XAS spectra reproduces the features of the experimental XAS of case A, shown in Fig. 6.15(a), including the two satellite peaks at comparable energy values.

The direct explanation of this result is the minimization of the energy of the d orbitals in **Ni(II)** ions in the coordination complex. The $d-$orbitals posses different shapes due to their different angular distributions, as shown in Fig. 6.18. Thus, once the **Ni(II)** ions bonds with the ligands, the electrons in the $d-$orbitals will experience an extra Coulomb repulsion with the ligands. Different ligands geometry affects each $d-$orbitals differently following the separation between the ligand and the $d-$orbital ($U \propto 1/r$) [45]. The orbital $d_{x^2-y^2}$ is the most destabilized state in

the square planar geometry with an energy separation of $10D_q = 1.8\,eV$, which is larger than the total pairing energy between the electrons, i.e. the summation of Coulomb pairing energy and exchange pairing energy. Therefore, occupying the two electrons in one orbital (d_{xy}) with an anti-parallel orientation is energetically more favorable than promoting one electron to occupy the energetically higher orbital ($d_{x^2-y^2}$) due to the energy expenditure, see Fig. 6.19. As a result, **Ni(II)** ions with $3d^8$ electronic configuration have a low spin state, $S = 0$, in a ligand field of square planar geometry.

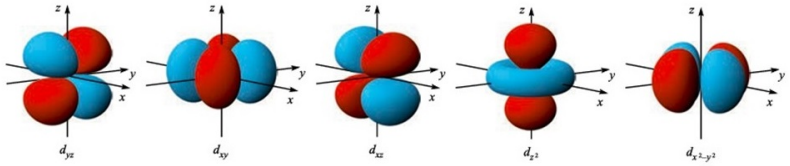

Figure 6.18: The shapes of five $d-$orbitals in Cartesian coordinates [32].

Contrary to the vanishing XMCD signal of case A (Fig. 6.15(a)) we find an enhanced XMCD signal for the same metallacrowns once they are dissolved in methanol solution, case B (Fig. 6.15(c)). The difference between these two findings can be attributed to the change of the energy splitting of $d-$orbitals due to the coordination with the methanol molecules. This, in turn, changes the spin state of **Ni(II)** ions according to the crystal field theory. The coordinated molecule breaks the square-planar geometry resulting in a square pyramidal ligand field geometry, as depicted in Fig. 6.19. One expects the $d_{x^2-y^2}$ orbital to remain the highest destabilized orbital due to the surrounding planar ligands, thus for simulation we can retain the value of $10D_q$ used in the previous simulation of square planar geometry, $10D_q = 1.8$ eV. However, the attached methanol molecule along $z-$direction will increase the energy of the d_{z^2} orbital due to the increase of Coulomb repulsion along this axis. The d_{xy} orbital will be reduced with the same amount d_{z^2} orbital energy got increased. Thus, the energy separation of those two orbitals will be almost vanishing and negligible, $D_S \simeq 0.0$ eV. We set the remaining parameter to zero as well, $D_t = 0.0$ eV. Figure 6.19 depicts the $d-$orbitals splittings of both geometries. The simulated XAS shown in Fig. 6.17(b) reproduce the experimentally observed one shown in Fig. 6.15(c). The simulated spectrum reveal the same satellite peak located at energy of 1.8 eV higher than maximum absorption peak of L_3 edge. The broadening of L_2 absorption peak is comparable although the simulated spectrum shows a split peak which is not seen in the experimental one. On the other hand, the simulated XMCD spectrum shows a strong signal reproducing the experimental one especially for the prevailing negative peak at the L_3 edge and the two positive peaks at the L_2 edge. This hints to the expected high-spin state of case B. The overall good agreement of the simulated

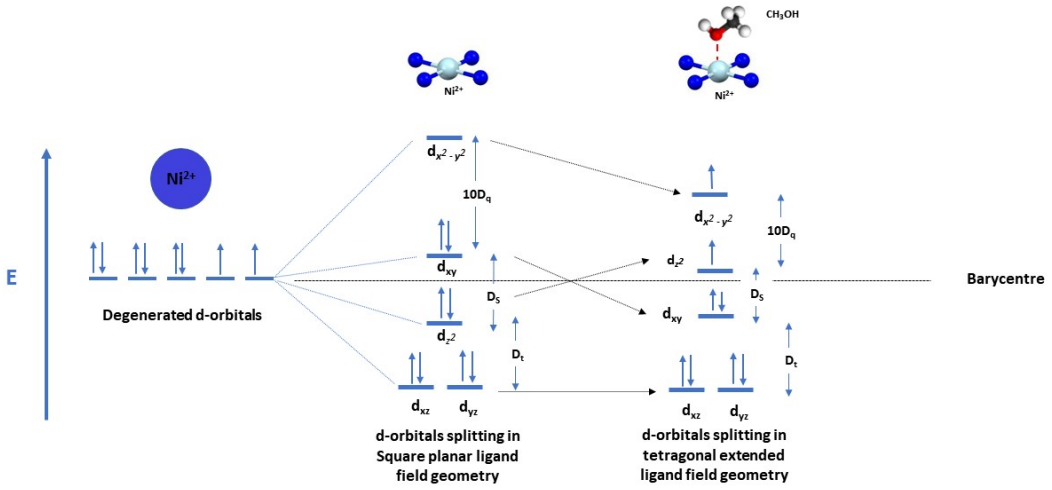

Figure 6.19: Scheme of the splitting of the **Ni(II)** ions d orbitals in the square planar field with their respective splitting parameters, resulting in the low-spin state S = 0 (Left, case A). In a square pyramid ligand field, the additional methanol molecule coordination affects the destabilization energy of the d-orbital except d_{xz} and d_{yz}. This redistribute the electrons in $d-$orbitals resulting with the high-spin state S = 1 (Right, case B).

and experimentally observed spectra confirms our hypothesis regarding the change of the ligand field geometry due to additional coordination of the **Ni(II)** ions with methanol molecules. Thus one can conclude that the energy splitting of $10D_q = 1.8$ eV between the highest level of $d_{x^2-y^2}$ orbital and the next one d_{z^2} orbital is smaller than the correlation energy. As a result, the two orthogonal orbitals are occupied by two electrons with parallel orientation leading to a high-spin state, $S = 1$, see Fig. 6.19. This transition from the low-spin state to the high-spin state takes place by reducing the energy splitting parameter D_S below 0.3 eV.

Another noteworthy finding in $\{\mathbf{TbNi_8}\}$ metallacrowns deposited from methanol solution is the slight change of the XAS spectra of the **Tb(III)** ions, as shown in Fig. 6.15(b),(d). In general, one expects no change of the XAS spectra of **RE(III)** ions due to the localization of their $4f-$orbitals, as it is observed for the XAS spectra of **Gd(III)** ions of $\{\mathbf{GdNi_8}\}$ metallacrowns in both cases, Fig. 6.14(b),(d). However, the absorption peak at the M_5 edge shown in case A has double peak compared to case B. An attempt of explanation of that can be obtained through the charge-transfer multiplet calculation with the corresponding simulated XAS of **Tb(III)** of both cases.

The intensity of XAS spectra yielded from the electronic transitions between the initial and final configurations, $3d^{10}4f^n \rightarrow 3d^9 4f^{n+1}$, is a result of the relative energy intensities of different terms , or multiplets. These relative energy intensities can be calculated from the matrix elements of the respective multiplet of different transitions. One term of these matrix element intensities is pertaining the Coulomb

electrons interactions:

$$\left\langle i|\frac{e^2}{r_{12}}|f\right\rangle = \sum_i f_i F^i + \sum_i g_i G^i, \tag{6.17}$$

where $|i>$ ($|f>$) stands to the initial (final) electronic configuration in terms of the corresponding quantum numbers. F^i (f_i) and G^i (g_i) are the Slater-Condon parameters for the radial (angular) part of the direct Coulomb repulsion and the Coulomb exchange interaction, respectively [365]. Those radial integrals are frequently refereed to as Slater integrals[4]. In the simulated XAS of **Tb(III)** for the both aforementioned geometries we could reproduce each spectra by reducing the Slater integral on the order of 10-30% of the atomic value, as shown in Fig. 6.20. One can attribute such reduction of the Slater integral to the change of the coordination geometry in each case which affect the Coulomb interactions within the metallacrowns differently in each case. The simulated XAS spectra of **Tb(III)** of each case in Fig. 6.20 shows good agreement with the corresponding experimental one except for the high-energy side of the M_4 edge, where the experimental spectra shows more asymptotic behavior than the simulated one. This can be tentatively explained by electronic excitations from the core to the continuum.

The spin magnetic moments summarized in Table 6.4 show varying values that are needed to be discussed briefly. Although the low-spin state expected for for the **Ni(II)** ions in {**TbNi$_8$**} metallacrowns drop-casted from dichloromethane solution (case A), the experimental result reveals a non-vanishing parallel **Ni(II)** moment of 0.09 μ_B. This small magnetic moment can be traced back to the remaining single **Ni(II)** ion with additional morpholin ligand. This ligand distortion deviates the coordination geometry from the square planar geometry which affects the spin state as well.

The increase of spin magnetic moment of **Ni(II)** ions once drop-casted from the methanol solution is not the same in {**TbNi$_8$**} and {**GdNi$_8$**} metallacrowns. In the {**TbNi$_8$**}.**CH$_3$OH** case, the **Ni(II)** spin magnetic moment is 0.3 μ_B, which is weaker than 0.9 μ_B in the {**GdNi$_8$**}.
CH$_3$OH case. This can be explained by virtue of the exchange coupling between the central **RE(III)** ion and the surrounding **Ni(II)** ions. In {**TbNi$_8$**} metallacrowns, the ferromagnetic exchange coupling **Ni(II)** − **Tb(III)** is relatively weak. Thus, the mutual antiferromagnetic exchange coupling between the **Ni(II)** ions dominates and causes the reduction of **Ni(II)** spin moments. Whereas the **Ni(II)** − **Gd(III)** exchange interaction is stronger and keeps **Ni(II)** spin moments in a parallel orientation with **Gd(III)**spin moments in {**GdNi$_8$**}.**CH$_3$OH** metallacrown. This can be attributed to the larger **Gd(III)** magnetic moment.

On conclusion, our results show the possibility of provoking a spin crossover from a low-spin state to a high-spin state without affecting the integrity of the molecule by chemical reactions. This is could be obtained due to the sensitivity of the **Ni(II)** ions in the metallacrowns to the local electrostatic ligand field showing different coordination geometries depending on the used solvent.

[4]Rigorous mathematical derivation can be found in ref. [384]

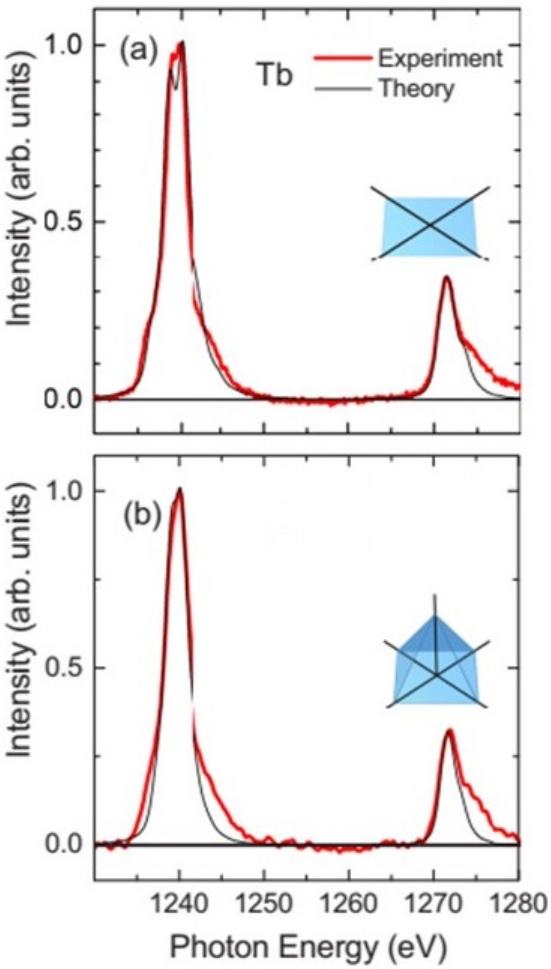

Figure 6.20: **Tb(III)** experimental XAS (solid red) compared to the corresponding XAS spectra simulated by charge transfer multiplet calculations (solid black) [383]. Panel (a) shows the comparison of both spectra for case A in a square planar ligand fields (low spin), as shown in the inset, the crystal-field parameters have been set to zero. The Slater integral reduction has been set to 90% of the atomic value. Panel (b) shows the comparison of the multiplet calculations and experimental data for case B (high spin) with the Slater integral reduction has been set to 70% of the atomic value. [346]

6.3 Anisotropy of 4f states in 3d-4f single molecular magnets

6.3.1 Experimental Procedure

This experiment has been carried out on a single-crystal of metallacrown molecules in the same end-station of previous experiments, VEKMAG at PM2 beamline in BESSY (II) synchrotron facility, but with the fluorescence-yield measurement mode (FY) at varying incident angles at a temperature of 14 K. We investigated a 12-MC-4 single crystal $(^{t}Bu_4N)[Ln^{III}(O_2CBu^{t})_4][12-MC-_{Mn(III)N(shi)}-4]\cdot 5CH_2Cl_2$, **Ln = Gd(III) and Tb(III)**, shortly called $\mathbf{LnMn_4}$, which was synthesized by our collaborator A. Athanasopoulou in the group of Prof. Rentschler, in the chemistry department of Mainz University, based on the synthetic method mentioned in Ref.[113]. Figure 6.21 shows the molecular structure of the single crystal of $\mathbf{LnMn_4}$.Further structure- and magnetic-related information can be found in section 3.1 of this thesis.

The approximate crystal size is 1 mm × 0.5 mm × 200 μm. We glued the crystal with carbon paste on a copper sample holder with the c-axis pointing along the surface normal. The incident x-ray beam has an elliptic spot shape with a size of 50 μm × 100 μm and it is focused on the center of the single crystal.

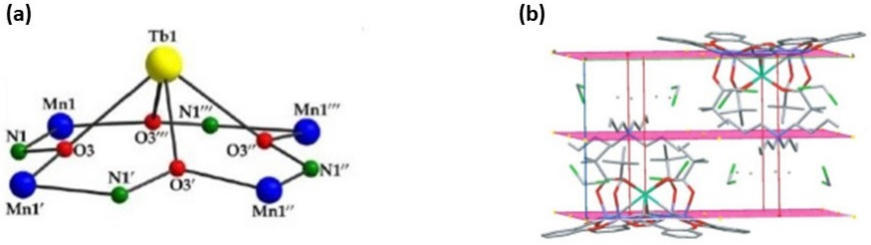

Figure 6.21: (a) Labeled molecular structure of the core $\mathbf{Mn_4^{III}Ln^{III}(\mu-NO_3)_4^{11+}}$of the $\mathbf{LnMn_4}$ complex, where $Ln = Tb(III), Dy(III)$. The colors code of the Elements is shown in the figure, the Hydrogen atoms are omitted for clarity. Image has been adapted from Ref. [113]. (b) Schematic representation of the unit cell of the $\mathbf{LnMn_4}$ complex molecular single crystal.

XAS for right-circular polarization, denoted by I^+, is measured with the applied magnetic filed $\overrightarrow{H}$ oriented parallel to the propagation vector $\overrightarrow{k}$ of the incident x-ray beam. Meanwhile, XAS for left-circular polarization, denoted by I^-, is measured with the applied magnetic filed $\overrightarrow{H}$ oriented anti-parallel to the propagation vector $\overrightarrow{k}$ of the incident x-ray beam. The motorized stage of the sample holder can rotate

around z-axis in both directions creating an angle θ between the normal axis of the single crystal and the incident beam. The measurements were done at varying angles starting from normal incidence ($\theta = 0^{\circ}$) to grazing incidence ($\theta = 80^{\circ}$). Total electron yield (TEY) mode was not a suitable choice for acquiring the drain current signal related to the absorption coefficient due to the electrical insulating properties of the single crystal. Thus, we have applied the fluorescence yield mode to acquire the signal of the fluorescence intensity regardless of the low probability of the fluorescence de-excitation channel (typically around 0.1%) [385]. The fluorescence detector was fixed at angle $\varepsilon = -20^{\circ}$ with respect to the normal axis of the single crystal and it rotates with the sample holder which keeps this angle fixed. Fig. 6.22 shows the schematic diagram of the experimental setup.

The diode quadratic surface has dimensions of 10 mm $\times$ 10 mm and it is placed at 25 mm away of the sample. The detector is covered by aluminum foil to prevent any photoemitted electrons to contribute to the signal.

Similar to previous experimental data of this thesis, the raw data has been post-processed before further data analysis. The experimental data of the fluorescence signal (I_f) of both positive and negative field directions has been normalized to the pre-edge values to account for any systematic field-dependence detection efficiency in the detector. The rest of experimental procedures and the rest of post-processing data regarding the background subtraction and the shift compensation of the two opposite-helicity spectra, can be found in section 6.1.1. Further data analysis of the fluorescence signal (I_f) is mentioned in details in the upcoming section 6.3.3.

6.3.2 Results

The X-ray absorption measurements can be done in three different modes: transmission mode, total-electron yield mode (TEY), and the fluorescence mode (FY). In the transmission mode, one measure the X-ray absorption cross-section (related to the absorption coefficient) directly by measuring the ratio between the intensity of the x-ray beam flux after passing through the sample I to the initial intensity I_0 , $\mu = ln(I/I_0)$. On the other hand, the absorption coefficient in the total electron (TEY) mode and in the fluorescence (FY) mode is measured indirectly from the drain current signal and from the emitted fluorescence photons I_{fl}, respectively [386, 387].

In FY mode, the fluorescence yield is proportional to the absorption coefficient just in the thin samples ($I_{fl} \propto \mu$) but not in the thick ones ($I_{fl} \propto \frac{\mu}{\mu+const.}$) [387]. The latter case is considered as a manifestation of the "saturation effect", where the recorded signal "saturates" and does not change according to the varying energy of the incident photons [272]. Thus, the fluorescence yield in this case is not proportional anymore to the photo-absorption cross-section in the sample. This effect results from several reasons: (i) The modulation of the generated fluorescence yield with the self-absorption to some fluorescence photons. (ii) The fluorescence decay is

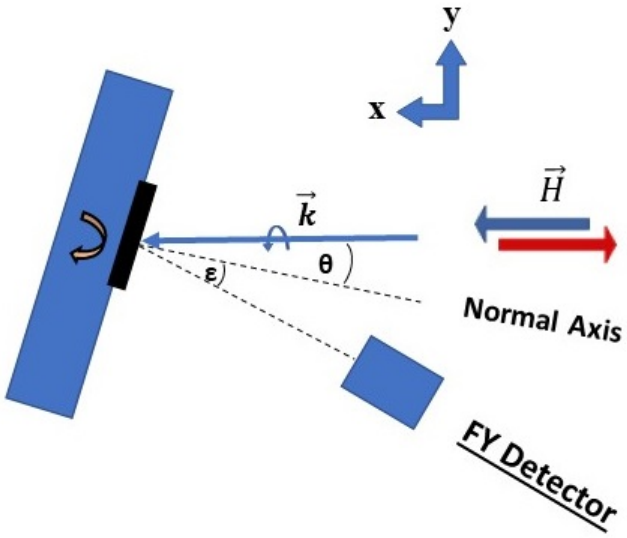

Figure 6.22: Top View: Schematic diagram of the angular-dependent X-ray absorption of $LnMn_4$ single crystal measurements. The Fluorescence Yield (FY) detector has a fixed angle of $\varepsilon = -20^{\circ}$ with respect to the normal axis of the single crystal (black rectangle). The applied magnetic field ($\overrightarrow{H}$) is parallel/anti parallel to the propagation vector ($\overrightarrow{k}$) of the incident polarized x-ray. The sample holder rotates clockwise around z-axis (orange curved arrow) creating an angle θ between the incident beam and the normal axis of the crystal. The measurements were done with varying angle from 0° to 80°.

an X-ray monochromatic emission process which makes it an inverse process to the X-ray absorption process. Thus, the fluorescence decay is dependent on the symmetry of the final state ($3d \rightarrow 2p$) in contrast to the Auger decay in the TEY mode. Consequently, the peaks at the maximum absorption at absorption edges in the FY mode are suppressed comparing to the ones in TEY mode [388]. (iii) The small penetration depth relative to the sampling depth, $\lambda_x cos\,\theta \ll \lambda_{fl}$, where the penetration length is the inverse of the absorption cross-section, $\lambda_x = \frac{1}{Y_{fl}}$, and the sampling depth, λ_{fl}, is the depth where either the Auger electrons or the fluorescence photons can escaped and are detected [389], as shown in Fig. 6.23.

The measured FY, in thick samples, is weighted with an exponential contribution from the generated florescence photons depending on their depth in the sample. Thus, integrating the fluorescence yield over the depth z with integration limits of $0 \rightarrow \infty$, will give us the measured fluorescence intensity $I_{m,fl}$ [389]:

$$I_{m,fl} = C\frac{1}{1+\frac{\lambda_{fl}}{\lambda_x\,cos\,\theta}}\,Y_{fl}, \tag{6.18}$$

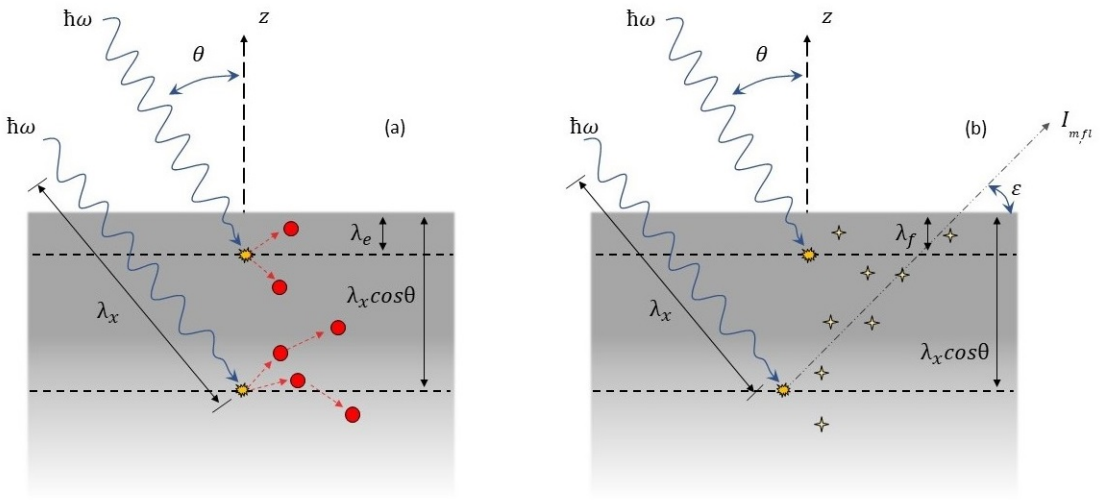

Figure 6.23: Schematic diagram of TEY measurement mode (a) and FY measurement mode (b). In X-ray absorption measurements, the absorbed atoms (yellow irregular shape) de-excite themselves via two de-excitation probabilistic channels either by releasing Auger electrons (red circles, 99.2%) or fluorescence photons (yellow stars, 0.8%). The incident X-ray photon with energy $\hbar\omega$ penetrates the sample with angle θ reaching a penetration depth of $\lambda_x cos\,\theta$. The electrons reach the sampling depth λ_e will contribute to the TEY intensity spectrum in TEY mode. In the FY mode, on the other hand, the measured FY spectra ($I_{m,fl}$) results from acquiring the generated fluorescence photons reached sampling depth and leaving the sample with take-off angle ε.

where $\lambda_x cos\,\theta$ is the angular-dependent x-ray penetration depth, λ_{fl} is the sampling depth, and the proportionality constant C is given by $C = \frac{I_0 G \lambda_{fl}}{cos\,\theta}$ where the G is the fluorescence gain function which describes the average number of detected fluorescence photons per absorbed x-ray photon. The fluorescence intensity corrected for self-absorption is denoted by Y_{fl}, which is the one related to the absorption coefficient, $Y_{fl} = \frac{1}{\lambda_x}$. The "saturation" has a geometry factor which makes it larger at grazing-incidence angles and weaker at normal-incidence angles [390]. The proportionality constant $C = \frac{I_0 G \lambda_{fl}}{cos\,\theta}$ reflects this property where it increases with increasing λ_{fl} and at grazing incidence according to the $cos\,\theta$ in the denominator. This can be attributed to the increased number of generated fluorescence photons close to the surface which can be detected. In fact, at grazing-incidence the lack of photons absorption is what creates the saturation of the FY signal where the generated fluorescence photons become more dependent on the incident photons energy instead being dependent on the absorption cross section of the sample [389].

By solving Eq. 6.18 for Y_{fl}, one obtains:

$$Y_{fl} = \frac{a}{1 - bI_{N,fl}} I_{N,fl}, \tag{6.19}$$

where $I_{N.fl} = \frac{I_{m,fl}}{I_0}$ is the normalized measured spectrum, the parameter $a = \frac{cos\,\theta}{G\lambda_{fl}}$ represents an energy-independent factor that is used to normalize Y_{fl} to its maximum value at the M_5 (L_3) maximum, and the parameter $b = \frac{1}{G}$ can be obtained from the branching ratio – $\frac{I(M_4)}{I(M_5)}$ for $4f$ and $\frac{I(L_2)}{I(L_3)}$ for $3d$ – of a reference XAS spectra of a drop-casted sample measured in TEY mode for the investigated element. Eq. 6.19 results the corrected FY intensity which is proportional to the absorption coefficient of the sample and the spin-polarized absorption.

6.3.2.1 XAS & XMCD of $TbMn_4$ single-crystal

Figure 6.24 shows the comparison between the as-measured fluorescence spectra $I_{m,fl}$ with the corrected fluorescence signal Y_{fl} derived from Eq. 6.19 for the metallacrown **$TbMn_4$** single crystal.

The XAS spectrum of **Mn** [Fig. 6.24(a) and 6.24(b)] is dissimilar to the absorption spectrum of pure **Mn(III)**[391]. In fact, the spectrum has some contribution from **Mn(II)** resulting with a narrow peak around 641 eV followed by two shoulder peaks at 3 eV and 5 eV on the high-energy side and a barley seen a shoulder peak around 639 eV on the low-energy side. The extended tail of the high-energy side of L_3 edge is a characteristic feature of the **Mn(III)** absorption spectra which is superimposed with the aforementioned shoulder peaks from **Mn(II)** spectrum in our case [Fig. 6.24(b)]. Besides that, the **Mn(III)** spectrum shows a significant peak at L_2 edge which is suppressed in case of the **Mn(II)** XAS spectrum. All these contributions suggest that the **Mn(III)** ions in the single crystal experience a partial photoreduction due to the X-ray radiation during the measurement on a time scale faster than the one of one spectrum. Furthermore, this reduction leads to changes in the magnetization state of the **Mn** ions in the single crystal. For the

Mn(III) state, one expects a vanishing XMCD signal due to the antiferromagnetic exchange interaction between theses peripheral ions. In contrast, one obtains a significant XMCD signal for the **Mn** ions as which is an indicator for the presence of a magnetic moment.

The FY of XAS spectra of **Tb(III)**[Fig. 6.24(c) and 6.24(d)] shows less saturation than the **Mn** ions. One can attribute this to the four times less **Tb(III)** ions number comparing to **Mn** ions. The fluorescence yield Y_{fl} XMCD signal, at normal incidence, shows a large negative peak at M_5 edge and a small positive peak at M_4 edge. The orbital and spin magnetic moments derived from the sum rules, Eq. 6.3 and Eq. 6.6, have the values of 3.3 μ_B and 3.0 μ_B, respectively. The effective spin magnetic moment deviates from the one calculated by Hund's rules due to the T_z term contribution [279, 392].

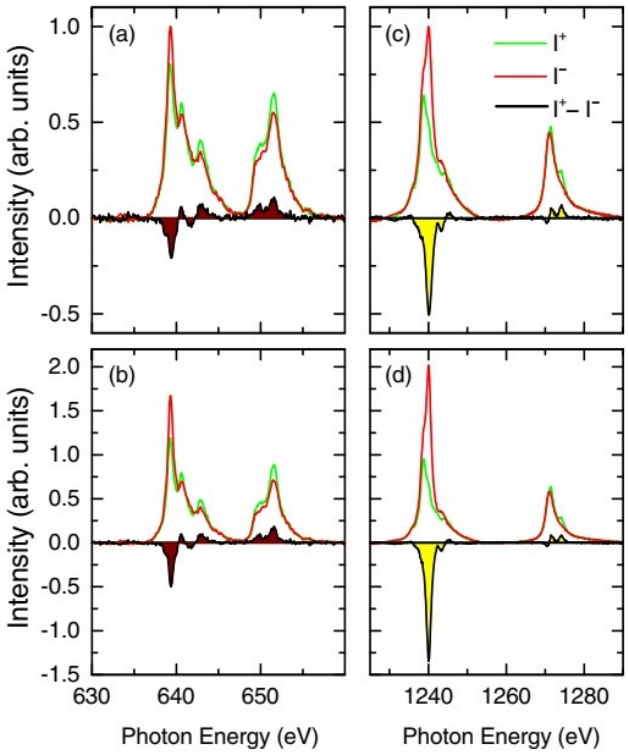

Figure 6.24: Panels (a)-(c) show the as-measured X-ray FY intensity $I_{m,fl}$ measured for circular polarized x-ray light parallel, I^+, and antiparallel, I^-, to the applied magnetic field for (a) **Mn** $L_{2,3}$ and (c) **Tb(III)** $M_{4,5}$. The XMCD signal is calculated from the difference of $I^+ - I^-$, and it is depicted as a black line. Panels (b)-(d) show the corrected FY intensity Y_{fl} from the above panels, following Eq. 6.19, for (b) **Mn** $L_{2,3}$ and (d) **Tb(III)** $M_{4,5}$. All spectra are measured at normal incidence on $\mathbf{TbMn_4}$ metallacrown. [347]

Figure 6.25(a) shows the angular-dependent X-ray fluorescence yield Y_{fl} spectra at $M_{4,5}$ absorption edges of **Tb(III)** in the $\mathbf{TbMn_4}$ single crystal. The spectral

shape retains its shape with negligible changes at the absorption peak at the M_4 edge. On the other hand, the absorption peak at the M_5 edge shows a change in the the ratio of two peaks A and B, located at 1238.9 eV and 1240.1 eV in the normal incidence spectrum, respectively. The peak ratio shows a systematic increase with decreasing the incident angle, as it is shown in Fig. 6.26(a). This can be attributed to an asymmetric occupation of $4f$ orbitals which will be discussed in the discussion part of this section.

The XMCD spectra show a slight angular-dependent variation at the positive pre-edge peak of the M_5 absorption edge, as shown in Fig. 6.25(b). This slight variation can be ascribed to a probing depth dependence and/or angular dependence of the saturation and self-absorption. Besides that, the XMCD at grazing angles shows an increase of the magnitude of the negative peak at the M_5 absorption edge.

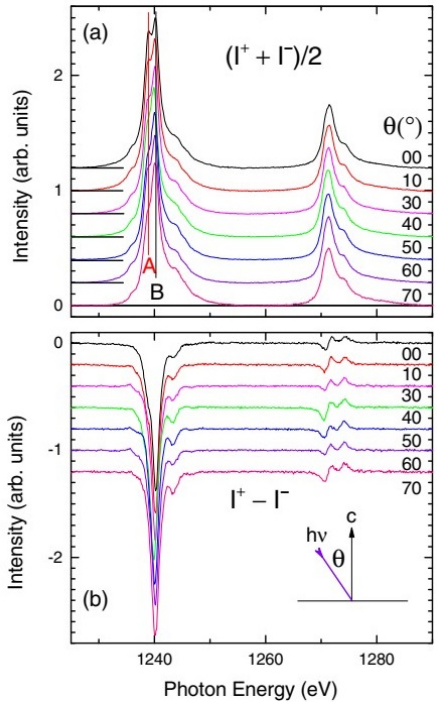

Figure 6.25: Angular-dependent (a) X-ray fluorescence yield Y_{fl} spectra at $M_{4,5}$ absorption edges of **Tb(III)** in the $\mathbf{TbMn_4}$ single crystal, $\frac{I^+ + I^-}{2}$, as a function of the incident photon's energy with angle θ. The two characteristic peaks are labeled with two straight lines named of **A** and **B.** The corresponding XMCD spectra $I^+ - I^-$ is shown in panel (b). [347]

The spin- and orbital-angular momenta calculated from the sum rules, Eq. 6.6 and Eq. 6.3, show a slight angular-dependence variation, see Fig. 6.26(b). One expects the effective spin magnetic moment values resulting from the sum-rules to deviate from the one calculated from the Hund's rules because of the T_z – dipole operator – term , $m_{spin}^{eff} = m_{spin} + 6 < \mathbf{T_z} >$. Because of the negative value of T_z, one expects the measured effective spin moment to be smaller than the Hund's values. Meanwhile the numerical calculations done by Ref. [279] shows the ground-state of $T_z = -0.243$, the Hund's rules predict $T_z = -0.333$. This lead to a reduction of the measured effective spin magnetic moment by $2\,\mu_B$ if the spin is fully aligned along the easy axis.

Due to the strong spin-orbit coupling of $4f$–orbitals, one can argue that T_z term is angular-independent leading to the rotation of spin density component with the charge component in the T_z term. Thus, this reduction is the same for all the measured effective spin magnetic moments at different angular values. We can recover the expected ionic value, $\mu_{spin} = 6\,\mu_B$, at grazing angles ($\theta \to 90°$), as shown in Fig. 6.26(b).

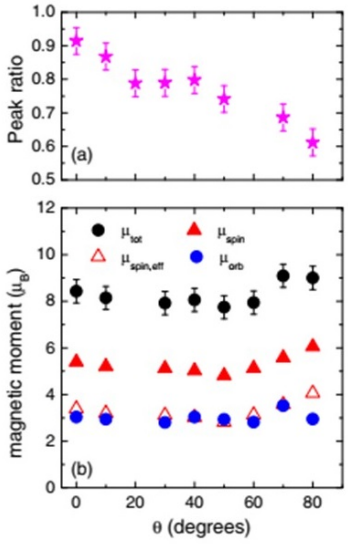

Figure 6.26: (a) The peak ratio of **A** and **B** peaks, in Fig. 6.25, as a function of the incident angle θ. (b) Angular-dependent **Tb(III)** magnetic moments. $\mu_{spin,eff}$ and μ_{orb} stand for the effective magnetic moment and orbital magnetic moment calculated from the XMCD sum-rules, respectively. μ_{spin} represents the corrected spin magnetic moment considering the T_z term. μ_{tot} is the total magnetic moment; $\mu_{tot} = \mu_{spin} + \mu_{orb}$. [347]

6.3.2.2 XAS & XMCD of $DyMn_4$ single-crystal

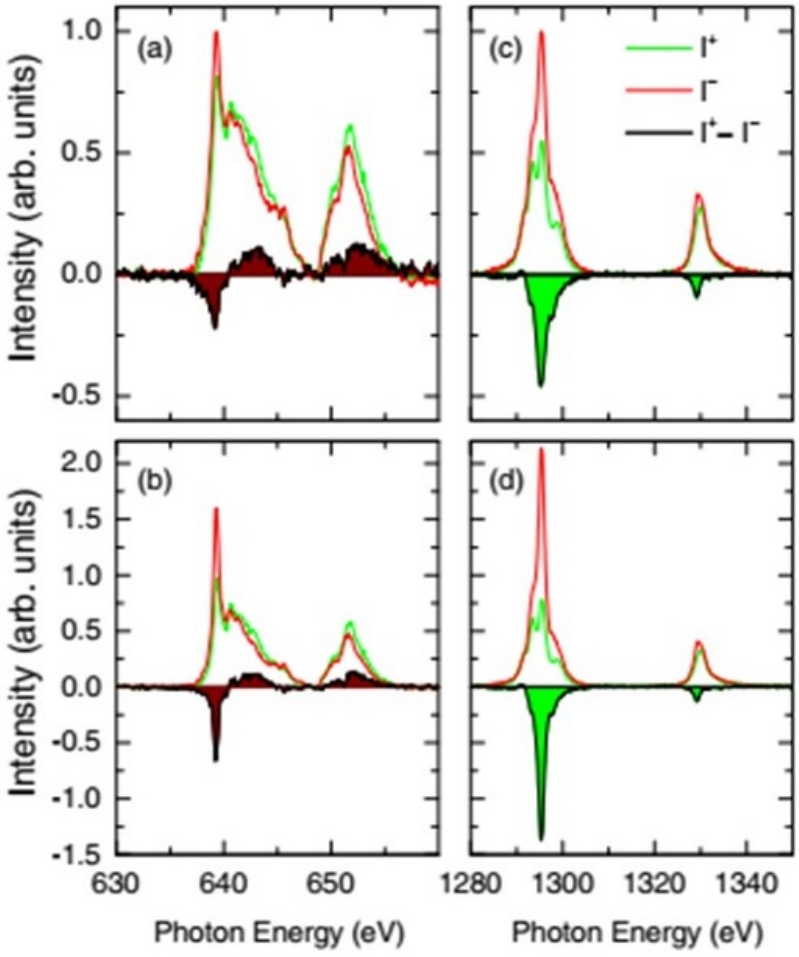

Figure 6.27: Panels (a)-(c) show the as-measured X-ray FY intensity $I_{m,fl}$ measured for circular polarized x-ray light parallel, I^+, and antiparallel, I^-, to the applied magnetic field for (a) **Mn(II)** $L_{2,3}$ and (c) **Dy(III)** $M_{4,5}$. The XMCD signal is calculated from the difference of $I^+ - I^-$, it is depicted as a black line. Panels (b)-(d) show the corrected FY intensity Y_{fl} from the above panels , following Eq. 6.19, for (b) **Mn(II)** $L_{2,3}$ and (d) **Dy(III)** $M_{4,5}$. All spectra are measured at normal incidence on the $\mathbf{DyMn_4}$ metallacrown. [347]

Figure 6.27 shows the comparison between the as-measured fluorescence spectra $I_{m,fl}$ [Panels 6.27(a) – 6.27(c)] with the corrected fluorescence signal Y_{fl} [Panels 6.27(b) – 6.27(d)] derived from Eq. 6.19 for the metallacrown $\mathbf{DyMn_4}$ s ingle crystal.

Similar to the previous case of $\mathbf{TbMn_4}$, the XAS spectrum of **Mn** [Fig. 6.27(a) and 6.27(b)], in the $\mathbf{DyMn_4}$ single-crystal, shows a mixture of **Mn(II)** and **Mn(III)**

ions contributions but with slightly different ratios. This is clear from the suppression of the two shoulder peaks on the high-energy side of L_3 edge, which they are more pronounced in the case of **$TbMn_4$** single-crystal. Correspondingly, the XMCD signal of **Mn** ion is different where it is slightly smaller than in the case of **$TbMn_4$**. This is attributed to the different contributions of **Mn(II)** in both cases.

The XAS of **Dy(III)** retrieve its characteristic shape after the saturation correction [Fig. 6.27(c) and 6.27(d)]. The XMCD signal shows pronounced negative peak at the absorption edge of M_5 and a smaller one at M_4 edge. The sum rule analysis of this XMCD spectrum yield an effective spin magnetic moment of 2.5 μ_B and an orbital magnetic moment of 2.9 μ_B. These values are around half of the values derived from Hund's rules. Since this measurement were recorded at normal incidence, then angular-dependent measurement can shed some light on the assumption of the anisotropy of this single crystal.

Figure 6.28(a) shows the angular-dependent X-ray fluorescence yield Y_{fl} spectra at $M_{4,5}$ absorption edges of **Dy(III)** in the **$DyMn_4$** single crystal. The XAS spectral shape does not show changes at different angles at the absorption peak of M_4 edge. On contrary, the absorption peak of M_5 edge shows a monotonous change of the ratio of two peaks **A** and **B**, located at 1293.5 eV and 1295.6 eV in the normal incidence spectrum, respectively. The peak ratio shows a systematic increase with decreasing the incident angle, as it is shown in Fig. 6.30(a). This result ties well with previous one of **$TbMn_4$** single-crystal indicating an asymmetric occupation of the $4f-$orbitals. In addition to that, the XMCD signal remains unchanged except for an increase of the magnitude of the negative peak at the M_5 edge at grazing angels, as shown in Fig. 6.28(b). The simulated angular-dependent XAS spectra, Fig. 6.29, is calculated using the quantum many-body program QUANTY [393].

The crystal-field Hamiltonian used for the calculation is

$$H_{CF} = H_{ATOM} + H_{FIELD}, \tag{6.20}$$

where H_{ATOM} yields the energy of the free atom including the kinetic , Coulomb interaction and the spin-orbit interaction. Meanwhile, the H_{FIELD} yields the Zeeman energy from the interaction with the magnetic induction field $\mathbf{B = 7T}$ and the surrounding ligands as a perturbation [365]. An asymmetric crystal field reproduces, with good agreement, the angular-dependent XAS of **Dy(III)** in the **$DyMn_4$** single crystal, Fig. 6.29(a). The spectral feature, peak **A** at the M_5 edge, is reproduced at varying angles and the peak ratios of the simulated XAS spectra match to a great extent the peak ratios of the measured XAS spectra, as shown in Fig. 6.30(a). The simulated XMCD, Fig. 6.29(b), also shows a comparable shape to the measured XMCD signal with increasing of the magnitude of the negative peak at the M_5 absorption edge at grazing angles.This asymmetric field generates an anisotropic charge distribution of the $4f$ states which in turn lead to an angular dependence of FY spectra. This effect was simulated by angular-dependent mixing of the circular left and right polarization with linear z-polarization in the calculated excitation spectra.

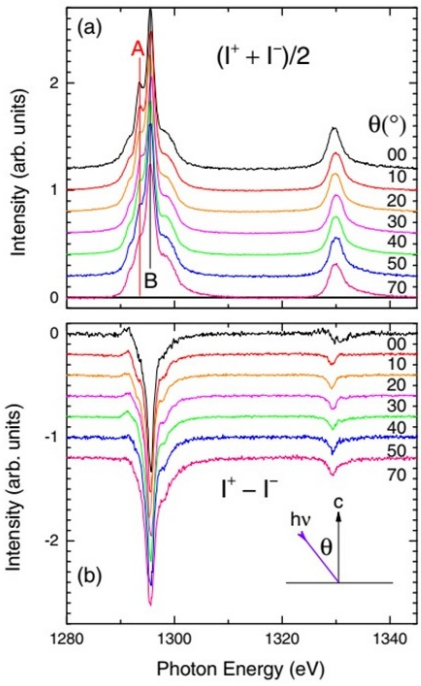

Figure 6.28: Angular-dependent (a) X-ray fluorescence yield Y_{fl} spectra at $M_{4,5}$ absorption edges of **Dy(III)** in the $\mathbf{DyMn_4}$ single crystal, $\frac{I^+ + I^-}{2}$, as a function of the incident photon's energy with angle θ. The two characteristic peaks are labeled with two straight lines named of **A** and **B.** The corresponding XMCD spectra $I^+ - I^-$ is shown in panel (b). [347]

The measured XMCD effective spin-magnetic moments and orbital moments of **Dy(III)**, calculated from corrected Y_{fl} spectra at varying angles, demonstrate the monotonous increase of the magnetic moment values from perpendicular to grazing incidence angles θ, as shown in Fig. 6.30(b). The orbital magnetic moment increases from 3 μ_B for perpendicular incidence to 5 μ_B at grazing incidence, which is close to Hund's value.

The effective spin magnetic moment for **Dy(III)** contains the anisotropic contribution from $\mathbf{T_z}$ dipole term, as written in Eq. 6.6. Based on that equation, one can deduce the maximum value of $\mathbf{T_z}$ from the difference between the maximum effective spin magnetic moment at grazing incidence and the expected pure spin moment calculated from Hund's rules ($\sim 5\ \mu_B$). This yields the value $T_z = -0.2\,\mu_B$ which is a reasonable value since it lies between Hund's rules value (-0.332) and the numerical calculation ($T_z = -0.128\,\mu_B$) derived from Ref. [279].

The total Dy moment increases from perpendicular incidence to grazing incidence to reach a maximum value of 11 μ_B at grazing incidence, as shown in Fig. 6.30(a). This value is larger than the ionic value of 10 μ_B, which entails a correction procedure to recover the magnetic moments values. The correction procedure takes the magnetic moments values calculated from the simulated spectra, Fig. 6.29, into account. Fig. 6.31 (a) shows the magnetic moments calculated by the sum-rules of the simulated spectra. Based on the ratio of the magnetic moments of the ionic value and the magnetic moment of the simulated spectra at each angle,

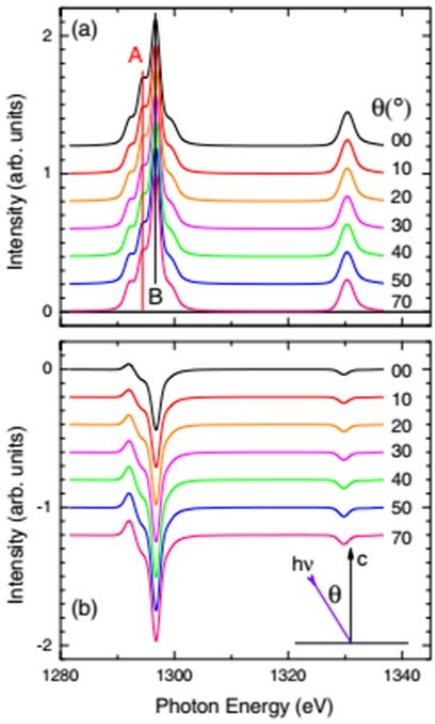

Figure 6.29: (a) Simulated XAS of the **Dy(III)** $M_{5,4}$ absorption edges as a function of the incident angle θ. (b)The corresponding Angular-dependent XMCD simulated spectra. [347]

an angular-dependent correction factor can be obtained. Fig. 6.31(b) shows the corrected **Dy(III)** magnetic moments, in single crystal $\mathbf{DyMn_4}$, yielded from the multiplication of the correction factor with the experimental values of Fig. 6.30(b).

The magnetic moments in Fig. 6.31(b) have values below the ionic value of 10 μ_B yet the absolute value has not been recovered. This can be attributed to the suppression of the FY spectra due to the final state dependence of florescence emission, which is not the case in TEY. In addition to that, the thermal energy of the finite temperature and the magnetic field of the experiment are additional factors to reduce the magnetic moment in the sample.

Overall these findings are in accordance with findings reported by Athanasopoulou et al. in Ref. [113] for the poly-crystalline material of the same molecule for the same temperature and the magnetic field. The most interesting observation in Fig. 6.30(b) is the clear dip of the magnetic moments at $\theta = 40°$ which is reduced by 30% with respect to the larger values observed for perpendicular and grazing incidence.

This reduction can be attributed to a magnetic anisotropy which is not considered in the crystal field Hamiltonian, Eq. 6.20. This will be discussed in detail in the discussion part of this subsection.

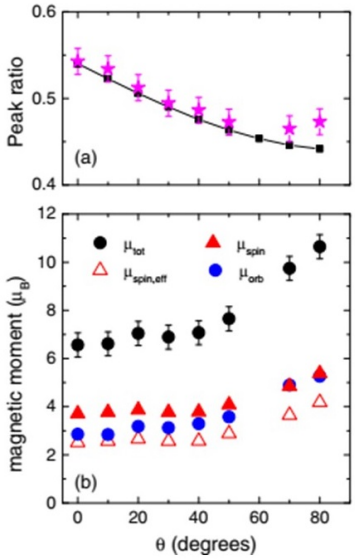

Figure 6.30: (a) The peak ratio of **A** and **B** peaks, in Fig. 6.28, as a function of the incident angle θ plotted with pink stars. The solid black dots represent the simulated values and the solid line is a guide for the eye. (b) Angular-dependent **Dy(III)** magnetic moments. $\mu_{spin,eff}$ and μ_{orb} stand for the effective magnetic moment and orbital magnetic moment calculated from the XMCD sum-rules, respectively. μ_{spin} represents the corrected spin magnetic moment considering the T_z term. μ_{tot} is the total magnetic moment; $\mu_{tot} = \mu_{spin} + \mu_{orb}$. [347]

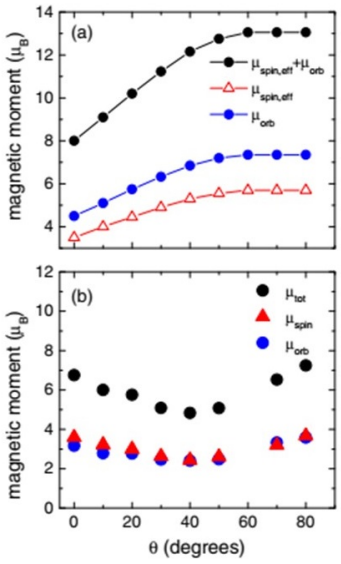

Figure 6.31: (a) Angular-dependent **Dy(III)** magnetic moments of the simulated XAS. $\mu_{spin,eff}$ and μ_{orb} stand for the effective magnetic moment and orbital magnetic moment calculated from the XMCD sum-rules for the simulated XAS spectra, respectively. μ_{tot} is the total magnetic moment; $\mu_{tot} = \mu_{spin} + \mu_{orb}$. (b) The corrected spin, orbital and total magnetic moments of **Dy(III)** according to the correction procedure mentioned in the text.[347]

6.3.3 Discussion

Due to the localization of the $4f-$ orbitals, one can consider the rare-earth ions in molecules, or even in solids, as if they are free ions. Hence, one expects the ground-state with total angular momentum J and its component $J_z = m_J$ to be obtained from Hund's rule, which is $^7F_6$ for **Tb(III)** and $^6H_{15/2}$ for **Dy(III)**. Following the localization of the $4f-$orbitals and being shielded by $5d$ and $6s$ orbitals, the crystal field of the surrounding ligand is considered as a perturbation on the $4f$ shells. This splits the ground multiplet state J into $2J+1$ m_J-states from $-J$ to $+J$ [370].

The different $4f-$orbitals have an ashperical angular-dependency shape ranging from oblate (equatorial expanded like a pill) to a prolate shape (like a cigar), as shown in Fig. 6.32(a). The number of electrons occupying these orbitals determine the overall shape of the shell electron distribution. Thus, the charge distribution shapes range from pure oblate (as in the case of **Ce(III)**) to the pure prolate (as in the case of **Yb(III)**) [394, 395].

As a matter of fact, each microstate m_J has its own unique angular dependence, and this is what leads to the slow relaxation of the magnetization in such molecules depending on the ligand field environment [395, 396]. The charge density of the ground state of the $4f-$orbital of **Tb(III)** ion (with $m_J = 6$) has an oblate shape, meanwhile the ground state of **Dy(III)** ion (with $m_J = 15/2$) has a barrel shape, as shown in Fig. 6.32(b).

The shell-selectivity of the XMCD measurements probes the projections of the orbitals in the direction of the incident polarized beam of photons. This enables us to detect the orbitals at different angles by shinning the polarized light at different angles on the sample. In the case of the absence of any anisotropy one expects the same total magnetic moment of the element to be the same at all the angles. Yet, Fig. 6.31(b) shows a systematic change in the total magnetic moment represented by a clear dip around $\theta = 40°$ and maximum values at grazing and perpendicular incidences.

The reduction in the total magnetic moment emerged from two origins: (i) The presences of the T_z term which is due to the anisotropic charge distribution of the $4f-$orbital itself [279]. This leads to a reduction of the spin magnetic moment. (ii) The anisotropy of the orbital magnetic moment orientation due to the minimization of the interaction energy with the surrounding ligand field [397].

The strong spin-orbit coupling in **RE(III)** ions causes the spin density and the charge density to rotate together leading to an angular-independent T_z term, as it is envisaged in Fig. 6.33. This makes the correction for the T_z term reduction easier than the case of weak spin-orbit coupling, as it has been done in the previous section.

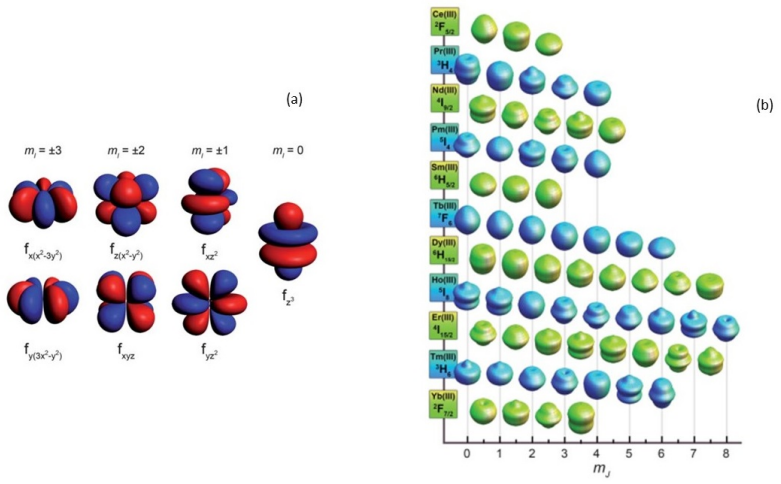

Figure 6.32: (a) Graphical representation of the charge density of $4f$-orbitals in **RE(III)** ions. The highest magnitude $m_l = \pm 3$ shows a pure oblate shape, meanwhile the lowest magnitude $m_l = 0$ shows a pure prolate shape. (b) Graphical Representations of several m_J state for the lowest spin-orbit coupled (J) state for **RE(III)** ions. Each m_J state has different angular dependence ranging from pure oblate to pure prolate for the same state for the same **RE(III)** ion, as in the **Tb(III)** ion. Images are taken from Ref.[395].

The dip at $\theta = 40°$ is a clear indication that the magnetic easy axis is along the fourfold symmetry axis and perpendicular to it. Meanwhile, the magnetic hard axis lies between them close to 45°. A plausible explanation can be introduced based on the electrostatic interaction between the surrounding ligand field and the $4f-$orbital charge density of the **RE(III)** ion. Several authors ran different computations to justify this simple model [398, 399]. But here, we stick solely to the qualitative explanation of the angular variation of the magnetic moments based on this model.

By approximating the surrounding ligand field in $\mathbf{REMn_4}$ crystals with an octahedral symmetry with small tetragonal distortion, the barrel shape of the ground state of **Dy(III)** ($m_J = 15/2$) will interact differently than the oblate shape of the ground state of **Tb(III)** ($m_J = 6$). Fig. 6.34(a) depicts the anisotropic energy due to the electrostatic interaction along certain directions.

The barrel-like **Dy(III)** $4f$ charge distribution of the ground state causes a maximum electrostatic energy for $\theta = 45°$ where the barrel edges approach the surrounding ligand charges and this increases the electrostatic energy and consequently contribute to the magnetic anisotropy energy. On the other hand, the minimum energy takes place when the symmetry axis is at $\theta = 0°, 90°$ where the electrostatic interaction is lowered. The oblate ellipsoidal $4f$ charge distribution of the ground state of the **Tb(III)** ion interacts differently with the surrounding ligand charges. The equatorial extended charge distribution experiences a minimum electrostatic interaction along the perpendicular symmetry axis orientation, at $\theta = 0°$. The electrostatic energy keeps increasing with increasing θ to reach the maximum at $\theta = 90°$, as shown in Fig. 6.34(a). This suggests a uniaxial magnetic anisotropy with an easy axis along $\theta = 0°$ and a hard magnetic axis along $\theta = 90°$.

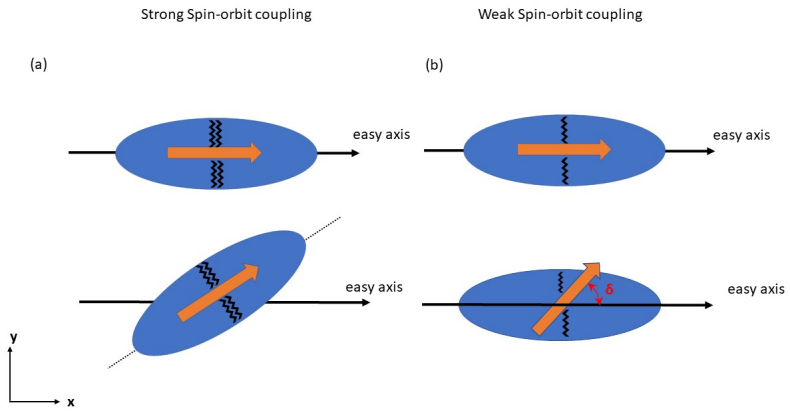

Figure 6.33: A schematic diagram for the spin and charge density co-rotation in a strong spin-orbit coupling **RE(III)** ion (a). This creates an angular-independent T_z term in the effective spin magnetic moment m_{spin}^{eff} in Eq. 6.6. In case of weak spin-orbit coupling (b), the T_z term is angular-dependent due to the deviation of angle δ between the spin density and the symmetry axis of the anisotropic charge density.

A multiplet calculations for spectral data were performed, by our collaborators, including an octahedral field with crystal-field parameters B_{40} and B_{60}. By setting $B_{40} = 0.04$ eV and $B_{60} = 0$, the calculated magnetic moments reduction of **Tb(III)** and **Dy(III)** have opposite values, as depicted in Fig. 6.34(b). This indicates an opposite sign of the fourth-order magnetic anisotropy constant in a sense that the magnetic hard axis of the **Dy(III)** at $\theta = 45°$ is an easy axis of **Tb(III)**. This dovetails with the suggested magnetic anisotropy of both molecules in Fig. 6.34(a). The larger the magnetic anisotropy is the larger the reduction of the magnetic moment and hence the minimum of the magnetic moment is obtained, which ties well the experimental corrected plot of Fig. 6.31(b). To substantiate the fourth-order anisotropy of **Dy(III)** ion, the magnetic moment reduction at $\theta = 45°$ has been plotted versus the crystal-field parameter B_{40} in Fig. 6.34(c). The reduction increases non-linearly with increasing the parameter B_{40} which is another proof of the fourth-order magnetic anisotropy on this molecule. Moreover, the calculated magnetization curves (with parameters $B_{40} = 0.04$ eV and $B_{60} = 0$ eV) along the hard- and easy-axis display a reduction of the magnetic moment with respect to the saturation around 60% and 80%, respectively, for $T = 14$ K and in a field of 7 Tesla, as shown in Fig. 6.34(d), which is in fair agreement with the experimental observation.

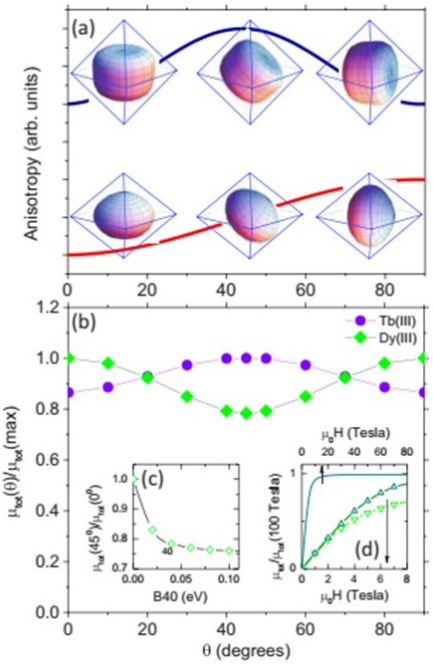

Figure 6.34: (a) Sketch of the fourth-order anisotropy energy of the $4f$ orbital ground state barrel-shape of **Dy(III)**(blue, Top) and the second-order oblate **Tb(III)** ground state (red, Bottom). The crystal-field is simulated with an octahedral ligand field with small tetragonal distortion. It is clear from the figure that **Dy(III)** has a hard axis at $\theta = 45°$, and easy axes along $\theta = 0°$and$\,90°$. Meanwhile, **Tb(III)** has an easy axis at $\theta = 0°$ and hard axis at $\theta = 90°$. (b) The angular-dependence magnetic moments derived from the multiplet calculation for **Tb(III)** (solid circle) and for **Dy(III)** (diamonds) normalized to the maximum value of each. The crystal ligand field parameters are $B_{40} = 0.04$ eV and $B_{60} = 0$ for T = 14 K and $\mu_0 H =$ 7 T. (c) The ratio of the **Dy(III)** magnetic moment along the magnetic hard axis to the easy axis as a function to the crystal-field parameter $B_{40} = 0.04$ eV for T = 14 K and $\mu_0 H = 7$ T. (d) Calculated magnetization curves for $B_{40} = 0.04$ eV for T = 14 K normalized to the saturation value at $\mu_0 H = 100$ T (solid line, top abscissa). The magnetization is calculated on smaller scale for $\mu_0 H = 7$ T (bottom abscissa) for $\theta = 0°$ (up-triangles, full line) and for $\theta = 45°$ (down-triangle, dotted line). [347]

In summary , the investigation of the heterometallic $3d-4f$ molecular complexes can be done in an element-wise manner down to the atomic level using the synchrotron-based XMCD technique. This is contrary to the conventional lab-based magnetometry techniques which provides us with the macroscopic magnetization measurements. Consequently, this can function as a considerable feedback for the rational designs of the molecular spintronics building blocks introduced earlier by several authors [395, 399, 400].

Our findings on the **REMn$_4$** single-crystals provide a clear support on such accuracy and controllability where we could observe an angular-dependent asymmetric occupation of the $4f-$orbitals in **RE(III)** ions caused by the varying angular-dependent crystal-field perturbation. Despite the limitations of the fluorescence-mode detection due to the saturation effect, we could correct the XAS deviation based on the branching ratio of the reference of the normal incident TEY XAS spectra for each element apart. However, the FY spectra still exhibit deviations from the pure absorption spectra -even after the corrections- due to the strong dependence of the fluorescence photons on the final state which affects the results of the sum-rule analysis. Thus, simulated angular-dependent FY spectra can be obtained using crystal field multiplet calculations.

The sum-rule analysis of these simulated spectra provided us with additional correction for the magnetic moments derived from the experimental XAS spectra. The magnetic moments of the **RE(III)** ions prevail the total molecular magnetic moment by virtue of their large orbital magnetic moment. This leads to a considerable magnetic anisotropy in the $3d-4f$ **REMn$_4$** molecular single-crystal emanating from the single ion magnetic behavior (SIM) of the **RE(III)** ion.

The analysis of the angular dependent XAS spectra found evidence for fourth-order magnetic anisotropy for **Dy(III)** ions with an easy axis parallel and perpendicular to the plane formed by the 4 **Mn** ions. This results from the electrostatic Coulomb interaction of the aspherical charge density of the ground state of the $4f-$orbitals with the circumferential ligand field charges. The multiplet calculations suggest that the parameter $B_{40} = 0.04$ eV is of utmost importance for the fourth-order anisotropy of **Dy(III)** in these single crystal. Another noteworthy mentioned finding is the second-order anisotropy of **Tb(III)** ions in **REMn$_4$** single crystal. The difference of the anisotropies between **DyMn$_4$** and **TbMn$_4$** originated from the difference in the aspherical shapes of the charge density of the ground states of the $4f-$orbitals of **Tb(III)** and **Dy(III)**, respectively.

From our results one can conclude that any future endeavor of engineering molecules possessing a slow-relaxation of magnetization should include an element-selective measurements technique. The non-damaging intensity of the X-ray beam in the XMCD end-station and the complement multiplet calculation can provide us with insightful evaluation of the magnetic characterization on the molecular level.

Chapter 7

Summary and Outlook

In this thesis, we explored several mixed 3d–4f metallic-centered molecules using highly selective magnetometry and spectroscopy techniques. Unlike simpler mono- or poly-homometallic molecules composed solely of transition metal or lanthanide centers, these mixed-metal systems exhibit complex magnetic exchange interactions, offering new insights into molecular spintronics.

The first part of the thesis focuses on exploratory research into possible spin excitations in $TbNi_2$ molecules deposited on an Fe substrate with varying magnetization orientations (Chapter 5). Initially, non-magnetic tips were employed to obtain topographic measurements of the substrate, ensuring the cleanliness of the W surface, as well as characterizing the coverage and morphology of the Fe thin films. To probe the spin-dependent contributions to these measurements, we utilized an antiferromagnetic Cr-coated tip. This revealed a compact magnetic landscape on the substrate, where regions of in-plane and out-of-plane magnetization coexist. The spin-polarized scanning tunneling spectroscopy (SP-STS) spectra confirmed the characteristic occupied states of the Fe monolayer (ML) and double-layer (DL) at distinct energies, 440 meV and 620 meV, respectively.

The integrity of the deposited molecules was confirmed by matching their measured dimensions with those expected from free gas-phase molecules. Line IETS measurements conducted across a molecule deposited on the Fe DL island showed systematic changes in the spectra as the tip approached the molecule, suggesting the occurrence of additional inelastic excitations. These inelastic excitations could arise from multiple mechanisms, such as Coulomb blockade, vibrational stretching modes, or spin excitations. However, the observed excitation energies, which are below 50 meV, allowed us to tentatively rule out Coulomb blockade and vibrational contributions. Consequently, we attributed the observed excitations to possible spin-related phenomena within the molecule.

Using a phenomenological model introduced in Chapter 6, we estimate the energy barrier for magnetization reversal in the molecule to be approximately 13 meV. This value is consistent with the first observed inelastic excitation energy for molecules deposited on both the Fe ML (Fig. 5.11) and DL (Fig. 5.12). However, such back-of-the-envelope calculation remains speculative without further $ab-initio$ cal-

culations to unravel the intricate $3d$–$4f$ magnetic exchange interactions present in the molecule. As such, caution must be exercised before definitively linking these inelastic excitations to the magnetization reversal of the shielded Tb(III) 4f ground state.

To our knowledge, this work represents the first report of inelastic excitations in mixed 3d–4f metallic-centered molecules deposited on a magnetic substrate and probed with a spin-polarized STM tip. This study lays the groundwork for future investigations into similar systems, with an emphasis on advanced theoretical approaches such as $ab-initio$ methods. In the outlook section that follows, we propose hypotheses and future experimental directions to further explore the origins and implications of these spin excitations.

One of the primary challenges in STM measurements is mitigating mechanical vibrations and electrical noise. To address mechanical vibrations, the STM system incorporates an internal eddy-current damper and is mounted on a damping platform equipped with an active piezo actuator. However, since the STM setup is located on the first floor rather than in a basement, it remains susceptible to low-frequency vibrations. This limitation necessitates conducting measurements overnight to minimize human-induced disturbances.

During the measurements, it was observed that the voltage divider connected to the lock-in amplifier introduced noise into the tunneling current signal, leading to its removal. As a result, the minimum achievable modulation voltage was approximately 6 mV, limited by the lock-in amplifier. This constraint hindered the exploration of potential spin excitations at lower energies, which would require modulation voltages in a reduced range. To mitigate statistical errors, multiple measurements with different microtips are typically required. However, due to time constraints, this approach could not be fully implemented in the current study. Nevertheless, 5–20 repetitions were conducted for some measurements, with reproducibility observed. The resulting data, later, were averaged to minimize noise.

In the spin-polarized scanning tunneling spectroscopy (SP-STS) experiments, the Cr-coated tip was pulsed multiple times to regenerate the microtip during measurements. This introduced another limitation, as the precise amount of Cr remaining on the W-tip after pulsing could not be determined. Despite this, the contrast observed in the dI/dU mapping images (Fig. 5.5) suggests that the tip remained spin-polarized, ensuring the validity of the spin-sensitive measurements.

The second part of the thesis presents results of series of experiments (Chapter 6) addressing the research question of whether the magnetic anisotropy energy barrier of SMMs based on MCs can be enhanced by incorporating a combination of TM and Ln(III) ions. Rare-earth mononuclear SMMs are known for their large energy barriers for magnetization reversal [70]. Conversely, mono- and polynuclear $3d$-based SMMs exhibit high-spin ground states due to strong intramolecular exchange interactions among their metal centers [66]. This makes the hypothesis that combining $3d$ and $4f$ ions within the same molecular scaffold could result in MCs with larger effective energy barriers for magnetization reversal a plausible direction for investigation. Furthermore, incorporating $3d$ ions could quench quantum tun-

neling of magnetization (QTM) by fostering strong exchange interactions between TM and Ln(III) ions, as demonstrated in prior studies [341, 401].

Two groups of metallacrown molecules, namely the heterometallic 12-MC-4 and 15-MC-5, were investigated in this thesis using element-selective synchrotron-based magnetometry technique, X-ray magnetic circular dichroism (XMCD). The $RENi_5$[15–MC–5] molecules and the $RENi_8$[12–MC–4] molecules were drop-cast from solutions onto Si-wafers, whereas $REMn_4$[12–MC–4] molecules were measured in their single-crystal form. Measurements were conducted at low temperatures (T = 7 K) and a magnetic field strength of 7 T, conditions well below the molecule's blocking temperatures and enough to saturate the magnetic moments against the thermal fluctuations. Importantly, the XAS spectra showed no significant changes, even after extended periods of measurement or exposure to radiation, with consistent results for each measured ion. This stability attests to the structural integrity of the molecules during the experiments, reinforcing the reliability of the XMCD technique.

The first investigated molecules is $RENi_5$[15–MC–5] molecules, where RE = Sm(III), Tb(III) and Dy(III). The $DyNi_5$ and $TbNi_5$ molecules are of utmost importance since their SQUID isothermal field-dependent magnetization measurement hints to the presence of an anisotropy energy barrier. Meanwhile, the $SmNi_5$ molecule shows a temperature-independent paramagnetic behavior.

The XMCD measurements revealed that Ni(II) ions are coupled antiferromagnetically. As a result, the Ni(II) scaffold ions, despite having high-spin states (S = 1), contribute minimally to the overall molecular magnetic moment. Also, XMCD measurements show that Ni(II) ions have antiparallel alignment with the central RE ion in the case of Sm(III) but aligned parallel to the central RE in the case of both Tb(III) and Dy(III). The central rare-earth ions, including Tb(III) and Dy(III), displayed spin and orbital moments lower than the theoretical values predicted by Hund's rules, an outcome attributed to the presence of finite magnetic anisotropy. Considering the powder average, the orientation of the projected orbital magnetic moments of RE(III) ion can be calculated as a functional of a tuning parameter for the ratio between the anisotropy and Zeeman energy (r). This tuning parameter (r) can determine the strength of the magnetic anisotropy and hence the ratio between the observed (projected) orbital magnetic moment to the absolute value (theoretical Hund's value), where the later ratio spans the range 0.5 – 1. Based on that, one can determine the anisotropy energy barrier which is found to be around 7 meV (85 K) in the case of Tb(III) and 28 meV (340 K) in the case of Dy(III). The spin-orbit coupling aligns both the spin and orbital moment, thus the ratio r obtained for the RE(III) ions for the orbital magnetic moment holds for the spin moment, too. Based on that, we could deduce the spin orbital magnetic moment from the calculated curve and found it close to the absolute value (Hund's rule) which justifies our model.

The second group of investigated molecules comprises double-decker $RENi_8$[12–MC–4], with RE = Gd(III) and Tb(III). The observed spin magnetic moment of Gd (III) ion is similar to Hund's values, although the orbital magnetic moment is non-vanishing attributing that to the limitations in the sum rules themselves.The

Tb(III) shows a discrepancy of the orbital magnetic moment between the observed and expected Hund's values attributed to anisotropy energy barrier. Following the above mentioned calculation, the energy barrier has value of 5.1 meV.

An intriguing finding was the significant enhancement of the Ni(II) spin moments, which increased threefold when the molecules were dissolved in methanol compared to dichloromethane. This phenomenon is likely due to a spin crossover from a low-spin square planar ligand field (S=1) to a high-spin square-pyramidal ligand field (S=0), caused by methanol molecules coordinating above the Ni(II) ions. This solvent-induced spin switching offers a promising approach to modulate the spin state of the double-decker metallacrown without compromising its structural integrity through chemical reactions.

The third group of molecules investigated includes single crystals of $REMn_4$[12–MC–4] molecules, where RE = Tb(III) and Dy(III). Due to the poor conductivity of these single crystals, fluorescence yield mode was employed for measurements. The fluorescence spectra were carefully processed to mitigate self-absorption and saturation effects resulting from the long escape depth through the thick crystals. Angular-dependent XMCD measurements revealed a dependence of the spin and orbital magnetic moments of Dy(III) on the angle of measurement, indicating the presence of fourth-order magnetic anisotropy. This behavior arises from the anisotropic charge distribution of the RE(III) 4f electrons in the tetragonal crystal field. Simulations of angular-dependent XAS and XMCD spectra, using crystal field multiplet calculations, facilitated the derivation of angular-dependent correction factors for the measured magnetic moments.

The introduced approach in calculating the magnetic anisotropy of $3d-4f$ heterometallic SMMs works well for powder samples in any $3d-4f$ SMMs and eliminates the need to grow highly oriented single crystal for anisotropy measurements. However, it is important to acknowledge the limitations of XMCD measurements. The sum-rule analysis is based on idealized assumptions, necessitating the inclusion of correction factors, which should be applied with caution. Furthermore, these measurements require extended data acquisition times at synchrotron facility beamline end stations.

Outlook

Future research efforts should prioritize theoretical calculations to achieve a more definitive understanding of the observed phenomena. Far-infrared Raman spectroscopy will also be critical for identifying and ruling out any vibrational modes associated with the Ln(III) or TM(II) bonds as potential sources of inelastic excitations observed in the IETS spectra.

A promising direction for future studies would be the synthesis of 3d-4f metallic-centered molecules exhibiting significant antiferromagnetic exchange interaction contribution between the $3d$ and $4f$ centers. This opens the possibility of addressing novel research questions, such as whether it is feasible to manipulate the spin states

of the Ln(III) 4f magnetic moment by altering the spin state of the 3d ion. In other words, can the 3d ion serve as a "knob" to toggle the state of the shielded 4f ion through antiferromagnetic exchange interactions?

Such a mechanism would enable the 4f ion's spin state to be electrically controlled, where the tunneling current from the STM tip interacts primarily with the 3d magnetic moments rather than the shielded 4f magnetic moment. This approach could pave the way for innovative methods of writing information onto shielded 4f ions, leveraging the 3d-4f exchange interaction for spintronics applications.

During the course of this thesis, the deposition of metallacrown (MC) molecules proved to be a significant challenge, with multiple techniques, including electrospray ionization (ESI) and physical vapor deposition (PVD), failing to achieve reliable results. ESI resulted in clogged nozzles, with no observable molecules on the substrate as verified by STM, while PVD caused the metallacrowns to get burned in the thermal evaporator crucibles. Although ESI showed limited success in depositing extremely thin films ($< 0.01\,\mathrm{ML}$) of simpler complexes like $CuCu_4$ and $CuFe_4$, the fragility of these molecules under high temperature or voltage remains a significant limitation. Furthermore, such techniques yield samples with poor signal-to-noise ratios in synchrotron measurements, necessitating alternative, innovative deposition methods.

To enable the integration of $3d{-}4f$ MCs into future devices, surface deposition is critical. A novel proposal was made during this thesis to design a UHV-compatible spin-coating system. The proposed system consists of a compact cubic chamber (~70 mm side length) with three feedthroughs, two viewing windows, and a load-lock valve connecting it to the UHV chamber. A micro-dosing valve injects the molecular solution through the top feedthrough, while a rotary feedthrough drives a lightweight, low-outgassing aluminum spin-coating plate. A third feedthrough with a wobblestick facilitates sample transfer.

To maintain the liquid phase of methanol-based solutions above 10^{-2} mbar at room temperature, the chamber will be flooded with argon gas using a controlled dosing valve. The spin-coating plate will then be rotated at high speed to deposit the molecules evenly. After spinning, the chamber will be evacuated back to high vacuum, allowing rapid sample transfer to the STM chamber within the UHV regime. This design offers a promising pathway for robust and controlled deposition of metallacrowns on surfaces. Time constraints hindered the implementation of this research proposal, but I hope it can be pursued in future research endeavors.

Bibliography

[1] J. M. Dudley. "Defending basic research". In: *Nat. Photonics* 7.5 (2013), pp. 338–339.

[2] O. Stern. "Ein Weg zur experimentellen Prüfung der Richtungsquantelung im Magnetfeld". In: *Zeitschrift für Physik* 7.1 (Dec. 1921), pp. 249–253. ISSN: 1434-601X. DOI: 10.1007/BF01332793.

[3] W. Gerlach and O. Stern. "Der experimentelle Nachweis der Richtungsquantelung im Magnetfeld". In: *Zeitschrift für Physik* 9.1 (Dec. 1922), pp. 349–352. ISSN: 1434-601X. DOI: 10.1007/BF01326983.

[4] G. E. Uhlenbeck and S. Goudsmit. "Spinning electrons and the structure of spectra". In: *Nat.* 117.2938 (Feb. 1926), pp. 264–265. ISSN: 1476-4687. DOI: 10.1038/117264a0.

[5] H. Johnston. *How the Stern–Gerlach experiment made physicists believe in quantum mechanics*. https://physicsworld.com/a/how-the-stern-gerlach-experiment-made-physicists-believe-in-quantum-mechanics/. Nov. 2022.

[6] J. J. Sakurai and Jim Napolitano. *Modern quantum mechanics*. Cambridge University Press, 2017, p. 568. ISBN: 9781108422413.

[7] R. Shankar. *Principles of Quantum Mechanics*. Springer, 2012. ISBN: 9781475705768.

[8] A. Fert et al. "Giant Magnetoresistance of (001)Fe/(001)Cr Magnetic Superlattices". In: *Phys. Rev. Lett.* 61 (21 Nov. 1988), pp. 2472–2475. DOI: 10.1103/PhysRevLett.61.2472.

[9] P. Greunberg et al. "Enhanced magnetoresistance in layered magnetic structures with antiferromagnetic interlayer exchange". In: *Phys Rev B* 39 (7 Mar. 1989), pp. 4828–4830. DOI: 10.1103/PhysRevB.39.4828.

[10] M. Julliere. "Tunneling between ferromagnetic films". In: *Phys. Lett. A* 54.3 (Sept. 1975), pp. 225–226. ISSN: 0375-9601. DOI: 10.1016/0375-9601(75)90174-7.

[11] S. Das Sarma et al. "Spintronics: Fundamentals and applications". In: *Rev. Mod. Phys.* 76 (2 Apr. 2004), pp. 323–410. DOI: 10.1103/RevModPhys.76.323.

[12] T. Tashiro et al. “Spin-current emission governed by nonlinear spin dynamics”. In: *Sci. Rep.* 5.1 (Oct. 2015). ISSN: 2045-2322. DOI: 10.1038/srep15158.

[13] G. Schmidt and L. W. Molenkamp. “Spin injection into semiconductors, physics and experiments”. In: *Semicond. Sci. Technol.* 17.4 (Mar. 2002), pp. 310–321. ISSN: 0268-1242. DOI: 10.1088/0268-1242/17/4/304.

[14] G. A. Prinz. “Magnetoelectronics”. In: *Science* 282.5394 (Nov. 1998), pp. 1660–1663. ISSN: 1095-9203. DOI: 10.1126/science.282.5394.1660.

[15] M. Johnson and R. H. Silsbee. “Interfacial charge-spin coupling: Injection and detection of spin magnetization in metals”. In: *Phys. Rev. Lett.* 55 (17 Oct. 1985), pp. 1790–1793. DOI: 10.1103/PhysRevLett.55.1790.

[16] T. Kimura et al. “Room-temperature generation of giant pure spin currents using epitaxial Co FeSi spin injectors”. In: *NPG Asia Mater.* 4.3 (Mar. 2012), e9–e9. ISSN: 1884-4057. DOI: 10.1038/am.2012.16.

[17] H. Ohno et al. “Electric-field control of ferromagnetism”. In: *Nat.* 408.6815 (Dec. 2000), pp. 944–946. ISSN: 1476-4687. DOI: 10.1038/35050040.

[18] A. Kirihara et al. “Flexible heat-flow sensing sheets based on the longitudinal spin Seebeck effect using one-dimensional spin-current conducting films”. In: *Sci. Rep.* 6.1 (Mar. 2016). ISSN: 2045-2322. DOI: 10.1038/srep23114.

[19] J. Fabian et al. “Theory of spin-polarized bipolar transport in magnetic $p - n$ junctions”. In: *Phys. Rev. B* 66 (16 Oct. 2002), p. 165301. DOI: 10.1103/PhysRevB.66.165301.

[20] M. W. Keller et al. “Nonwhite frequency noise in spin torque oscillators and its effect on spectral linewidth”. In: *Physical Review B—Condensed Matter and Materials Physics* 82.5 (2010), p. 054416.

[21] S. Parkin. *Shiftable magnetic shift register and method of using the same.* US Patent 6,834,005. Dec. 2004.

[22] S. Das Sarma et al. “Spin electronics and spin computation”. In: *Solid State Commun.* 119.4–5 (July 2001), pp. 207–215. ISSN: 0038-1098. DOI: 10.1016/S0038-1098(01)00111-9.

[23] G. E. Moore. “Lithography and the future of Moore’s law”. In: (May 1995). Ed. by Marylyn H. Bennett. ISSN: 0277-786X. DOI: 10.1117/12.209195.

[24] A. Aviram and M. A. Ratner. “Molecular rectifiers”. In: *Chem. Phys. Lett.* 29.2 (Nov. 1974), pp. 277–283. ISSN: 0009-2614. DOI: 10.1016/0009-2614(74)85031-1.

[25] C. Joachim et al. “Electronics using hybrid-molecular and mono-molecular devices”. In: *Nat.* 408.6812 (Nov. 2000), pp. 541–548. ISSN: 1476-4687. DOI: 10.1038/35046000.

[26] J. P. Launay and M. Verdaguer. *Electrons in Molecules.* Oxford University Press, Nov. 2018. ISBN: 9780198814597. DOI: 10.1093/oso/9780198814597.001.0001.

[27] S. Sanvito. “Molecular spintronics”. In: *Chem. Soc. Rev.* 40.6 (2011), pp. 3336–3355.

[28] G. Szulczewski et al. “A spin of their own”. In: *Nat. Mater.* 8.9 (Sept. 2009), pp. 693–695. ISSN: 1476-4660. DOI: 10.1038/nmat2518.

[29] J. Takeya et al. “Very high-mobility organic single-crystal transistors with in-crystal conduction channels”. In: *Appl. Phys. Lett.* 90.10 (Mar. 2007). ISSN: 1077-3118. DOI: 10.1063/1.2711393.

[30] A. Cornia and P. Seneor. “The molecular way”. In: *Nat. Mater.* 16.5 (Apr. 2017), pp. 505–506. ISSN: 1476-4660. DOI: 10.1038/nmat4900.

[31] E. Schrödinger. “Quantisierung als Eigenwertproblem”. In: *Annalen der physik* 385.13 (1926), pp. 437–490. DOI: 10.1515/9783112596647-007.

[32] C. E. Housecroft and A. G. Sharpe. *Inorganic chemistry*. Pearson, 2018, p. 1296. ISBN: 978-1-292-13414-7.

[33] T. A. Albright et al. *Orbital Interactions Chemistry*. Wiley-Interscience, 2002, p. 570. ISBN: 9780471080398.

[34] Warren J. Hehre. “Ab initio molecular orbital theory”. In: *Accounts of Chemical Research* 9.11 (1976), pp. 399–406.

[35] E. Barim and F. Akman. “Synthesis, characterization and spectroscopic investigation of N-(2-acetylbenzofuran-3-yl)acrylamide monomer: Molecular structure, HOMO–LUMO study, TD-DFT and MEP analysis”. In: *J. Mol. Struct.* 1195 (Nov. 2019), pp. 506–513. ISSN: 0022-2860. DOI: 10.1016/j.molstruc.2019.06.015.

[36] J. Bredas. “Mind the gap!” In: *Mater. Horiz.* 1.1 (2014), pp. 17–19. ISSN: 2051-6355. DOI: 10.1039/c3mh00098b.

[37] T. Methfessel et al. “Spin scattering and spin-polarized hybrid interface states at a metal-organic interface”. In: *Phys Rev B* 84.22 (Dec. 2011), p. 224403. ISSN: 1550-235X. DOI: 10.1103/physrevb.84.224403.

[38] S. Soubatch et al. “Site-Specific Polarization Screening in Organic Thin Films”. In: *Phys. Rev. Lett.* 102.17 (May 2009), p. 177405. ISSN: 1079-7114. DOI: 10.1103/PhysRevLett.102.177405.

[39] I. Fernández Torrente et al. “Spectroscopy of C60single molecules: the role of screening on energy level alignment”. In: *J. Phys.: Condens. Matter* 20.18 (Apr. 2008), p. 184001. ISSN: 1361-648X. DOI: 10.1088/0953-8984/20/18/184001.

[40] A. M. Scheer et al. “Unoccupied orbital energies of 1,4-benzenedithiol and the HOMO–LUMO gap”. In: *Chem. Phys. Lett.* 466.4–6 (Dec. 2008), pp. 131–135. ISSN: 0009-2614. DOI: 10.1016/j.cplett.2008.10.057.

[41] C. J. Jones. “Coordination compounds”. In: *d- and f- Block Chemistry*. The Royal Society of Chemistry, Feb. 2001. Chap. CH.4, pp. 54–70. ISBN: 9781847550682. DOI: 10.1039/9781847550682-00054.

[42] S. Seda et al. “Synthesis and structural characterisation of nickel 15-metallacrown-5 complexes with lanthanide(III) and lead(II) ions: Influence of the central metal ion size on the spin state of peripheral nickel(II) ions”. In: *Inorganic Chemistry Communications* 9.8 (Aug. 2006), pp. 792–796. ISSN: 1387-7003. DOI: 10.1016/j.inoche.2006.04.026.

[43] R. Sessoli et al. “Magnetic bistability in a metal-ion cluster”. In: *Nature* 365.6442 (Sept. 1993), pp. 141–143. ISSN: 1476-4687. DOI: 10.1038/365141a0.

[44] G. Christou et al. “Single-Molecule Magnets”. In: *MRS Bull.* 25.11 (2000), pp. 66–71. DOI: 10.1557/mrs2000.226.

[45] B. W. Pfennig. “Principles of Inorganic Chemistry”. In: Wiley, 2015. Chap. 16, pp. 512–525. ISBN: 978-1–118-85910-0.

[46] H. Bethe. “Termaufspaltung in Kristallen”. In: *Ann. Phys.* 395.2 (Jan. 1929), pp. 133–208. ISSN: 1521-3889. DOI: 10.1002/andp.19293950202.

[47] B. C. Guha. “Magnetic properties of some paramagnetic crystals at low temperatures”. In: *Proceedings of the Royal Society of London. Series A. Mathematical and Physical Sciences* 206.1086 (May 1951), pp. 353–373. ISSN: 2053-9169. DOI: 10.1098/rspa.1951.0075.

[48] V. Gadet et al. “High-T_C molecular-based magnets: a ferromagnetic bimetallic chromium (III)-nickel (II) cyanide with T_C = 90 K”. in: *J. Am. Chem. Soc.* 114.23 (1992), pp. 9213–9214.

[49] W. R. Entley et al. “High-temperature molecular magnets based on cyanovanadate building blocks: spontaneous magnetization at 230 K”. in: *Science* 268.5209 (1995), pp. 397–400.

[50] T. Mallah et al. “High-T_C molecular-based magnets: ferrimagnetic mixed-valence chromium (III)-chromium (II) cyanides with T_C at 240 and 190 kelvin”. In: *Science* 262.5139 (1993), pp. 1554–1557.

[51] S. M. Holmes et al. “Sol-Gel Synthesis of KV^{II} $[Cr^{III}$ $(CN)_6].2H_2O$: A Crystalline Molecule-Based Magnet with a Magnetic Ordering Temperature above 100° C”. in: *Journal of the American Chemical Society* 121.23 (1999), pp. 5593–5594.

[52] B. Sieklucka and D. Pinkowicz. *Molecular Magnetic Materials: Concepts and Applications. Concepts and Applications*. Wiley Sons, Incorporated, John, 2016, p. 512. ISBN: 978-3-527-69420-4.

[53] K. V. Raman et al. “Interface-engineered templates for molecular spin memory devices”. In: *Nat.* 493.7433 (Jan. 2013), pp. 509–513. ISSN: 1476-4687. DOI: 10.1038/nature11719.

[54] M. Cavallini et al. “Single molecule magnets: from thin films to nano-patterns”. In: *Phys. Chem. Chem. Phys.* 10.6 (2008), pp. 784–793. ISSN: 1463-9084. DOI: 10.1039/b711677b.

[55] A. Zabala-Lekuona et al. “Single-Molecule Magnets: From Mn12-ac to dysprosium metallocenes, a travel in time”. In: *Coord. Chem. Rev.* 441

(Aug. 2021), p. 213984. ISSN: 0010-8545. DOI: 10.1016/j.ccr.2021.213984.

[56] D. Gatteschi et al. “Single-molecule magnets based on iron (iii) oxo clustersDedicated to the memory of Professor Olivier Kahn.” In: *Chem. Commun.* 9 (2000), pp. 725–732.

[57] K. Weighardt et al. “Hydrolysis products of the monomeric amine complex (C H N) FeCl : The Structure of the Octameric Iron (III) Cation of [[(C H N) Fe (-O) (-OH)] Br (H] Br.8H O”. in: *Angew. Chem.* 23.1 (1984), pp. 77–78.

[58] C. J. Milios et al. “A record anisotropy barrier for a single-molecule magnet”. In: *J. Am. Chem. Soc.* 129.10 (2007), pp. 2754–2755.

[59] D. Gatteschi and R. Sessoli. “Quantum tunneling of magnetization and related phenomena in molecular materials”. In: *Angew. Chem. - Int. Ed.* 42.3 (2003), pp. 268–297.

[60] J. Villain et al. “Magnetic relaxation in big magnetic molecules”. In: *Europhys. Lett.* 27.2 (1994), p. 159.

[61] D. Woodruff et al. “Lanthanide single-molecule magnets”. In: *Chemical reviews* 113.7 (2013), pp. 5110–5148.

[62] L. Thomas et al. “Nonexponential Dynamic Scaling of the Magnetization Relaxation in Mn Acetate”. In: *Phys. Rev. Lett.* 83 (12 Sept. 1999), pp. 2398–2401. DOI: 10.1103/PhysRevLett.83.2398.

[63] J. M. Zadrozny et al. “Slow magnetization dynamics in a series of two-coordinate iron(ii) complexes”. In: *Chem. Sci.* 4.1 (2013), pp. 125–138. ISSN: 2041-6539. DOI: 10.1039/C2SC20801F.

[64] A. Fort, A. Rettori, et al. “Mixed Quantum-Thermal Relaxation in Mn_{12} Acetate Molecules”. In: *Phys. Rev. Lett.* 80 (3 Jan. 1998), pp. 612–615. DOI: 10.1103/PhysRevLett.80.612.

[65] G. Aromi and E. K. Brechin. “Synthesis of 3d Metallic Single-Molecule Magnets”. In: *Single-Molecule Magnets and Related Phenomena*. Springer-Verlag, 2006, pp. 1–67. ISBN: 3540332391. DOI: 10.1007/430_022.

[66] A. M. Ako et al. “A Ferromagnetically Coupled Mn_{19} Aggregate with a Record S=83/2 Ground Spin State”. In: *Angew Chem-ger Edit* 118.30 (July 2006), pp. 5048–5051. ISSN: 1521-3757. DOI: 10.1002/ange.200601467.

[67] A. Athanasopoulou. “Ln(III) Metallacrown Complexes: NovelSystems and Single-Molecule Magnet (SMM) Properties”. PhD thesis. Johannes Gutenberg University, JGU, Mainz, 2019.

[68] L. Bogani and W. Wernsdorfer. “Molecular spintronics using single-molecule magnets”. In: *Nat. mat.* 7.3 (2008), pp. 179–186.

[69] J. Stoehr and H. C. Siegmann. *Magnetism (Springer Series in Solid-State Sciences)*. Springer, 2006, p. 838. ISBN: 978-3-540-30282-7.

[70] N. Ishikawa et al. “Lanthanide double-decker complexes functioning as magnets at the single-molecular level”. In: *J. Am. Chem. Soc.* 125.29 (2003), pp. 8694–8695.

[71] L. Sorace et al. “Lanthanides in molecular magnetism: old tools in a new field”. In: *Chem. Soc. Rev.* 40.6 (2011), p. 3092. ISSN: 1460-4744. DOI: 10.1039/c0cs00185f.

[72] N. Ishikawa et al. “Mononuclear Lanthanide Complexes with a Long Magnetization Relaxation Time at High Temperatures: A New Category of Magnets at the Single-Molecular Level”. In: *The Journal of Physical Chemistry B* 108.31 (June 2004), pp. 11265–11271. ISSN: 1520-5207. DOI: 10.1021/jp0376065.

[73] J. Rinehart and J. Long. “Exploiting single-ion anisotropy in the design of f-element single-molecule magnets”. In: *Chem. Sci.* 2.11 (2011), p. 2078. ISSN: 2041-6539. DOI: 10.1039/c1sc00513h.

[74] L. Feltham and S. Brooker. “Review of purely 4f and mixed-metal nd-4f single-molecule magnets containing only one lanthanide ion”. In: *Coord. Chem. Rev.* 276 (2014), pp. 1–33.

[75] S. Osa et al. “A Tetranuclear 3d−4f Single Molecule Magnet [Cu LTb $(hfac)_2]_2$”. In: *J. Am. Chem. Soc.* 126.2 (Dec. 2003), pp. 420–421. ISSN: 1520-5126. DOI: 10.1021/ja037365e.

[76] W. Wernsdorfer et al. “Exchange-biased quantum tunnelling in a supramolecular dimer of single-molecule magnets”. In: *Nat.* 416.6879 (Mar. 2002), pp. 406–409. ISSN: 1476-4687. DOI: 10.1038/416406a.

[77] A. Nitzan et al. “Electron Transport in Molecular Wire Junctions”. In: *Science* 300.5624 (May 2003), pp. 1384–1389. ISSN: 1095-9203. DOI: 10.1126/science.1081572.

[78] M. Galbiati et al. “Spinterface: Crafting spintronics at the molecular scale”. In: *MRS Bull.* 39.7 (July 2014), pp. 602–607. ISSN: 1938-1425. DOI: 10.1557/mrs.2014.131.

[79] H. Vazquez et al. “Dipole formation at metal/PTCDA interfaces: Role of the Charge Neutrality Level”. In: *Europhys. Lett.* 65.6 (Mar. 2004), pp. 802–808. ISSN: 1286-4854. DOI: 10.1209/epl/i2003-10131-2.

[80] N. Atodiresei et al. “Design of the Local Spin Polarization at the Organic-Ferromagnetic Interface”. In: *Phys. Rev. Lett.* 105 (6 Aug. 2010), p. 066601. DOI: 10.1103/PhysRevLett.105.066601.

[81] M. Callsen et al. “Magnetic Hardening Induced by Nonmagnetic Organic Molecules”. In: *Phys. Rev. Lett.* 111 (10 Sept. 2013), p. 106805. DOI: 10.1103/PhysRevLett.111.106805.

[82] T. Dietl. “Ferromagnetic semiconductors”. In: *Semicond. Sci. Technol.* 17.4 (Mar. 2002), pp. 377–392. ISSN: 0268-1242. DOI: 10.1088/0268-1242/17/4/310.

[83] S. L. Kawahara et al. “Large Magnetoresistance through a Single Molecule due to a Spin-Split Hybridized Orbital”. In: *Nano Lett.* 12.9 (Aug. 2012), pp. 4558–4563. ISSN: 1530-6992. DOI: 10.1021/nl301802e.

[84] J. Brede et al. “Spin- and Energy-Dependent Tunneling through a Single Molecule with Intramolecular Spatial Resolution”. In: *Phys. Rev. Lett.* 105 (4 July 2010), p. 047204. DOI: 10.1103/PhysRevLett.105.047204.

[85] P. Stoll et al. “Magnetic anisotropy in surface-supported single-ion lanthanide complexes”. In: *Phys. Rev. B* 94.22 (22 Dec. 2016), p. 224426. ISSN: 2469-9969. DOI: 10.1103/PhysRevB.94.224426.

[86] D. Klar et al. “Hysteretic behaviour in a vacuum deposited submonolayer of single ion magnets”. In: *Dalton Trans.* 43.28 (2014), pp. 10686–10689. ISSN: 1477-9234. DOI: 10.1039/C4DT01005A.

[87] S. Stepanow et al. “Spin and Orbital Magnetic Moment Anisotropies of Monodispersed Bis(Phthalocyaninato)Terbium on a Copper Surface”. In: *J. Am. Chem. Soc.* 132.34 (Aug. 2010), pp. 11900–11901. ISSN: 1520-5126. DOI: 10.1021/ja105124r.

[88] A. Lodi Rizzini et al. “Coupling Single Molecule Magnets to Ferromagnetic Substrates”. In: *Phys. Rev. Lett.* 107.17 (17 Oct. 2011), p. 177205. ISSN: 1079-7114. DOI: 10.1103/PhysRevLett.107.177205.

[89] Alberto Lodi Rizzini et al. “Coupling of single, double, and triple-decker metal-phthalocyanine complexes to ferromagnetic and antiferromagnetic substrates”. In: *Surf. Sci.* 630 (Dec. 2014), pp. 361–374. ISSN: 0039-6028. DOI: 10.1016/j.susc.2014.07.008.

[90] H. Wende et al. “Substrate-induced magnetic ordering and switching of iron porphyrin molecules”. In: *Nat. Mater.* 6.7 (June 2007), pp. 516–520. ISSN: 1476-4660. DOI: 10.1038/nmat1932.

[91] A. Mugarza et al. “Electronic and magnetic properties of molecule-metal interfaces: Transition-metal phthalocyanines adsorbed on Ag(100)”. In: *Phys. Rev. B* 85 (15 Apr. 2012), p. 155437. DOI: 10.1103/PhysRevB.85.155437.

[92] J. Brede and R. Wiesendanger. “Spin-resolved characterization of single cobalt phthalocyanine molecules on a ferromagnetic support”. In: *Phys Rev B* 86.18 (Nov. 2012), p. 184423. ISSN: 1550-235X. DOI: 10.1103/PhysRevB.86.184423.

[93] S. Sanvito and A. Rocha. “Molecular-spintronics: The art of driving spin through molecules”. In: *J. Comput. Theor. Nanosci.* 3.5 (2006), pp. 624–642.

[94] M. Ouyang and D. Awschalom. “Coherent Spin Transfer Between Molecularly Bridged Quantum Dots”. In: *Science* 301.5636 (2003), pp. 1074–1078. DOI: 10.1126/science.1086963.

[95] S. Lumetti et al. “Single-molecule devices with graphene electrodes”. In: *Dalton Trans.* 45.42 (2016), pp. 16570–16574. ISSN: 1477-9234. DOI:

10.1039/C6DT02445A.

[96] D. Shao and X. Wang. "Development of Single-Molecule Magnets". In: *Chin. J. Chem.* 38.9 (June 2020), pp. 1005–1018. ISSN: 1614-7065. DOI: 10.1002/cjoc.202000090.

[97] R. Sessoli and A. Powell. "Strategies towards single molecule magnets based on lanthanide ions". In: *Coord. Chem. Rev.* 253.19–20 (Oct. 2009), pp. 2328–2341. ISSN: 0010-8545. DOI: 10.1016/j.ccr.2008.12.014.

[98] A. Barra et al. "Superparamagnetic-like behavior in an octanuclear iron cluster". In: *Europhys. Lett.* 35.2 (July 1996), pp. 133–138. ISSN: 1286-4854. DOI: 10.1209/epl/i1996-00544-3.

[99] C. Sangregorio et al. "Quantum Tunneling of the Magnetization in an Iron Cluster Nanomagnet". In: *Phys. Rev. Lett.* 78 (24 June 1997), pp. 4645–4648. DOI: 10.1103/PhysRevLett.78.4645.

[100] W. Wernsdorfer and R. Sessoli. "Quantum Phase Interference and Parity Effects in Magnetic Molecular Clusters". In: *Science* 284.5411 (Apr. 1999), pp. 133–135. ISSN: 1095-9203. DOI: 10.1126/science.284.5411.133.

[101] H. Wang et al. "Single-molecule magnetism of tetrapyrrole lanthanide compounds with sandwich multiple-decker structures". In: *Coord. Chem. Rev.* 306 (Jan. 2016), pp. 195–216. ISSN: 0010-8545. DOI: 10.1016/j.ccr.2015.07.004.

[102] L. Vitali et al. "Electronic Structure of Surface-supported Bis(phthalocyaninato) terbium(III) Single Molecular Magnets". In: *Nano Lett.* 8.10 (Sept. 2008), pp. 3364–3368. ISSN: 1530-6992. DOI: 10.1021/nl801869b.

[103] D. Klar et al. "Antiferromagnetic coupling of $TbPc_2$ molecules to ultrathin Ni and Co films". In: *Beilstein J. Nanotechnol.* 4 (May 2013), pp. 320–324. DOI: 10.3762/bjnano.4.36.

[104] C. Ganivet et al. "Influence of Peripheral Substitution on the Magnetic Behavior of Single-Ion Magnets Based on Homo- and Heteroleptic TbIII Bis(phthalocyaninate)". In: *Chem. A Euro. J.* 19.4 (Nov. 2012), pp. 1457–1465. ISSN: 1521-3765. DOI: 10.1002/chem.201202600.

[105] J. Xiong et al. "Hydroxide-bridged five-coordinate Dy^{III} single-molecule magnet exhibiting the record thermal relaxation barrier of magnetization among lanthanide-only dimers". In: *Chem. Sci.* 8.2 (2017), pp. 1288–1294. ISSN: 2041-6539. DOI: 10.1039/C6SC03621J.

[106] J. Rinehart et al. "Strong exchange and magnetic blocking in N^{3} -radical-bridged lanthanide complexes". In: *Nat. Chem.* 3.7 (May 2011), pp. 538–542. ISSN: 1755-4349. DOI: 10.1038/nchem.1063.

[107] F. Guo et al. "Magnetic hysteresis up to 80 kelvin in a dysprosium metallocene single-molecule magnet". In: *Science* 362.6421 (Dec. 2018), pp. 1400–1403. ISSN: 1095-9203. DOI: 10.1126/science.aav0652.

[108] J. Baldovi et al. “Rational Design of Single-Ion Magnets and Spin Qubits Based on Mononuclear Lanthanoid Complexes”. In: *Inorg. Chem.* 51.22 (Oct. 2012), pp. 12565–12574. ISSN: 1520-510X. DOI: 10.1021/ic302068c.

[109] D. Aravena and E. Ruiz. “Shedding light on the single-molecule magnet behavior of mononuclear DyIII complexes”. In: *Inorg. Chem.* 52.23 (2013), pp. 13770–13778.

[110] P. Happ et al. “12-MC-4 metallacrowns as versatile tools for SMM research”. In: *Coord. Chem. Rev.* 289–290 (Apr. 2015), pp. 238–260. ISSN: 0010-8545. DOI: 10.1016/j.ccr.2014.11.012.

[111] P. Happ and E. Rentschler. “Enforcement of a high-spin ground state for the first 3d heterometallic 12-metallacrown-4 complex”. In: *Dalton Trans* 43.41 (2014), pp. 15308–15312. ISSN: 1477-9234. DOI: 10.1039/c4dt02275k.

[112] A. Rauguth et al. “3d/4f Sandwich Complex Based on Metallacrowns”. In: *Inorg. Chem.* 60.18 (Aug. 2021), pp. 14031–14037. ISSN: 1520-510X. DOI: 10.1021/acs.inorgchem.1c01356.

[113] A. Athanasopoulou et al. “Synthesis, Structural, and Magnetic Characterization of a Mixed 3d/4f 12-Metallacrown-4 Family of Complexes”. In: *Inorganics* 6.3 (July 2018), p. 66. ISSN: 2304-6740. DOI: 10.3390/inorganics6030066.

[114] C. Zaleski et al. “Single Molecule Magnet Behavior of a Pentanuclear Mn-Based Metallacrown Complex: Solid State and Solution Magnetic Studies”. In: *Inorg. Chem.* 50.22 (Oct. 2011), pp. 11348–11352. ISSN: 1520-510X. DOI: 10.1021/ic2008792.

[115] P. Happ et al. “Analyzing the enforcement of a high-spin ground state for a metallacrown single-molecule magnet”. In: *Phys. Rev. B* 93.17 (May 2016), p. 174404. ISSN: 2469-9969. DOI: 10.1103/PhysRevB.93.174404.

[116] Y. Qin et al. “Four Mixed 3d-4f 12-Metallacrown-4 Complexes: Syntheses, Structures and Magnetic Properties”. In: *J. Cluster Sci.* 28.3 (Sept. 2016), pp. 891–903. ISSN: 1572-8862. DOI: 10.1007/s10876-016-1083-y.

[117] M. Azar et al. “Controllable formation of heterotrimetallic coordination compounds: systematically incorporating lanthanide and alkali metal ions into the manganese 12-metallacrown-4 framework”. In: *Inorg. Chem.* 53.3 (2014), pp. 1729–1742.

[118] A. Alhassanat et al. “Element-specific magnetic properties of mixed 3d-4f metallacrowns”. In: *Phys. Rev. B* 98.6 (Aug. 2018), p. 064428. ISSN: 2469-9969. DOI: 10.1103/PhysRevB.98.064428.

[119] M. Clemente-León et al. “Langmuir–Blodgett Films of Single-Molecule Nanomagnets”. In: *Angew. Chem. - Int. Ed.* 37.20 (1998), pp. 2842–2845. DOI: 10.1002/(SICI)1521-3773(19981102)37:20<2842::AID-ANIE2842>3.0.CO;2-B.

[120] A. Cornia et al. “Preparation of Novel Materials Using SMMs”. In: *Single-Molecule Magnets and Related Phenomena*. Springer-Verlag, pp. 133–161. ISBN: 3540332391. DOI: 10.1007/430_029.

[121] A. Cornia et al. “Direct Observation of Single-Molecule Magnets Organized on Gold Surfaces”. In: *Angewandte Chemie International Edition* 42.14 (Apr. 2003), pp. 1645–1648. DOI: 10.1002/anie.200350981.

[122] H. B. Heersche et al. “Electron Transport through Single Mn_{12} Molecular Magnets”. In: *Physical Review Letters* 96.20 (May 2006), p. 206801. ISSN: 1079-7114. DOI: 10.1103/PhysRevLett.96.206801.

[123] M. Cavallini et al. “Multiple length scale patterning of single-molecule magnets”. In: *Nano Lett.* 3.11 (2003), pp. 1527–1530.

[124] J. Means et al. “Films of Mn12-acetate deposited by low-energy laser ablation”. In: *J. mag. mag. mat.* 284 (2004), pp. 215–219.

[125] S. Fahrendorf et al. “Accessing 4f-states in single-molecule spintronics”. In: *Nat. Commun.* 4.1 (Sept. 2013). ISSN: 2041-1723. DOI: 10.1038/ncomms3425.

[126] T. Frauhammer. “Single-Molecule Magnets and their Electronic andMagnetic Interactions with Metallic Surfaces”. PhD thesis. Karlsruher Instituts für Technologie, Nov. 2020.

[127] N. Domingo et al. “Advances on structuring, integration and magnetic characterization of molecular nanomagnets on surfaces and devices”. In: *Chem. Soc. Rev.* 41.1 (2012), pp. 258–302. ISSN: 1460-4744. DOI: 10.1039/c1cs15096k.

[128] F. Luis et al. “Long-Range Ferromagnetism of Mn_{12} Acetate Single-Molecule Magnets under a Transverse Magnetic Field”. In: *Phys. Rev. Lett.* 95 (22 Nov. 2005), p. 227202. DOI: 10.1103/PhysRevLett.95.227202.

[129] D. Gatteschi et al. “EPR of molecular nanomagnets”. In: *Coord. Chem. Rev.* 250.11–12 (June 2006), pp. 1514–1529. ISSN: 0010-8545. DOI: 10.1016/j.ccr.2006.02.006.

[130] Z. Salman et al. “Local magnetic properties of a monolayer of Mn_{12} single molecule magnets”. In: *Nano letters* 7.6 (2007), pp. 1551–1555.

[131] U. del Pennino et al. “Valence band resonant photoemission of Mn_{12} single molecules grafted on Au (111) surface”. In: *Surface science* 600.18 (2006), pp. 4185–4189.

[132] M. Mannini et al. “XAS and XMCD Investigation of Mn_{12} Monolayers on Gold”. In: *Chemi. A Euro. J.* 14.25 (Aug. 2008), pp. 7530–7535. ISSN: 1521-3765. DOI: 10.1002/chem.200800693.

[133] M. Mannini et al. “Magnetic memory of a single-molecule quantum magnet wired to a gold surface”. In: *Nat. Mater.* 8.3 (Feb. 2009), pp. 194–197. ISSN: 1476-4660. DOI: 10.1038/nmat2374.

[134] S. Stepanow et al. "Giant spin and orbital moment anisotropies of a Cu-phthalocyanine monolayer". In: *Phys Rev B* 82.1 (July 2010), p. 014405. ISSN: 1550-235X. DOI: 10.1103/PhysRevB.82.014405.

[135] S. Stepanow et al. "Spin and orbital magnetic moment anisotropies of monodispersed bis (phthalocyaninato) terbium on a copper surface". In: *J. Am. Chem. Soc.* 132.34 (2010), pp. 11900–11901.

[136] L. Margheriti et al. "X-ray detected magnetic hysteresis of thermally evaporated terbium double-decker oriented films". In: *Adv. Mater* 22.48 (2010), pp. 5488–5493.

[137] V. Corradini et al. "Successful grafting of isolated molecular Cr_7Ni rings on Au (111) surface". In: *Phys Rev B* 79.14 (2009), p. 144419.

[138] V. Corradini et al. "Grafting molecular Cr_7Ni rings on a gold surface". In: *Dalton Trans.* 39.20 (2010), pp. 4928–4936.

[139] R. Biagi et al. "X-ray absorption and magnetic circular dichroism investigation of bis (phthalocyaninato) terbium single-molecule magnets deposited on graphite". In: *Phys. Rev. B* 82.22 (2010), p. 224406.

[140] M. Gonidec et al. "Surface Supramolecular Organization of a Terbium(III) Double-Decker Complex on Graphite and its Single Molecule Magnet Behavior". In: *J. Am. Chem. Soc.* 133.17 (Apr. 2011), pp. 6603–6612. ISSN: 1520-5126. DOI: 10.1021/ja109296c.

[141] A. Scheybal et al. "Induced magnetic ordering in a molecular monolayer". In: *Chem. Phys. Lett.* 411.1–3 (Aug. 2005), pp. 214–220. ISSN: 0009-2614. DOI: 10.1016/j.cplett.2005.06.017.

[142] M. Ternes et al. "Spectroscopic manifestations of the Kondo effect on single adatoms". In: *J. Phys.: Condens. Matter* 21.5 (Dec. 2008), p. 053001. ISSN: 1361-648X. DOI: 10.1088/0953-8984/21/5/053001.

[143] A. Zhao et al. "Controlling the Kondo Effect of an Adsorbed Magnetic Ion Through Its Chemical Bonding". In: *Science* 309.5740 (Sept. 2005), pp. 1542–1544. ISSN: 1095-9203. DOI: 10.1126/science.1113449.

[144] L. Gao et al. "Site-Specific Kondo Effect at Ambient Temperatures in Iron-Based Molecules". In: *Phys. rev. lett.* 99.10 (Sept. 2007), p. 106402. ISSN: 1079-7114. DOI: 10.1103/physrevlett.99.106402.

[145] K. Katoh et al. "Direct Observation of Lanthanide(III)-Phthalocyanine Molecules on Au(111) by Using Scanning Tunneling Microscopy and Scanning Tunneling Spectroscopy and Thin-Film Field-Effect Transistor Properties of Tb(III)- and Dy(III)-Phthalocyanine Molecules". In: *J. Am. Chem. Soc.* 131.29 (July 2009), pp. 9967–9976. ISSN: 1520-5126. DOI: 10.1021/ja902349t.

[146] K. von Bergmann et al. "Spin Polarization of the Split Kondo State". In: *Phys. Rev. Lett.* 114.7 (Feb. 2015), p. 076601. ISSN: 1079-7114. DOI: 10.1103/PhysRevLett.114.076601.

[147] V. Iancu et al. “Manipulating Kondo temperature via single molecule switching”. In: *Nano letters* 6.4 (2006), pp. 820–823.

[148] V. Iancu et al. “Manipulation of the Kondo effect via two-dimensional molecular assembly”. In: *Phys. Rev. Lett.* 97.26 (2006), p. 266603.

[149] W. Liang et al. “Kondo resonance in a single-molecule transistor”. In: *Nat.* 417.6890 (2002), pp. 725–729.

[150] J. Park et al. “Coulomb blockade and the Kondo effect in single-atom transistors”. In: *Nat.* 417.6890 (June 2002), pp. 722–725. ISSN: 1476-4687. DOI: 10.1038/nature00791.

[151] D. Goldhaber-Gordon et al. “Kondo effect in a single-electron transistor”. In: *Nat.* 391.6663 (Jan. 1998), pp. 156–159. ISSN: 1476-4687. DOI: 10.1038/34373.

[152] X. Chen et al. “Probing Superexchange Interaction in Molecular Magnets by Spin-Flip Spectroscopy and Microscopy”. In: *Phys. Rev. Lett.* 101.19 (19 Nov. 2008), p. 197208. ISSN: 1079-7114. DOI: 10.1103/PhysRevLett.101.197208.

[153] C. Iacovita et al. “Visualizing the Spin of Individual Cobalt-Phthalocyanine Molecules”. In: *Phys. Rev. Lett.* 101.11 (Sept. 2008), p. 116602. ISSN: 1079-7114. DOI: 10.1103/PhysRevLett.101.116602.

[154] F. Ara et al. “Spin properties of single-molecule magnet of double-decker Tb(III)-phthalocyanine ($TbPc_2$) on ferromagnetic Co film characterized by spin polarized STM (SP-STM)”. in: *J Appl Phys* 125.18 (May 2019). ISSN: 1089-7550. DOI: 10.1063/1.5079964.

[155] L. Voelker. “Molekularer Magnetismus Metallakronen-basierter Komplexverbindungen”. PhD thesis. Johannes Gutenberg-Universität Mainz, 2018.

[156] A. Athanasopoulou et al. “Field-induced slow magnetic relaxation in the first Dy(III)-centered 12-metallacrown-4 double-decker”. In: *Dalton Trans.* 48.41 (2019), pp. 15381–15385. ISSN: 1477-9234. DOI: 10.1039/c9dt02432h.

[157] R. Carlin. *Magnetochemistry*. Springer Science & Business Media, 2012.

[158] R. Ranecki et al. “Competing Intramolecular Superexchange Interactions in the CuFe4 Metallacrown on Au(111) An Inelastic Tunneling Spectroscopy Study”. In: *J. Phys. Chem. C* 126.37 (Sept. 2022), pp. 15907–15914. ISSN: 1932-7455. DOI: 10.1021/acs.jpcc.2c02551.

[159] N. Tsukahara et al. “Adsorption-Induced Switching of Magnetic Anisotropy in a Single Iron(II) Phthalocyanine Molecule on an Oxidized Cu(110) Surface”. In: *Phys. Rev. Lett.* 102.16 (Apr. 2009), p. 167203. ISSN: 1079-7114. DOI: 10.1103/PhysRevLett.102.167203.

[160] B. Liu et al. “An Iron-Porphyrin Complex with Large Easy-Axis Magnetic Anisotropy on Metal Substrate”. In: *ACS Nano* 11.11 (Oct. 2017), pp. 11402–11408. ISSN: 1936-086X. DOI: 10.1021/acsnano.7b06029.

[161] L. Gragnaniello et al. “Uniaxial 2D Superlattice of Fe4 Molecular Magnets on Graphene”. In: *Nano Lett.* 17.12 (Nov. 2017), pp. 7177–7182. ISSN: 1530-6992. DOI: 10.1021/acs.nanolett.6b05105.

[162] T. Komeda et al. “Observation and electric current control of a local spin in a single-molecule magnet”. In: *Nat. Commun.* 2.1 (Mar. 2011). ISSN: 2041-1723. DOI: 10.1038/ncomms1210.

[163] B. Warner et al. “Sub-molecular modulation of a 4f driven Kondo resonance by surface-induced asymmetry”. In: *Nat. Commun.* 7.1 (Sept. 2016). ISSN: 2041-1723. DOI: 10.1038/ncomms12785.

[164] V. Vieru et al. “Increasing the Magnetic Blocking Temperature of Single-Molecule Magnets”. In: *Angewandte Chemie International Edition* 63.2 (Sept. 2023). ISSN: 1521-3773. DOI: 10.1002/anie.202303146.

[165] A. Kredel. “Auf Metallakronen Basierende 3d-4f Sandwichkomplexe”. PhD thesis. 2015.

[166] V. Pecoraro. “Structural characterization of $[VO_{(\text{salicylhydroximate})}(CH_3OH)]_3$: Applications to the biological chemistry of vanadium (V)”. in: *inorganica Chimica Acta* 155 (1989).

[167] C. Pedersen. “Cyclic polyethers and their complexes with metal salts”. In: *J. Am. Chem. Soc.* 89.26 (1967), pp. 7017–7036.

[168] G. Mezei et al. “Structural and Functional Evolution of Metallacrowns”. In: *Chem. Rev.* 107.11 (Nov. 2007), pp. 4933–5003. ISSN: 1520-6890. DOI: 10.1021/cr078200h.

[169] P. Czaja. “Oberflächenuntersuchungen von adsorbierten und funktionalisierten, mehrkernigen Übergangsmetallkomplexen”. de. PhD thesis. 2019. DOI: 10.25358/OPENSCIENCE-3756.

[170] C.J. Powell. “Recent progress in quantification of surface analysis techniques”. In: *Applications of Surface Science* 4.3 (1980), pp. 492–509. ISSN: 0378-5963. DOI: 10.1016/0378-5963(80)90093-8.

[171] W. Gonzalez-Vinas et al. “An Introduction to Materials Science”. In: Princeton University Press, 2015. Chap. 11, p. 158. ISBN: 9781400880058. DOI: 10.1515/9781400880058.

[172] G. Binnig et al. “Tunneling through a controllable vacuum gap”. In: *Applied Physics Letters* 40.2 (1982), pp. 178–180. DOI: 10.1063/1.92999.

[173] G. Binnig et al. “Surface Studies by Scanning Tunneling Microscopy”. In: *Phys. Rev. Lett.* 49 (1 July 1982), pp. 57–61. DOI: 10.1103/PhysRevLett.49.57.

[174] G. Binnig et al. “(111) facets as the origin of reconstructed Au(110) surfaces”. In: *Surface Science* 131.1 (1983), pp. L379–L384. ISSN: 0039-6028. DOI: 10.1016/0039-6028(83)90112-7.

[175] H.p. Bonzel and S. Ferrer. “A New Model For The Reconstructed (110)-1×2 Surfaces Of Ir, Pt And Au”. In: *Surface Science Letters* 118.1 (1982), pp. L263–L268. ISSN: 0167-2584. DOI: 10.1016/0167-2584(82)90317-6.

[176] G. Binnig et al. “7 x 7 Reconstruction on Si(111) Resolved in Real Space”. In: *Phys. Rev. Lett.* 50 (2 Jan. 1983), pp. 120–123. DOI: 10.1103/PhysRevLett.50.120.

[177] Royal Swedish Academy of Sciences. *Press Release Of Nobel Prize In Physics 1986*. Oct. 1986. URL: https://www.nobelprize.org/prizes/physics/1986/press-release/.

[178] J. Stroscio et al. “Electronic Structure of the Si(111)2 × 1 Surface by Scanning-Tunneling Microscopy”. In: *Phys. Rev. Lett.* 57 (20 Nov. 1986), pp. 2579–2582. DOI: 10.1103/PhysRevLett.57.2579.

[179] R. M. Feenstra et al. “Atom-selective imaging of the GaAs(110) surface”. In: *Phys. Rev. Lett.* 58 (12 Mar. 1987), pp. 1192–1195. DOI: 10.1103/PhysRevLett.58.1192.

[180] D. M. Eigler and E. K. Schweizer. “Positioning Single Atoms With A Scanning Tunnelling Microscope”. In: *Nature* 344.6266 (Apr. 1990), pp. 524–526. DOI: 10.1038/344524a0.

[181] T. Seifert et al. “Longitudinal And Transverse Electron Paramagnetic Resonance In A Scanning Tunneling Microscope”. In: *Science Advances* 6.40 (Oct. 2020). DOI: 10.1126/sciadv.abc5511.

[182] S. Yoshida et al. “Optical Pump-probe Scanning Tunneling Microscopy For Probing Ultrafast Dynamics On The Nanoscale”. In: *The European Physical Journal Special Topics* 222.5 (July 2013), pp. 1161–1175. DOI: 10.1140/epjst/e2013-01912-2.

[183] E. Stelzer. “Beyond The Diffraction Limit?” In: *Nature* 417.6891 (June 2002), pp. 806–807. DOI: 10.1038/417806a.

[184] P. Weinberger. “Revisiting Louis De Broglie’s Famous 1924 Paper In The Philosophical Magazine”. In: *Philosophical Magazine Letters* 86.7 (July 2006), pp. 405–410. DOI: 10.1080/09500830600876565.

[185] L. de Broglie. “The Reinterpretation of Wave Mechanics”. In: *Foundations of Physics* 1.1 (Mar. 1970), pp. 5–15. DOI: 10.1007%2FBF00708650.

[186] M. Born. “Quantenmechanik der Stoßvorgänge”. In: *Z. für Phys.* 38.11-12 (Nov. 1926), pp. 803–827. DOI: 10.1007/BF01397184.

[187] R. W. Wood. “A New Form Of Cathode Discharge And The Production Of X-rays, Together With Some Notes On Diffraction. Preliminary Communication”. In: *Phys. Rev. (Series I)* 5 (1 July 1897), pp. 1–10. DOI: 10.1103/PhysRevSeriesI.5.1.

[188] L. Nordheim. “Zur Theorie Der Thermischen Emission Und Der Reflexion Von Elektronen An Metallen”. In: *Z. für Phys.* 46.11-12 (Nov. 1928), pp. 833–855. DOI: 10.1007/BF01391020.

[189] R. Fowler et al. “Electron emission in intense electric fields”. In: *Proc. R. Soc. London A.* 119.781 (May 1928), pp. 173–181. DOI: 10.1098/rspa.1928.0091.

[190] I. Giaever. "Electron Tunneling Between Two Superconductors". In: *Phys. Rev. Lett.* 5.10 (Nov. 1960), pp. 464–466. DOI: 10.1103/PhysRevLett.5.464.

[191] J. C. Fisher and I. Giaever. "Tunneling Through Thin Insulating Layers". In: *J Appl Phys* 32.2 (Feb. 1961), pp. 172–177. DOI: 10.1063/1.1735973.

[192] J. Bardeen. "Tunnelling from a Many-Particle Point of View". In: *Physical Review Letters* 6.2 (Jan. 1961), pp. 57–59. DOI: 10.1103/PhysRevLett.6.57.

[193] J. Tersoff and D. R. Hamann. "Theory and Application for the Scanning Tunneling Microscope". In: *Phys. Rev. Lett.* 50.25 (June 1983), pp. 1998–2001. DOI: 10.1103/PhysRevLett.50.1998.

[194] J. Tersoff and D. R. Hamann. "Theory of the scanning tunneling microscope". In: *Phys Rev B* 31.2 (Jan. 1985), pp. 805–813. DOI: 10.1103/PhysRevB.31.805.

[195] D. J. Griffiths. *Introduction to Quantum Mechanics*. Cambridge University Press, 2016, p. 465. ISBN: 978-1-107-17986-8.

[196] B. Voigtländer. *Scanning Probe Microscopy Atomic Force Microscopy and Scanning Tunneling Microscopy. Atomic Force Microscopy and Scanning Tunneling Microscopy*. Springer, 2015. ISBN: 978-3-662-45240-0.

[197] J. Nicol et al. "Direct Measurement of the Superconducting Energy Gap". In: *Phys. Rev. Lett.* 5.10 (Nov. 1960), pp. 461–464. DOI: 10.1103/PhysRevLett.5.461.

[198] J. Chen. *Introduction to Scanning Tunneling Microscopy Third Edition*. Oxford University Press, 2021. ISBN: 9780198856559.

[199] J. Chen. "Origin of atomic resolution on metal surfaces in scanning tunneling microscopy". In: *Phys. Rev. Lett.* 65 (4 July 1990), pp. 448–451. DOI: 10.1103/PhysRevLett.65.448.

[200] C. Noguera. "Voltage dependence of the tunnelling current: an exact expression". In: *J. Microsc.* 152.1 (Oct. 1988), pp. 3–9. DOI: 10.1111/j.1365-2818.1988.tb01356.x.

[201] C. Noguera. "Validity of the transfer Hamiltonian approach : application to the STM spectroscopic mode". In: *J. Phys.* 50.18 (1989), pp. 2587–2599. DOI: 10.1051/jphys:0198900500180258700.

[202] J. Chen. "Theory of scanning tunneling spectroscopy". In: *J. Vac. Sci. Technol. A: Vac. Surf. Films* 6.2 (Mar. 1988), pp. 319–322. DOI: 10.1116/1.575444.

[203] J. Chen. "Tunneling matrix elements in three-dimensional space: The derivative rule and the sum rule". In: *Phys Rev B* 42.14 (Nov. 1990), pp. 8841–8857. DOI: 10.1103/PhysRevB.42.8841.

[204] D. Papaconstantopoulos. *Handbook of the Band Structure of Elemental Solids*. Springer US, 2015. DOI: 10.1007/978-1-4419-8264-3.

[205] M. Posternak et al. “Self-consistent electronic structure of surfaces: Surface states and surface resonances on W(001)”. In: *Phys. Rev. B* 21 (12 June 1980), pp. 5601–5612. DOI: 10.1103/PhysRevB.21.5601.

[206] S. Weng et al. “Experimental and theoretical study of the surface resonances on the (100) faces of W and Mo”. In: *Phys. Rev. B* 18 (4 Aug. 1978), pp. 1718–1740. DOI: 10.1103/PhysRevB.18.1718.

[207] A. Baratoff. “Theory of scanning tunneling microscopy — methods andapproximations”. In: *Physica B+C* 127.1-3 (Dec. 1984), pp. 143–150. DOI: 10.1016/S0378-4363(84)80022-4.

[208] J. Blanco et al. “STM-theory: Image potential, chemistry and surface relaxation”. In: *Prog. Surf. Sci.* 81.10-12 (Jan. 2006), pp. 403–443. DOI: 10.1016/j.progsurf.2006.07.004.

[209] D. Drakova. “Theoretical modelling of scanning tunnelling microscopy, scanning tunnelling spectroscopy and atomic force microscopy”. In: *Rep. Progr. Phys.* 64.2 (Jan. 2001), pp. 205–290. DOI: 10.1088/0034-4885/64/2/202.

[210] S. Heinze et al. “First-Principles Interpretation of Scanning Tunneling Microscopy Applied to Transition-Metal Surfaces: Buried CuIr/Cu(001) Surface Alloys”. In: *Phys. Status Solidi A* 187.1 (Sept. 2001), pp. 215–226. ISSN: 1521-396X. DOI: 10.1002/1521-396x(200109)187:1<215::aid-pssa215>3.0.co;2-x.

[211] A. Smith et al. “Aspects of spin-polarized scanning tunneling microscopy at the atomic scale: experiment, theory, and simulation”. In: *Surf. Sci.* 561.2-3 (July 2004), pp. 154–170. DOI: 10.1016/j.susc.2004.05.011.

[212] G. Binnig and H. Rohrer. “Scanning tunneling microscopy”. In: *Surf. Sci.* 126.1-3 (Mar. 1983), pp. 236–244. DOI: 10.1016/0039-6028(83)90716-1.

[213] J. Regel. “Scanning Tunneling Microscopy and Spectroscopyof Surface States with Different Step Decorationson Re(0001) and Mobility Investigations of Ni onRe(0001) at low Temperatures”. en. PhD thesis. 2020. DOI: 10.25358/openscience-5641.

[214] R. Wiesendanger. “Scanning probe microscopy and spectroscopy. methods and applications”. In: Cambridge University Press, 1994. Chap. 1, pp. 84–87. ISBN: 0521418100.

[215] Stanford Research System. *MODEL SR830DSP Lock-In Amplifier*. 1290-D Reamwood Avenue Sunnyvale, California 94089: Stanford Research System, Oct. 2011.

[216] L. Bartels et al. “Controlled vertical manipulation of single CO molecules with the scanning tunneling microscope: A route to chemical contrast”. In: *Appl. Phys. Lett.* 71.2 (July 1997), pp. 213–215. DOI: 10.1063/1.119503.

[217] R. M. Feenstra and A. P. Fein. “Surface morphology of GaAs(110) by scanning tunneling microscopy”. In: *Phys. Rev. B* 32.2 (July 1985), pp. 1394–1396. DOI: 10.1103/PhysRevB.32.1394.

[218] A. Bryant et al. “Anomalous distance dependence in scanning tunneling microscopy”. In: *Appl. Phys. Lett.* 49.15 (Oct. 1986), pp. 936–938. DOI: 10.1063/1.97489.

[219] A. Bryant et al. “Imaging in real time with the tunneling microscope”. In: *Appl. Phys. Lett.* 48.13 (Mar. 1986), pp. 832–834. DOI: 10.1063/1.96682.

[220] P. Ghosh. *Introduction to photoelectron spectroscopy*. Wiley, 1983, p. 377. ISBN: 978-0-471-06427-5.

[221] R. Ranecki et al. “Spin-Flip Inelastic Electron Tunneling Spectroscopy on a CuCu4 Metallacrown Complex on Au(111)”. In: *The Journal of Physical Chemistry C* 127.27 (June 2023), pp. 13186–13195. ISSN: 1932-7455. DOI: 10.1021/acs.jpcc.3c01291.

[222] B. C. Stipe, M. A. Rezaei, and W. Ho. “Single-Molecule Vibrational Spectroscopy and Microscopy”. In: *Science* 280.5370 (June 1998), pp. 1732–1735. ISSN: 1095-9203. DOI: 10.1126/science.280.5370.1732.

[223] D. T. Pierce et al. “The GaAs spin polarized electron source”. In: *Rev. Sci. Instrum.* 51.4 (Apr. 1980), pp. 478–499. ISSN: 1089-7623. DOI: 10.1063/1.1136250.

[224] D. Pierce. “Spin-polarized electron microscopy”. In: *Phys. Scripta* 38.2 (Aug. 1988), pp. 291–296. ISSN: 1402-4896. DOI: 10.1088/0031-8949/38/2/035.

[225] E. Stoner. “Collective electron ferromagnetism”. In: *Proceedings of the Royal Society of London. Series A. Mathematical and Physical Sciences* 165.922 (Apr. 1938), pp. 372–414. ISSN: 2053-9169. DOI: 10.1098/rspa.1938.0066.

[226] M. Bode. “Spin-polarized scanning tunnelling microscopy”. In: *Rep. Progr. Phys.* 66.4 (Mar. 2003), pp. 523–582. ISSN: 0034-4885. DOI: 10.1088/0034-4885/66/4/203.

[227] J. C. Slonczewski. “Conductance and exchange coupling of two ferromagnets separated by a tunneling barrier”. In: *Phys Rev B* 39.10 (Apr. 1989), pp. 6995–7002. ISSN: 0163-1829. DOI: 10.1103/PhysRevB.39.6995.

[228] D. Wortmann et al. “Resolving Complex Atomic-Scale Spin Structures by Spin-Polarized Scanning Tunneling Microscopy”. In: *Phys. Rev. Lett.* 86.18 (Apr. 2001), pp. 4132–4135. ISSN: 1079-7114. DOI: 10.1103/PhysRevLett.86.4132.

[229] A. Schlenhoff et al. “Bulk Cr tips with full spatial magnetic sensitivity for spin-polarized scanning tunneling microscopy”. In: *Appl. Phys. Lett.* 97.8 (Aug. 2010), p. 083104. ISSN: 1077-3118. DOI: 10.1063/1.3474659.

[230] O. Pietzsch et al. “Real-Space Observation of Dipolar Antiferromagnetism in Magnetic Nanowires by Spin-Polarized Scanning Tunneling Spectroscopy”. In: *Phys. Rev. Lett.* 84.22 (May 2000), pp. 5212–5215. ISSN: 1079-7114. DOI: 10.1103/PhysRevLett.84.5212.

[231] M. Bode et al. “Spin-Polarized Vacuum Tunneling into the Exchange-Split Surface State of Gd(0001)”. In: *Phys. Rev. Lett.* 81.19 (Nov. 1998), pp. 4256–4259. ISSN: 1079-7114. DOI: 10.1103/PhysRevLett.81.4256.

[232] R. Wiesendanger et al. “Observation of vacuum tunneling of spin-polarized electrons with the scanning tunneling microscope”. In: *Physical Review Letters* 65.2 (July 1990), pp. 247–250. ISSN: 0031-9007. DOI: 10.1103/PhysRevLett.65.247.

[233] R. Allenspach et al. “Tunneling experiments involving magnetic tip and magnetic sample”. In: *Z. Phys. B Condens. Matter* 67.1 (Mar. 1987), pp. 125–128. ISSN: 1434-6036. DOI: 10.1007/BF01307314.

[234] G. Binnig et al. “Conductivity sensitivity of inelastic scanning tunneling microscopy”. In: *Phys Rev B* 32.2 (July 1985), pp. 1336–1338. ISSN: 0163-1829. DOI: 10.1103/PhysRevB.32.1336.

[235] B.N.J. Persson et al. “Inelastic electron tunnelling from a metal tip”. In: *Solid State Commun.* 57.9 (Mar. 1986), pp. 769–772. ISSN: 0038-1098. DOI: 10.1016/0038-1098(86)90856-2.

[236] J. Gauyacq et al. “Excitation of local magnetic moments by tunneling electrons”. In: *Prog. Surf. Sci.* 87.5–8 (May 2012), pp. 63–107. ISSN: 0079-6816. DOI: 10.1016/j.progsurf.2012.05.003.

[237] J. Burgess et al. “Magnetic fingerprint of individual Fe4 molecular magnets under compression by a scanning tunnelling microscope”. In: *Nat. Commun.* 6.1 (Sept. 2015). ISSN: 2041-1723. DOI: 10.1038/ncomms9216.

[238] S. Kahle et al. “The Quantum Magnetism of Individual Manganese-12-Acetate Molecular Magnets Anchored at Surfaces”. In: *Nano Lett.* 12.1 (Dec. 2011), pp. 518–521. ISSN: 1530-6992. DOI: 10.1021/nl204141z.

[239] S. Gregory. “Inelastic tunneling spectroscopy and single-electron tunneling in an adjustable microscopic tunnel junction”. In: *Phys. Rev. Lett.* 64.6 (Feb. 1990), pp. 689–692. ISSN: 0031-9007. DOI: 10.1103/PhysRevLett.64.689.

[240] T. Komeda. “Chemical identification and manipulation of molecules by vibrational excitation via inelastic tunneling process with scanning tunneling microscopy”. In: *Prog. Surf. Sci.* 78.2 (Jan. 2005), pp. 41–85. ISSN: 0079-6816. DOI: 10.1016/j.progsurf.2005.05.001.

[241] P. Hansma. “Inelastic electron tunneling”. In: *Phys. Rep.* 30.2 (Apr. 1977), pp. 145–206. ISSN: 0370-1573. DOI: 10.1016/0370-1573(77)90054-0.

[242] A. J. Heinrich et al. “Single-Atom Spin-Flip Spectroscopy”. In: *Science* 306.5695 (Oct. 2004), pp. 466–469. ISSN: 1095-9203. DOI: 10.1126/science.1101077.

[243] T. Balashov et al. “Magnon Excitation with Spin-Polarized Scanning Tunneling Microscopy”. In: *Phys. Rev. Lett.* 97.18 (Nov. 2006), p. 187201. ISSN: 1079-7114. DOI: 10.1103/PhysRevLett.97.187201.

[244] A. A. Khajetoorians et al. “Itinerant Nature of Atom-Magnetization Excitation by Tunneling Electrons”. In: *Phys. Rev. Lett.* 106.3 (Jan. 2011), p. 037205. ISSN: 1079-7114. DOI: 10.1103/PhysRevLett.106.037205.

[245] Y. Fu et al. “Identifying Charge States of Molecules with Spin-Flip Spectroscopy”. In: *Phys. Rev. Lett.* 103 (25 Dec. 2009), p. 257202. DOI: 10.1103/PhysRevLett.103.257202.

[246] S. Loth et al. “Controlling the state of quantum spins with electric currents”. In: *Nat. Phys.* 6.5 (Mar. 2010), pp. 340–344. ISSN: 1745-2481. DOI: 10.1038/nphys1616.

[247] J. Kondo. “Resistance Minimum in Dilute Magnetic Alloys”. In: *Prog. Theor. Phys.* 32.1 (July 1964), pp. 37–49. ISSN: 1347-4081. DOI: 10.1143/PTP.32.37.

[248] C. Hirjibehedin et al. “Large Magnetic Anisotropy of a Single Atomic Spin Embedded in a Surface Molecular Network”. In: *Science* 317.5842 (Aug. 2007), pp. 1199–1203. ISSN: 1095-9203. DOI: 10.1126/science.1146110.

[249] N. Lorente et al. “Efficient Spin Transitions in Inelastic Electron Tunneling Spectroscopy”. In: *Phys. Rev. Lett.* 103 (17 Oct. 2009), p. 176601. DOI: 10.1103/PhysRevLett.103.176601.

[250] M. Persson. “Theory of Inelastic Electron Tunneling from a Localized Spin in the Impulsive Approximation”. In: *Phys. Rev. Lett.* 103 (5 July 2009), p. 050801. DOI: 10.1103/PhysRevLett.103.050801.

[251] J. Fransson. “Spin Inelastic Electron Tunneling Spectroscopy on Local Spin Adsorbed on Surface”. In: *Nano Lett.* 9.6 (May 2009), pp. 2414–2417. ISSN: 1530-6992. DOI: 10.1021/nl901066a.

[252] J. Fernandez-Rossier. “Theory of Single-Spin Inelastic Tunneling Spectroscopy”. In: *Phys. Rev. Lett.* 102 (25 June 2009), p. 256802. DOI: 10.1103/PhysRevLett.102.256802.

[253] A. Otte et al. “The role of magnetic anisotropy in the Kondo effect”. In: *Nat. Phys.* 4.11 (Sept. 2008), pp. 847–850. ISSN: 1745-2481. DOI: 10.1038/nphys1072.

[254] M. Ternes. “Spin excitations and correlations in scanning tunneling spectroscopy”. In: *New J. Phys.* 17.6 (June 2015), p. 063016. ISSN: 1367-2630. DOI: 10.1088/1367-2630/17/6/063016.

[255] J. Gauyacq et al. “Magnetic transitions induced by tunneling electrons in individual adsorbed M-phthalocyanine molecules (M = Fe and Co)”. In: *Phys Rev B* 81.16 (Apr. 2010), p. 165423. ISSN: 1550-235X. DOI: 10.1103/physrevb.81.165423.

[256] C. Davisson and L. H. Germer. “Diffraction of Electrons by a Crystal of Nickel”. In: *Phys. Rev.* 30 (6 Dec. 1927), pp. 705–740. DOI: 10.1103/PhysRev.30.705.

[257] A. Zangwill. *Physics at surfaces*. Cambridge university press, 1988.

[258] M. VanHove et al. *Low-Energy Electron Diffraction: Experiment, Theory and Surface Structure Determination (Springer Series in Surface Sciences)*. Ed. by Springer-Verlag Berlin. Vol. 38. 7. Springer, July 1987, pp. 404–404. ISBN: 9783540162629. DOI: 10.1002/maco.19870380711.

[259] E. Wood. "Vocabulary of Surface Crystallography". In: *J. Appl. Phys.* 35.4 (Apr. 1964), pp. 1306–1312. DOI: 10.1063/1.1713610.

[260] E.G. McRae. "Self-consistent multiple-scattering approach to the interpretation of low-energy electron diffraction". In: *Surf. Sci.* 8.1–2 (July 1967), pp. 14–34. ISSN: 0039-6028. DOI: 10.1016/0039-6028(67)90071-4.

[261] E. Weihreter. *Compact synchrotron light sources*. World Scientific, 1996, p. 216. ISBN: 9810224591.

[262] Deutsches Elektronen-Synchrotron DESY. *How does a synchrotron radiation source work?* URL: https://photon-science.desy.de/research/students__teaching/primers/synchrotron_radiation/index_eng.html.

[263] Lightsources. *Light sources of the world*. https://lightsources.org/lightsources-of-the-world/.

[264] S. Mobilio et al. *Synchrotron Radiation: Basics, Methods and Applications. Basics, Methods and Applications*. Springer Berlin Heidelberg, 2015, p. 823. ISBN: 978-3-642-55314-1. DOI: 10.1007/978-3-642-55315-8.

[265] D. M. Mills et al. "Report of the Working Group on Synchrotron Radiation Nomenclature – brightness, spectral brightness or brilliance?" In: *J. Synchrotron Rad.* 12.3 (May 2005), p. 385. DOI: 10.1107/S090904950500796X.

[266] Wikipedia. *Synchrotron$_r$adiation*. https://en.wikipedia.org/wiki/Synchrotron$_r$adiation. URL: https://en.wikipedia.org/wiki/Synchrotron_radiation.

[267] H. Winick. "Synchrotron Radiation Sources – Present Capabilities and Future Directions". In: *J. Synch. Radiat.* 5.3 (May 1998), pp. 168–175. ISSN: 0909-0495. DOI: 10.1107/S0909049597018761.

[268] P. Willmott. *An Introduction to Synchrotron Radiation Techniques and Applications. Techniques and Applications*. Wiley, Mar. 2019, p. 504. ISBN: 9781119280392. DOI: 10.1002/9781119280453.

[269] J. Als-Nielsen. "X-rays and matter – the basic interactions". In: *Comptes Rendus. Physique* 9.5–6 (Apr. 2008), pp. 479–486. ISSN: 1878-1535. DOI: 10.1016/j.crhy.2008.01.002.

[270] G. Bunker. *Introduction to XAFS. A practical guide to X-ray Absorption Fine Structure Spectroscopy*. Cambridge University Press, 2010, p. 270. ISBN: 978-0521767750.

[271] W. Bambynek et al. "X-Ray Fluorescence Yields, Auger, and Coster-Kronig Transition Probabilities". In: *Rev. Mod. Phys.* 44 (4 Oct. 1972), pp. 716–813. DOI: 10.1103/RevModPhys.44.716.

[272] R. Carboni et al. “Self-absorption Correction Strategy for FluorescenceYield Soft Xray Near Edge Spectra”. In: *Phys. Scripta* (2005), p. 986. ISSN: 0031-8949. DOI: 10.1238/Physica.Topical.115a00986.

[273] A. Sapozhnik. “Magnetic Properties of Antiferromagnetic Mn Au: Exchange Interaction and Domain Manipulation”. PhD thesis. Johannes Gutenberg Unversität-Mainz, 2018.

[274] P. Carra et al. “X-ray circular dichroism and local magnetic fields”. In: *Phys. Rev. Lett.* 70 (5 Feb. 1993), pp. 694–697. DOI: 10.1103/PhysRevLett.70.694.

[275] B. T. Thole et al. “X-ray circular dichroism as a probe of orbital magnetization”. In: *Phys. Rev. Lett.* 68 (12 Mar. 1992), pp. 1943–1946. DOI: 10.1103/PhysRevLett.68.1943.

[276] Y. Teramura et al. “Effect of Coulomb Interaction on the X-Ray Magnetic Circular Dichroism Spin Sum Rule in 3dTransition Elements”. In: *J. Phys. Soc. Japan* 65.4 (Apr. 1996), pp. 1053–1055. ISSN: 1347-4073. DOI: 10.1143/JPSJ.65.1053.

[277] J. Jackson. *Classical electrodynamics*. Wiley, 1975, p. 848. ISBN: 978-0471431329.

[278] J. Stöhr. “X-ray magnetic circular dichroism spectroscopy of transition metal thin films”. In: *Journal of Electron Spectroscopy and Related Phenomena* 75 (1995), pp. 253–272.

[279] Y. Teramura et al. “Effect of Coulomb Interaction on the X-Ray Magnetic Circular Dichroism Spin Sum Rule in Rare Earths”. In: *J. Phys. Soc. Japan* 65.9 (Sept. 1996), pp. 3056–3059. ISSN: 1347-4073. DOI: 10.1143/JPSJ.65.3056.

[280] C. C. Yang and Q. Jiang. “Size and interface effects on critical temperatures of ferromagnetic, ferroelectric and superconductive nanocrystals”. In: *Acta Mater.* 53.11 (June 2005), pp. 3305–3311. DOI: 10.1016/j.actamat.2005.03.039.

[281] X. F. Cui et al. “Curie transition temperature of ferromagnetic low-dimensional metals”. In: *Thin Solid Films* 472.1-2 (Jan. 2005), pp. 328–333. DOI: 10.1016/j.tsf.2004.07.063.

[282] D. Sander. “The magnetic anisotropy and spin reorientation of nanostructures and nanoscale films”. In: *J. Phys.: Condens. Matter* 16.20 (May 2004), R603–R636. DOI: 10.1088/0953-8984/16/20/R01.

[283] H. j. Elmers. “Ferromagnetic Monolayers”. In: *Internat. J. Modern Phys. B* 09.24 (Oct. 1995), pp. 3115–3180. DOI: 10.1142/S0217979295001191.

[284] E. Lassner et al. *Tungsten: Properties, Chemistry, Technology of the Element, Alloys, and Chemical Compounds*. Springer, 1999, p. 416. ISBN: 0-306-45053-4.

[285] D. R. Lide. *CRC Handbook Chemistry and Physics, 85th Edition*. CRC, 2004, p. 2656. ISBN: 978-0-8493-0485-9.

[286] U. Gradmann and G. Waller. "Periodic lattice distortions in epitaxial films of Fe(110) on W(110)". In: *Surf. Sci.* 116.3 (May 1982), pp. 539–548. DOI: 10.1016/0039-6028(82)90363-6.

[287] H. J. Elmers et al. "Submonolayer Magnetism of Fe(110) on W(110): Finite Width Scaling of Stripes and Percolation between Islands". In: *Phys. Rev. Lett.* 73 (6 Aug. 1994), pp. 898–901. DOI: 10.1103/PhysRevLett.73.898.

[288] H. J. Elmers et al. "Magnetic Frustration in Ultrathin Fe Films". In: *Phys. Rev. Lett.* 75.10 (Sept. 1995), pp. 2031–2034. DOI: 10.1103/PhysRevLett.75.2031.

[289] H. J. Elmers et al. "Dipolar superferromagnetism in monolayer nanostripes of Fe(110) on vicinal W(110) surfaces". In: *Phys Rev B* 57.2 (Jan. 1998), R677–R680. DOI: 10.1103/PhysRevB.57.R677.

[290] H. J. Elmers et al. "Perpendicular magnetization and dipolar antiferromagnetism in double layer nanostripe arrays of Fe(110) on W(110)". In: *Appl. Phys. Lett.* 72.24 (June 1998), pp. 3211–3213. DOI: 10.1063/1.121552.

[291] H. J. Elmers et al. "Onset of perpendicular magnetization in nanostripe arrays of Fe on stepped W(110) surfaces". In: *Phys. Rev. B* 59 (5 Feb. 1999), pp. 3688–3695. DOI: 10.1103/PhysRevB.59.3688.

[292] H. J. Elmers et al. "Reorientation of magnetization states in Fe-nanostripe arrays on stepped W(110) caused by adsorption of CO, H2 and O2". In: *J. Magn. Magn. Mater.* 198-199 (June 1999), pp. 222–224. DOI: 10.1016/S0304-8853(98)01065-8.

[293] H. J. Elmers et al. "Morphology and magnetism of Fe on vicinal W(110) surfaces with different step orientation". In: *J. Magn. Magn. Mater.* 221.1-2 (Nov. 2000), pp. 219–223. DOI: 10.1016/S0304-8853(00)00374-7.

[294] R. M. Stern. "TUNGSTEN (110) SURFACE CHARACTERISTICS IN LOW-ENERGY ELECTRON DIFFRACTION". in: *Appl. Phys. Lett.* 5.11 (Dec. 1964), pp. 218–220. DOI: 10.1063/1.1723595.

[295] R. Baudoing and R.M. Stern. "Metastable surface structureof the W(110) face". In: *Surf. Sci.* 10.3 (June 1968), pp. 392–398. DOI: 10.1016/0039-6028(68)90107-6.

[296] M. Bode et al. "On the preparation and electronic properties of clean W(110) surfaces". In: *Surf. Sci.* 601.16 (Aug. 2007), pp. 3308–3314. DOI: 10.1016/j.susc.2007.06.017.

[297] I. Horcas et al. "WSXM: A software for scanning probe microscopy and a tool for nanotechnology". In: *Rev. Sci. Instrum.* 78.1 (Jan. 2007), p. 013705. DOI: 10.1063/1.2432410.

[298] M.A. Van Hove and S.Y. Tong. "Surface structures of W(110) and W(100) faces by the dynamical LEED approach". In: *Surf. Sci.* 54.1 (Jan. 1976), pp. 91–100. DOI: 10.1016/0039-6028(76)90090-X.

[299] J.P. Bourdin et al. “Is the (110) face of tungsten reconstructed?” In: *Solid State Commun.* 47.4 (July 1983), pp. 279–282. DOI: 10.1016/0038-1098(83)90563-x.

[300] P.J. Berlowitz et al. “Overlayer growth and chemisorptve properties of ultra-thin Fe films on W(110) and W(100)”. In: *Surf. Sci.* 231.3 (May 1990), pp. 315–324. DOI: 10.1016/0039-6028(90)90200-R.

[301] J. Kołaczkiewicz and E. Bauer. “V and Fe on the W(110) face”. In: *Surf. Sci.* 450.1-2 (Apr. 2000), pp. 106–116. DOI: 10.1016/S0039-6028(00)00056-X.

[302] M. Przybylski and U. Gradmann. “Ferromagnetic order in a Fe(110) monolayer on W(110) by Mössbauer spectroscopy”. In: *Phys. Rev. Lett.* 59 (10 Sept. 1987), pp. 1152–1155. DOI: 10.1103/PhysRevLett.59.1152.

[303] J. Korecki and U. Gradmann. “In Situ Mössbauer Analysis of Hyperfine Interactions near Fe(110) Surfaces and Interfaces”. In: *Phys. Rev. Lett.* 55 (22 Nov. 1985), pp. 2491–2494. DOI: 10.1103/PhysRevLett.55.2491.

[304] M. Bode et al. “Scanning tunneling spectroscopy of Fe/W(110) using iron covered probe tips”. In: *J. Vac. Sci. Technol. A: Vac. Surf. Films* 15.3 (May 1997), pp. 1285–1290. DOI: 10.1116/1.580577.

[305] R. Wiesendanger et al. “Spin-Polarized Scanning Tunneling Microscopy with Antiferromagnetic Probe Tips”. In: *Phys. Rev. Lett.* 88 (5 Jan. 2002), p. 057201. DOI: 10.1103/PhysRevLett.88.057201.

[306] M. Bode et al. “Spin-polarized scanning tunneling spectroscopy on Fe nanowires”. In: *Applied Physics A Materials Science &amp Processing* 72.S2 (Apr. 2001), S149–S153. DOI: 10.1007/s003390100792.

[307] U. Köhler et al. “Misfit-related effects in the epitaxial growth of iron on W(110)”. In: *Surf. Sci.* 331-333 (July 1995), pp. 878–884. DOI: 10.1016/0039-6028(95)00166-2.

[308] L. Z. Mezey et al. “The Surface Free Energies of Solid Chemical Elements: Calculation from Internal Free Enthalpies of Atomization”. In: *Jpn. J. Appl. Phys.* 21.11R (Nov. 1982), p. 1569. DOI: 10.1143/JJAP.21.1569.

[309] U. Gradmann et al. “Ferromagnetism in the thermodynamically stable monolayer Fe(110) on W(110), coated by Ag”. In: *App. Phys. A Sold. and Surf.* 49.6 (Dec. 1989), pp. 563–571. DOI: 10.1007/BF00616981.

[310] V. Hess. “Scanning tunneling microscopy of single-molecule magnets and hybrid-molecular magnets: Two approaches to molecular spintronics”. PhD thesis. Universität zu Köln, 2016.

[311] S. Mørup et al. “A new interpretation of Mössbauer spectra of microcrystalline goethite: -ferromagnetism”or -spin-glass”behaviour?” In: *J. Magn. Magn. Mater.* 40.1-2 (Dec. 1983), pp. 163–174. DOI: 10.1016/0304-8853(83)90024-0.

[312] R. Wiesendanger et al. “Magnetism of nanoscale Fe islands studied by spin-polarized scanning tunneling spectroscopy”. In: *Phys Rev B* 63.14 (Mar. 2001), p. 140407. DOI: 10.1103/PhysRevB.63.140407.

[313] R. Wiesendanger et al. “Spin-polarized scanning tunneling microscopy study of 360 walls in an external magnetic field”. In: *Phys. Rev. B* 67.2 (2003), p. 020401. DOI: 10.1103/PhysRevB.67.020401.

[314] R. Wiesendanger et al. “Domain Wall Orientation in Magnetic Nanowires”. In: *Phys. Rev. Lett.* 92.7 (Feb. 2004), p. 077207. DOI: 10.1103/PhysRevLett.92.077207.

[315] R. Wiesendanger et al. “Real-Space Observation of a Right-Rotating Inhomogeneous Cycloidal Spin Spiral by Spin-Polarized Scanning Tunneling Microscopy in a Triple Axes Vector Magnet”. In: *Phys. Rev. Lett.* 103 (15 Oct. 2009), p. 157201. DOI: 10.1103/PhysRevLett.103.157201.

[316] H. J. Elmers et al. “Adsorption-driven spin reorientation transition in sesquilayers of Fe(110) on W(110)”. In: *J. Magn. Magn. Mater.* 172.1-2 (Aug. 1997), pp. L1–L8. DOI: 10.1016/S0304-8853(97)00114-5.

[317] J. Stroscio et al. “Tunneling Spectroscopy of bcc (001) Surface States”. In: *Phys. Rev. Lett.* 75 (16 Oct. 1995), pp. 2960–2963. DOI: 10.1103/PhysRevLett.75.2960.

[318] M. Bode et al. “Magnetization-Direction-Dependent Local Electronic Structure Probed by Scanning Tunneling Spectroscopy”. In: *Phys. Rev. Lett.* 89 (23 Nov. 2002), p. 237205. DOI: 10.1103/PhysRevLett.89.237205.

[319] M. Pratzer and H. J. Elmers. “Magnetic and electronic properties of binary alloy monolayers: Fe_xMn_{1-x} and $Co_{1-x}Fe_x$ on W(110)”. In: *Phys Rev B* 69.13 (Apr. 2004), p. 134418. ISSN: 1550-235X. DOI: 10.1103/PhysRevB.69.134418.

[320] V. Ukraintsev. “Data evaluation technique for electron-tunneling spectroscopy”. In: *Phys. Rev. B* 53 (16 Apr. 1996), pp. 11176–11185. DOI: 10.1103/PhysRevB.53.11176.

[321] P. Ferriani et al. “Origin of the spin polarization of magnetic scanning tunneling microscopy tips”. In: *Phys. Rev. B* 82.5 (5 Aug. 2010), p. 054411. ISSN: 1550-235X. DOI: 10.1103/PhysRevB.82.054411.

[322] J. G. Smith. “Organic chemistry”. In: McGraw-Hill, 2010. Chap. 13 Mass Spectrometry and Infrared Spectroscopy, pp. 463–488. ISBN: 978-0-07-337562-5.

[323] J. M. North et al. “A Raman study of the single molecule magnet Mn -acetate and analogs”. In: *Solid State Commun.* 123.1–2 (July 2002), pp. 75–79. ISSN: 0038-1098. DOI: 10.1016/s0038-1098(02)00209-0.

[324] A. B. Sushkov et al. “Spin-vibrational coupling in the far-infrared spectrum of Mn -acetate”. In: *Phys. Rev. B* 66.14 (Oct. 2002), p. 144430. ISSN: 1095-3795. DOI: 10.1103/PhysRevB.66.144430.

[325] M. R. Pederson et al. “Fourth-Order Magnetic Anisotropy and Tunnel Splittings in Mn from Spin-Orbit-Vibron Interactions”. In: *Phys. Rev. Lett.* 89.9 (Aug. 2002), p. 097202. ISSN: 1079-7114. DOI: 10.1103/physrevlett.89.097202.

[326] Naoto Ishikawa et al. “Determination of Ligand-Field Parameters and f-Electronic Structures of Double-Decker Bis(phthalocyaninato)lanthanide Complexes”. In: *Inorg. Chem.* 42.7 (Mar. 2003), pp. 2440–2446. ISSN: 1520-510X. DOI: 10.1021/ic026295u.

[327] S. Fahrendorf. “Single NdPc Molecules on Surfaces: Adsorption, Interaction, and Molecular Magnetism”. PhD thesis. Universität zu Köln, 2013.

[328] M. Steinbrecher et al. “Absence of a spin-signature from a single Ho adatom as probed by spin-sensitive tunneling”. In: *Nat. Commun.* 7.1 (Feb. 2016). ISSN: 2041-1723. DOI: 10.1038/ncomms10454.

[329] A. A. Khajetoorians et al. “Spin Excitations of Individual Fe Atoms on Pt(111): Impact of the Site-Dependent Giant Substrate Polarization”. In: *Phys. Rev. Lett.* 111.15 (Oct. 2013), p. 157204. ISSN: 1079-7114. DOI: 10.1103/physrevlett.111.157204.

[330] Sebastian Loth et al. “Spin-polarized spin excitation spectroscopy”. In: *New J. Phys.* 12.12 (Dec. 2010), p. 125021. ISSN: 1367-2630. DOI: 10.1088/1367-2630/12/12/125021.

[331] Y. Yayon et al. “Observing Spin Polarization of Individual Magnetic Adatoms”. In: *Phys. Rev. Lett.* 99.6 (Aug. 2007), p. 067202. ISSN: 1079-7114. DOI: 10.1103/physrevlett.99.067202.

[332] Vadapalli Chandrasekhar et al. “Trinuclear Heterobimetallic Ni_2Ln complexes $[L_2Ni_2Ln][ClO_4]$ (Ln = La, Ce, Pr, Nd, Sm, Eu, Gd, Tb, Dy, Ho, and Er; LH_3= (S)P[N(Me)N CH−C_6H_3-2-OH-3-OMe]$_3$): From Simple Paramagnetic Complexes to Single-Molecule Magnet Behavior”. In: *Inorg. Chem.* 47.11 (May 2008), pp. 4918–4929. ISSN: 1520-510X. DOI: 10.1021/ic800199x.

[333] David Coffey et al. “Antiferromagnetic Spin Coupling between Rare Earth Adatoms and Iron Islands Probed by Spin-Polarized Tunneling”. In: *Sci. Rep.* 5.1 (Sept. 2015). ISSN: 2045-2322. DOI: 10.1038/srep13709.

[334] E Burzo et al. “On the R 5d band polarization in rare-earth–transition metal compounds”. In: *J. Phys. Condens. Matter* 23.2 (Dec. 2010), p. 026001. ISSN: 1361-648X. DOI: 10.1088/0953-8984/23/2/026001.

[335] J.J.M. Franse and R.J. Radwański. “Magnetic properties of binary rare-earth 3d-transition-metal intermetallic compounds”. In: *Handbook of Magnetic Materials*. Elsevier, 1993. Chap. 5, pp. 307–501. DOI: 10.1016/s1567-2719(05)80046-0.

[336] Börje Johansson et al. “Magnetism in Rare-Earth Metals and Rare-Earth Intermetallic Compounds”. In: *Phys. Scripta* T39 (Jan. 1991), pp. 100–109. ISSN: 1402-4896. DOI: 10.1088/0031-8949/1991/t39/014.

[337] I A Campbell. "Indirect exchange for rare earths in metals". In: *J. Phys. F: Met. Phys.* 2.3 (May 1972), pp. L47–L50. ISSN: 0305-4608. DOI: 10.1088/0305-4608/2/3/004.

[338] Dante Gatteschi et al. "Synthesis, crystal structure, and magnetic properties of tetranuclear complexes containing exchange-coupled dilanthanide-dicopper(lanthanide = gadolinium, dysprosium) species". In: *Inorg. Chem.* 29.9 (May 1990), pp. 1750–1755. ISSN: 1520-510X. DOI: 10.1021/ic00334a031.

[339] O. Kahn et al. "Crystal structure and magnetic properties of [Ln2Cu4] hexanuclear clusters (where Ln = trivalent lanthanide). Mechanism of the gadolinium(III)-copper(II) magnetic interaction". In: *JACS* 115.5 (Mar. 1993), pp. 1822–1829. ISSN: 1520-5126. DOI: 10.1021/ja00058a029.

[340] S. K. Singh et al. "Role of Magnetic Exchange Interactions in the Magnetization Relaxation of 3d-4f Single-Molecule Magnets: A Theoretical Perspective". In: *Chem. - Eur. J.* 22.2 (Nov. 2015), pp. 672–680. DOI: 10.1002/chem.201503102.

[341] T. Gupta and Other. "Role of Single-Ion Anisotropy and Magnetic Exchange Interactions in Suppressing Zero-Field Tunnelling in 3d-4f Single Molecule Magnets". In: *Inorg. Chem.* 55.21 (Oct. 2016), pp. 11201–11215. ISSN: 1520-510X. DOI: 10.1021/acs.inorgchem.6b01831.

[342] Jordi Cirera and Eliseo Ruiz. "Exchange coupling in Cu Gd dinuclear complexes: A theoretical perspective". In: *Comptes Rendus. Chimie* 11.10 (Aug. 2008), pp. 1227–1234. ISSN: 1878-1543. DOI: 10.1016/j.crci.2008.04.012.

[343] J. Dreiser et al. "Direct observation of a ferri-to-ferromagnetic transition in a fluoride-bridged 3d–4f molecular cluster". In: *Chem. Sci.* 3.4 (2012), pp. 1024–1032. DOI: 10.1039/C2SC00794K.

[344] S. K. Singh et al. "Theoretical studies on 3d-Gd and 3d-Gd-3d complexes: Effect of metal substitution on the effective exchange interaction". In: *Polyhedron* 66 (Dec. 2013), pp. 81–86. ISSN: 0277-5387. DOI: 10.1016/j.poly.2013.02.037.

[345] *Noll et. al, The mechanics of the VEKMAG experiment, Proc. of MEDSI2016, Barcelona, Spain.* 2016, pp. 370–373.

[346] A. Alhassanat et al. "Solvent-induced High-spin Transition In Double-decker 3d-4f Metallacrowns". In: *Phys Rev B* 99.10 (Mar. 2019), p. 104404. DOI: 10.1103/PHYSREVB.99.104404.

[347] A. Rauguth et al. "Anisotropy of 4f states in 3d-4f single-molecule magnets". In: *Phys Rev B* 105.13 (Apr. 2022), p. 134415. DOI: 10.1103/PHYSREVB.105.134415.

[348] D. J. Griffiths. *Introduction To Electrodynamics*. Cambridge University Press, 2018. Chap. Ch.3, pp. 151–166. ISBN: 978-1-108-42041-9.

[349] S. Tsoi et al. “van der Waals Screening by Single-Layer Graphene and Molybdenum Disulfide”. In: *ACS Nano* 8.12 (Dec. 2014), pp. 12410–12417. DOI: 10.1021/nn5050905.

[350] K. Jackson et al. “Si clusters are more metallic than bulk Si”. In: *J. Chem. Phys.* 145.24 (Dec. 2016), p. 244302. DOI: 10.1063/1.4972813.

[351] E. Zaremba et al. “Van Der Waals Interaction Between An Atom And A Solid Surface”. In: *Phys. Rev. B* 13 (6 Mar. 1976), pp. 2270–2285. DOI: 10.1103/PhysRevB.13.2270.

[352] H. J. Butt. *Surface and Interfacial Forces*. Wiley-VCH, 2010, p. 421. ISBN: 9783527408498.

[353] J. F. Dobson. “Beyond Pairwise Additivity In London Dispersion Interactions”. In: *Int. J. Quantum Chem.* 114.18 (Feb. 2014), pp. 1157–1161. DOI: 10.1002/qua.24635.

[354] J. Hermann et al. “First-principles Models For Van Der Waals Interactions In Molecules And Materials: Concepts, Theory, And Applications”. In: *Chem Rev* 117.6 (Mar. 2017), pp. 4714–4758. DOI: 10.1021/acs.chemrev.6b00446.

[355] A. Ambrosetti et al. “Wavelike Charge Density Fluctuations And Van Der Waals Interactions At The Nanoscale”. In: *Science* 351.6278 (Mar. 2016), pp. 1171–1176. DOI: 10.1126/science.aae0509.

[356] M. Goerz. *Report on the Construction of the PM2-Beamline at BESSY II*. tech. rep. Fortgeschrittenenpraktikum Physik. Freie Universität Berlin, Nov. 2007.

[357] G. Van der Laan et al. “X-ray magnetic circular dichroism—A versatile tool to study magnetism”. In: *Coord. Chem. Rev.* 277-278 (Oct. 2014), pp. 95–129. DOI: 10.1016/j.ccr.2014.03.018.

[358] G. Van der Laan et al. “Angular dependent photoelectric yield.” In: *J. Electron Spectrosc. Relat. Phenom.* 46.1 (1988), pp. 123–129. DOI: 10.1016/0368-2048(88)80010-0.

[359] P. Bandyopadhyay. *X-ray absorption edges calculator(Au)*. URL: http://csrri.iit.edu/cgi-bin/period-form?ener=&name=Au.

[360] J. P. Crocombette et al. “The Importance Of The Magnetic Dipole Term In Magneto-circular X-ray Absorption Dichroism For 3d Transition Metal Compounds”. In: *J. Phys.: Condens. Matter* 8.22 (May 1996), pp. 4095–4105. DOI: 10.1088/0953-8984/8/22/013.

[361] S. P. Collins et al. “An Investigation Of Uranium $M_{4,5}$ Edge Magnetic X-ray Circular Dichroism In US”. in: *J. Phys.: Condens. Matter* 7.48 (1995), p. 9325.

[362] R. Wu et al. “First Principles Investigations Of Mcd Spectra And Sum Rules For 3d Transition Metal Surfaces”. In: *Journal of magnetism and magnetic materials* 132.1-3 (1994), pp. 103–123.

[363] C. T. Chen et al. “Experimental Confirmation Of The X-ray Magnetic Circular Dichroism Sum Rules For Iron And Cobalt”. In: *Physical review letters* 75.1 (Feb. 1995), p. 152. DOI: 10.1107/S1600576719014092.

[364] J. Ph. Schillé et al. “4f Orbital And Spin Magnetism In Cerium Intermetallic Compounds Studied By Magnetic Circular X-ray Dichroism”. In: *Phys Rev B* 50.5 (1994), p. 2985.

[365] F. Hippert. *Neutron and X-ray Spectroscopy*. Springer, 2005, p. 566. ISBN: 1402033362.

[366] B. T. Thole et al. “3d x-ray-absorption lines and the 3d 4f ^{1} multiplets of the lanthanides”. In: *Phys. Rev. B* 32 (8 Oct. 1985), pp. 5107–5118. DOI: 10.1103/PhysRevB.32.5107.

[367] G. Kaindl et al. “M-edge x-ray absorption spectroscopy of 4f instabilities in rare-earth systems (invited)”. In: *J Appl Phys* 55.6 (Mar. 1984), pp. 1910–1915. DOI: 10.1063/1.333517.

[368] T. Jo and G. Sawatzky. “Ground state of ferromagnetic nickel and magnetic circular dichroism in Ni 2p core x-ray-absorption spectroscopy”. In: *Phys Rev B* 43 (10 Apr. 1991), pp. 8771–8774. DOI: 10.1103/PhysRevB.43.8771.

[369] G. Van der Laan et al. “Multiplet Structure In The $L_{2,3}$ X-ray-absorption Spectra: A Fingerprint For High-and Low-spin Ni^{2+} Compounds”. In: *Phys Rev B* 37.11 (1988), p. 6587.

[370] J. M. D. Coey. *Magnetism and magnetic materials*. Cambridge University Press, 2010, p. 614. ISBN: 978-0-521-81614-4.

[371] P. Motais et al. “On the relative intensities of the M_{IV} and M_V absorption and emission spectra of La^{3+}”. In: *J. Phys. F: Met. Phys.* 11.7 (July 1981), pp. L169–L171. DOI: 10.1088/0305-4608/11/7/007.

[372] M. Arrio et al. “XMCD Measurements in a high T_C molecular based magnet”. In: *Proceedings of the 11th International Conference on Vacuum Ultraviolet Radiation Physics*. Ed. by T. Miyahara et al. Amsterdam: Elsevier, 1996, pp. 203–208. ISBN: 978-0-444-82245-1. DOI: 10.1016/B978-0-444-82245-1.50054-6.

[373] D. Klar et al. “Oxygen-tuned magnetic coupling of Fe-phthalocyanine molecules to ferromagnetic Co films”. In: *Phys. Rev. B* 88 (22 Dec. 2013), p. 224424. DOI: 10.1103/PhysRevB.88.224424.

[374] B. T. Thole et al. “Strong magnetic dichroism predicted in the $M_{4,5}$ X-ray absorption spectra of magnetic rare-earth materials”. In: *Phys. Rev. Lett.* 55.19 (1985), p. 2086.

[375] T. Brown. “Chemistry the central science. the central science”. In: 12th ed. Prentice Hall, 2012, pp. 987–995. ISBN: 978-0-321-69672-4.

[376] Clare F. Macrae et al. “Mercury 4.0: from visualization to analysis, design and prediction”. In: *J. Appl. Crystallogr.* 53.1 (Feb. 2020), pp. 226–235. ISSN: 1600-5767. DOI: 10.1107/s1600576719014092.

[377] B. T. Thole et al. “Branching Ratio in X-ray Absorption Spectroscopy”. In: *Phys Rev B* 38.5 (1988), p. 3158.

[378] I.D. Ryabov. “On the Generation of Operator Equivalents and the Calculation of Their Matrix Elements”. In: *J. Magn. Reson.* 140.1 (Sept. 1999), pp. 141–145. DOI: 10.1006/jmre.1999.1783.

[379] C. Bonnelle et al. “Photoabsorption in the vicinity of 3d edges of Eu and Gd”. In: *J. Phys. B: At. Mol. Phys.* 10.5 (Apr. 1977), pp. 795–801. DOI: 10.1088/0022-3700/10/5/015.

[380] C. W. Chuang et al. “Electronic structure investigation of GdNi using x-ray absorption, magnetic circular dichroism, and hard x-ray photoemission spectroscopy”. In: *Phys Rev B* 101.11 (Mar. 2020), p. 115137. DOI: 10.1103/PhysRevB.101.115137.

[381] M. Mizumaki and o. “Verification of Ni magnetic moment in $GdNi_2$ Laves phase by magnetic circular dichroism measurement”. In: *Phys Rev B* 67.13 (Apr. 2003), p. 132404. DOI: 10.1103/PhysRevB.67.132404.

[382] K. Yano et al. “Revelation of Ni magnetic moment in GdNi single crystal by soft X-ray magnetic circular dichroism”. In: *Solid State Commun.* 136.2 (Oct. 2005), pp. 67–70. DOI: 10.1016/j.ssc.2005.07.004.

[383] E. Stavitski et al. “The CTM4XAS program for EELS and XAS spectral shape analysis of transition metal L edges”. In: *Micron* 41.7 (Oct. 2010), pp. 687–694. DOI: 10.1016/j.micron.2010.06.005.

[384] R. D. Cowan. “The Theory of Atomic Structure and Spectra”. In: University of California Press, Dec. 1981. Chap. 6, pp. 156–165. DOI: 10.1525/9780520906150.

[385] M. Pompa et al. “Self-absorption Effect in Fluorescence Xas of Polarization Dependent White Lines”. In: *Phys. B: Condens. Matter* 208 (1995), pp. 143–144.

[386] A. Erbil et al. “Total-electron-yield current measurements for near-surface extended x-ray-absorption fine structure”. In: *Phys Rev B* 37.5 (Feb. 1988), pp. 2450–2464. DOI: 10.1103/PhysRevB.37.2450.

[387] J. Jaklevic et al. “Fluorescence detection of exafs: Sensitivity enhancement for dilute species and thin films”. In: *Solid State Commun.* 23.9 (Sept. 1977), pp. 679–682. DOI: 10.1016/0038-1098(77)90548-8.

[388] F. M. F. de Groot et al. “Fluorescence yield detection: Why it does not measure the X-ray absorption cross section”. In: *Solid State Commun.* 92.12 (Dec. 1994), pp. 991–995. DOI: 10.1016/0038-1098(94)90027-2.

[389] R. Nakajima et al. “Electron-yield saturation effects in L-edge x-ray magnetic circular dichroism spectra of Fe, Co, and Ni”. In: *Phys. Rev. B* 59 (9 Mar. 1999), pp. 6421–6429. DOI: 10.1103/PhysRevB.59.6421.

[390] S. Eisebitt et al. “Determination of absorption coefficients for concentrated samples by fluorescence detection”. In: *Phys Rev B* 47.21 (June 1993), pp. 14103–14109. DOI: 10.1103/PhysRevB.47.14103.

[391] S. Voss et al. “Electronic structure of Mn_{12} derivatives on the clean and functionalized Au surface”. In: *Phys Rev B* 75.4 (Jan. 2007), p. 045102. DOI: 10.1103/PhysRevB.75.045102.

[392] N. Y. Schmidt et al. “Structural and magnetic properties of FePt-Tb alloy thin films”. In: *Phys Rev B* 100.6 (Aug. 2019), p. 064428. DOI: 10.1103/PhysRevB.100.064428.

[393] M. W. Haverkort et al. “Multiplet Ligand-field Theory Using Wannier Orbitals”. In: *Phys Rev B* 85.16 (Apr. 2012), p. 165113. DOI: 10.1103/PhysRevB.85.165113.

[394] J. Sievers. “Asphericity of 4f-shells in their Hund’s rule ground states”. In: *Z. Phys. B Condens. Matter* 45.4 (Dec. 1982), pp. 289–296. DOI: 10.1007/BF01321865.

[395] J. Rinehart et al. “A N_2^{3-} Radical-bridged Terbium Complex Exhibiting Magnetic Hysteresis At 14 K”. in: *J. Am. Chem. Soc.* 133.36 (2011), pp. 14236–14239.

[396] J. Liu et al. “Symmetry strategies for high performance lanthanide-based single-molecule magnets”. In: *Chem. Soc. Rev.* 47.7 (2018), pp. 2431–2453. DOI: 10.1039/c7cs00266a.

[397] J. Stoehr. “Exploring the microscopic origin of magnetic anisotropies with X-ray magnetic circular dichroism (XMCD) spectroscopy”. In: *J. Magn. Magn. Mater.* 200.1-3 (Oct. 1999), pp. 470–497. DOI: 10.1016/S0304-8853(99)00407-2.

[398] N. F. Chilton et al. “An electrostatic model for the determination of magnetic anisotropy in dysprosium complexes”. In: *Nat. Commun.* 4.1 (Oct. 2013). DOI: 10.1038/ncomms3551.

[399] S. Jiang and S. Qin. “Prediction of the quantized axis of rare-earth ions: the electrostatic model with displaced point charges”. In: *Inorg. Chem. Front.* 2.7 (2015), pp. 613–619. DOI: 10.1039/c5qi00052a.

[400] M. Briganti et al. “Magnetic Anisotropy Trends along a Full 4f-Series: The f^{n+7} Effect”. In: *J. Am. Chem. Soc.* 143.21 (May 2021), pp. 8108–8115. DOI: 10.1021/jacs.1c02502.

[401] S. K. Langley et al. “A Cr Dy Single-Molecule Magnet: Enhancing the Blocking Temperature through 3d Magnetic Exchange”. In: *Angew. Chem-ger. Edit.* 125.46 (Sept. 2013), pp. 12236–12241. ISSN: 1521-3757. DOI: 10.1002/ange.201306329.

List of Figures

List of Tables

Appendix

A.1. Fitting the dI/dU spectra to the background tunneling function

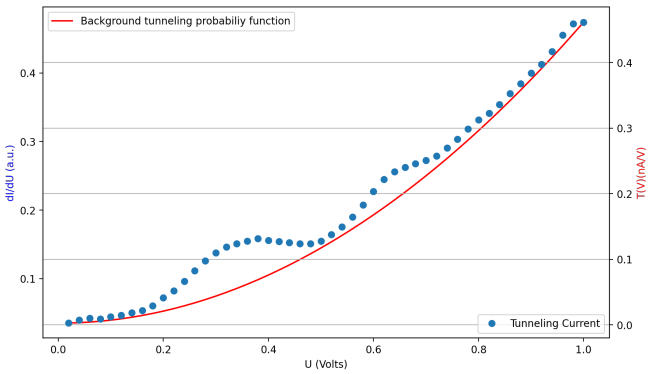

Figure 7.1: Fitting the dI/dU spectra at positive voltages (> 0.5 V) to the background tunneling function.

Fitting parameters	A	B	C	D
Values	1.49×10^6	8.8×10^{-5}	6.66	2.98×10^6

Table 7.1: The fitting optimized parameters of the tunneling background function from the data.